Spring 3-27-2018

Development of a Novel Framework for the Application of Signature Based Safeguards (SBS) to Pyroprocessing

Philip Leo Lafreniere
University of New Mexico

Philip Lafreniere
Candidate

Nuclear Engineering
Department

This dissertation is approved, and it is acceptable in quality and form for publication:

Approved by the Dissertation Committee:

Cassiano Endres De Oliviera , Chairperson

Edward Blandford

Edward Arthur

Adam Hecht

Plamen Atanassov

Mark Williamson

Ben Cipiti

DEVELOPMENT OF A NOVEL FRAMEWORK FOR THE APPLICATION OF SIGNATURE BASED SAFEGUARDS (SBS) TO PYROPROCESSING

by

PHILIP LAFRENIERE

M.S. Nuclear Engineering, University of New Mexico, 2014
B.S., Nuclear Engineering, University of New Mexico, 2013

DISSERTATION

Submitted in Partial Fulfillment of the
Requirements for the Degree of

Doctorate of Philosophy
Engineering

The University of New Mexico
Albuquerque, New Mexico

May, 2018

DEDICATION

To Kathy, my Moose sponsor, may you rest in peace.

ACKNOWLEDGEMENTS

The author would like to acknowledge several individuals without whom the work of this thesis would have not been possible. First and foremost my advisor Edward Blandford, who introduced me to the subject of pyroprocessing safeguards and provided me guidance throughout my PhD.

I would also like to acknowledge my committee members. I would like to acknowledge Edward Arthur of the University of New Mexico for your perspective and assistance that you have provided as well as taking the lead in the last year as my primary point of contact for advancing my research. To Benjamin Cipiti of Sandia National Lab, without whose initial work, analyses, and advice, this work may not have been carried out as well as the permission to use and modify Echem SSPM for the purpose of this research. To Adam Hecht, for bringing his own safeguards perspective outside PM to the dissertation and to Plamen Attanasov for his perspective on electrochemistry outside of pyroprocessing. To Mark Williamson for contributing support through knowledge learned from many years of pyroprocessing experience as well as support through the internship opportunity I had at the Argonne National Lab to expand my experimental knowledge. Finally, thank you to Cassiano De Oliviera for agreeing to serve and act as chair on my committee and providing a perspective outside of safeguards and electrochemistry for my work.

In addition, this work would not have been possible without the assistance of several parties. I cannot express enough gratitude to Robert Hoover of INL who taught me most of the basic knowledge that I posses about electrochemistry. To Michael Simpson, Devin Rappleye, and Chao Zhang of the University of Utah, your support and collaboration with this work has been instrumental to its direction and completion.

Finally, thank you to Il Soon Hwang of Seoul National University and Man-Sung Yim of KAIST for developing and allowing the use of REFIN and ERAD.

Finally, I would like to say thank you to my family, East Heights Moose Lodge 2241, my church, my roommates (Big guy, Marquez, and Trader Vic), and God who kept me motivated and focused throughout this entire process.

DEVELOPMENT OF A NOVEL FRAMEWORK FOR THE APPLICATION OF SIGNATURE BASED SAFEGUARDS (SBS) TO PYROPROCESSING

by

PHILIP LAFRENIERE

M.S. Nuclear Engineering, University of New Mexico, 2014
B.S., Nuclear Engineering, University of New Mexico, 2013
PhD Engineering, University of New Mexico, Spring 2018

ABSTRACT

Traditional nuclear material accountancy (NMA) faces several challenges when applied to pyroprocessing facilities. To address these challenges, alternative methods of safeguarding nuclear material are being developed. One method is process monitoring (PM). PM involves taking operational process data and applying it to safeguards using an advanced framework. Signature Based Safeguards (SBS), a proposed PM framework, involves the identification of anomalous scenarios and the subsequent identification and detection of their respective PM signatures from a system of measurements. SBS has previously focused on failure modes that result in transfer of mass to unexpected places in the mass flowsheet. This work developed a methodology for the identification of failure modes and determined their effect on the facility mass balance. To develop a methodology for the identification of off-normal scenarios, a modified failure mode and effects analysis (FMEA) was developed with a safeguards focus and applied to a commercial pyroprocessing electrorefiner (ER). The modified FMEA significantly expands the understanding of ER failures. To determine the effect of the failure modes on

the mass balance, work was first performed to determine if the computational ER model Enhanced REFIN with Anodic Dissolution (ERAD) could be used as modeling tool for SBS. This was done by performing experiments to act as analogues for a postulated failure mode. These experiments were then modeled in ERAD and the computational and analytical data compared. The results indicated that ERAD is an effective tool for qualitative analysis of pyroprocessing but not for quantitative design purposes. Simulations of several failure modes identified by the modified FMEA were undertaken to produce data to be integrated into the pyroprocessing systems model Echem SSPM. Eleven different identified failure modes were simulated for four base operational cases. The simulations effectively produced results that could be used as ER data in the SSPM Echem. Simulations in Echem utilizing this integrated ERAD data allow the impact of the failure mode on the mass balance of the facility to be assessed. The results of these simulations implied that failures modes can affect the mass balance and must be assessed for operational effects.

TABLE OF CONTENTS

LIST OF FIGURES

LIST OF TABLES

CHAPTER 1: INTRODUCTION

1.1: PROBLEM

Electrochemical reprocessing, more commonly known as pyroprocessing, has been suggested as an alternative to aqueous methods for recycling used nuclear fuel (UNF) [1]. Pyroprocessing utilizes electrochemical methods within high temperature eutectic salt baths enclosed within hot cells [2]. This is contrary to aqueous reprocessing's room temperature reaction chemistry and chemical reactor vessels [3]. The fuel produced is a metallic product that can be utilized in fast reactors, minimizing the total waste inventory and effectively closing the fuel cycle [2]. Pyroprocessing is considered a favorable option for fuel processing due to both operational and safeguards advantages [1]. From an operations perspective, pyroprocessing requires a significantly smaller geographic footprint than aqueous facilities and produces more compact waste products [4]. The safeguards advantages are reduced physical access to material, as all operations are within a hot cell. In addition, electrochemical operations do not include a separates Pu stream as in aqueous reprocessing [4]. Weapons grade Pu can only be obtained through further aqueous treatment of the used fuel product. However, electrochemical reprocessing faces several challenges in effectively implementing material safeguards to meet the requirements of the International Atomic Energy Agency (IAEA) [1].

The most difficult challenge in implementing safeguards in a proposed pyroprocessing facility is the ability to perform mass balancing adequately on the material flow within the facility [5]. This is an issue not unique to pyroprocessing facilities and has been seen in the completed Japanese Rokkasho facility which despite

construction has yet to commence operations due to not being able to meet IAEA safeguards material balance requirements [6]. The most difficult aspect of this is that traditional nuclear material accountancy (NMA) methods cannot produce a standard error of inventory difference (SEID) of the mass balance that meets the 95 percent confidence interval required in a high throughput facility with current safeguards technology [5]. As all material present is not produced in bulk forms, e.g. fuel assemblies in a nuclear power plant or canisters of UF_6 in enrichment facilities, each product and input must be assessed for special nuclear material. The accuracy of current material quantification techniques is not accurate enough to reduce the total error to the required SEID.

The challenge for attaining an adequate SEID is exacerbated by several unique qualities of pyroprocessing [1]. The first quality is the lack of an input accountability tank (IAT) as in an aqueous facility that contains a homogenous mixture of dissolved fuel that can be sampled to determine the input of nuclear material [1]. Instead, pyroprocessing facility operators are required to utilize less accurate fuel assembly assay methods and modeled burnup data to develop the input mass inventory. In addition, for economic reasons, a pyroprocessing facility cannot be effectively flushed out for an end of balance period assessment [1]. This is due to the need for the ER salt inventory to be at steady state for effective separations operations. To flush it out would require the ER inventory to be built up to a steady state at the start of the next balance period. As a result, a flush out would be time intensive and significantly reduce facility throughput.

To address these challenges, alternative safeguards methods are being developed to assist in reducing the SEID [5, 7, 8, 9]. The two primary alternative methods currently being explored are near real time accountancy (NRTA) and process monitoring (PM).

NRTA involves performing the mass balance over shorter balance periods to determine the flow of material as it happens utilizing integrated mass quantification measurements [1, 5]. PM determines signatures of anomalous operations from process data such as temperature, density, pressure etc [5, 8, 10, 11]. From this data, the goal is to determine if material diversion scenarios are occurring through monitoring process data and alerting the operator if they occur. PM is proposed as a complementary method to mass balance techniques to reduce the SEID of the facility [5]. The work of this dissertation is performed to assess the PM method known as signature based safeguards (SBS) on facility SEID [9].

SBS is a proposed PM method that relies on a sequence of major steps [9]. The first of these steps is selection of models for both the entire system to be safeguarded, in this case a pyroprocessing facility, and the models to be utilized to simulate unit operations and PM measurements. The second step is the identification of off-normal operations that could potentially occur within a selected unit operation. The third step is the simulation of these off normal operations within unit operations models and the identification of signatures unique to the anomalous operation. The final step involves the simulation of the failure modes within the context of the entire system to determine their effects on mass balance and PM measurement response. The results of this final step inform the design and further refine the model to simulate and detect off-normal occurrences within the system increasing the overall probability of detection (POD). This sequence of steps is visualized in the flow sheet in Figure 1.

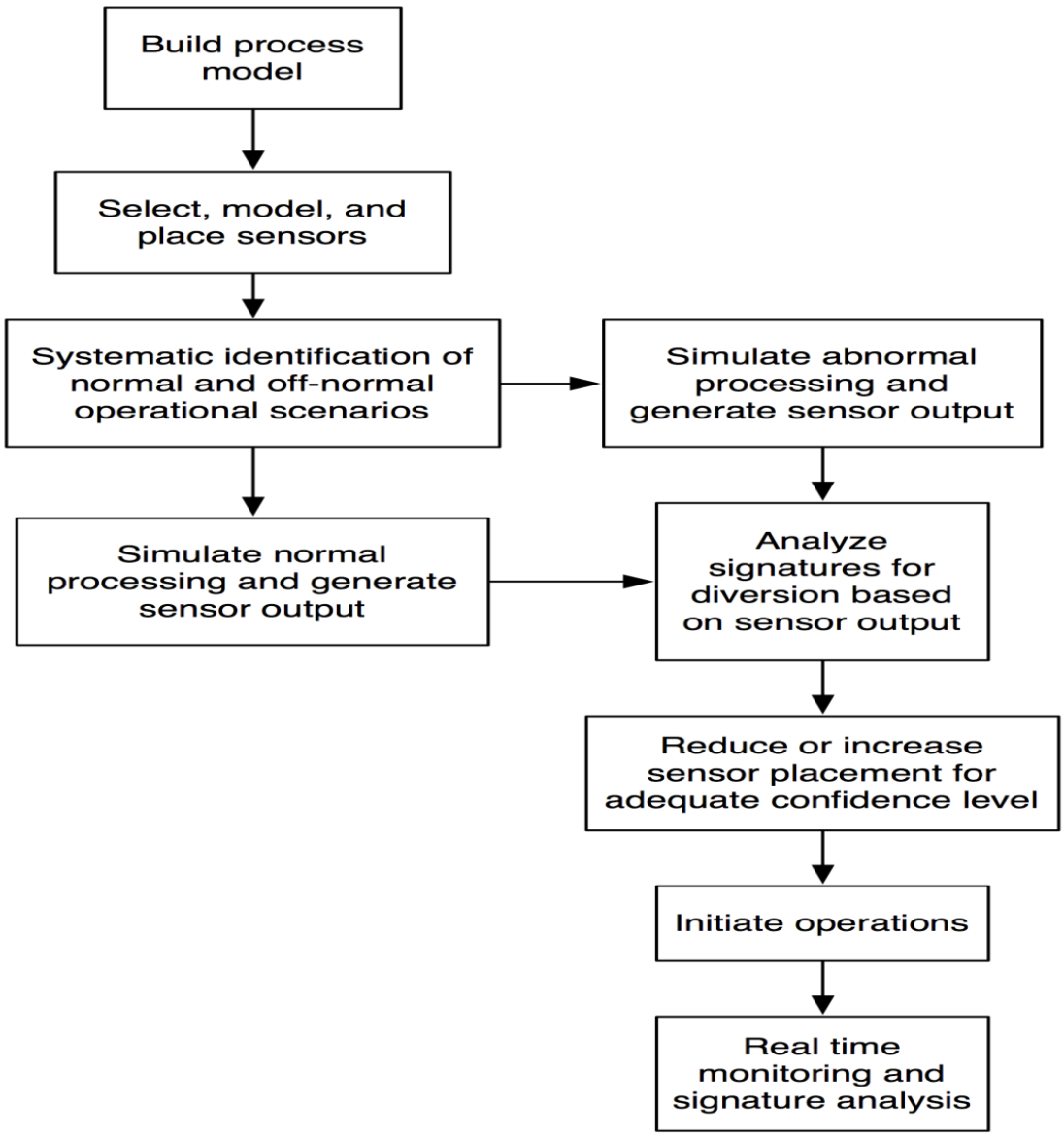

Figure 1-Flowsheet of SBS Method [9]

1.2: MOTIVATION

Current investigations of SBS involve applying the method to anomalous scenarios involving failure modes in unit operation equipment. Past research focused on failures in the unit operations of the electrorefiner (ER) and cathode processor (CP). This

dissertation focuses solely on failure modes in the ER. The research in the past operated with the assumption that failure modes can cause issues in traditional NMA by mass transferring to locations in the flow sheet where it is not expected. The previous work confirmed these assumptions [12]. However, no work has been performed to develop a systematic method to identify and classify failure modes for the purpose of simulation. In addition, no work has been performed to determine via simulation the effect of failure modes on the mass balance from the perspective of the entire facility. A better understanding of these effects could help to better judge the role of SBS in predicting and detecting these anomalous occurrences. I undertook the research of this dissertation to address these two issues.

Developing an organized methodology of failure mode identification is beneficial to expanding the scope of the simulation campaigns undertaken to inform design in SBS. Failure modes need to be identified as they can have effects from both an operations and safeguards perspective. The major operation effects are the need for holdup for repairs. From a safeguards perspective, failure modes can generate transport of materials to locations within the flowsheet in which they are not expected potentially disrupting the mass balance of the facility [12]. Past identification efforts have involved collaborative discussion among researchers for identification and effects analysis, but did not follow a set framework for their identification and documentation [13]. This work applies techniques involving traditional Failure Mode and Effects Analysis (FMEA) to expand the failure modes identified and to give a better sense of the small and large scale effects as well as to assess their potential severity for safeguards related effects. This FMEA is modified to have a safeguards rather than safety focus with regards to effects and

severity. In doing so, I develop an approach to better carry out this stage and further expand the simulation campaigns beyond what has in the past been performed. Also, the organized method allows the design process to focus specifically on addressing more relevant scenarios with higher severity in their design process.

In addition to ranking and identifying the failure modes, I developed a manner of assessing, via simulation, the effects of the failure modes on unit operations and at the systems level. The ultimate purpose was to determine the effectiveness of SBS in identifying and detecting failure modes and with that assess how it may assist in the safeguarding of a facility when combined with NMA. To do this, I integrated physical simulation data into a systems model to have the best understanding of the effects of failure modes on the safeguard mass balance. To do so, I first needed to ensure experimentally that the model previously used for ER simulation, ERAD, was an adequate tool for the simulation of ER failure modes. I performed experimental research to analyze the assumptions and applicability of ERAD. ERAD is a one-dimensional electrochemical transport code which calculates cell potential and changes in material composition within an ER cell at a set current and total operation time [14]. ERAD has had little previous experimental work applied to determine its efficacy and potential usefulness for analysis of off-normal operations. An analytical experimental campaign allows the ERAD to be used with greater confidence as a tool for simulating failure mode and other anomalous scenarios. I performed analogous experiments for a failure mode scenario and compared the results to data from ERAD simulations of that same failure mode. Thus, from providing input into the applicability of the ERAD model, this experimental work provides insights into the results of the ERAD simulations used to

assess the efficacy of the developed FMEA method and the data produced for failure mode simulation at the systems level.

With an understanding of the applicability of ERAD, simulations were performed of identified failure modes from the FMEA to produce data to analyze systems level effects. These simulations expand the scope normal and off-normal scenario unit operation simulations well beyond the studies previously performed [15]. By simulating identified failure modes to test predictions from FMEA analysis, the use of FMEA to as the primary method for identifying failure modes can be verified. In addition to assisting FMEA methods and application development, the ERAD simulations of failure modes significantly assist in the development of systems models of pyroprocessing systems. It does so by producing datasets that can be integrated into a subsystem model within a pyroprocessing system model to simulate ER operations. Currently, systems models do not utilize actual transport calculations but use assumptions as to the separation efficiencies of the unit operation equipment. These assumptions are informed by past operational experience, particularly at the fuel condition facility (FCF) at the Idaho National Laboratory (INL), formerly Argonne National Laboratory (ANL) West [1, 16]. The data produced from ERAD simulations of failure modes in this dissertation are integrated within the Sandia safeguards systems model code known as Echem Separation and Safeguards Performance Model (SSPM) [1]. This data is only to provide a qualitative assessment of failure mode effects and their impact on the mass balance. The simulated operations are along the scale of an engineering scale operation, but actual assessment with real throughputs is not possible as it requires proprietary design information that makes it beyond the scope of this dissertation. These results provide information as to the

applicability of the SBS method and where its assessment and detection values lie independent of design quantitative values.

In integrating ER data into Echem SSPM, the effects of failure mode operation on the mass balance of the pyroprocessing system under a NRTA framework are assessed. Improvements to the systems model and assessment of the needs of measurement technology placement can be determined. In particular the effect of the failure modes on the standard error of inventory difference (SEID) is of great interest. The primary hypothesis is that disruption of the flowsheet by off-normal operations will affect the ability to compute the mass balance and potentially produce a false alarm indicating that diversion may have occurred causing significant unnecessary downtime. The nature of the effects of failure modes on the mass balance utilizing integrated failure mode data will be presented in this dissertation and conclusions will be discussed in detail. In addition, recommendations are made as to how safeguards systems containing PM technologies and facility operations can best be designed from this information.

1.3: Dissertation Overview

This dissertation is organized into seven additional chapters as well as appendices and a bibliography. Chapter 2 provides a significant amount of background on pyroprocessing, pyroprocessing modeling, current safeguards methodologies and PM methodologies being developed, and the FMEA method for determining failure modes. Chapter 3 provides an overview of the methods and approaches of the work performed. Chapter 4 details the experimental work performed to determine if ERAD could be utilized as an effective tool for failure mode prediction. Chapter 5 details how a traditional FMEA approach for design safety was repurposed and utilized for

identification of safeguards relevant failure modes. Chapter 6 details the ERAD simulations of select pyroprocessing failure modes identified from the FMEA in chapter 5. Chapter 7 details the importation of ER failure mode data into the SSPM Echem model and the simulation of this data to determine the effects of the failure modes on the material SEID. Finally, chapter 8 summarizes the conclusions of the work and the future work that can and should be performed. Following these chapters are a set of appendices. Appendix A covers the FMEA worksheets produced during the FMEA analysis in chapter 5. Appendix B covers additional figures and results from the computational analysis performed. Appendix C lists the initialisms used throughout this dissertation.

CHAPTER 2: BACKGROUND

Given the motivation of the introduction, I will provide a foundation of the past work in pyroprocessing, safeguards, failure mode analysis, and simulation models. This background chapter addresses each of these covering topics such as fundamental theory, commonly accepted approaches and assumptions, and past work performed.

2.1 PYROPROCESSING

2.1.1 PYROPROCESSING HISTORY

Electrochemical refining of metals is not a novel concept in metallurgy. The utilization of electrochemistry to remove impurities from metals has long been utilized in both the aluminum and copper industry [17]. These techniques have also been applied to the separation of fissile material from UNF to produce new metal fuel for use within fast reactor systems. By recycling fuel, the potential for closing the nuclear fuel cycle becomes possible as well as potentially reducing high-level waste inventory that contain isotopes that have a much shorter lifetime as long lived actinides are effectively removed [2].

Research in this area of electrochemical treatment of nuclear fuel and fissile isotopes has a long history. Electrochemistry applied to nuclear materials effectively started with the production of UO_2 from molten UO_2Cl_2 using electrochemistry. This was first discovered at the end of the 19^{th} century [18]. Work for the development of electrochemical production of fuel was performed primarily in the United States within the national laboratory complex. Brookhaven National Lab (BNL), Los Alamos National Labs (LANL), and Oak Ridge National Labs (ORNL) all led early research in separations of U from salt for metal fuel [18]. This salt separations work gave rise to the current

extraction process seen today. The first major efforts to extract heavy metal from spent fuel in electrorefiner equipment with molten salt eutectic (NaCl-KCl) occurred at LANL in the early 1960s [18].

The early work carried out by Argonne National Lab (ANL) at their Idaho site is of the most significance to modern pyroprocessing [2]. The first efforts at ANL involved the fuel of the EBR-II reactor that was processed via pyroprocessing in the mid to late 1960s [2]. The other effort that led to the current understanding of pyroprocessing was that to treat the fuel from the proposed Integral Fast Reactor (IFR). This is the first instance where a LiCl-KCl salt eutectic was used for the processing, the most common salt eutectic in current designs [18]. This work uses a electrorefiner model having a fuel basket that acts as the anode with a solid metal cathode where dendrites of U are transported. This approach is still the major starting point from which most pyroprocessing electrorefiners are developed [2, 18].

Currently, electrochemical reprocessing is of interest to Japan, the Republic of Korea (ROK), and the United States. In particular, the ROK performs a significant amount of the modern research and development. For example, the Korea Atomic Energy Research Institute (KAERI) is investigating pyroprocessing for the back end of their nuclear fuel cycle due to safeguards agreements that restrict the use of aqueous methods of reprocessing. [4]. KAERI has pursued research to design of unit operations of pyroprocessing and has created its own demonstration facility [4]. This demonstration facility is known as the PyRoprocess Inactive integrated DEmonstration (PRIDE) Facility which does not utilize used active fuel. The next stage in KAERI's development is the development of a Reference Engineering Scale Pyroprocessing Facility (REPF) that will

continue to scale up the facilities from PRIDE and will handle materials more akin to those of the commercial reprocessing facilities [19]. REPF will be the last stage before commercial scale facilities are constructed and utilized.

2.1.2 Pyroprocessing Flowsheet

Pyroprocessing facilities and models developed follow similar flowsheets. Establishing a flowsheet allows for the identification of the key unit operations as well as assisting in developing systems models of pyroprocessing facilities. A detailed pyroprocessing facility flowsheet model will be utilized here when discussing facility design and failure mode effects [16].

Pyroprocessing facilities have several different hot cells within the facility that contain the unit operations of the facility [4]. The first hot cell is that of the head end processing cell [16]. This hot cell consists of an air atmosphere and is where used fuel assemblies are disassembled, cladding removed, and the fuel rods chopped into smaller pieces for increased surface area for increased performance within the electrochemical cells of the process cell. A voloxidation process to reduce the UNF into a fine powder for the purpose of sampling for input accountancy has also been suggested to occur within this head end cell. In addition to the head end cell, there is an air atmosphere hot cell at the tail end of the process to process nuclear fuel and waste forms. Within these cells, metal actinide products separated are consolidated into fuel pins for fast reactors, and high level waste is consolidated into ceramic and vitrified waste forms.

Between the head end cells and the tail end cells is an argon atmosphere process cell where the actual electrochemical treatment and separation of fuels occurs. A graphic of the process cell flowsheet is shown in Figure 2.

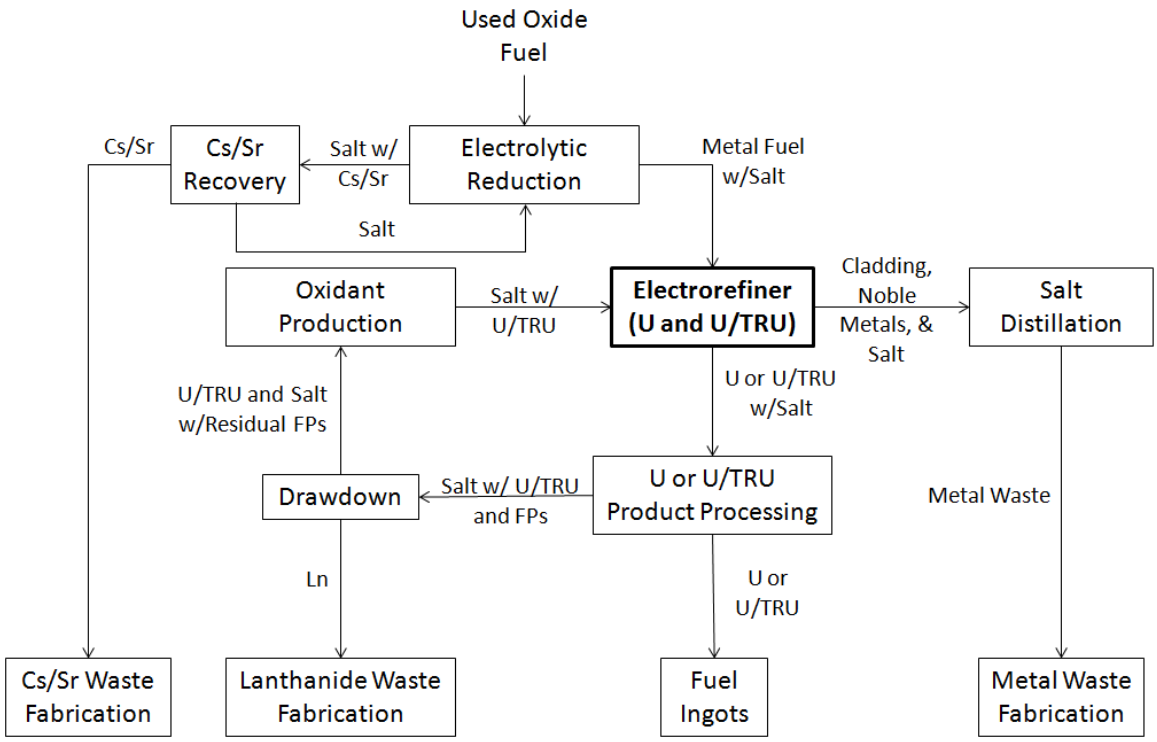

Figure 2- Pyroprocessing Flowsheet

As seen in Figure 2, the process cell has several discrete steps that differ slightly depending on the type of fuel to be recycled. If fast reactor metal fuel is being processed, the process starts in the electrorefiner. If oxide fuel is being processed, an oxide reduction step must occur first. During this step, the oxide fuel (UO_2) is reduced to metallic fuel for processing in the electrorefiner stage [20]. The ER is the next major step in which the chopped metal fuel is submerged in a LiCl-KCl eutectic salt bath and a charge passed so that the actinides and rare earths are transported into the salt with the U is deposited at the metal cathode. In addition, a liquid cadmium cathode (LCC) may be utilized for the deposition and separation of U and transuranics in the salt. At the end of each ER operation, the cathode is removed and the product and salt are scraped into the CP [21]. Here the excess salt is distilled out, and the dendrites within the CP crucible are

consolidated and prepared for melting within the final step of ingot casting. After ingot casting, the finished ingots are transferred to the tail end hot cells for fuel pin processing.

As also seen in the flowsheet, several waste streams follow from the ER. The noble metals remain in the anode fuel basket in the ER during its operation. These metal wastes are processed in a metal waste furnace into a consolidated waste form. In addition, the ER salt is periodically treated. During this step, the U and transuranics within the salt are removed via an electrowinning process (not shown) [22]. In addition, the rare earth elements in the salt are treated through a combination of ion exchange columns and oxygen sparging to produce high level waste forms for disposal [23, 24, 25].

Within the context of this dissertation, the work focuses on the operations of the ER and its effect on the mass flow in the flowsheet under different operating conditions. Within the ER, U and other actinides are separated out and off-normal conditions occur can be moved to portions of the material flowsheet that they would not occur in under normal operation. Thus, there is a need to focus safeguards research efforts on this specific unit operation.

2.1.3 ELECTROREFINING CELLS

Electrorefining cells differ in size, geometry, and arrangement, but all designs follow same principles in terms of their design and science. By understanding these dynamics, proper experiments and computer modeling can be performed. These specific characteristics of ER cells are discussed within this subsection. A diagram of typical ER cell is seen in Figure 3.

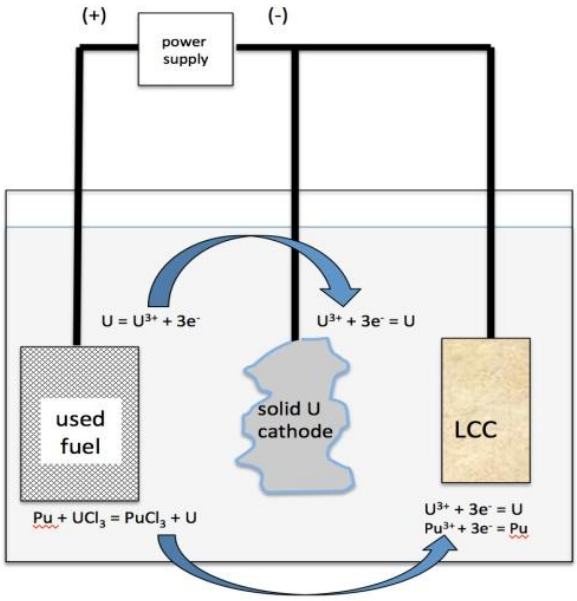

Figure 3-General Electrorefining Cell [15]

The first major similarity between ER cells pertains to the materials utilized. The eutectic selected is a LiCl-KCl eutectic salt that has a low melting point and whose constituent elements with highly negative reduction potentials [16]. This allows it to operate as an electrolyte for the transport of metal ions. The anode in each of these cells consists of reactive metal stored within a basket made of an inert metal, most commonly stainless steel. The mesh of this anode basket must provide enough porosity for electrolyte contact and diffusion of metal ions while retaining noble metals that will not react with the electrolyte. The cathode is also typically made of some inert metal or solid surface. This metal is typically either steel (for many commercial designs) or tungsten (for many experimental designs) and there are current investigations being undertaken determining the viability of utilizing graphite cathodes for ER applications [26]. Finally, the reference electrode is typically an Ag/AgCl reference electrode utilizing porous ceramic tubing such as mullite for the housing of a LiCl-KCl-AgCl salt and a silver wire

electrode [27]. The cathode and anode are connected to a power source through power leads and all three electrodes are connected to a data collection system.

Utilizing this ER electrode arrangement, current is passed from the anode to the cathode within the eutectic salt [28]. The electrode potential between both the cathode and anode with the reference electrode are registered by the data collection system. Operation can be commenced in one of two manners, potentiostatic or galvanostatic [28]. Potentiostatic means that operation is commenced at a constant potential while galvanostatic requires a constant current. Galvanostatic control, using a galvanostat for the power source and data collection, is the focus of the research in this dissertation.

As current is passed, reactions occur at the electrode and drives the current and the electrorefining process. These reactions both involve a cathode reaction and an anode reaction. These reactions are seen in equations 1 and 2.

$$\textit{Anode:}\ U \rightarrow U^{3+} + 3e^{-} \quad (1)$$

$$\textit{Cathode:}\ U^{3+} + 3e^{-} \rightarrow U \quad (2)$$

As can be seen the reactions during normal operation involve the 3+ ions of U. This reaction is the same 3+ reaction for the actinides of interest such as Pu and Cm and many of the rare earth elements.

This arrangement allows for manipulation of several different parameters. The electrodes can be raised and lowered. The material in the salt and at the anode can be changed. The anode basket allows for the filling or removal of metallic elements to be separated or to limit the reaction. The eutectic salt allows for different elemental compositions at startup of operation in terms of starting concentration of actinide chlorides in the melted salt such as UCl_3. Finally the furnace allows for manipulations in

temperature. These different parameters can be varied both experimentally and in computational models like ERAD. By running the same scenario in both ERAD and experimentally, results could be compared and conclusions over efficacy of ERAD as a trend prediction mechanism can be determined. Research of this form is discussed in Chapter 4.

2.2 International Safeguards

2.2.1 Traditional IAEA Safeguards: Definitions

International safeguards are defined by the IAEA as, "The timely detection of a diversion of significant quantity (SQ) of nuclear material from peaceful nuclear activities". A SQ is defined by the IAEA as, "The approximate amount of nuclear material for which the possibility of manufacturing a nuclear explosive device cannot be excluded." [29] The value of SQ is in the units of mass and varies depending on the material elements and isotopes and the physical form of the material. Table 1 shows these different values of SQ's for various types of special nuclear material (SNM) [30].

Table 1-Example SQ values

SNM	SQ
Pu	8 kg
U-233	8 kg
HEU (U-235 > 20%)	25 kg U-235
LEU (U-235 < 20%)	75 kg U-235
Natural U	10 Mt

International safeguards are applied to all declared nuclear facilities for states not possessing nuclear weapons, Non-nuclear Weapons States (NNWS), and that are signatories to the Nuclear Nonproliferation Treaty (NPT) [31]. International safeguards are applied through a comprehensive safeguards agreement (CSA) made between the IAEA and the state level safeguarding agency and government [29]. Typical nuclear safeguards have been historically applied through a method known as NMA. NMA involves a performing a material mass balance. This mass balance can be summarized in equation 3.

$$ID = I - O - H \tag{3}$$

Where *ID* stands for inventory difference, *I* represents input mass, *O* represents output mass, and *H* represents holdup measured mass. When all three of these major values are balanced, the value should be zero for what is known the inventory difference. In other words, whatever mass of SNM comes into the facility should come out of the facility modified by material determined to be held up in the unit operational equipment.

This material mass balance is performed over a period known as the mass balance period. This is a set period of time over which the mass accounted for. This period varies in length depending on facility and can range over periods from one month to one year. One advanced method of mass accountancy known as NRTA shortens the balance period significantly to ensure there is not a loss in continuity of knowledge (COK) and to reduce the total uncertainty of the mass balance [1, 7, 32]. NRTA is proposed for separated material facilities such as pyroprocessing and is the subject of much computational investigation. These investigations will be further described in the background section

about models and its key role in the research performed for this dissertation will be presented.

Under the determined CSA, the facilities that are to be under IAEA safeguards are declared, the method and objectives for the safeguards regime are established, and the inspection protocol is defined. This inspection protocol is subjected additionally to what is known as the Additional Protocol (AP) for those states, including the ROK, that are party to it [33]. Details of the inspection protocol for NMA are discussed in subsection 2.2.3. This knowledge is fundamental to understanding how PM methods can be integrated into facility protocols to assist NMA in the safeguarding of facilities.

NMA methods have had success when applied to bulk handled materials and facilities like fuel assemblies at nuclear power plants or UF_6 cylinders at enrichment facilities, but have faced difficulties when applied to separated materials in reprocessing facilities [1]. This is due to the challenges with assessing the mass constituency of separated SNM with high fidelity using current measurement technologies (e.g. Destructive Assay, Mass Spec analysis). The measure of fidelity of ID is known as the SEID and is considered to be a normal distribution. To satisfy IAEA requirements, the ID with SEID must fall within the 95% Confidence interval, thus 1SQ/3.3 is the required SEID for SNM being tracked through the facility [5]. This level of confidence is unattainable for high throughput reprocessing facilities with current mass measurement technologies.

2.2.2 Process Monitoring Safeguards: Definitions

As described in the introduction, methods involving process monitoring (PM) techniques are being investigated to support traditional NMA safeguards in fuel

reprocessing facilities. PM involves taking signals from various process measurements throughout the facility to infer details about facility health and off-normal occurrences that are occurring in real time within the facility. This can inform both the safeguard inspector as well as the maintenance and operation schedule of the facility for the operator.

PM methods can be applied through two different approaches: process centric PM and system centric PM [5]. Significant research has been performed to expand upon both of these methods as applied to both aqueous and pyroprocessing facilities. The majority of current research occurs within the computer modeling space. Process centric PM focuses on identifying anomalous occurrences within a specific unit operation (e.g. electrorefiner of pyroprocessing plant) [32]. Measurements associated with the selected process are chosen and applied to the unit operation. The measurement data for both normal and off-normal operations of this specific process are measured and statistically compared. Utilizing a Page's test, deviations of measurement data from normal operation can be registered with a tunable level of confidence. Current simulation research on process centric PM has involved utilizing statistical software to generate stimulant data and perform Page's test on generated data [32]. These results have shown improvements to the overall detection probability (DP) of material unaccounted for (MUF).

System centric PM methods are like process centric methods as they attempt to detect anomalous scenarios [10]. However, system centric methods utilize a system of measurements throughout a facility and do not focus on one unit operations process. Thus, the effects on the facility of off-normal operations as well as the source anomalous occurrence can be detected in real time. Both must be monitored, as the effects of an

anomalous occurrence in a single unit operation are not generally confined to that unit operation. Thus, additional data from throughout the facility can significantly assist in determining the root anomaly and its consequence. Work in system centric PM has involved the use of system models and assumptive physics models to determine the DP from a network of measurements placed throughout the facility for identified diversion scenarios [8]. SBS as referenced in the introduction falls under this category of system centric PM and is a focus of this dissertation.

In placing PM technologies, the process measurements need to be classified based on how they are performed and how measurement error is addressed. To do so, PM measurements have been divided into three different measurement groups: continuous direct measurements, discrete direct measurements, and discrete indirect measurements. These distinctions have been made to clarify the difference in the measurements based on time scale of the measurement and the method by which the quantity being measured is determined.

Continuous direct measurements are those that are continuously measured and returned to the operator and the quantity desired is measured directly with no need for significant further analysis to determine its value. For example, a reference electrode measures the potential between the cathode and the reference electrode directly and continuously reports the data to the operator to ensure that the operating potential matches that required for metal deposition.

Discrete direct measurements are measurements that measure the quantity desired directly at set specific time intervals. Thus, the data and information the operator receives is only a select number based of the number of measurements made total and feedback to

the operator is not continuous. An example of a discrete direct measurement is that of the mass measurement of the scraped U cathode deposits in the ER. These deposits are measured directly after an ER operation and its subsequent distillation of salt in the cathode processor has been completed.

A discrete indirect measurement takes places at specified time intervals like the discrete direct measurements. The difference is that the discrete indirect measurements measure a desired quantity by measuring a different physical property, and fundamental physics are utilized to determine the quantity of interest. An example of this is the double bubbler apparatus in an ER that determines the pressure at two different depths in the ER salt bath and utilizes the differential pressure between the two to provide the operator both the salt depth and density.

2.2.3 Traditional IAEA Safeguards: Error Estimation and Sources

The IAEA provides standards for approaches to error estimation for measurement techniques applied to NMA such as scales and mass spectroscopic analysis tools [34]. Thus, for the techniques involved in the PM analysis of an ER, these same standards and techniques will be utilized as well. These techniques can be broken down into five separate areas: measurements of standards, calibration of measurement system, measurements of non-standard materials, error estimation in the presence of rounding errors, and interlaboratory test data.

Measurement of standards is one method for error estimation in applied measurement techniques [34]. These techniques quantify error using physical standards. Physical standards are those whose physical value are known either without error or with

supplied error. By comparing measured values versus standard values, the systematic error can be determined and corrected for a given measurement technique and its manufactured technology. Given known uncertainties and multiple measurements, the systematic and random errors can be estimated for a specific piece of measurement equipment. In addition, corrections for biases produced by times between measurements can also be generated. This form of error estimation can be applied to all continuous and discrete direct measurement technologies involved in PM assuming they have properly established standards.

Calibration of measurement systems are errors resulting from the use of calibration functions [34]. To be specific, these are measurements that are a function of another measurement. For example, an estimation of material actinide content has a calibration curve for mass of Pu as a function of radiation count. These error estimates have estimation techniques for linear calibration curves, multiple calibration data sets, and calibrations with a single data point or non linear calibration functions. For this reason, indirect measurements and their associated technologies with known uncertainties will be analyzed for error estimation utilizing these methods tuned for the specific technology utilized.

Measurements of non-standard of materials involve estimation of error utilizing data from measurements of non-standard sources without a well known physical quantity [34]. This is used as an additional method to standard measurement in order to better quantify random error as the emphasis with measurement standard of materials systematic though it can be utilized for both. These non-standard methods can be utilized as a supporting factor to the measurements of standards and will be of a greater

importance for assessing random error of measurements once the measurement technologies are placed within the hot cell where they cannot be compared to a standard. This method, like the standard measurement methods, only applies to direct continuous and discrete measurement technologies.

Error estimation in the presence of rounding error is errors generated by the rounding of measurement data to a determined number of significant figures [34]. Depending on the number of significant figures where the rounding occurs at and the method of rounding such as truncation, flooring etc., the impact of rounding error can be significant. Within the context of the ER, measurements such as the temperature, output of pressure transducers within the double bubbler, and the scales for cathode deposits all can be significantly affected by rounding error for the data streams associated with them.

Interlaboratory test data errors are those due to the use of multiple laboratories and the differences caused from results generated between each lab [34]. These types of errors are difficult to assess within the model chosen and utilized within this dissertation project. For this reason, measurements chosen are not those that would require the use of multiple or off-site analysis labs such as salt sampling for salt concentration. All measurements selected in the analysis can be performed within the hot cell itself.

2.2.4 Traditional IAEA Safeguards: Inspection Process

Inspections are made by the IAEA to ensure that the book values recorded by a nuclear facility are accurate and to ensure that no diversion is occurring [34]. This is done with the assumption that errors are made in the book value as the operator of a facility may attempt to mask diversion by reporting inaccurate book values. Thus, IAEA inspectors must carefully plan their inspection strategies.

IAEA inspections can be classified into two different kinds of inspection: attributes and variable inspection [34]. Attributes inspections are those in which the unit inspected is classified as being defective or non-defective, or the number of defects in the unit of a product is counted with respect to a set requirement. Inspection by variables is inspection wherein a specified quality characteristic on a unit of product is measured such as pounds, inches, and feet per second.

Attributes inspections consist of two types of specific inspections: records inspections and measurement data inspections [34]. Records inspections involves checking the material accounting book values to determine what errors in calculations may have occurred, what effects these type of errors may have had, checking data in the books versus IAEA reports of the same data for the same period, and checking for data for sampling of individual items for MUF calculation. The MUF is the quantity of material unaccounted for as result of the mass balance equation. Inspection of measurement data involves counting of items included in the records and use of an attribute tester to detect defects that NMA could not otherwise determine. Attribute testers can be anything from tipping a container to determine that the weight is similar to that listed to using a detector to ensure that has roughly the book listed enrichment of the U present within it. Attribute inspection occurs with the goal to detect the defect of a significant quantity of material from falsification of data at a specific key measurement point (KMP). If diversion takes places over multiple locations, attributes testing has significant difficulty detecting such diversion unless the diversion is greater than 1 SQ at that specific KMP.

Variable inspection involves two separate kinds of measurements that aim to verify the measurement data [34]. Variable inspections first look to determine small defects that would otherwise escape the general measurements of the testers from attribute inspection. The second goal is to determine small defects that may exist for item measurements that occur at a specific KMP.

In utilizing these two different types of inspections, a principal test to determine probability of detection is performed with several different supplemental tests. The principal test involves two different combinations of tests [34]. The first combination involves determining the gross defects in the book results to actual using an attributes tester, the second is the testing for medium defects that fall between small error based defects and gross defects (these being the greatest chance of being used for diversion), and the test for the facility MUF adjusted by bias. The bias is determined by the measurement campaign of the inspector. The second combination of principal tests is the same as the first for the first two tests on gross and medium defects, but in addition has a test for the significance of the bias value determined by the inspector and a test for the significance of the facility MUF. In addition to these principal tests, supplementary tests can be added at the inspector's discretion. These tests include things such as tests for the significance of the shipper and receiver difference and tests for randomness and small calculation errors in the book calculations.

From the perspective of PM, data must be recorded in such a way as to be accessible, testable, and of great assistance in performing inspection-based testing. Thus data produced by PM, depending on measurement selected, should be applicable to either attribute or variable testing if need be. In addition, data streams must not be so large that

they are incomprehensible by inspector but must be provided in a way that can assist in the inspector in verifying that the facility has operated as planned. To that point, from the perspective of principal tests, the PM in the context of this dissertation must be able to best assist in the principal test that addresses the significance of the MUF value and the correlation between that and the bias calculated by the investigator. In reducing the uncertainty of the MUF, the principal test increases the confidence of the MUF and the probability of detection calculated by the inspector. In doing so, the necessary SEID can be met for IAEA requirements.

2.2.5 Process Monitoring Safeguards: Identified Measurements

Tables 2-5 displays the different measurements assessed for this research with regards to the ER. Each measurement provides which quantity is measured, what technology is utilized to measure it, what type of measurement classification it falls under, and, in the case of indirect measurement, the actual physical parameter assessed and the underlying physical equation of this assessment. Following these tables, a description of each technique and how uncertainty is addressed by each is provided.

Table 2- Measurement Evaluation for Cell Properties Measurements

Quantity Measured (Units)	Technique	Measurement Type	Quantity Assessed/ Physical Equation
Temperature (K)	Thermocouple	Continuous Direct	N/A
Density (g/cm^3)	Double Bubbler	Discrete Indirect	Pressure/Laplace Equation
Stirrer Rotational Speed (RPM)	Rotation Meter (Tachometer)	Continuous Direct	N/A
Salt Level (cm)	Double Bubbler	Discrete Indirect	Pressure/ Laplace Equation
Cell Current (A)	Reference Electrode	Continuous Direct	N/A

Table 3- Measurement Evaluation for Salt Concentration Measurements

Quantity Measured (Units)	Technique	Measurement Type	Quantity Assesed/ Physical Equation
Salt Concentration (mol/cm^3)	CV Scans	Discrete Indirect	Peak Current/ Fick's Second Law
Salt Concentration (mol/cm^3)	Pulse Voltammetry	Discrete Indirect	Peak Current/Fick's Second Law
Salt Concentration (mol/cm^3)	CP	Discrete Indirect	Potential/ Sand Equation
Salt Concentration (mol/cm^3)	CA	Discrete Indirect	Current/Cottrell Equation

Table 4- Measurement Evaluation for Electrode Properties Measurements

Quantity Measured (Units)	Technique	Measurement Type	Quantity Assesed/ Physical Equation
Anode Surface Area (cm^2)	CV Scans	Discrete Indirect	Peak Current/Fick's Second Law
	Double Bubbler +Electrode Manipulator	Discrete Indirect	Pressure/Laplace Equation
Anode Rotational Speed (RPM)	Rotation Meter	Continuous Direct	N/A
Anode Potential (Volts)	Reference Electrode	Continuous Direct	N/A
Cathode Surface Area (cm^2)	CV Scans	Discrete Indirect	Peak Current/ Fick's Second Law
	Double Bubbler+ Electrode Manipulator	Discrete Indirect	Pressure/Laplace Equation
Cathode Rotational Speed (RPM)	Rotation Meter	Continuous Direct	N/A
Cathode Potential (V)	Reference Electrode	Continuous Direct	N/A
Cathode Deposit Mass (kg)	Electronic Balance	Discrete Direct	N/A

Table 5- Measurement Evaluation for Radiation Detectors

Quantity Measured (Units)	Technique	Measurement Type
Gamma Radiation in Environment (Rem)	SiC Semiconductor Detector	Continuous Direct
Neutron Radiation in Environment (Rem)	SiC Semiconductor Detector	Continuous Direct
Radiation Count Cathode Deposit	Advanced NDA instrument/Technique	Discrete Direct

2.2.5.1 Thermocouple

A thermocouple is a device utilized for the assessment of temperature in a system [35]. A thermocouple determines the temperature through utilizing what is known as the Seebeck effect. It is based around the concept that for an open circuit there is a direct relation between voltage gradient and temperature gradient as represented by equation 4.

$$\nabla V = S(T)\nabla T \tag{4}$$

Where *V* is voltage, *T* is absolute temperature, and *S(T)* is what is known as the Seebeck coefficient. Thus with the knowledge of a calibrated reference temperature, a thermocouple attached to an open circuit can determine what the temperature of a system is. Thus, the quantity actually measured by a thermocouple is the voltage gradient within the open circuit and this is subsequently converted to temperature through the equation. Work has been performed to determine the uncertainty of this determination in terms of absolute temperature, particularly in high temperature and radiation environments and results indicate that given a normal distribution the relative uncertainty is ±2-3% [35].

2.2.5.2 Double Bubbler

A double bubbler is a device developed by the Idaho National Labs (INL) for the purpose of measuring both the density of eutectic salt and the depth of the salt in situ [36,

37]. The device consists of two separate tubes that are submerged at two different depths of difference *h* with the depth of the more shallow tube being a distance *x* from the salt surface. The two tubes are connected to a controlled argon gas flow through which bubbles are created within the salt. The pressure required to produce such bubbles are measured utilizing pressure transducers that are attached to both tubes and a pressure transducer between each tube that allows for the assessment in differences in generated pressures. This device as described is seen in Figure 4.

The average density of the salt is determined through the use of equation 5 [36],

$$\rho_{ave} = \frac{\sum_1^N \Delta p}{Ngh} \tag{5}$$

Where ρ_{ave} is the average density, N is the number of times the measurements are taken, g is the gravitational constant, h is the difference in depth between the two tubes, and Δp is the difference in pressure between the two tubes. Thus, for the calculation of the density uncertainty comes from two different sources. The first is that of the pressure difference which is due to the uncertainty of the pressure transducer. The uncertainty of the pressure transducer is quantified in its development. The second source of uncertainty is the measurement of h which has a small uncertainty based off the significant figures to which the distance h can be measured.

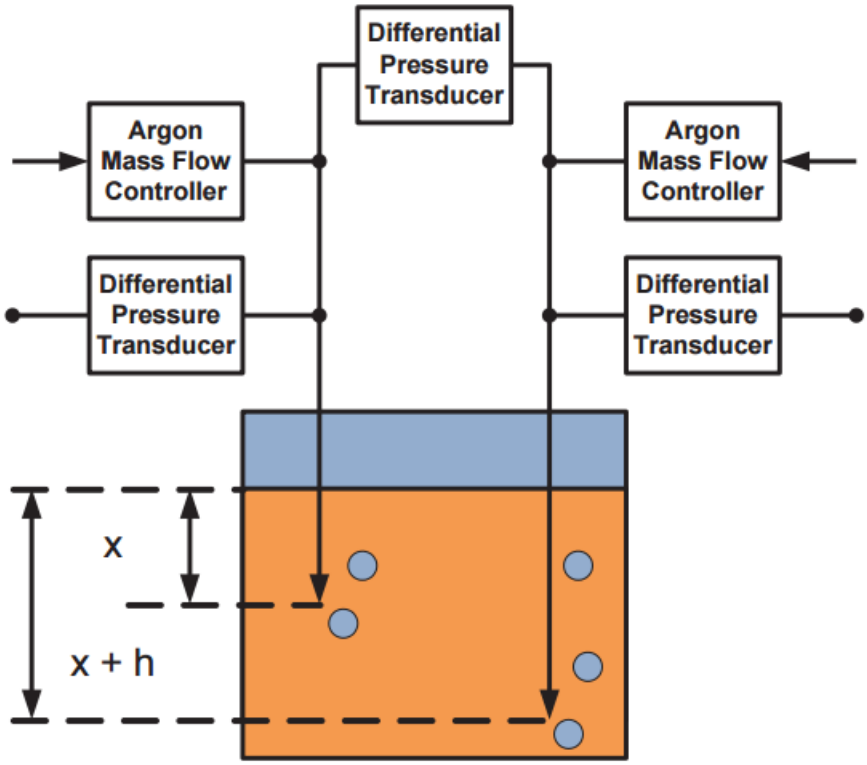

Figure 4- Double Bubbler Diagram [36]

Thus for the calculation of density the uncertainty must be propagated through this equation. In addition, as the density is an average the uncertainty must be averaged over the mean so the uncertainty is not given a normal distribution for the standard deviation, but the standard deviation of the mean value.

The depth of the salt can be determined through the application of equation 6 [36]:

$$X_{ave} = \frac{P_{1,gauge}+P_{2,gauge}}{2\rho g} + \frac{h}{2} \quad (6)$$

Where X_{ave} is the average depth, $P_{1,gauge}$ and $P_{2,gauge}$ are the pressures of the first and second tubes respectively. Like the density equation as there are sources of error from both the pressures and the difference in height error must be propagated through to the salt depth.

With the knowledge of the depth of the salt, it can be easily determined by volume displacement the surface area of the electrodes due to known surface areas and designs of the electrode. One can easily determine from a change in salt depth, the volume of the electrode submerged and with it the surface area knowing things such as the radius or edge lengths in the case of the cruciform anode.

Previous efforts have been made to quantify the error expectation of the double bubbler. These efforts found that the density determination has an expected error of 0.7% and the depth determination has an expected error of 2.1% [37].

2.5.2.3 Reference Electrode and Potentiostat

A reference electrode is a tool utilized both for continuous measurement, for example monitoring of current and voltage, as well as discrete voltammetric measurements methods utilized for quantification of salt concentration. Reference electrodes in pyroprocessing systems often utilize an Ag/AgCl reference electrode with a known potential versus the standard hydrogen electrode. This difference in potential is dependent on the concentration of Ag/AgCl present within the electrode housing [27]. More specifically these electrodes consist of AgCl placed in the bottom of a mullite tube that is molten in the electrochemical eutectic furnace. An Ag wire is placed within this molten bath and this allows for the performance of the redox reaction seen in equation 7,

$$AgCl(s) + e^- \leftrightarrows Ag(s) + Cl^- \quad (7)$$

The reference electrode reaction allows measurement of the potential at the cathode between the reference electrode and the cathode without passing current through the reference electrode, thus directly determining the type of reaction occurring at the

cathode. A potentionstat will maintain or change the potential measured by altering the current and providing output of the current data.

The potential measurements made by an Ag/AgCl and their associated uncertainties must be quantified for each system where they are utilized and are dependent on such factors as the contact area of the silver wire, the extent to which the AgCl melted, and time spent to allow the reference electrode to reach equilibrium [38]. Most reference electrodes are prepared and have their uncertainty quantified via calculation of the value over multiple measurements with its mean and associated standard deviation calculated to produce its uncertainty. These are then compared to a known value for the standard potential of the electrode reaction to understand if the known value falls within the margin of error of the measured thus validating the measurement and its uncertainty.

In addition, the potentionstat measures current via Ohm's law by manipulating the current to maintain a specified potential between the reference electrode and working electrode. These current changes can be chronicled and analyzed and error estimation and propagation performed in a similar manner to that of the a reference electrode

2.2.5.4 Cyclic Voltammetry (CV)

CV is an electrochemical technique in which a potentionstat is utilized to measure the current response at a range of potentials at the working electrode. In doing so, peaks in current are produced at the reduction and oxidation peaks within the system. A general representation of this type of measurement is seen in Figure 5. The position of each peak can be utilized to determine which species are present within the salt.

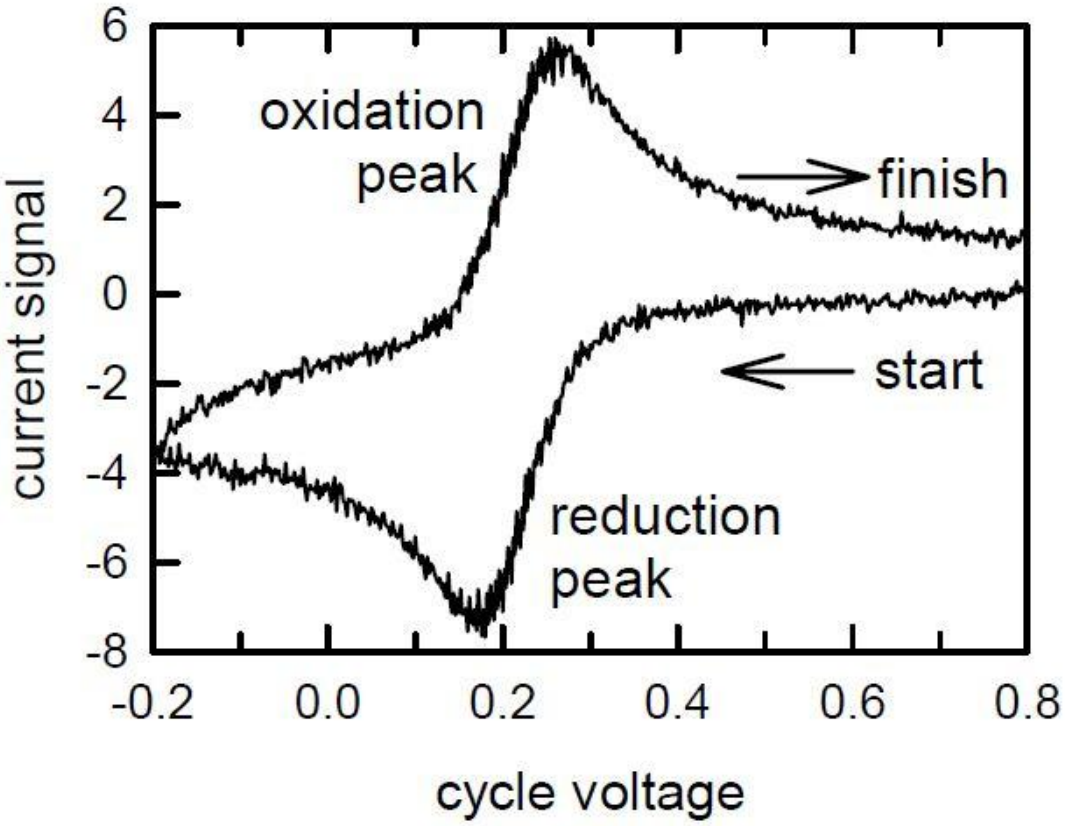

Figure 5- General Plot of CV measurement

The peak current of the CV measurement can determine the concentration of the species using equation 8 [39]:

$$i_p = 0.4463nFAC_{\mathrm{A}}^{b}\left(\frac{nF}{RT}\right)^{1/2} D_{\mathrm{A}}^{1/2} v^{1/2} \qquad (8)$$

Where i_p is the peak current, n is the number of electrons transferred in reaction, F is Faraday's constant, A is surface area, $C_A{}^b$ is the concentration of species A, R is the ideal gas constant, T is the absolute temperature, D_A is the diffusion coefficient of species A, and v is the scan rate volts per second. Thus, the uncertainty must be propagated through this expression in determining the concentration from such variable with known measurement uncertainties such as peak current, surface area of electrode, temperature,

diffusion coefficient, and scan rate. Only after this propagation can the uncertainty of the concentration be calculated.

2.2.5.5 Pulse Voltammetry (PV)

Pulse voltammetry involves providing a pulse of potential and measuring the current response utilizing a potentionstat to infer information about the concentration. There are two methods by which this is typically performed: square wave voltammetry (SWV) and normal pulse voltammetry (NPV) [39]. Like CV measurements, pulse voltammetry measurements face uncertainty sourced from electrode depth, diffusion coefficient values, and measured peak current in response to the potential pulse. In addition, the time of the pulse must be accounted for in concentration diagnostics as well the addition of a source of uncertainty to the quantified value. An additional method utilizing pulse voltammetric techniques is the development of a calibration curve based off known measured concentrations by plotting peak current versus the concentration as they are directly proportional to one another. This has been demonstrated to be effective for low current concentrations, but the uncertainty factors of both values must be taken into account if the method was to be utilized [40].

2.2.5.6 Chronoamperometry (CA)

CA is an electrochemical technique that operates an electrochemical cell at a constant potential measured by a reference electrode versus the working electrode with the current being measured as operation occurs. From this measured response current, the concentration of a species within the cell can be calculated through the Cottrell equation which is derived from and obeys Fick's second law of diffusion. The Cottrell equation is seen in equation 9 [39].

$$i = \frac{nFAC_A^b\sqrt{D_A}}{\sqrt{\pi t}} \quad (9)$$

Where *t* is time in seconds. Thus, sources of uncertainty in the formulation and calculation of the concentration come from the measured current, the surface area of the electrode, the diffusion coefficient. In addition, the time of operation also has an associated uncertainty resulting from the timing mechanism of the software utilized to operate the potentionstat. This must be factored in for calculating the concentration given the physics of the electrochemical method.

2.2.5.7 Chronopotentiomettry (CP)

CP is an electrochemical method that involves operating an electrochemical cell at a constant current and measuring the potential response of the working electrode utilizing a reference electrode. The response of the potential to the applied current follows the Nernst equation and allows for the determination of the concentration from this information. This determination is a result of solving the Sand equation seen in equation 10 [39],

$$i\tau^{1/2} = \frac{nFA(D_A\pi)^{\frac{1}{2}}C^b}{2} \quad (10)$$

Where τ is the transition time which is the elapsed time between the initiation of constant-current experiment and the time at which the concentration of the electroactive species reaches zero at the electrode surface. CP is one of the earliest forms of electrochemical measurements used for quantification of materials though it is not as commonly used as CA and CV [39]. The sources of error that must be propagated in the determination of the concentration due to the physics of the problem is that of the current, the surface area of the electrode, the diffusion coefficient, and the transition time all with their own determined uncertainties.

2.2.5.8 Rotation Meter

A rotation meter, more formally referred to as a tachometer, can be applied to an ER to determine the rotation rate in terms of rotations per minute (RPM) of the stirrer or the electrodes and report the data continuously as it happens. Two different types of tachometers are produced, mechanical and optical [41]. Optical tachometers use a reflector attached to rotating object that determines the rotation rate of the device. Mechanical tachometers utilize a surface speed sensor and a calibrated distance from center of rotating device and through the application of both, the rotation speed can be calculated. The type of tachometer is dependent on application. The optical tachometer may be the better choice for ER's as there may be difficulties in replacing the surface speed disc in a mechanical tachometer. For both types, the manufacturer normally has quantified uncertainties from calibration sheets that vary on type and fidelity of the tachometer and further assessment of the uncertainty by the facility operator would not be required [41, 42].

2.2.5.9 Electronic Balance

Electronic balances are a common measurement technology used for assessing the mass of a measured quantity. Electronic balances are calibrated utilizing mass standards which then calculate the mass of an object by measuring the force exerted upon their plate and utilizing this weight and known gravitational acceleration to calculate the mass of the object [43]. The uncertainty of an electronic balance differs based on the manufacturer and quantity of mass designed for (large mass objects versus small mass). These uncertainties are often assessed and tabulated by the manufacturer and provide the

operator a choice as to which is most applicable and offers the lowest uncertainty as a tradeoff. In addition, guides are often provided with which to assess measurement uncertainties coming from sources such as temperature, position of placement, rounding, repeatability, and calibration weight and determining the specific uncertainty of the specific measurement environment [43].

2.2.5.10 SiC Semiconductor Detector

The SiC semiconductor detector is a radiation detector designed specifically to monitor gamma and neutrons in high mixed radiation flux environment as appropriate for a pyroprocessing hot cell [44]. Other detector designs utilizing semiconductors for gammas or ionization chambers for neutrons are options. However, the method for determining the uncertainty of a radiation count is the same regardless of type of radiation or detector. This is addressed as the count is covered by the square root rule for counting experiments seen in equation 11 [45]:

$$(average\ number\ of\ events\ in\ time\ T) = v \pm \sqrt{(v)} \tag{11}$$

Where v is the observed count rate.

2.2.5.11 Advanced NDA Method

To address material constituency without utilizing sampling and destructive analysis, NDA analysis utilizing radiation measurements have been under continuous development by the nuclear material management community [46]. These measurements utilize neutron, gamma, or both types of radiation measurements to determine what the materials and concentrations are present within a sample to assess SNM mass and assist in the material balance. For each manner of measurement, the method by which the mass quantity is assessed requires its own specific methods for uncertainty quantification.

These methods allow for the uncertainty of counting measurements to be further propagated as uncertainty of their mass estimations. For example, a multiplicity counter calculates the total count rate as well as the double and triple coincidence count rates to determine the quantity of fissions that have occurred versus those generated through other neutron generating mechanisms such as (α,n) reactions. The total count rate uncertainty is addressed via the square root count rule common for all detectors, but the double and triples coincidence rates have their own specific methods of quantifying uncertainty within the measurements. In addition, the mass estimated by these techniques have their own uncertainty quantification method [46].

2.2.6 IAEA Classification of PM Data

The IAEA classifies PM data streams from all types of measurements into three separate levels: levels 1, 2, and 3 [47]. Level 1 data is known as state of health data and concerns data that can be used to arrange timely response to indicate the monitoring systems are operating abnormally. Level 2 data is known as summary data and is used to prepare for inspection activities. This data helps to assist the inspector that the operator has continuously operated the facility as designed during the mass balance period without any form of significant anomalous occurrence or to demonstrate where anomalous occurrences may have occurred and generated consequences. Level 3 data is known as detailed data and is for providing data useful in drawing safeguards conclusions. Level 3 data actually provides data that can assist in inferring the masses of SNM in the unit operation processes and assists in the overall mass balance. A summary of each of the measurement data streams and the classification that I have given them is seen in Table 6.

Table 6- Classification of Measurement Data Streams by IAEA standards

Measurement Data Stream	IAEA Classification
Temperature (K)	Type 2
Density (g/cm^3)	Type 2
Stirrer Rotational Speed (RPM)	Type 2
Salt Level (cm)	Type 2
Salt Concentration (mol/cm^3)	Type 3
Anode Surface Area (cm^2)	Type 2
Anode Rotational Speed (RPM)	Type 2
Anode Potential (Volts)	Type 2
Cathode Surface Area (cm^2)	Type 2
Cathode Rotational Speed (RPM)	Type 2
Cathode Potential (V)	Type 2
Cathode Deposit Mass (kg)	Type 3
Cell Current (A)	Type 2
Gamma Radiation in Environment (Rem)	Type 2
Neutron Radiation in Environment (Rem)	Type 2
Radiation Count Cathode Deposit	Type 3

Inspecting the table, a clear distinction can be drawn for why a measurement data stream is labeled as type 2 or as type 3. For type 2, the data measured are those that are important to system health but do not specifically classify the movement of SNM within the system. For example, both the temperature and ER stirrer RPM have a known role in determining the transport properties of the ER system, however knowing that these changed or did not change does not give an quantifiable sense of the nature of mass flow in the system. Thus if temperature decreases or rotation rate increases, one could assume that the transport of material to undesired material streams is potentially present but does not provide information on the total quantity of SNM mass transported. The data however can indicate that the system is unhealthy and, that if linked to other measurements in the facility unit operations, can produce an indirect estimation of the effect on SNM flow and thus potentially reduce the quantified SEID.

Type 3 data was classified as such as it can assist in directly determining a mass of SNM in a given process stream of the pyroprocessing facility. For example, a mass measurement of the cathode deposit can provide an SNM mass value to be integrated into the total mass balance. In addition, concentration measurements can play a role as they can provide information as to ER holdup mass when calculating the material balance as well during shutdown for inspection. Outside these MB centered applications, measurements of factors such as mass and concentration are required by the inspector periodically (not just at the end of every balance period) to determine if the ER is operating as planned and that the correct form of transport will be taking place or that salt cleanup must be ordered. Thus, these measurements also serve a process monitoring role and thus can be integrated into the PM data stream analysis for real time safeguards and operation analysis by the facility operator.

From the perspective of IAEA inspections, these data streams can be subject to the two different types of IAEA inspection. In particular, attribute testing can be applied significantly to the type 2 data as it is bulk reported data and its accuracy is more based off of measurement technology health. Thus, attribute inspections applied to PM measurements to compare to book values of measurement response should be a role taken on by IAEA inspectors in fuel cycle facilities. Inspections tests can be applied to type 3 measurements such as recent (with regards to inspection) tests of salt concentration data as well as a selected sample of labeled cathode deposits that have undergone radiation assay for SNM data analysis. These inspection tests can assist the significance of MUF tests as the PM data's goal is to reduce the variance of the MUF. These tests would verify

the role of PM under the proposed developed framework to reduce the MUF's variance value.

2.2.7 Inferences Derived from PM Data

With an understanding of each of the measurements and their techniques as well as how data can be assesed by operators and IAEA inspectors, the application of PM data to a SBS safeguards framework can be investigated. To best apply PM data it must be understood regarding what physical inferences can be based off of changes in data. For example, what is the effect on the physical processes and what can be concluded if a large change in temperature were to occur? Each measurement is addressed individually here to determine the impact of each measured quantity on the physics of the system and what an operator or inspector can infer about the physical processes present. This inference is much more significant for type 2 data than type 3 as the mass of material is not measured directly.

2.2.7.1 Temperature

The temperature of the eutectic salt in the ER is a quantity that must be constantly monitored. Temperature has an impact on both the thermodynamics and electrokinetics of transport in the salt. With regards to the thermodynamics of the ER system, the standard reaction potential is determined by the Nernst equation where one of the dependent variables is temperature along with species concentration [28]. Thus assuming generally steady state concentrations of oxidating and reducing species, temperature will be the main factor in determining the reduction potential. Thus deviations from the normal potential determined by a reference electrode measurement may be due to temperature. In this case, normal operation may be occurring though an alarm is set off

and inspection by operator must be used to determine the cause and to determine what mechanically has gone wrong.

From the perspective of kinetics, the temperature is a dependent variable of the Butler-Volmmer equation [28]. With increases in temperature, the partial currents will increase and with decreases in temperature they will decrease. The other impact with regards to kinetics due to temperature is that the diffusion coefficient is positively dependent on the temperature. Thus with increases in temperature, the diffusion coefficient's values increase while with decreases in temperature they decrease. This is especially important to note as the limiting current density is directly proportional to the diffusion coefficient. A drop in temperature can lead to a reduction in the limiting current density thus resulting in a situation in which codeposition occurs at the cathode. Measurements to determine if temperature is the cause of codeposition must be linked to other PM measurements in the system such as potential.

2.2.7.2 Density

The density of the salt is an important factor to monitor between ER runs as it provides an indication of the salt's constituents. As the salt is a mixture of LiCl-KCl salt, rare earths, and actinides, the more reactions that occur within the salt the more the density will change as certain species are transported into the salt and certain species such as U are transported out [28]. As U is transported out and other TRU actinides continue to build up in concentration in salt, the expectation would be that the density of the salt will increase. If too great a concentration of TRU is present than codeposition will occur and the density of the salt will start to decrease. If the decrease continues, it will eventually reach another steady state value where only U deposition is occurring. Thus,

monitoring the nature of the salt combined with other measurements such as potential can assist in indicating the potential or the detection of an anomalous occurrence. In addition, density measurements can help indicate when a concentration measurement should be taken for sampling. This concentration measurement would inform the operator of whether or not more eutectic salt should be added and/or the salt cleanup process should be applied to some of the current eutectic. Thus for an operator to make these cost sensitive decisions, knowledge of the density should be a significant part of the operators decision making process.

2.2.7.3 Rotational Speed

The speed of rotation of the rotating electrodes/stirrer provides information about the potential nature of reactions occurring within the ER system. This is due to, for a rotational system, the Nernst diffusion layer thickness is inversely proportional to the angular momentum of the rotating body [39]. Thus, the faster the stirrer or electrode rotates, the smaller the diffusion layer thickness is. Conversely, the slower it rotates the larger this layer is. This is important to note as the limiting current density is inversely proportional to the diffusion layer thickness. So, a small diffusion layer leads to a large limiting current density while a large diffusion layer thickness leads to a smaller limiting current density for a species. Thus, if the rotation of the electrode or stirrer becomes slower than there is a potential for codeposition to occur. To determine if codeposition has occurred at the cathode or undesired species have migrated at the anode as result of these issue of rotation, these rotational speed measurements must be link to measurements such as electrode potential and concentration sampling.

2.2.7.4 Electrode Surface Area

The electrode surface area is an important quantity to measure before each ER run. This is because the surface area determines the current density of the electrode. This will in turn affect the nature of the reaction at the electrode [28]. As the current density is the current divided by the surface area, a reduced electrode surface area will increase the current density of the electrode. In the case of the cathode current density, if it exceeds the limiting current density determined by the Butler Volmer equation for U then reactions of Pu and other actinides will occur at the cathode. Physically this is because the total current density is the sum of the reaction current densities for the species in the salt and the two must be equal for the operation of the cell. The same logic governs the reaction at the anode for the oxidation of metals at the anode. If it is too great, undesired metals may oxidize to maintain the current density of the cell thus polluting the salt, with for example, U (IV) metal ions. A surface area measurement by itself cannot communicate whether or not the current density will exceed that of the limiting current densities decided by the Butler-Volmer equation. This surface area measurement must be paired with other measurements such as electrode potential and current to draw conclusions as to whether or not codeposition of metal has occurred at the cathode or undesired species are oxidizing at the anode.

2.2.7.5 Electrode Potential

The potentials of the anode and the cathode versus the reference electrode allow inferences about the reaction taking place at each electrode [28]. During normal operation, the cathode potential should be that of the reduction potential of U. During a significant off-normal operation this cathode potential would be more negative than

normal operation. This leads to the codeposition of TRU and rare earths at the cathode. Depending on this off normal reading, the types of species codeposited can be inferred, but not the total mass of each species. Monitoring the anode potential is also important as it monitors the oxidation reaction and ensures that undesired oxidation reactions do not occur. The most important reaction is the oxidation of U (IV) metal ions which cannot be reduced at the cathode. Thus monitoring the anodic potential to ensure it does not become increasingly positive is also important and allows an estimation of the type of species present in the salt that can be confirmed by other measurements such as mass spectrometry.

2.2.7.6 Current

By definition, current represents the amount of ions passed per time [28]. Thus, current is the reflection of rate of oxidation at the anode, transport in the salt, and the reduction of metal at the cathode. A higher current indicates that the rate of reaction is greater within the electrorefiner and thus a greater total amount of material will be deposited at the cathode. A lower current indicates that less total mass of material will be deposited at the cathode. Current data does not provide details as to if codeposition has occurred at the cathode. Thus, current is more valuable when combined with other measurements such as electrode potential, but still by itself provides insight as to the general movement of total material mass in the ER.

2.2.7.7 Radiation Count

Radiation counting measurements can be of two different varieties. The first is environmental radiation monitoring and the other is mass accountancy NDA measurements. The environmental radiation monitoring provides data on the state of the

overall hot cell and that materials are being moved when they are supposed to being moved as opposed to when they are not supposed to be doing so [48]. As such, very little information about transport within the ER can be inferred from these measurements. However, a large enough jump in radiation counts around the ER can be correlated with measurements on salt density and concentration to indicate that there is an increased number of TRU actinides in the salt and salt cleanup may be required. This is because as the concentration of TRU in the salt increases the neutron source in the salt subsequently increases.

As for NDA measurements for mass accountancy, these can be performed on ingots to determine the constituents and their total masses depending on the method used [46]. The counts in the NDA detector can determine whether or not codeposition has occurred and can be connected to measurement results from the ER. This type of analysis and linking of measurements has already been performed in previous studies related to SBS in which single and double coincidence count rates increased in an NDA coincidence counter as a result of codeposition of Pu occurring within the ER [12].

2.2.7.8 Concentration

Concentration measurements of eutectic salt are useful for both NMA and PM applications. The measurements of concentration during a balance period can provide an estimate of the total actinide concentration of the eutectic salt which can be utilized to infer the mass of actinides in the salt [49]. This calculated value can be utilized as part of the holdup calculation for the material balance. From the perspective of PM, concentration is important to monitor as it can infer the nature of the reactions occurring in the ER. As the limiting current density is directly proportional to the concentration of

the limiting species, a significantly reduced concentration of U and a higher concentration of TRU indicates that a codeposition reaction is more likely to occur [28]. Thus, concentration when connected to other measurements like electrode potential and current can lead to a conclusion as to the reason for an anomalous occurrence occurring. In addition, consistent concentration measurements when coupled with salt density measurements can assist the operator in making the decision to add UCl_3 to the eutectic or treatment of the salt to remove U/TRU.

2.2.7.9 Cathode Deposit Mass

The mass of the cathode deposits after being distilled and formed in an ingot are significant in both mass accountancy and PM. The total mass of the ingot themselves will very likely fill the outgoing inventory factor for the book values of the facility operator's material balance and thus will be subject to some degree of testing by IAEA inspectors. As for PM, doing a measurement of each ingot after they are produced can provide supporting measurements to potential alarms produced by ER measurements, in particular those that indicate codeposition of actinides at the cathode [50]. If a continuous type design for ingot manufacturing is being used like has been designed by KAERI for future engineering and commercial scale pyroprocessing facilities, dendrites will be cast into a turntable of equal sized molds and melted down within them [26]. Thus if only U is being deposited at the cathode, these final ingots should be roughly the same mass, within a margin of error, due to the scale and the nature of the turntable method utilized to continuously cast the ingot. If the cast has a significantly deviating weight in the positive direction, i.e. it weighs more than normal outside the margin of error, this would indicate a codeposition of actinides due to the greater mass of Pu and other TRU elements. If it

weighs less than normal, this would indicate that there is a large concentration of lighter metals such as zirconium and rare earth metals with less negative potentials starting to react in significant amounts at the cathode. Thus, each measured ingot should be weighed versus expected and known trends and then cross-referenced to potential ER signatures if an anomaly has been indicated.

2.3. Failure Modes and Effects Analysis

Failure mode identification is key step for simulation in this investigation of SBS. Without sufficiently identified and fleshed out failure modes, simulations for signatures and mass balance effects cannot be made. Thus, a standard method by which failure modes can be identified and evaluated as to their potential significance is required. Work performed in this dissertation was performed by adapting a methodology known as failure modes and effects analysis (FMEA) for safeguards related problems. FMEA was a method originally developed by the US Department of Defense to determine potential failures in military equipment and facilities and determine the effects on human health and safety as a result [51, 52, 53].

A Failure Modes and Effects Analysis (FMEA) is an approach to analyzing a system, particularly a mechanical system, to determine what potential failures a system can have, the results of these failures, as well as the manners to prevent and mitigate them. The FMEA is performed early within the design process to make corrections for potential failures and apply redundancy where needed before actual construction occurs as to save on the cost of future retrofits in a constructed facility [53]. Thus quantifying what these failures are, their frequency, and their impact on the system as a whole is of

great importance. With regards to pyroprocessing and safeguards development, performing an FMEA can be of great benefit as it can predict potential failure modes. These in turn could produce safeguards relevant results in that the system operates with material transporting to unexpected or undesired location due to component failure. These deviations from normal operation, if allowed to continue or occurring in significant magnitudes, can significantly disrupt the mass balance of the system leading inspectors to believe that diversion has occurred where it has not [12].

The FMEA methodology is applied through a general set of steps and associated actions. These steps are summarized in Table 7.

Table 7- Summary of FMEA Steps

FMEA Step	Associated Measures
1. Preliminary Measures	Selecting the team Defining the standard Defining the reporting procedure Defining the boundaries of the system Organizing design information
2. FMEA Evaluation Process	Evaluating the effects of each failure mode on the system Identifying failure detection methods/corrective actions Arranging audits Arranging practical FMEA tests Producing Recommendations
3. Finalization of Results	Produce final FMEA report for review

Providing detail as to what is associated with each of these three steps, the preliminary measures starts with the selecting and delegation of a team for the purpose of the analysis. FMEAs are typically organized and compiled by an individual but in the completion of the FMEA enlists a team of experts experienced in developing and classifying failure modes [51]. Thus, adequate care in many cases must be performed to select which experts are best suited for input into the report. Defining reporting

procedures involve the defining of exactly what manner the final report is produced and who is subject to reviewing the FMEA report and the chain of command of those for whom the report is being produced. The defining of the boundaries is the most important step of the preliminary measures as it defines the component of the FMEA that will be analyzed and defines what effects would be the most significant. This portion focuses on the operational and physical boundaries of the systems and are usually analyzed and displayed graphically as a block flow diagram. The final step of the preliminary analysis is the preparation of design data. This means determining up to date design information on which failure modes will be postulated and developing paperwork such as worksheets and forms by which those performing the FMEA can best suggest corrective action and demonstrate the nature of each failure mode.

The process of identifying and evaluating the effects of failure modes is often performed via collective brainstorming among those familiar with the system. The testing of actual systems to ensure compliance with the recommendations of the FMEA as well as to determine if the postulated effect of failures is present is a practical application of the FMEA to the design. This testing can be done using scaled laboratory studies or simulations.

2.4 PYROPROCESSING SIMULATION

2.4.1 ER SIMULATION

ERAD is computer code developed for the purpose of simulating mass transport within ER operation [54, 55]. ERAD is a modification of the REFIN code developed at Seoul National University [54]. This code is the primary code used for SBS related research. ERAD utilizes an iterative method to calculate mass transport. It calculates

mass transport in one dimension with a differential equation solver known as Livermore solver for ordinary differential equations (LSODE) in FORTRAN.

ERAD requires several input values and produces several different output files that can be applied to both operations and safeguards [54]. In terms of inputs, the first set of inputs involves the elements of interest. The elements of interest are the elements of the ER salt bath (Li, K, and Cl) as well as seven metal species chosen by the user, most importantly actinides, rare earths, and zirconium. For each species, the fundamental electrochemical data are provided for a selected temperature input. This fundamental data includes exchange current density, standard potentials, valence state, diffusion coefficient, activity coefficient, transfer coefficients. This data define the species data for computation and allows that any elements with determined data can be utilized within the ERAD model. On top of fundamental data, information for operation of the ER is then provided. This information includes time of operation and time steps, current of operation, electrode surface area, and electrode characteristics. This information allows proper application of the fundamental data to an actual ER operation. The next set of inputs involve solver settings for LSODE such as tolerance and methodology. Finally, data for the concentration of the species in the anode, eutectic salt, and cathode as well as the initial mass and volume of these specific portions of the ER cell are provided. With an input file known as an *inpref* file of this data allows initiation of ERAD. A summary of these variable inputs are seen in Table 8.

Table 8- Modifiable Input Variables for ERAD

Variable	Unit
Temperature	K
Diffusion Coeffient	cm^2/s
Valence States	unitless
Time	hours
Current	A
Diffusion Layer Thickness	μm
Starting Anode Composition	wt%
Starting Salt Composition	wt%
Electrode Area	cm^2
Starting Salt Mass	grams
Starting Anode Mass	grams

In terms of outputs, several different sets of data for the simulated ER operation are produced. These outputs fall into four major categories. The first is the content of the electrodes versus time step. This is computed for both anode and cathode as well as for the electrolyte salt. The second set of output data is that of the electrode currents and potentials. This is computed against the reference electrode specified by the input data for standard potential. This data is for currents and potentials versus time. The third set of output data is that of the concentration of electrode surfaces. This data is computed for species in the salt at the surface of the electrodes. The final major set of output data computes the concentrations in the diffusion layer of the specified diffusion layer of the electrodes from the input file.

A flowsheet of the method in which ERAD utilizes the input file to produce the output data required is seen in Figure 6 [56].

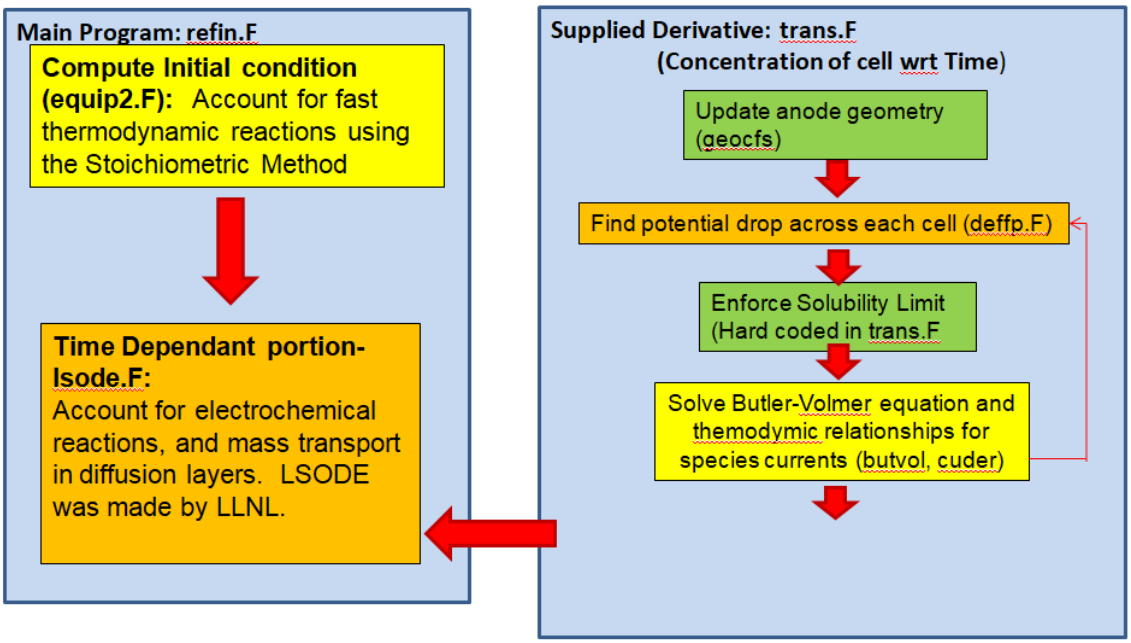

Figure 6-ERAD Method Flowsheet

As demonstrated by the flowsheet, the *inpref* file is first read into *refin.f* which operates as a master file that communicates to all other subprograms to compute the transport and thermodynamic properties of the ER operations. This master file is responsible for initializing the time dependent portions of the code after calculating and storing the fundamental data. It performs this by initializing by the transport and electrochemical related scripts as well as the LSODE solver. For the purpose of the solver, the ER system is divided into a mesh of cells with a certain number applied to a different portion of the cell. The solid anode, cathode, and bulk electrolyte salt are assumed to each be a single one dimensional cell for the purpose of calculating the concentration term of the mass transport equation. For the anode, there is a variable size diffusion/migration layer that can be made to be between 20 and 200 cells depending on the user's preference. This layer is between the solid anode cell and the diffusion/migration boundary layer for the anode which is made up of 20 to 200 cells.

There is a diffusion/migration boundary layer between the cathode and the bulk salt and is of the same tunable size as the anode diffusion layer. These diffusion layer cells act as the region between the solid reaction surface and the bulk salt and demands the majority of the computational time. The metal surfaces and bulk salts are simplified into single cells to enable efficient computation.

The first step in the time dependent portion is the updating of the anode geometry. This feature is the defining modification of the original REFIN code that has been applied to the improved ERAD code [56]. The anode geometry is updated based on whether cladding is present within the anode basket. If clad is present, then the anode is assumed to be cylindrical, and the dissolution occurs across the flat surfaces of the cylinder (i.e. top and bottom) and the volume is updated along these boundaries. If cladding is not present, dissolution and volume updating occurs over the curved surface of a solid metal cylinder. At each time step, the volume is updated as a function of concentration. The volume is updated based on the concentration initially present and the amount present at a given time step according to equation 12.

$$\Delta V_{U,cyl} = V_{cyl,0}\left(\frac{U}{U_0} - 1\right) \tag{12}$$

Where $\Delta V_{U,cyl}$ is the change in the U volume in the anodic cylinder, $V_{cyl,0}$ is the initial cylinder volume, U is the concentration of U at a given time, and U_o is the initial concentration of U in the anode.

After the anode has been updated for the given time step, ERAD then calculates the potential drop across each cell utilizing calculated species currents from either an initial guess of potential from the *inpref* file or for all time steps other than the initial from the calculation of species current utilizing the Butler-Volmer equation. In addition

to the potential drops, a coded solubility limit is applied to the cells in the anode diffusion layer.

After these potential drop and solubility limit calculations are undertaken, another time dependent loop is utilized to calculate the electrochemical properties of the cell for each time step to be implemented in the time dependent mass transport portion of the code. It performs this by solving two fundamental electrochemical equations. The first is the Nernst equation which is utilized to calculate the electrochemical potential of each species adjusted for concentration and temperature from the inputted standard potential. The Nernst equation is seen in equation 13,

$$E_{eq,r} = E_{0,r} + \frac{RT}{n_r F} \ln\left(\frac{\gamma X_{ox,i}}{\gamma X_{red,i}}\right) \tag{13}$$

Where $E_{eq,r}$ is the equilibrium reduction potential, $E_{0,r}$ is the standard reduction potential, R is the ideal gas constant, T is the temperature, n_r number of electrons transferred, F is the Faraday constant, γ is the activity coefficient, and $X_{ox,i}$ and $X_{red,I}$ are the concentrations of oxidation and reduction of the species i in the salt.

With the equilibrium potential known, the non-equilibrium overpotential (η_r) can be calculated to be implemented within the Butler-Volmer equation. This overpotential is just the difference between the electrode potential and the equilibrium potential calculated by the Nernst equation.

The Butler-Volmer equation is utilized for calculating the partial current for each species reacting at the electrode surface. The Butler-Volmer equation is seen in equation 14.

$$i = i_o \left(\frac{X_{Ox}(0,t)}{X^*_{Ox}} \exp\left(\frac{\alpha n F}{RT}(\eta_r)\right) - \frac{X_{Red}(0,t)}{X^*_{Red}} \exp\left(-\frac{(1-\alpha) n F}{RT}(\eta_r)\right)\right) \tag{14}$$

Where i is the species current, i_o is the exchange current density, and α is the transfer coefficient. The exchange current density is calculated utilizing the input of the standard exchange current density through the application of equation 15.

$$i_o = Fk_0 X_{Ox}^{*\,(1-\alpha)} X_{Red}^{*\,\alpha} \tag{15}$$

where k_o is the transfer coefficient.

These values calculated for the partial current densities for each species and for each electrode are then applied to the time dependent mass transport portion of the code where the transport within each cell is calculated for each time step. The partial current densities sum to be the total current density specified by the user and these two values assist in calculating the mass transfer occurring at the electrode surfaces for each species. The mass transport equation utilized by ERAD is given in equation 16.

$$\frac{\partial y_i}{\partial t} = -D_i \frac{\partial^2 y_i}{\partial x^2} - \frac{FD_i n_i}{RT} \frac{\partial}{\partial x} y_i \frac{\partial \Phi}{\partial x} \tag{16}$$

where y_i is the concentration of species i, x is the 1D spatial dimension, D_i is the diffusion coefficient of the species i, and the term $\frac{\partial \Phi}{\partial x}$ is what is known as the potential gradient. The potential gradient is a function of concentration and current density and is calculated utilizing equation 17.

$$\frac{\partial \Phi}{\partial x} = -\frac{I_{tot} + \sum_i \left(D_i n_i F \frac{\partial y_i}{\partial x} \right)}{\sum_i \left(\frac{F^2 n_i^2 D_i}{RT} y_i \right)} \tag{17}$$

where I_{tot} is the total electric current density.

For each time step, the LSODE solver is applied to the mass transport equation. The calculated results for the concentration terms, potential terms, and current terms are then written to their respective output files and the same process occurs iteratively until all set time steps have been covered and the outputs written for each one.

ERAD is used within this dissertation to simulate failure mode conditions within the ER. This produces data that can be integrated within systems scale facility simulations. However, ERAD has not had a significant amount of experimental work to determine if it is an effective choice to be applied in this manner. For this reason, experimental work was performed as part of this dissertation to determine its efficacy.

2.4.2 Facility Simulations

To simulate pyroprocessing facilities, system models have been developed on multiple different computational platforms. The one focused on in the research of this dissertation is that of the SSPM Echem developed by Sandia National Laboratories [1]. SSPM Echem simulates the entires pyroprocessing flowsheet for ceramic fuels as determined by ANL. SSPM Echem is scripted in Simulink with certain submodels linked to MATLAB functions [1, 16]. The model simulates the mass transport of elements 1-99 in a pyroprocessing system in addition to the total salt mass in the form of a 1x100 matrix. Using the masses for U and Pu at every step in the flowsheet, the model is able to compute an ID and SEID for a given balance period. In addition, a Cumulative ID can be computed for a given operational period.

ID and SEID are calculated in EChem using an NRTA mass balance scheme. For a selected balance period, 28 hours for the simulations of this dissertation, the ID and SEID are calculated via a mass balance from input, inventory, and output measurements [1]. The same calculation method is utilized for the entire of the operational period for each balance period during that time. The ID and SEID are calculated within the same MATLAB script at the same time using input signals from Simulink.

To calculate ID and SEID in Echem SSPM, several signals need to be recorded to calculate the material balance, in particular input measurements, inventory measurements, and output measurements. The input measurement of the fuel is the integration of the signal after the fuel chopping stage integrated over the time of the balance period. In addition, inventory measurements are taken for each unit operation. All inventory measurements are in the form of an integrated signal over the balance period with the exception of the ER and electroreducer which are assumed to be sampled every balance period to determine mass. Finally, output mass measurements take place which are the integration over the balance period of the mass signal for the output product streams. For each of these measurements, only the signals of the U and Pu are utilized in the computation of the ID and SEID. The ID and SEID are computed for both U and Pu individually.

The signals recorded from the input, output, and inventory that are integrated and utilized as the input of the ID and SEID calculations consist of six parts that form a 6x1 input vector. The first is the mass signal of U. The second is the random measurement error of U inputted by the user multiplied by the mass signal and by a random number to simulate the distribution of the error. The third is the systematic measurement error of U inputted by the user multiplied by the mass signal for U and by a random number to simulate the distribution of the error. The fourth through sixth value are the same mass signal, random error, and systematic error calculated in the same way as the U values except in this case for Pu.

These six integrated signals are then used to calculate the ID and SEID for the balance period. The ID is calculated by subtracting the sum of the inventory measurement

mass signals and output measurement mass signals from the input mass signal. This calculation is seen in equation 18. For the first balance period, the calculation is calculated as described. For all subsequent mass balances after the first, the previous inventory measurement for each unit operation is carried over to the new mass balance and added to the overall balance. The IDs calculated for each of these balance periods during the total operational time are summed with one another to generate the cumulative ID.

$$ID(i) = Input - INV(i) + Inv(i-1) - Out \quad (18)$$

where *i* signifies the balance period, *Input* is the input mass at the assembly chopper, *Inv* is the sum of the measurements at the unit operations, and *Out* is the mass of the metal product and U product.

The SEID is calculated using all six signals. Each mass signal measurement is first squared and multiplied by the sum of the squares of the random error and systematic error signals. These values are summed with the inventory measurement values being multiplied by two. The square root is taken of this sum of values to form the SEID for each balance period for both U and Pu. The SEID calculation is written out in equation19.

$$SEID = \sqrt{\sum_j MEAS(j) * (\sigma_{sys}^2 + \sigma_{rand}^2)} \quad (19)$$

where *j* signifies the measurement location, σ is the measurement uncertainty, and *MEAS* is the integrated mass signal for the given measurement point.

The masses transported within SSPM Echem are assumed to be batch transfers throughout the facility. Thus, mass is transported in the form of pulses of material that are moved between each step in the flowsheet. The form of these pulses in terms of elemental

constituents is selected by the operator of the program as multiple different burnups for commercial fuel can be called by SSPM Echem. This burnup data comes from calculations in the burnup code ORIGEN. The front end steps of the flowsheet include fuel chopping and voloxidation as well as a step for electrolytic reduction. At this step 100% of the off-gas products are removed from the mass matrix being transported as well as 100% of the tracked Cs/Sr/Ba/Rb/Tc/I that remain in the salt phase of the reducer. Some salt remains from reducer in the tracked mass matrix and proceeds to the next step of the ER. The ER is where the separation process occurs and the product of the operation is produced in three forms: a metal waste product, a U product, and U/TRU product. The metal waste product is the remains of the anode fuel basket. The U product is a product assumed to be 100% separated U, and the U/TRU product is assumed to be 70% U and 30% TRU. These products are formed with a constant separation efficiency developed from previous work at the FCF. All three of these products with their entrained salt are transported to three separate product processing stages, where the salt is distilled off and final products are forged. The salt distilled off then undergoes a drawdown process from which fission products are removed to form their own waste products. In addition the salt is treated for U/TRU products and the salt is processed and returned to the ER while the salt processed that does not contain U/TRU is returned to the electrolytic reducer. A representation of this total flowsheet is portrayed in Figure 7.

In addition to calculating the mass flow and general safeguards calculations, SSPM Echem also possesses the ability to simulate diversion scenarios by having a certain percentage of SNM removed at a given step every time the mass batch passes by given step, e.g. 3 percent of U is removed between the electrolytic reducer and the ER

[1]. To calculate and determine if an diversion is occurring a Page's test can be performed on the ID, SEID, and Cumulative ID data with parameters that can be set to meet false alarm and detection sensitivity goals. Each measurement of mass that goes into calculating these values occurs at every unit operations step and the random and systematic uncertainty of which can be set by the user. This allows the user to determine what detection requirements are needed for measurement technology in facility design and what goals to set in measurement technology development.

Despite these advantages, the SSPM Echem still requires several improvements that are being actively pursued. The first is that the unit operations are based off assumptions of separation efficiencies instead of actual physical modeling. Actual electrochemical simulations should be integrated via either direct or indirect means. Work related to this is a major objective of this dissertation. In addition, improvements in the monitoring subsystems to reflect actual measurements are currently being performed jointly between Sandia and the University of Tennessee. With these improvements a more robust Echem SSPM can be utilized in the safeguard and facility design process.

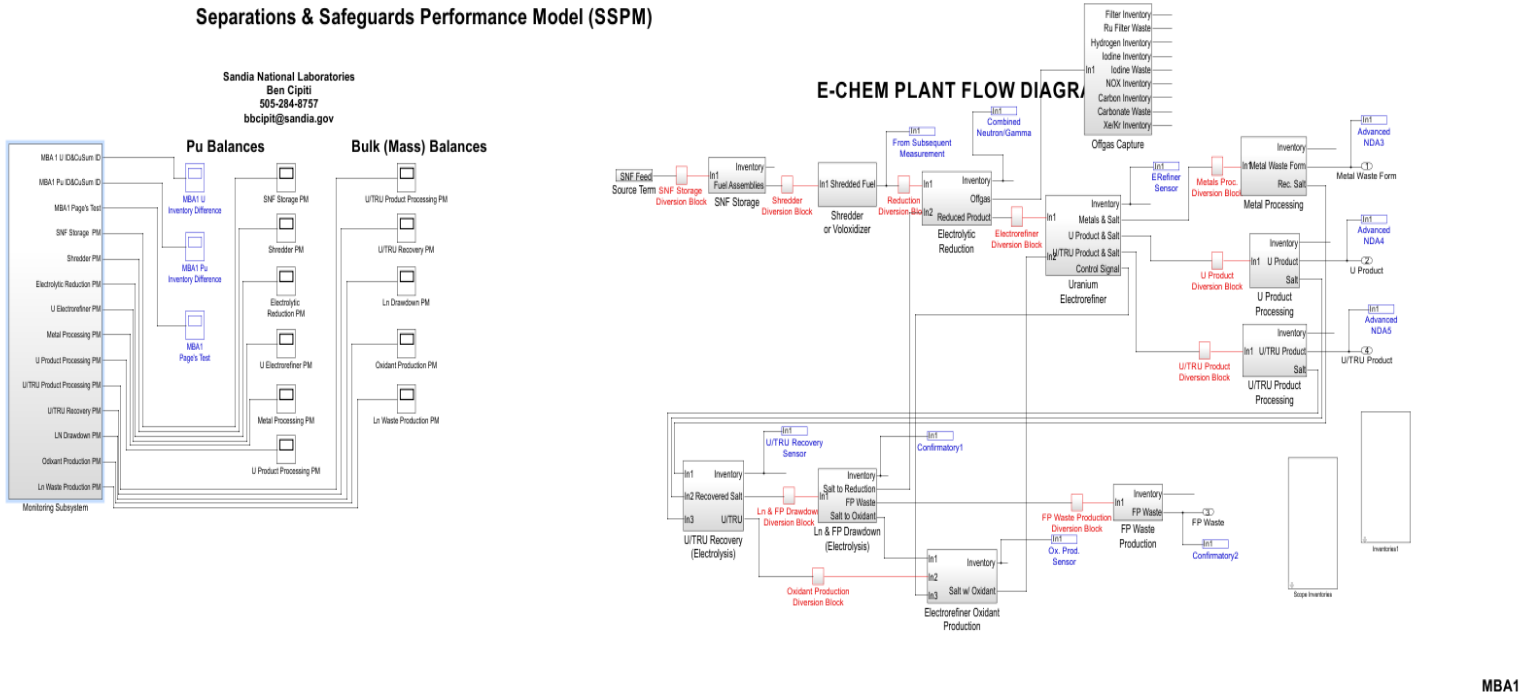

Figure 7- SSPM Flowsheet and NMA Module

CHAPTER 3: METHODS AND APPROACHES

A strategy combining several different approaches, both experimental and computational, has been developed to best fulfill the objectives laid out in the introduction. This brief chapter contains a high level discussion of the approaches to meet the objectives. These approaches cover the experimental validation of ERAD's assumptions, the FMEA process in its application to pyroprocessing unit operation equipment, simulation of failure modes in ERAD, and the integration and simulation of failure mode data in SSPM Echem.

3.1 EXPERIMENTAL INVESTIGATION OF ERAD

I performed multiple experimental campaigns to confirm ERAD's assumptions experimentally and determine if the code was a suitable tool to simulate failure modes. I along with collaborators at several institutions performed these experiments on a laboratory scale utilizing a three electrode setup of an anode, cathode/working electrode, and a reference electrode. The anode was a basket of stainless steel containing U, the cathode was W or stainless steel wire, and the reference electrode was an Ag/AgCl reference electrode using a porous ceramic housing. These were submerged in a LiCl-KCl salt bath heated to 500 C°. UCl_3 salt as well as a surrogate chloride salt to represent $PuCl_3$, often MgCl or $GdCl_2$, were mixed in with the LiCl-KCl salt to provide a starting concentration of U and the surrogate metal. The results presented in this dissertation cover an experimental campaign concerning Gd codeposited with U. Gd was chosen as the difference of reduction potential between Gd and U is about -0.3 V, similar to that of

the difference between Pu and U [57, 58]. During codeposition, U starts to deposit first followed by Gd and the presence of codeposition can be identified by observing the cathode potential as current is passed. If the cathode potential is at or more negative than the Gd reduction potential than codeposits of Gd are expected in the final metal product extracted. I performed these experiments over an experimental matrix of different cathode surface areas. I selected this test range to simulate a change in ER cathode surface area due to a failure in the equipment required to submerge the cathode in the salt bath. For each experimental run, data for electrode potentials from the reference electrode were collected along with deposits at the cathode sampled for mass analysis.

The experimental runs were then modeled and simulated in ERAD using the experimental parameters. The results of both the reference electrode response and the mass deposits at the cathode were compared between the analytical and computational results to determine relevant conclusions. Chapter 4 of this dissertation details the most conclusive experimental campaign as well as the set up, method, and test matrix utilized.

3.2 FMEA OF PYROPROCESSING UNIT OPERATIONS

An FMEA was performed on a pyroprocessing ER with the key definitions modified to reflect a safeguards rather than safety focus. This was done by following the steps described for a general FMEA in Chapter 2. I first selected a standard and a lowest indenture level. I then developed a worksheet from the standard redefining the columns of the worksheet to have a safeguards focus. After the worksheet was established, I decomposed the ER into individual components and related each component to one another via a flowsheet. I then systematically addressed each component for potential failures and the effects of these failures. After, reviewing the potential failures, I make

recommendations as to possible simulation campaigns that can confirm the effects postulated as well as understand their effects on the mass balance of the system. These FMEA steps are detailed in Chapter 5 of this dissertation.

3.3 ERAD Simulations of Identified Failure Modes

With failure modes identified from the FMEA, the next step is to determine which failure modes to simulate using ERAD and to then simulate them. To do so, I analyze the failure modes to determine which are significant and which could be the subject of a simulation campaign. These failure modes are then inspected individually to determine which failure modes to simulate by manipulation of individual variables in ERAD. Thus, simulations are not performed on failure modes that cannot be simulated in ERAD given limitations in inputs. After selecting failure modes for simulation, I generated a test matrix for each failure by varying the dependant input to ERAD e.g. varying the cathode surface area for failure of the electrode retraction mechanism. These simulations model this test matrix over a range of cases to determine the sensitivity of the mass transport and electrode potential to that failure. ERAD simulations over this test matrix collect two types of data: short-term and long-term data. Short-term data are data produced at the end of a single 24 hour run. This provides information about a single run and the impact of the affected component on the overall transport of the system. It also allows conclusions to confirm or alter the conclusions with regards to the severity of a given failure mode as documented in the FMEA worksheet. Long-term data documents the long term effects of the failure mode over an entire mass balance period. To do this, the salt output of an ERAD run is used as the input of the subsequent ERAD salt composition input in perpetuity for the number of specified ERAD simulations. By performing this simulation

over a number of operational cycles, the results show the effects of ER operations over a long period of time assuming no salt treatment to remove actinides from the salt has occurred over that operational period. Chapter 6 expounds on the test matrices and the specifics of short and long term simulations.

3.4 Simulation of Failure Modes in SSPM Echem

With short and long term data produced from ERAD simulations of both normal operations and off-normal failure modes, the next step was to integrate this data into SSPM Echem. The only data used is long-term data. To produce functions of mass deposits at the cathode, anode mass, and electrode potential as a function of time, I performed Regression analysis on the long term data. I integrated these fits as piecewise functions into the ER subsystem of the SSPM Echem. At this point, simulations of the entire pyroprocessing system to analyze the safeguards impact of failure modes could be performed. Three separate studies were performed using this modified model with the modeled ER data. The first was on the impact of the measurement uncertainty of the mass analysis at the U product manufacturing stage. The second was on the impact of the failure modes on the SEID of the safeguards system. The last study was based on varying the NRTA balance period to determine the effects of longer balance periods occurring with regularity and to determine what possible balance periods could be used for an NRTA mass balance scheme. Chapter 7 fleshes out the specifics of the manner of which the data was analyzed and integrated as well as the described simulation studies.

CHAPTER 4: EXPERIMENTAL EVALUATION OF ERAD AS A TREND PREDICTION TOOL

As indicated in the introduction as well as the methods and approaches section, multiple experimental campaigns were undertaken to determine the role of ERAD as a trend prediction mechanism. This chapter details the experimental campaign undertaken at the University of Utah Metallurgy Department in December of 2015 [59]. This set of experiments provides the most repeatable results and the most reliable conclusions.

4.1 METHOD

My collaborators and I performed all experiments in an argon atmosphere glovebox with oxygen and water both below 0.1 ppm throughout the tests. UCl_3 and $GdCl_3$ (99.99% anhydrous, Alfa Aesar) were dissolved in approximately 50 g of premixed LiCl-KCl eutectic (99.99% anhydrous, SAFC Hitech). An alumina crucible contained this salt mixture, which was heated in a Kerr Auto Electro-melt furnace. The salt mixture was maintained at 773 ±1 K. A thermocouple monitored the temperature of the salt and was removed during operation of the cell.

The electrochemical test methods were carried out in a three electrode setup that included a working electrode (cathode during constant current deposition), a counter electrode (anode during constant current deposition), and a reference electrode. The working electrode was a W wire 1 mm in diameter. It was attached to a vertical translator (as shown in Figure 8), which allowed the precise movement of 0.005 mm per step. The counter electrode consisted of U metal sheets that were placed in a stainless steel basket. The reference electrode was an Ag wire (99.9%, Alfa-Aesar) and 5 mol % AgCl (99.9%

anhydrous, Strem Chemicals) in LiCl-KCl eutectic in a close ended thin mullite tube. The electrodes were connected to an Autolab PGSTAT302N potentionstat.

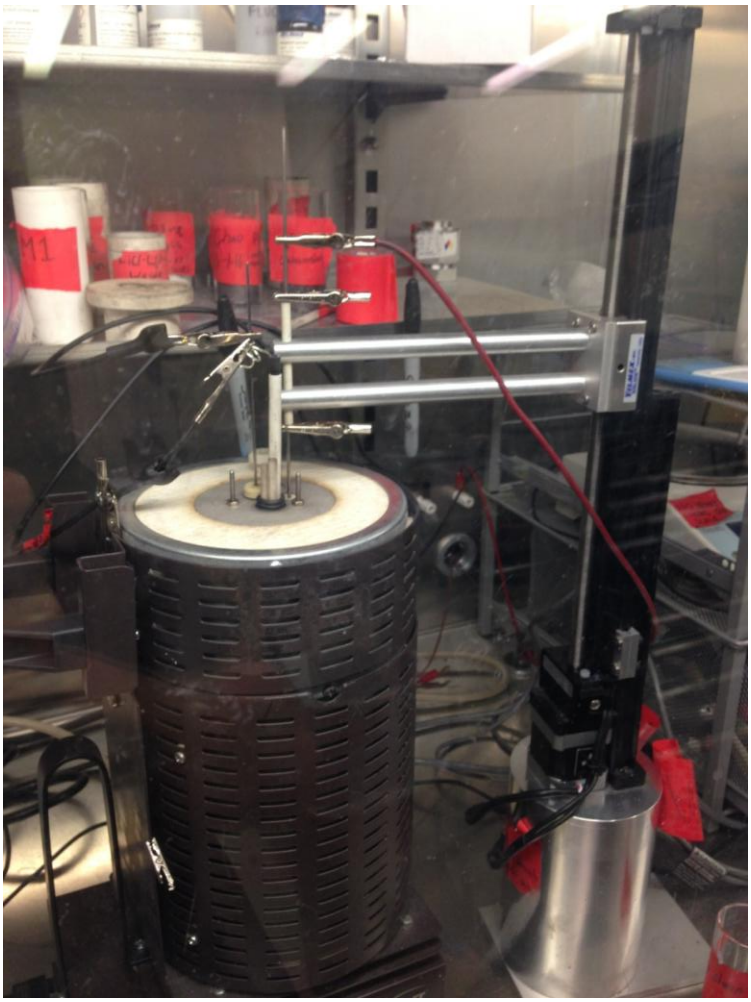

Figure 8-Experimental Setup featuring a high temperature Kerr furnace, electrodes, and vertical translator

The objective of the experimental study was to determine if the calculated effect cathode surface area variations have on the relative amounts of co-deposition of two metals matched those determined analytically. After mixing and melting the salt in the furnace pictured in Figure 8, cyclic voltammetry scans were performed with the working electrode fully submerged in the salt to determine the achievable current density (A/cm^2)

during deposition experiments. Then a series of constant current deposition runs were performed. For constant current tests, the working electrode served as the cathode, and the counter electrode served as the anode. The immersion depth of the cathode was changed to increase or decrease the current density from run to run. The salt mixture used for this study was a combination of LiCl-KCl eutectic, UCl_3 salt (1.3 wt%), and $GdCl_3$ (3.2 wt%).

The alumina crucible with the salt mixture was then placed within the furnace and heated up to a temperature of 530^{o}C over a period of two hours. The reference electrode was placed before the heating right above the surface of the eutectic salt. The salt was then determined to be melted and to be at 500^{o}C through the use of a thermocouple submerged within the eutectic salt mixture. The anode basket, cathode, and reference electrode were then submerged within the melted salt. The reference electrode was only submerged approximately 12 cm into the furnace to allow the tip to penetrate the surface of the mixture. The anode and cathode were fully submerged within the salt to touch the bottom of the crucible. The three electrodes were then attached to the leads of the potentionstat.

After a period of about 30 minutes, the system was assumed to be at thermal equilibrium and CV analysis was performed for two purposes. The first was to determine the salt level in the crucible and to determine the operating currents for the experimental analyses. To determine the salt level, the cathode was raised 1 cm from the bottom of the crucible, and a CV measurement was taken. The Gd reduction peak height was then recorded. The peak height was then recorded by raising the cathode in 0.4 cm increments all the way to 3 cm above the bottom of the crucible. The peak height data was then

plotted to determine the total salt depth which was estimated to be 31.40 mm. Knowing this, the surface area of the cathode could be adjusted accordingly with regards to submersion depth within the salt.

To determine the operating currents, a CV analysis was undertaken at a base working electrode depth of 30.58 mm. The operating current was then identified by inspecting the CV plot. Experiments would be undertaken at two separate currents. The first was at a current corresponding to the potential just to the left of the Gd peak potential on the CV diagram. The second was a current corresponding to the potential at the start of the Gd peak. With the current and salt depth known, the test matrix for the actual experimental runs could be determined and investigated. The test matrix of the experimental runs undertaken in this investigation is seen in Table 9.

Table 9- Test Matrix for Experimental Runs

Run	Current (A)	Time (s)	Depth of Cathode (mm)
1	0.6	60	30.58
2	0.6	60	26.76
3	0.6	60	23.39
4	0.6	60	19.12
5	0.6	60	15.30
A	0.1	60	30.58
B	0.1	60	26.76
C	0.1	60	23.39
D	0.1	60	19.12
E	0.1	60	15.30

The experimental study consisted of ten constant current runs. Before each run, the cathode wire was adjusted to the surface area desired. CV analysis was then performed to "clean" the cathode of any residual or present deposited material by operating the scan at an upper limit potential of 0.4 V. The current was then applied for a total time of 60 seconds after which there was a 10 second period of which no power was supplied to the

cell but measurements for potential were still recorded. Both CV and potential data for these constant current experiments were recorded using the NOVA potentionstat software. After the constant current operation, the cathode was removed from the furnace and the portion of the cathode containing deposits was cut and placed within a sample vial for composition analysis. The cathode was then replaced, and the process was repeated. In addition, before and after each run a salt sample of nominally 0.05 grams was taken from the salt.

For composition analysis of both the cathode deposits and salt samples, inductively coupled mass spectrometry (ICP-MS) analysis was utilized. ICP-MS was used to analyze the mass concentrations of U and Gd in all samples. In addition, for Runs 1-5 ICP-MS was used to determine concentrations of Li and K to determine if Li had been reduced at the cathode.

When the cathode was raised out of the salt mixture for sampling, a small amount of the salt inevitably adhered and froze onto the W wire. The salt deposited could not simply be rinsed off with water because there was possibly Li metal deposited that would have reacted with water. Additionally, the metal deposit might not all be tightly packed, therefore there was a risk that some deposit could be rinsed off.

Consequently, the cathode sample sections were each transferred into a beaker with about 26 ml of aqua regia to dissolve all the salt and metal deposit. A small amount of W is expected to dissolve, but that should not interfere with the analysis of Li, K, Gd, and U. The beakers were covered with watch glasses and heated on a hot plate to almost dryness. The beakers were cooled to room temperature then 5ml HNO_3 and approximately 35 ml ultrapure water was added. Then the beakers were heated to boil and cooled to room

temperature. Thereafter, the solutions were collected into a 100 ml volumetric flask and diluted with ultrapure water. Finally, the samples were diluted with 5 vol% HNO_3 to the appropriate dilution for ICP-MS analysis for Li, K, Gd, and U.

The salt samples were directly dissolved into 5 vol% HNO_3 in 100 ml volumetric flasks and diluted for ICP-MS analysis for Li, K Gd, and U. The mass of residual salt on each cathode sample was calculated using the salt composition, deposit weight, and composition.

4.2 Results and Analysis

The results from the CV analysis of the salt mixture are seen in Figure 9. The circles on the plot indicate the operating currents chosen for the subsequent constant current depositions. The currents selected were 0.6 and 0.1 A.

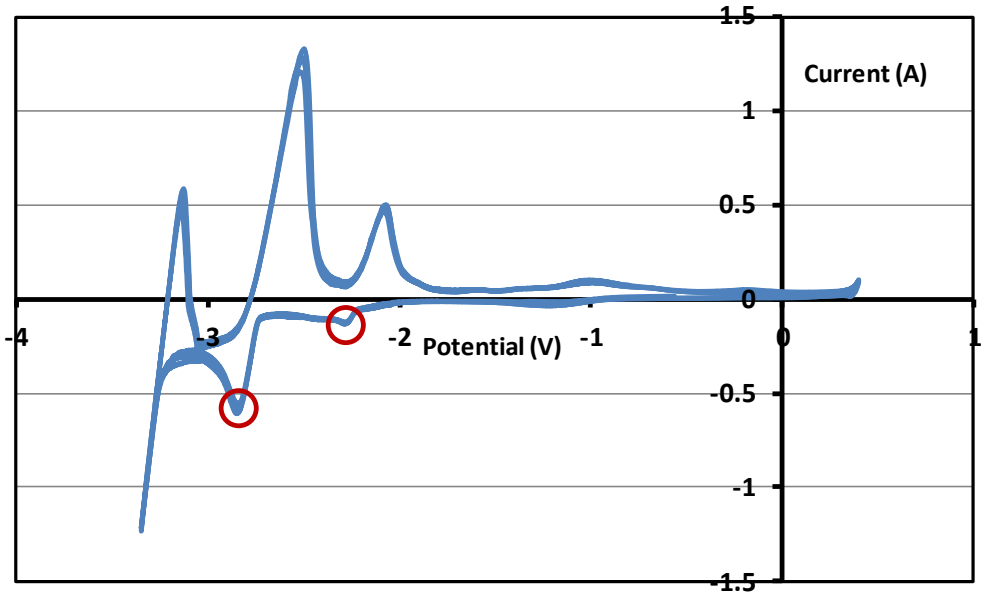

Figure 9- Results with circles indicating where operating currents were selected

Calculations were performed using ERAD to simulate constant current electrorefining at the conditions of the experiments. Starting concentrations of salt for ERAD input were

determined through mass analysis of salt samples that occurred between runs. The diffusion layer thickness for each run was set at 30 micrometers thick and this value was used for each modeled case. For the setup, this diffusion thickness is chosen as to be significantly larger than that which would be produced by natural convection. In doing so, ERAD captures the changing diffusion layer thickness as it calculates the concentration profile in the diffusion layer. The diffusion layer thickness was determined to be sufficiently large if the concentration profile of the outermost cell of the electrode was constant. The concentration profiles of both electrodes' diffusion layers are calculated and are an output of the code.

Plots of the experimentally determine results for cathode potential are seen in Figure 10 and Figure 11. As expected, the potentials are lower for the 0.6 A runs compared to the 0.1 A runs, for which experiment and model are in agreement. For the 0.6 A depositions, the potential rapidly settles at a value of about -3.3 V. This indicates that Li should be depositing on the cathode along with U and gadolinium based on the CV shown in Figure 2. For the 0.1 A depositions, potentials initially drop quickly as low as -3.0 V, but all eventually reach a steady value of -2.8 V. Based on the CV in Figure 9, this indicates that deposition of Gd is occurring with U, but no Li should be depositing.

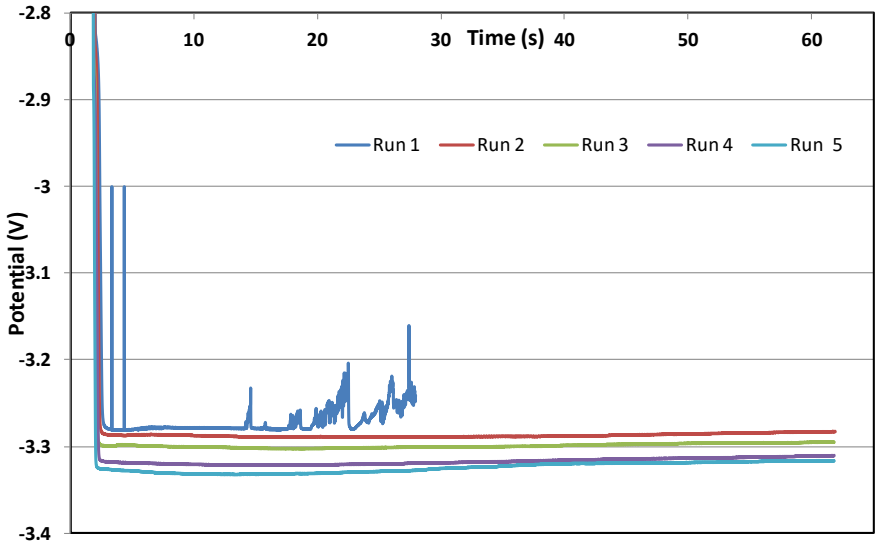

Figure 10- Experimental Potential (V) versus time (s)of Runs 1-5, 773 K, 0.6 A, Surface Areas: (0.556, .0483, 0.410, 0.337,0.265 cm2), W Working Electrode, Ag/AgCl working electrode adjusted for Cl-/Cl reference electrode

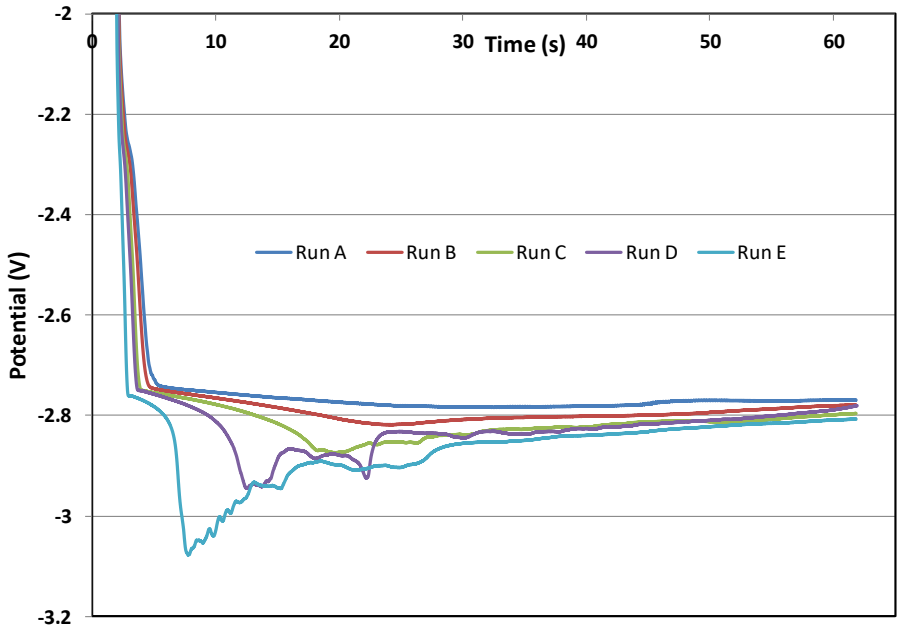

Figure 11- Experimental Potential (V) versus time (s) of Runs A-E, 773 K, 0.1 A, Surface Areas: (0.556, .0483, 0.410, 0.337,0.265 cm2), W Working Electrode, Ag/AgCl working electrode adjusted for Cl-/Cl reference electrode

The results for the calculated potentials from Runs 1-5 and A-E are depicted in Figure 12 and Figure 13, respectively. While the model does not fit the data values, it does reproduce the effect of cathode surface area. Depth of the cathode decreases from Run 1 to 5, which causes the surface area to decrease. The potential responds by becoming more negative as the area decreases.

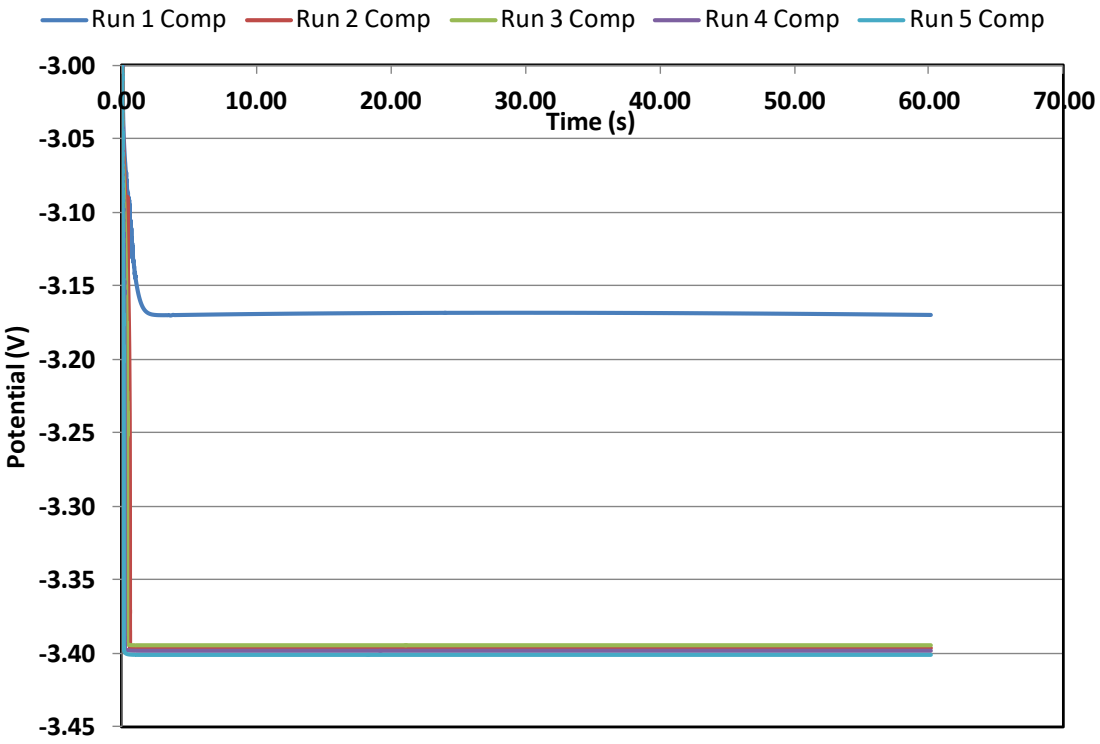

Figure 12- Computational Potential (V) versus time (s) of Runs 1-5, 773 K, 0.6 A, Surface Areas: (0.556, .0483, 0.410, 0.337,0.265 cm2), W Working Electrode, Ag/AgCl working electrode adjusted for Cl-/Cl reference electrode

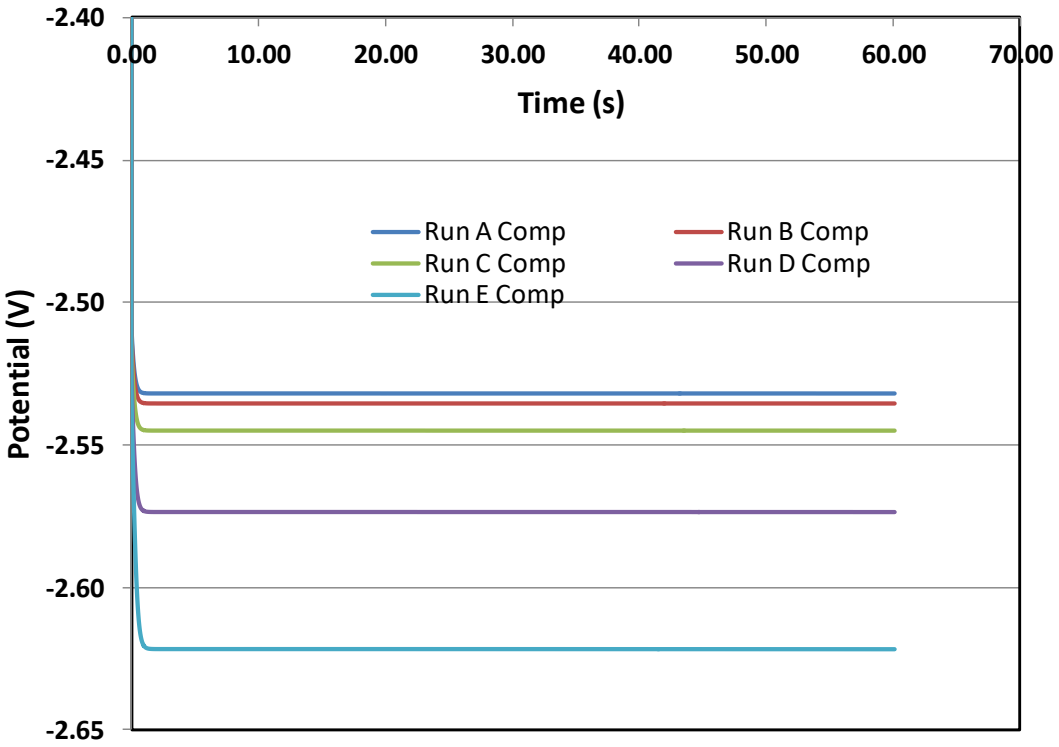

Figure 13- Calculated Potential (V) versus time (s) of Runs A-E, 773 K, 0.1 A, Surface Areas: (0.556, .0483, 0.410, 0.337,0.265 cm2), W Working Electrode, Ag/AgCl working electrode adjusted for Cl-/Cl reference electrode

It is important to state that the same 50 gram mixture of LiCl-KCl-UCl_3-$GdCl_3$ was used for all of the tests from Run 1 through Run 5 and then Run A through Run E. There should be some loss of U and Gd from the mixture as a consequence of electrodeposition. Salt samples were taken before and after each deposition run and analyzed via ICP-MS for U, Gd, Li, and K concentrations. The results are shown in Table 10. It can be seen from the U and Gd concentrations reported in this table that the salt composition remained relatively constant within the statistical variance of the sampling and measurement method. Thus, concentration in the salt can be assumed to be virtually constant during each deposition run. This may partially explain why the modeled

potentials are steady with time after the first few seconds as seen in Figure 12 and Figure 13.

Table 10- Composition of Salt Samples (Samples taken before an experiment are labeled with i, while samples taken after an experiment are labeled with f)

Sample	Sample wt.	Gd (wt%)	U (wt%)	Li (w%)	K (wt%)
1-i	0.0845	1.865	0.794	7.695	28.588
1-f	0.0522	1.803	0.829	7.340	28.596
2-f	0.043	1.940	0.782	7.978	28.570
3-f	0.0591	1.807	0.722	7.547	28.627
4-f	0.0571	1.805	0.728	7.340	28.625
5-f	0.0596	1.972	0.752	7.298	28.569
A-f	0.0342	1.948	0.848	8.225	28.548
B-f	0.0442	2.019	0.891	8.417	28.514
C-f	0.049	1.981	0.850	8.192	28.538
D-f	0.0521	1.945	0.879	7.992	28.540
E-f	0.1076	1.863	0.844	7.625	28.574

The results of ICP-MS analysis of the metallic deposits on the cathodes are presented in Table 11. The calculated masses for cathode deposits from the ERAD simulations are given in Table 12. Note that the mass of U deposited for each run is much less than the theoretical 25 mg for 0.6 A or 4.2 mg for 0.1 A. This anomaly indicates that most of the U deposits at the cathode fell off before the cathode was extracted from the salt.

Table 11- ICP-MS Results of Experimentally Measured Cathode Deposits

Run	Current (A)	Current Density	Deposited Gd (mg)	Deposited U (mg)	Deposited Li (mg)	Total Deposit (mg)	Gd/U Mass Ratio
1	0.6	0.41	1.75	1.49	0.431	3.66	1.18
2	0.6	0.47	4.22	2.14	1.10	7.46	1.98
3	0.6	0.55	3.86	1.47	1.90	7.23	2.63
4	0.6	0.66	7.46	3.10	0	10.56	2.41
5	0.6	0.82	4.70	1.85	3.48	10.03	2.54
A	0.1	0.069	0.72	2.09	0	2.81	0.34
B	0.1	0.078	0.13	2.08	0	2.22	0.07
C	0.1	0.092	0.95	1.14	0	2.09	0.83
D	0.1	0.11	0.81	1.57	0	2.38	0.52
E	0.1	0.14	0.77	1.32	0	2.09	0.58

Table 12- Computational Mass Deposition Results of Simulations of Experiments

Run	Current (A)	Current Density	Deposited Gd (mg)	Deposited U (mg)	Deposited Li (mg)	Gd/U
1	0.6	0.41	12.8	10.2	1.00E-06	1.26
2	0.6	0.47	11.5	9.39	2.54E-01	1.23
3	0.6	0.55	10.6	7.65	5.17E-01	1.39
4	0.6	0.66	8.32	5.94	9.72E-01	1.40
5	0.6	0.82	6.72	4.84	1.28E+00	1.39
A	0.1	0.069	0	4.94	1.00E-06	0.000
B	0.1	0.078	0	4.94	1.00E-06	0.000
C	0.1	0.092	0	4.94	1.00E-06	0.000
D	0.1	0.11	0	4.94	1.00E-06	0.000
E	0.1	0.14	0	4.94	1.00E-06	0.000

Table 12 indicates that the trends in model calculations agree with what was initially expected—less negative cathode potentials (see Figure 12 and Figure 13) favor U deposition over Gd or Li. The higher the current density, the more Gd and Li should deposit onto the cathode. This same trend is observed experimentally in the results shown in Table 11.

Experimentally, the results are more scattered—presumably due to the likely phenomenon of deposits falling off of the cathode as dendrites. In the low current runs (A-E), the primary metal deposited was U. Relatively small amounts of Gd are deposited, and no Li was detected. In the high current runs (1-5), co-deposition of U, Gd, and Li was detected with exception of run 4 in which Li was not detected. Li measurements may be non-prototypical, since it forms a liquid metal and likely rises to the surface of the molten salt. The other issue was that analysis of K and Li was used to subtract the estimated salt contribution from each analysis of the deposits. High error for this method can lead to high error in the deduced concentration of metallic Li. Since Li is a major component of

the salt, any Li metal on the cathode may be been dominated by Li from the salt. As a result, Li is depositing, but the reported measured Li depositions possess a high uncertainty. This is a result of both the challenges in mass analysis of K in ICP-MS as well as the potential for dissolution of Li into the salt due to it being a liquid and not adhering to the cathode. The dissolution of Li is evident in Run 4 as there is no deposit present and that in the cell with a total charge of 36 Coulombs passed a total of 0.37 millimoles of electrons deposited at the cathode but only 0.106 milliequivalents are measured to have deposited indicating that the much of the metal is missing. This 0.37 millimoles of electrons deposited is also reflected by the results of the mass deposition simulations of what is equal to 0.37 milliequivalents. The experimental analytical result is difficult to compare to quantitative computational results, but it can be compared to expected qualitative conclusions. A qualitative conclusion being that with increased current density the total mass of Li codeposited increases as well which is an expected result and is reflected in the experimental results presented here.

A plot of the ratio of the experimentally measured and modeled Gd/U ratio of the deposited metals at the cathode versus current density is seen in Figure 14. As seen in this plot, with increasing current density, there is an increase in the ratio of Gd to U. This is expected because as current density increases, its value exceeds the limiting current density of U by a greater amount with each increase.

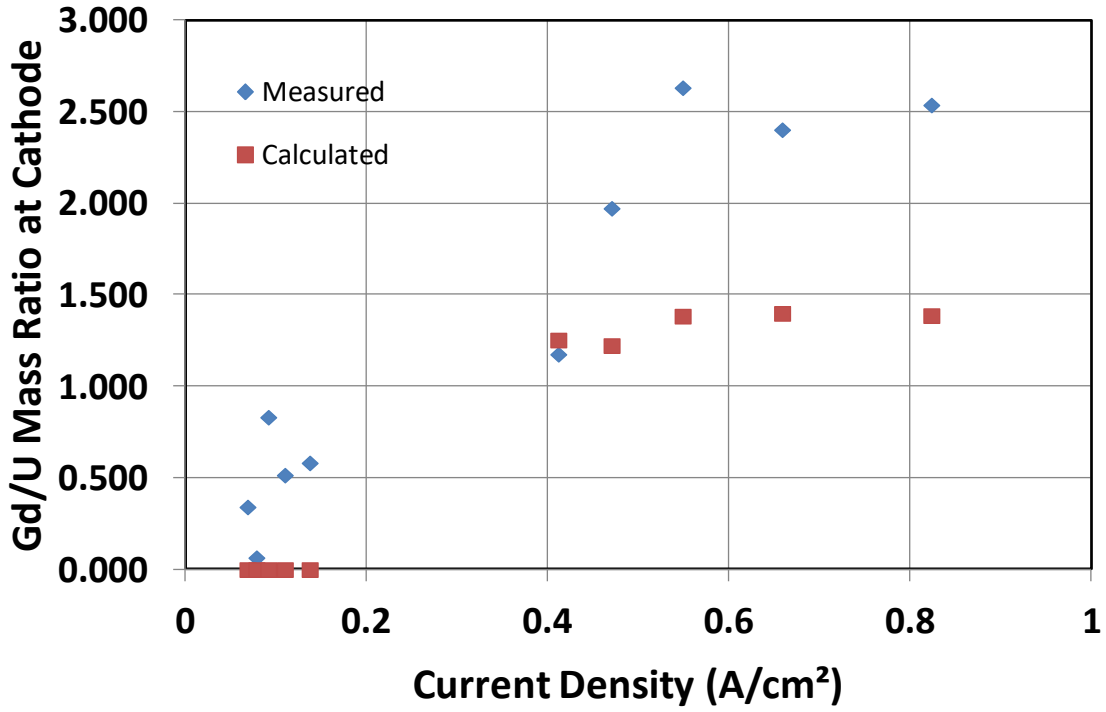

Figure 14- Plot of Gd/UMass Ratio versus Current Density (A/cm2) for Measured and Calculated Cathode Depositions

With each increasing excess of the limiting current density, the greater fraction of the current applied to the transport of the Gd until it meets the limit dependent mass transport qualities of each species in the salt and the current density exceeds the sum of both the limiting current densities of both the U and Gd, resulting in the demonstrated codeposition of Li. The trends seen experimentally are reflected by the calculated results illustrating the potential efficacy of the use of ERAD as predictive tool of failure modes and codeposition scenarios. Specifically, ERAD demonstrates that it can predict the effect of the change of a significant parameter, in this case current density, on the nature of the deposit, Gd/U ratio, for use in further identified failure modes such temperature variations or change cathodic and anodic properties.

At the higher current density operations of runs 1-5, the ERAD calculations match well with experimental measurements. And those potentials correctly predict the codeposition of U, Gd, and Li at the cathode. There is some difference at very early times in each run, but that may be due to nucleation effects that are not addressed at all in ERAD. However, ERAD is able to model the average steady state potential that eventually develops in the experimental system. Thus from the perspective of SBS, ERAD is usable assuming that the average potential is the signal to be integrated into a systems framework. This is certainly the case, since nucleation is only the very beginning of each electrorefining run and represents a tiny fraction of the total run time.

Comparing the results from the experiments and ERAD simulations for the lower current density operations, Runs A-E, the differences are apparent. Potential results demonstrate that for the low current density runs that the computational calculations are less negative and the cell operates at a potential where only U is deposited at the cathode while the potentials from the experimental operations indicate that the operating potential will involve the codeposition of U and Gd. The resulting deposits reflect this significant difference in the nature of the operating potential as there is a noticeable codeposition that changes with changing current density for the actual experiments while the simulations result in the same mass of U deposit for the same operation. Thus, for lower current density operations and those in which are derived from the start of the slope of the Gd reduction peak of CV curve will not produce a modeled codeposition in ERAD by itself. To best model the conditions of the cell, an optimization of the input parameters, such as the electrochemical data input in it as well as changes in cathode surface area as a result of removal of salt and metal over time from the cell, is required to best predict

trends utilizing ERAD. Higher current density operations illustrate that ERAD can produce predictions of off normal events that are reflected in results from experimental operations. The inputs can be optimized to visualize the trends seen in the lower current density operations experimentally and best improve the model when analyzing future failure mode scenarios computationally allowing for the confirmation of the predictions of safeguards relevant failure modes.

For all sets of runs, the mass transport calculations of ERAD calculates a greater total mass of metal deposited at the cathode for a given electrorefiner run compared to the experiments. Theoretically, by Faraday's law of electrolysis in the 0.1 A current runs 4.94 mg of U should deposit at the cathode. This theoretical value is the same as is calculated by ERAD. Thus, ERAD captures from the perspective of its idealized assumptions such as fully developed boundary layer and perfect mixing of salt the theoretical value of the mass deposit at the cathode. The discrepancy between experimental and computational values comes from both these assumptions as well as the likely possibility that some deposits fell off upon removal from the cell as well as during the handling and preparation of the ICP-MS samples.

From the perspective of utilizing ERAD to model SBS related off-normal scenarios, ERAD may be adequate from the perspective of expected reference electrode signals and calculating cathode deposits. The trends in electrode potential behavior predicted by ERAD matches those observed experimentally. There is a notable difference though between the calculated an measured value. ERAD successfully predicts the onset of co-deposition of metals, allowing it to simulate various scenarios involving U, Pu, and minor actinides. ERAD is able to predict the trends demonstrated by the experiments and be

utilized for determining the validity of postulated failure modes. Without optimizing its input parameters, it ERAD should not be expected to generate accurate predictions for potentials and masses of deposited metals. Rather it can be used to determine relationships and trends to guide development of safeguards methods and signatures for off-normal operations.

4.3 Summary and Conclusions

This study was performed by performing multiple experimental runs on a selected off-normal occurrence--that of a change in cathode surface area resulting in greater current density due to the jamming or malfunction of the cathode in the ER. These results demonstrated that codeposition will occur and will often match the predictions made from theory in terms of the changes of species partial currents and the ratio of mass deposits at the cathode. Both experimental and computational results demonstrate that with increased current densities the ratio of U/Gd increases demonstrating that ERAD possesses the ability to determine trends in failure mode scenarios that are also seen in experimental results. In addition, the trends with regards to change in potential with increasing current density are observed to be the same with both computed and experimental analysis. This demonstrates that ERAD can be utilized to determine qualitative failure mode trends, but still require improvements in application and extensive experimental validation.

In particular, ERAD requires improvements with regards to electrochemical transport and thermodynamic calculations that account for non-steady state conditions. In addition, an optimization of parameters and improvements to modeling of growth on the cathode has been demonstrated to be of importance in the further use of ERAD as applied to

failure mode related problems. With these improvements, off-normal condition identification and simulation for SBS will be significantly improved and can improve confidence in terms of the analysis of failure mode effects and the viability of their impact on a modeled system.

Despite these needs for improvement, the experiment results allow a greater confidence to be placed in ERAD with regards to failure mode scenario analysis, though only from a qualitative perspective. This confidence was demonstrated in subsequent failure mode simulation campaigns as is detailed in Chapter 6.

CHAPTER 5: REPURPOSED FMEA FOR SAFEGUARDS APPLICATION

A systematic method for identifying off-normal scenarios and their consequences is a fundamental need for applying SBS to any facility. In this chapter, a modified FMEA approach is applied to a pyroprocessing system with fundamental FMEA definitions modified to have a safeguards focus. As discussed in the methods and approaches chapter, an FMEA consists of three primary steps that are fundamental to its application. First, preliminary measures are undertaken for the selection of the standard and defining the worksheets by which the analysis will occur. The second is the FMEA evaluation process during which the system is decomposed, failure modes and effects identified, and recommendations made. The third is the finalization and reporting of results which finds form in this chapter of the dissertation.

5.1 PRELIMINARY MEASURES OF FMEA FOR PYRO ANALYSIS

I have attempted to follow the described steps of the FMEA. The first preliminary step is the selection of a standard. There are several standards used to produce an FMEA; however, they all relate to safety in terms of examples and many definitions as opposed to safeguarding against material flowsheet disruption. Thus in the course of following the FMEA standard, I as the analyzer must provide new definitions such as for ranking severity and defining failure to best fit the format of the overall standard itself. The standard chosen is the US DoD MIL-STD-1629A [51]. This standard sets out the guidelines for undertaking an FMEA and reporting it. The standard outlines several planning steps that make up the preliminary stage that the selected team is to carry out to meet the requirements set by the standard.

The planning stage involves setting the ground rules of the analysis and underlying assumptions, defining failure, developing a coding system, developing the format of worksheets and decomposition diagrams, and setting the indenture level [51]. There are several assumptions of this analysis. This analysis is performed on a commercial pyroprocessing facility's electrorefiner stage and focuses only on failures that occur within this unit operation. The effects from failures will be specifically the effects of the failures on departure of material from the expected mass flow sheet of the system, as for example, Pu transported to the final U product processing. The analysis will take a functional approach "top-down" approach. Thus, this will require a significant defining and decomposition of the ER system and the development of block diagrams and flow diagrams.

Within this analysis, the definition a failure is an event that affects one component of the decomposed system enough to disrupt operation and cause the system to operate differently than the expected commercial manner expected. The effects produced the failure's disruption of the operation has on the disruption of the mass flow sheet determines the severity of the failure.

To best address the postulation of each failure, a lowest indenture level is set. Indenture levels are the item levels which identify or describe the relative complexity of assembly or function. These levels progress from the more complex to the simpler parts. The lowest indenture level for this analysis is the individual component parts of the ER. Thus, a thorough decomposition at the individual component level of the ER is necessary before identifying failures.

Finally, to establish and develop an FMEA, worksheets of are key to the performance and organization of the FMEA analysis. There are many columns in the worksheet to fill in and the remainder of this section deals with the defining of each of these columns, the first being the classification system. An identification tag is attributed to every identified component. The format of this tag is as follows:

ID: X-## (20)

X signifies an alphabetic identifier for the location of the component in the ER Vessel. The letters A-D classify this identifier. An "A" component is a component outside the vessel with impact to the system itself. A "B" component is a component that is a member of the ER system but is not in direct interaction with the salt environment. A "C" component is a component that is a member of the ER system and is in direct contact with the eutectic bath. A "D" component is a component that is part of the sensing and control system that is also a member of the PM framework. The notation ## denotes the specific numeric identifier of each component. When decomposing the system into a flow diagram for my chosen functional approach, I assign the identification tags to each component in the flow sheet.

The item/functional identification further specify the component labeled by the identification number by name. The function column describes the actual function of the identified part. The columns for failure mode and causes describe the physical nature of the problem itself, e.g. the cathode has cracked due to radiation stresses. The operational mode describes the type of operation that is occurring within the ER vessel when the

stated failure occurred, e.g. during the passing of current for deposition of U at the cathode.

After the identification columns in the worksheet, the worksheet's columns focus on failure effects, detection, and severity classification. Three different levels of failure effects are considered. Local effects deal with the effect on the electrorefiner during that initial failure of operation. Next level effects focus on the impact of the failure on the output of the electrorefiner. The end effects focus on the overall impact the failure potentially has on the mass balance of the entire plant facility and thus its potential for false alarm. False alarms are of great importance as they increase the difficulty for the operator and safeguards inspectors assessing the facility. False alarms can be divided into two types false positives and false negatives. A false positive is a case where the mass balance measurement system concludes diversion of SNM is occurring when it in fact is not. A false negative is where diversion is occurring, but the mass balance measurement system concludes that it is not. Failure modes can have an impact on the occurrence of both depending on the nature of the failure. Failure detection methods catalog the measurements that are utilized to recognize that the failure has occurred and to mitigate it.

These effects are then classified on an effect's severity scale that utilizes defined levels of severity defined by the analyzer. For the purpose of this specific safeguard focused FMEA, three severity levels classify the failure modes. These severity levels are summarized in Table 13.

Table 13- Summary of Failure Severity Levels

Severity Level	Name	Description
Category I	Significant	Produces a significant impact on the overall mass flow of material greater in excess that a significant quantity of SNM.
Category II	Potentially Significant	Does not cause immediate effects on material mass flow but left unattended can have effects that accumulate over time that result in disruption of the mass flow.
Category III	Insignificant	Failures that are either so great that they cease all operations entirely or only result in small amounts SNM (< 1 SQ) displaced within the mass flow of the facility.

5.2 Definition of ER Pyroprocessing System

With the definitions of the FMEA components and development of the worksheet completed, the next step of the FMEA is the defining of the system and its associated components as well as its operational modes. This FMEA study with regards to the pyroprocessing ER focuses on a general ER design based around current and past design information taking inspiration from the Mark-IV ER at INL [60]. Figure 15 shows a technical drawing of the Mark-IV [61]. My analysis does not focus on the Mark-IV specifically, I only reference and provide the diagram to provide context of what the general ER design consists of.

The electrorefiner in question will operate for commercial purposes to both refine and treat used oxide and metal fuel. Table 14 catalogs the individual ER components. 26 distinct components spread among the four categories previously defined for the classification system comprise the ER. A facility power supply provides power for the entire system. The facility uses both large internal and external power sources that don't just power the ER or the hot cell but the entire facility itself. These power sources provide power to the heater of the ER made up of a series of inductive coils, the individual power sources of both the cathode and the anode as well as the motor of the screw type agitator stirrer of the salt used to maintain homogeneity of the species in the salt. A LiCl-KCl salt bath is where the bulk of the reactions take place. To maintain a molten LiCl-KCl salt bath, an inductive heater provides constant heating. Separating the salt from the heater is a salt container vessel or crucible and a layer of insulation.

Table 14- Components of Commercial ER

Identification Number	Item/Functional Idenfitication
A-01	Facility Power Source
A-02	Computer Control System
A-03	Manual Manipulator System
B-01	Inductive heater
B-02	Insulation Layer
B-03	Anode Power Source
B-04	Cathode Power Source
B-05	Stirrer Motor
B-06	Anode Motor
B-07	Cathode Motor
C-01	Salt Stirrer
C-02	Anode Retraction Linkages
C-03	Cathode Retraction Linkages
C-04	Anode Basket
C-05	Cathode Rod
C-06	Cathode Perforated Surface
C-07	Salt Bath Container
C-08	LiCl-KCl Salt Bath
D-01	Reference Electrode
D-02	Thermocouple
D-03	Anode Tachometer
D-04	Cathode Tachometer
D-05	Stirrer Tachometer
D-06	Double Bubbler

During a normal operational campaign, an inductive heater maintains the salt at a temperature of about 500 C° with some variation around this value. For each separations process, the electrode power sources lower the anode basket containing the spent fuel as well as the solid cathode rod sheathed in a perforated surface into the salt utilizing a retraction arm attached to the motor of each electrode. The motor then rotates the retraction arm and with it the electrode. In addition, the stirrer motor rotates the screw

type agitator stirrer in the salt. Once this rotation develops the diffusion layer for transport, the power source passes a high current between the anode and the cathode in the negative direction. During this current passing period, actinides and rare earths oxidize at the anode, and only U reduces at the cathode while the remainder of the oxidized species remains in the salt during normal operation. Noble metals do not react at the anode basket. At the end of each operating period, the operator transfers the anode basket with noble metals contained to a waste processing stage. This current operates for a period of 24 hours at which point the operator removes the cathode and scrapes its product into a separate crucible for processing. The anode is removed and sent to waste processing at the end of each operation. Facility employees control manual manipulators for the removals and insertions of electrodes in the hot cell. As discussed earlier, various measurement technologies are present continuously monitoring the nature of the ER bath and its components. These measurement technologies report their signals to a computer control system which then commands the entire process operation based on received signals. The facility performs batch operations for four-month periods. At the end of these periods, the operator performs a mass balance and logs the results for future inspection from the IAEA. Figure 16 provides a flowsheet showing the relationship of the identified components to one another.

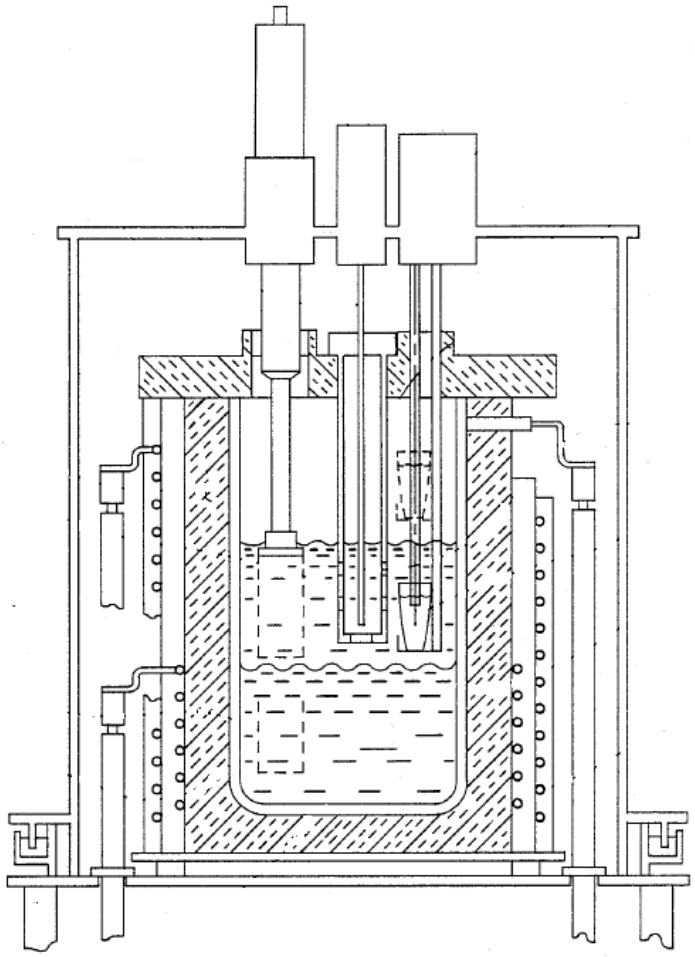

Figure 15-Drawing of Mark IV ER

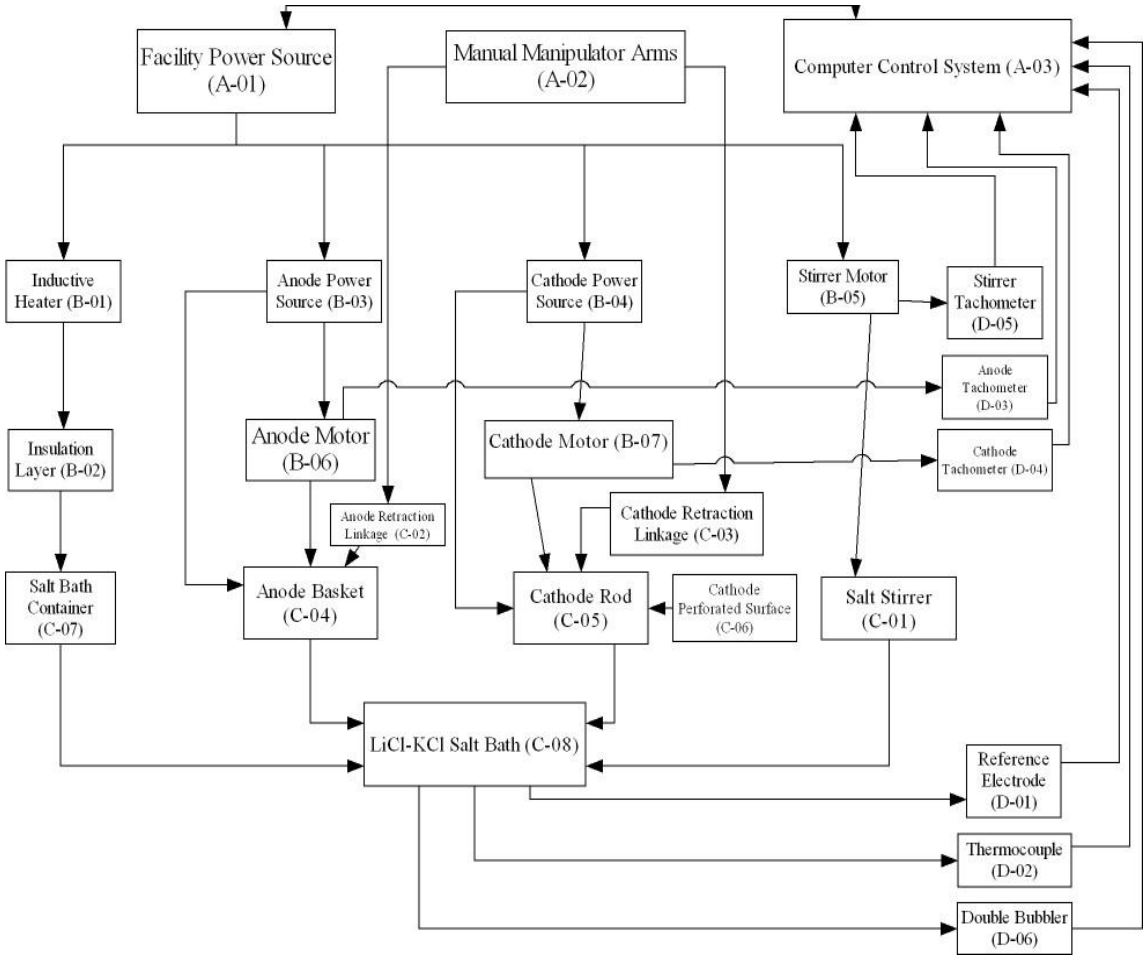

Figure 16-Flow Diagram of ER Process

5.3 Summary of FMEA Evaluation

The complete FMEA evaluation utilized the worksheet to identify 42 failure modes among the 26 identified components. Appendix A contains the completed FMEA worksheets. What follows in this section is a summary of the failure modes and conclusions derived from this exercise.

I organize this summary of results by focusing on both the severity classes and grouping of components individually. There are only a few failure modes initially classified as Class I. The assumptions with regards to this classification came from past simulation studies. Work from ER simulation demonstrated that cathode diffusion layer thickness was a significantly sensitive variable. This led to the conclusion that it

classified as a Class I failure if the cathode motor is to stop working or rotate at a slower speed. In addition, failures involving large surges in power over extended periods of time are a potential issue from a material balance standpoint whether or not codeposition does occur. The other failure modes from Class I deal with the unaccounted loss of material due to leaking of salt or loss of dendrites in manipulation of cathode. In addition, issues with measurement technologies and their feedback are given the designation Class I as a facility can operate with codeposition undetected if the measurement technologies fail and report inaccurate data whether due to malicious action or natural failure.

The majority of the failures detailed in the worksheets fall under the category of Class II severity. This is due to an unknown nature of the sensitivity of these failures to difficulties in the material balance and assumptions arising from the governing physical equations of the electrochemical separations process that inform the classification. Future computational investigations may reclassify them, but with current knowledge it is impossible to make a conclusion other than I know that these Class II failures may cause a mass balance disruption. The computational investigations of several of these failures to ascertain additional information as to their severity classification will be detailed in the recommendations.

Class III failures were either complete failure of critical equipment or measurement technologies that would result in a halt of operations. This included total failures of the heater, power sources, measurement technologies, and the computer control networks. Class III failures are important to note from an operations and design perspective as a Class III failure will generally require immediate maintenance which

holds up operation as they do not allow the ER to operate in any capacity, but significant further investigation from the perspective of safeguards impact is not required.

Type “A” components and their failures deal mostly with outside influences. Failures in the facility power source are due to issues such as loss of off-site power powering the facility or an unexpected surge in power. Both are difficult to assign failure data based off of testing but require knowledge of the surrounding factors and their influence on the facility power supply. Other failures involve outside human influence that have a potential to occur such as cyber-attacks on the facilities computer control system or human error with the use of manipulators within the hot cell.

Type “B” components have an assorted range of identified failures. These failures included failures in the heating system whether be due to a failure in the inductive heater itself or the insulation layer. An inductive heater failure leads to a reduction in salt temperature while an insulation layer failure leads to an increase in salt temperature. Both alter material transport in the salt, and future investigations should be performed on them. Electrode power sources were also determined to be a potential location of failure for both complete and partial failures. The partial failures that involve a surge in power supplied to the electrode potentially have a significant impact on the operations of the ER and the mass balance of the whole facility. In addition, failures can occur with the motors of both electrodes as well as the stirrer where the rotation of the electrode can stop entirely, speed up, or slow down due to issues arising on the component level within their electric motor. Issues with the anode and stirrer motors were labeled as being class II failures as their effect would not cause codeposition directly. Mass flow disruption could occur in the long term. Thus, these failure modes will require long term ER simulations.

The slow down and stop rotation of the cathode failures are Class I due to previous investigations involving the change in diffusion layer thickness of the cathode and the sensitivity of that variable to change with regards to potential codeposition.

Type "C" components have similar failure mode effects to many directly linked components within the "B" components list. Cracking of the retraction linkages of the electrodes leads to changes in surface area of electrode impacting the current density which can have both long-term effects as the cracking can expand over time leading to the severing of the electrode into the salt bath. In addition, codeposition effects as a result of the reduction of the cathode surface area are a possibility. Deterioration of the stirrer would lead to the same loss of homogeneity seen in the failures of the stirrer motor in that the limiting current density would be affected and could lead to long term effects in the transport properties of the salt bath of the ER. In addition, this analysis identified several significant failure modes that would lead to irrecoverable loss of material within the ER. These were the damage to the wire mesh of anode, significant cracking and surface damage of the cathode rod, and the failure of the salt bath container. This would lead to the leaking of either metal or salt that could over time be equivalent to an SQ. This would be similar to the failure seen at the UK's aqueous Sellafield facility when a pipe for the accountability tank leaked resulting in the loss of multiple SQs of Pu [62].

As for the measurement technologies or Type "D" components, the failures mostly came in two types, the first failure being the complete failure of the measurement that would result in the halt of operation until replacement occurs as dictated by the computer control system. The second and more significant identified is the failure of calibration that leads to the reading being normal operation while the actual operation of

the ER is actually off normal. This type of failure could have significant contributions if undetected off-normal operations continue for extended periods of time. In addition, component failures of the measurement technologies themselves associated with the reference electrode housing and double bubbler tubing can lead to high error results that mask the actual conditions of the ER analagous as a miscalibration, but with much larger errors.

5.4 RECOMMENDATIONS

Taking all the various failure modes from the worksheet into account, recommendations for future computational study utilizing ERAD to model the ER are made. The ER simulations inspect the short-term and long-term effects of each of these selected failure modes from the perspective of ER transport. This produces datasets for both short term operation and long-term operation of the ER that can then be imported into a systems model. In this case the selected systems model is the SSPM Echem. Thus, the purpose of these investigations is to see what the operational effects and the resulting safeguards effects are on the system as a whole. In addition, ER simulations confirm and/or reassess the classifications and postulated effects of the failure modes.

The failures to be investigated via further ERAD simulation coupled with SSPM simulation to see overall system mass balance effects are as follows:

1) Unexpected large surge in power in facility power source
2) Partial heater failure
3) Failure of thermal insulation
4) Surge in power in electrode power sources
5) Complete failure of anode rotation motor
6) Increase in anode rotation speed due to failure in commutator
7) Decrease in anode rotation speed due to failure in windings in electric motor

8) Complete failure of cathode rotation motor
9) Increase in cathode rotation speed due to failure in commutator
10) Decrease in cathode rotation speed due to failure in windings in electric motor
11) Partial fracture of electrode retraction linkages

5.5 Conclusions

A modified FMEA approach for safeguards has been effectively demonstrated for a pyroprocessing electrorefiner. As previous efforts have been only able to demonstrate a small select number of cases, the work here demonstrates that a systematic approach generates a greater total number of failure modes to provide a better understanding of the total effects and potential severity. This ranked approach allows for easier recommendations of further studies as demonstrated by the expanded number of studies applied in the subsequent chapters. As a result, I recommend FMEA as a very effective approach in SBS application as applied to other critical process equipment in particular the electrowinner stage where the end effects are of potentially greater severity.

Knowing the recommended failure modes for computational investigation, the next chapter details ERAD simulations of each of the 11 cases to determine what the local and next-level effects actually are beyond the postulation of the worksheets. In addition, the severity of the failure modes is determined with greater certainty, resulting in the updating of the results within the FMEA worksheets developed.

CHAPTER 6: ERAD SIMULATION OF POSTULATED FAILURE MODES

With a set of recommended failure modes for further analysis from the FMEA analysis, the next step was to simulate these failure modes utilizing ERAD to produce data for a systems model to utilize. To do so, I created multiple studies by varying parameters relevant to and defined by the failure modes. This chapter first discusses the test matrices of these failure mode studies specifying the variables manipulated and how I programmed these studies in ERAD. After this, I present the results for these studies and discuss conclusions coming from them.

6.1 TEST MATRICES FOR ERAD SIMULATION

6.1.1 BASE CASE RUNS

In developing test matrices for the ERAD runs, various assumptions need to be made and base case conditions developed. The first assumptions are the basics of the ERAD runs and the type of data to be calculated. The ERAD runs undertaken are constant current and last a period of 24 hours each. The data collected will be of both the short-term and long-term variety. Short term data is the data produced for a single 24 hour run. This case provides information about a single run and the effect of the impacted component on the overall transport of the ER. The data allow the confirmation or modification of the conclusions with regards to the severity of a postulated failure mode. Long term data documents the effects of the failure mode over an entire mass balance period. The mass balance period for these long-term runs is a period of 4 months or approximately 120 days. This period of time is selected due to private oral correspondence I had with Dr. Yongsoo Hwang of the Korean Institute of Nuclear

Nonproliferation and Control, the ROK's state safeguarding agency. He stated that this was the shortest balance period feasible while still maintaining an economically viable facility. Assuming that each run lasts 24 hours and there are 4 hours of downtime between runs for removal and replacement of electrodes as well as holdup from other unit operations, this results in a total of 28 hours per cycle. Thus, data for a total of 104 operational ER cycles are calculated per each long term data run. During this period, after each ER run calculation, the salt concentration at the end of each cycle becomes the starting concentration for the next ER cycle. Output files collect the data for salt and electrode compositions as well as electrode potential data for each cycle.

For the collection of both kinds of data, a definition of normal operation in the form of base cases is developed to compare to simulated off-normal results. Using data from previous work in failure mode investigation, Table 15 summarizes the base cases utilized [12].

Table 15- Base Case Runs

Run	A	B	C	D
Current (A)	72	11.5	85	30
Time (h)	24	24	24	24
Surface Area Cathode (cm^2)	1350	1350	1350	1350
Surface Area Anode (cm^2)	800	800	800	800
Anode Diffusion Layer Thickness (µm)	50	50	50	50
Cathode Diffusion Layer Thickness (µm)	150	150	150	150
Temperature (K)	773	773	773	773
Pu/U Ratio in Salt	0.03075	0.1483	0.3368	1.627

The primary difference in the four base cases lies in the differences in current and in initial ratio of Pu/U. The currents occur over a range that would be seen in an engineering-scale facility. The throughput is high enough to produce ingot products

larger that the lab scale (>1 g) and on the order of kilograms. The Pu/U ratio reflect a range of starting salt concentrations that could be used depending on the amount of eutectic added and the amount of salt recycling in the facility. These base cases provide a variety of conditions in which failure modes can have different effects and impact.

For all evaluations of both normal and off-normal operations, the output files collect several sets of short term data. The code calculates and saves the concentrations and masses of the isotopes of the anode, cathode, and salt versus time. The code also collects the anode and cathode potential versus time. For long-term data, the code records the final value of each of these short-term data sets for each cycle. I catalog this long-term data to compare to the cycle number that produced the data. After collecting all data for both normal and off-normal operations for both short- and long-term operations, regression analysis develops data fits that allow for importing the data into the Echem SSPM model. With the base cases set, I used them to develop the test matrices for ERAD analysis of off-normal operations that follow.

6.1.2 Unexpected Large Surge in Facility Power Source

For an unexpected large surge in facility power source, I make the following assumptions in the simulations. I assume that the surge in power is only for a short period of the entire operating period of the ER. Thus, I program ERAD to operate as normal for the majority of the 24 hour period. For 0.5 hour period to simulate the power surge from the grid, I include an increase into total current operation of the ER for the same time period. Thus, 23.5 hours are operating as expected, but 0.5 hours are operating off-normal per each operational ER cycle. The powers range in values of 110% to 150% of normal power representing an incredibly large surge in power that would most likely trigger an

alarm, but should be investigated for overall effects on the ER output nonetheless. Table 16 shows these selected values of elevated current.

Table 16- Test Matrix for Unexpected Large Surge in Facility Power Source

Case	Current (A)	**Case**	Current (A)	**Case**	Current (A)	**Case**	Current (A)
A-1	79.2	**B-1**	12.65	**C-1**	93.5	**D-1**	33
A-2	86.4	**B-2**	13.8	**C-2**	102	**D-2**	36
A-3	93.6	**B-3**	14.95	**C-3**	110.5	**D-3**	39
A-4	100.8	**B-4**	16.1	**C-4**	119	**D-4**	42
A-5	108	**B-5**	17.25	**C-5**	127.5	**D-5**	45

6.1.3 Partial Heater Failure

To model a partial heater failure, I assumed that the temperature will be less than the normal 500 C° while still allowing the ER to operate. Thus, I simulate ERAD for temperatures below normal but above the melting point of the salt. The test matrix developed ranges from 450 C° to 495 C° in increments of 5 C° for the evaluation. This amounts to a total of 40 runs over the four different base cases. Table 17 below portrays this test matrix.

Table 17- Test Matrix for Partial Heater Failure

Case	Temperature (C°)
(A,B,C,D)-1	450
(A,B,C,D)-2	455
(A,B,C,D)-3	460
(A,B,C,D)-4	465
(A,B,C,D)-5	470
(A,B,C,D)-6	475
(A,B,C,D)-7	480
(A,B,C,D)-8	485
(A,B,C,D)-9	490
(A,B,C,D)-10	495

6.1.4 Failure of Heater Insulation

If the heat insulation in the ER fails, then the overall temperature of the salt will increase. To model this, I run the four ERAD base cases with an operating temperature of 505 C° to 525 C° in 5 C° increments. This produces results for 20 different cases. Table 18 represents this test matrix.

Table 18- Test Matrix for Failure of Heater Insulation

Cases	Temperature (°C)
(A,B,C,D)-11	505
(A,B,C,D)-12	510
(A,B,C,D)-13	515
(A,B,C,D)-14	520
(A,B,C,D)-15	525

6.1.5 Surge in Power of Electrode Power Sources

A surge in power of the electrode power sources, like the facility power source case, will lead to an increase in overall current. However, in this case, I assume that the increased current is for the entirety of the period of operation as opposed to for just a short period of a single run. I also assume that the current is smaller than that of a facility power source surge. The increased current is only 105% and 110% of the base case value for a total of 8 cases. Table 19 displays this test matrix.

Table 19- Test Matrix for Surge in Power of Electrode Power Sources

Case	Current (A)	**Case**	Current (A)	**Case**	Current (A)	**Case**	Current (A)
A-1	75.6	**B-1**	12.075	**C-1**	89.25	**D-1**	31.5
A-2	79.2	**B-2**	12.65	**C-2**	93.5	**D-2**	33

6.1.6 Increase and Decrease of Rotational Speed, Failure of Anode Motor

The failure of the anode motor affects the same variable whether there an increase in rotational speed or decreases in rotational speed. This variable is the anodic diffusion layer thickness. For this study, I varied the anodic diffusion layer thickness around its base value of 150 micrometers. To simulate a decrease in rotational speed, the diffusion layer thickness increases to a value greater than 150 micrometers. For an increase in speed, the diffusion layer thickness decreases to a value less than 150 micrometers. Table 20 shows the test matrix for this failure mode.

Table 20- Test Matrix for Changes in Anode Rotation Speed

Run	Anode Diffusion Layer Thickness (μm)
(A,B,C,D)-1	50
(A,B,C,D)-2	60
(A,B,C,D)-3	70
(A,B,C,D)-4	80
(A,B,C,D)-5	90
(A,B,C,D)-6	100
(A,B,C,D)-7	110
(A,B,C,D)-8	120
(A,B,C,D)-9	130
(A,B,C,D)-10	140
(A,B,C,D)-11	150
(A,B,C,D)-12	160
(A,B,C,D)-13	170
(A,B,C,D)-14	180
(A,B,C,D)-15	190
(A,B,C,D)-16	200
(A,B,C,D)-17	210
(A,B,C,D)-18	220
(A,B,C,D)-19	230
(A,B,C,D)-20	240
(A,B,C,D)-21	250

6.1.7 Increase and Decrease of Rotational Speed, Failure of Cathode Motor

Like the failures of the anode motor, the result of the failures in the cathode motor results in either an increase or decrease of diffusion layer thickness of the cathode. Thus, like the anode motor failure test matrix, the cathode motor test matrix occurs over a range of cathode diffusion layer thicknesses around the base 150 micrometer thickness. The number of cases varies depending on the base case that it is derived from. Table 21 provides this test matrix.

Table 21- Test Matrix for Failures in Cathode Rotation Motor

A Case	δ (μm)	**B Case**	δ (μm)	**C Case**	δ (μm)	**D Case**	δ (μm)
A-1	50	**B-1**	50	**C-1**	50	**D-1**	50
A-2	75	**B-2**	150	**C-2**	75	**D-2**	75
A-3	100	**B-3**	200	**C-3**	100	**D-3**	100
A-4	125	**B-4**	250	**C-4**	125	**D-4**	110
A-5	150	**B-5**	300	**C-5**	150	**D-5**	115
A-6	175	**B-6**	350	**C-6**	175	**D-6**	117
A-7	200	**B-7**	400	**C-7**	200	**D-7**	118
A-8	225	**B-8**	450	**C-8**	210	**D-8**	119
A-9	250	**B-9**	500	**C-9**	215	**D-9**	120
A-10	255			**C-10**	217	**D-10**	121
A-11	256			**C-11**	218	**D-11**	122
A-12	257			**C-12**	219	**D-12**	123
A-13	258			**C-13**	220	**D-13**	130
A-14	259			**C-14**	225	**D-14**	140
A-15	260			**C-15**	230	**D-15**	150
A-16	261			**C-16**	240	**D-16**	160
A-17	262			**C-17**	250	**D-17**	170
A-18	263			**C-18**	260	**D-18**	180
A-19	264			**C-19**	270	**D-19**	190
A-20	265					**D-20**	200

6.1.8 Partial Failure of Electrode Retraction Linkages

The partial failure of the electrode retraction linkages of the electrodes leads to a decrease in the surface area of the electrode in contact with the salt. As a result, the electrode current density increases and has potential negative consequences in terms of codeposition at the cathode. Thus, simulations must be performed for both electrodes individually for data set development. The simulations are performed over a range of programmed surface areas less than that of the base value. Table 22 shows the test matrix for a partial failure of the anode retraction linkage. Table 23 shows the cathode retraction linkage partial failure test matrix.

Table 22- Test Matrix for Anode Electrode Retraction Linkage Partial Failure

Run	Anode Surface Area (cm^2)
(A,B,C,D)-1	1350
(A,B,C,D)-2	1300
(A,B,C,D)-3	1250
(A,B,C,D)-4	1200
(A,B,C,D)-5	1150
(A,B,C,D)-6	1100
(A,B,C,D)-7	1050
(A,B,C,D)-8	1000
(A,B,C,D)-9	950
(A,B,C,D)-10	900
(A,B,C,D)-11	850
(A,B,C,D)-12	800

Table 23-Failure in Cathode Retraction Linkage Test Matrix

A Case	Area (cm^2)	B Case	Area (cm^2)	C Case	Area (cm^2)	D Case	Area (cm^2)
A-1	800	**B-1**	800	**C-1**	800	**D-1**	800
A-2	700	**B-2**	700	**C-2**	700	**D-2**	775
A-3	600	**B-3**	600	**C-3**	600	**D-3**	750
A-4	500	**B-4**	500	**C-4**	575	**D-4**	725
A-5	475	**B-5**	400	**C-5**	555	**D-5**	700
A-6	470	**B-6**	300	**C-6**	549	**D-6**	675
A-7	468	**B-7**	200	**C-7**	548	**D-7**	650
A-8	467	**B-8**	100	**C-8**	547	**D-8**	625
A-9	466	**B-9**	80	**C-9**	546	**D-9**	600
A-10	464	**B-10**	77	**C-10**	545	**D-10**	575
A-11	463	**B-11**	76	**C-11**	540	**D-11**	550
A-12	462	**B-12**	75	**C-12**	530	**D-12**	525
A-13	461	**B-13**	74	**C-13**	520	**D-13**	500
A-14	460	**B-14**	73	**C-14**	510		
A-15	455	**B-15**	72	**C-15**	500		
		B-16	71				
		B-17	70				
		B-18	69				
		B-19	67				
		B-20	65				

6.2 Results of ERAD Simulations

The base cases as well as the listed failure modes were simulated according to the specified computational test matrices. Most simulations continued to completion over the long-term, but some were incomplete due to limitations in the ERAD solver. These cases are addressed in this section. The following eight sections cover the base cases and the failure modes simulated in ERAD with results for both short-term and long-term data focusing primarily on the long-term data.

6.2.1 Base Cases

The results of the base cases provide the data to compare with all failure modes and address their severity. The results provided here depict the short and long-term data for U and Pu masses at both electrodes and in the eutectic salt, as well as electrode potentials. Figure 17 shows the results of the cathode depositions for short term data. Figure 18 and Figure 19 shows the results for long term data for U and Pu deposition, respectively. Inspecting the short-term results, one sees that for all cases the deposition of mass of both U and Pu at the cathode follows a linear trend. Cases A through C do not have deposition of Pu at the cathode for the first operational cycle while the conditions of case D, with the higher concentration of Pu to U in the salt, generates codeposition during the first cycle. This plot depicts that the transport over a single operation can be translated into a systems code as a linear relationship based off of the final mass depositions determined from the long term results using the difference between final and initial masses divided by operation time to determine the slope.

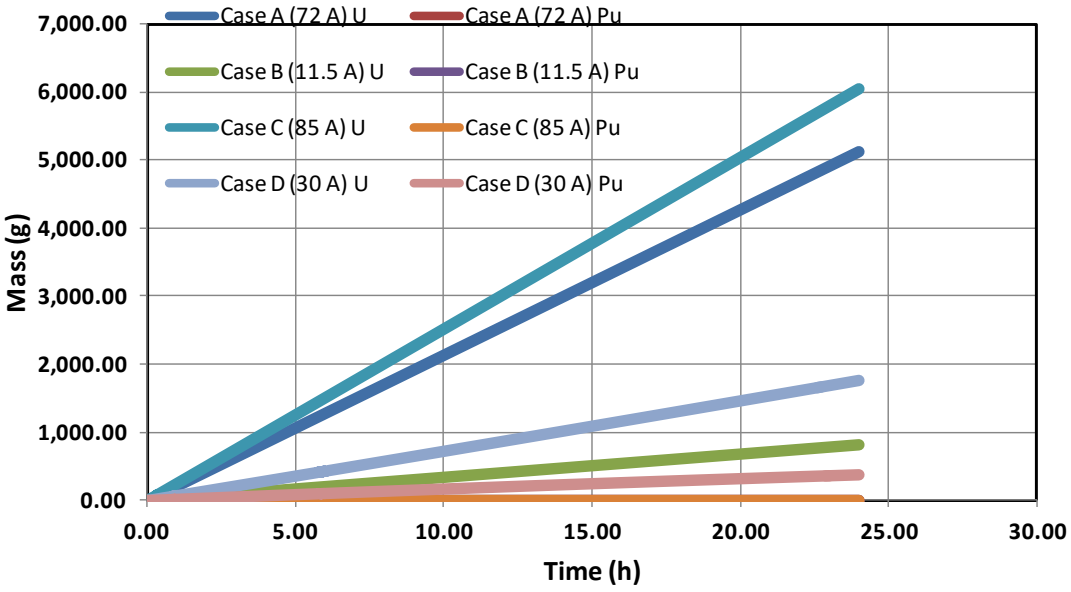

Figure 17- Short Term Results of Cathode Depositions for Base Cases

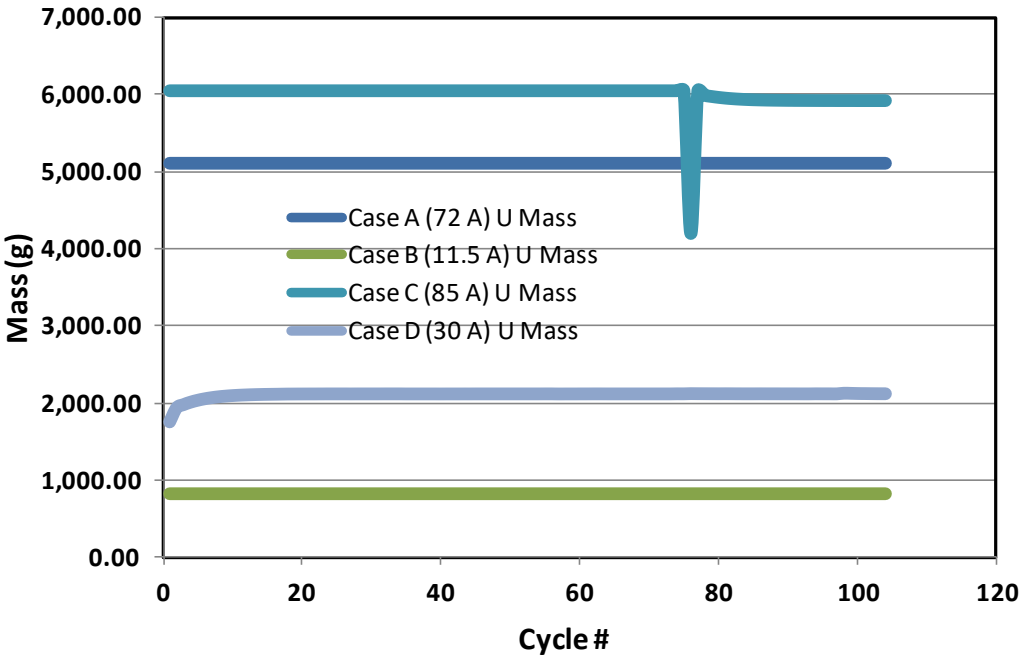

Figure 18- Long Term Results of U Cathode Deposition for Base Cases

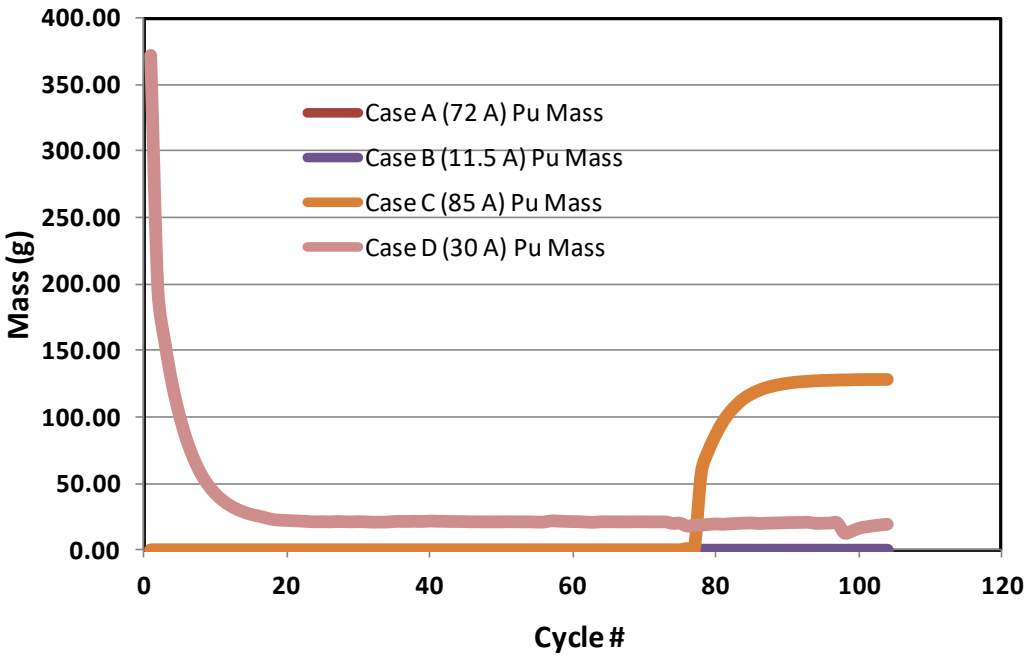

Figure 19- Long Term Results of Pu Cathode Deposition for Base Cases

Long term results show that for the cases with low Pu/U ratios (A and B) do not result in codeposition over the long-term and are translatable into a systems code as constant functions. However, for the case of higher Pu/U ratios, Case C sees codepositions after about 75 cycles. At cycle 76, codeposition occurs with both U and Pu depositing at the cathode. After this, the mass of Pu codeposited steadily increases and the mass of U deposited decrease with each successive cycle. Over the long-term, Case D experiences a decreasing Pu mass codeposited and increased U mass deposited with time. Eventually the Pu exhausts itself, and the amount of Pu mass codeposited is of the order of 10 g. Because of codeposition, combined with measurement uncertainty, both case C and D could be postulated to generate a false alarm over a long-term operation. For cases C & D, piecewise functions are potentially usable to represent the long-term data when programmed into a systems model.

Figure 20 depicts short-term data for mass transport at the anode of the U in cases A-D. The short-term data shows that the transport of U into the salt is dependent on current rather than the condition of the salt. The higher the current, the greater the mass of actinides transported into the salt. In addition, the transport follows a linear trend and can be modeled as simple linear relationship like the cathode. These trends for U transport into the salt are observable for the Pu transport into the salt. The quantity of the Pu being transported into the salt from the anode is less than U transported into the salt as there is less Pu in the anode basket than U. Though not depicted, the long-term data demonstrate that the transport does not change significantly with time and thus only short-term data will be translated into a systems code.

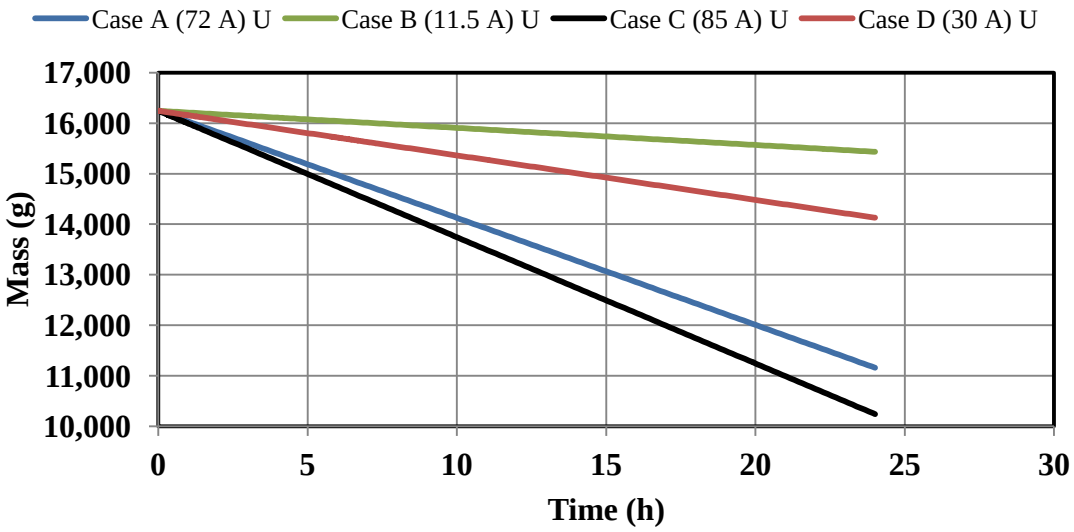

Figure 20- Short Term Anode Data for Base Cases

In Figure 21 the long-term data for U and Pu salt concentration in terms of weight percentages present in the eutectic salt bath versus cycle number are shown. For case C, a similar trend to cases A and B is seen until the time in which codeposition of U and Pu

occurs. When codeposition of Pu and U at the cathode begins, the Pu weight percentage decreases as it codeposits at the cathode while the U weight percentage levels out as the amount of U transported into the salt is closer to that transported into the salt from the anode. Finally, in case D, U decreases steadily as it is the primary deposited species at the cathode for each cycle and Pu is level as in later runs. The mass deposited at the cathode is similar to that being transported into the salt.

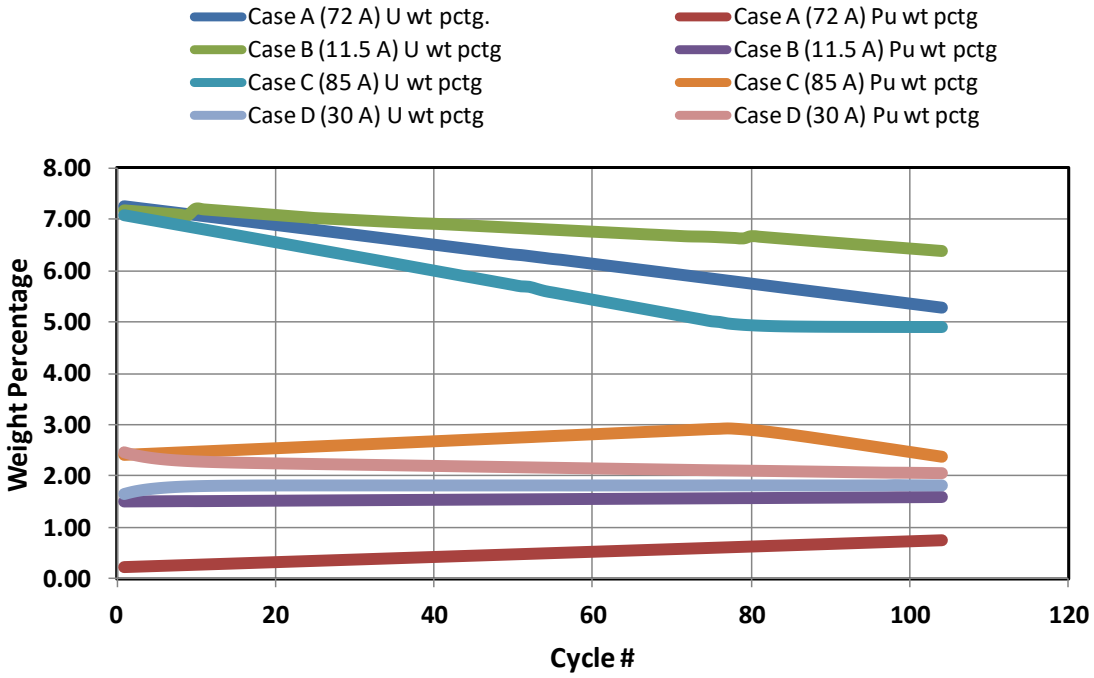

Figure 21- Long Term Data for U and Pu Weight Percentage in the Salt Bath for Base Cases

It is important to note that the results for mass transport indicate that the starting concentration and ratio of Pu and U are important to the operation and monitoring of a commercial electrorefiner. Commercial design documents often assume that UCl_3 salt is added to address this, but in the case of the long term ERAD model this addition does not occur as to generate a worst case scenario in which "dirty" salt with high concentrations of actinides is not replenished with "clean" salt containing eutectic and UCl_3.

Figure 22-Figure 25 plot the short-term and long-term results of the electrode potentials. Inspecting the anode potential results, the potential of operation becomes more positive as current increases as expected. The anode potential follows a long-term trend resembling a straight line that becomes slightly more positive as time progresses. Thus, the potential would be programmed into a systems model as a constant value as a function of operation cycle.

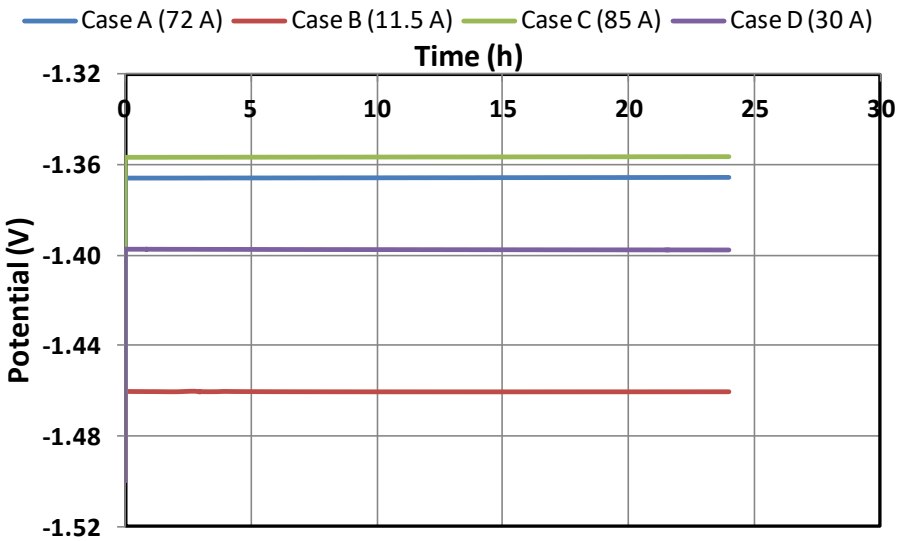

Figure 22- Short Term Anode Potential Results for Base Cases

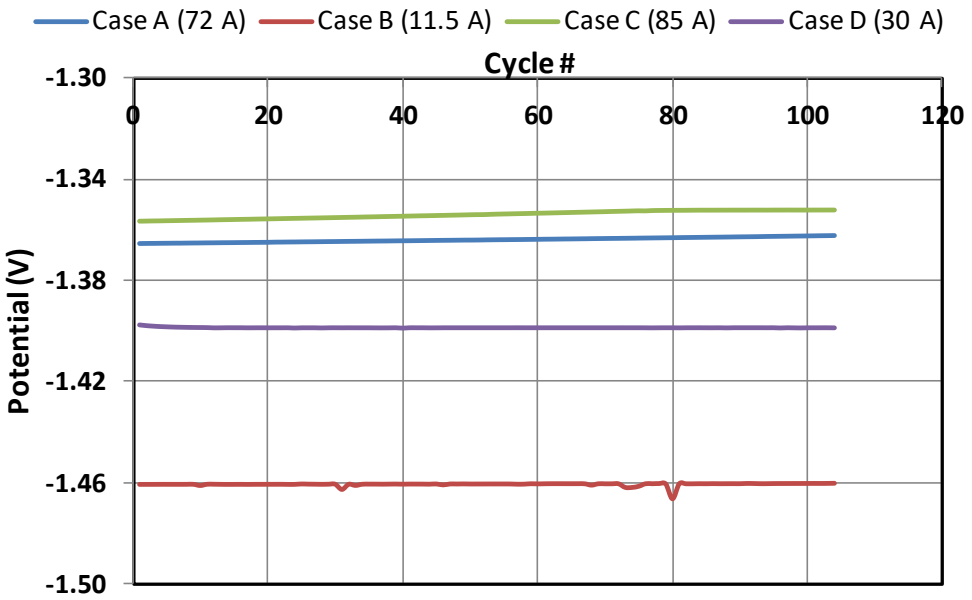

Figure 23- Long Term Anode Potential Results for Base Cases

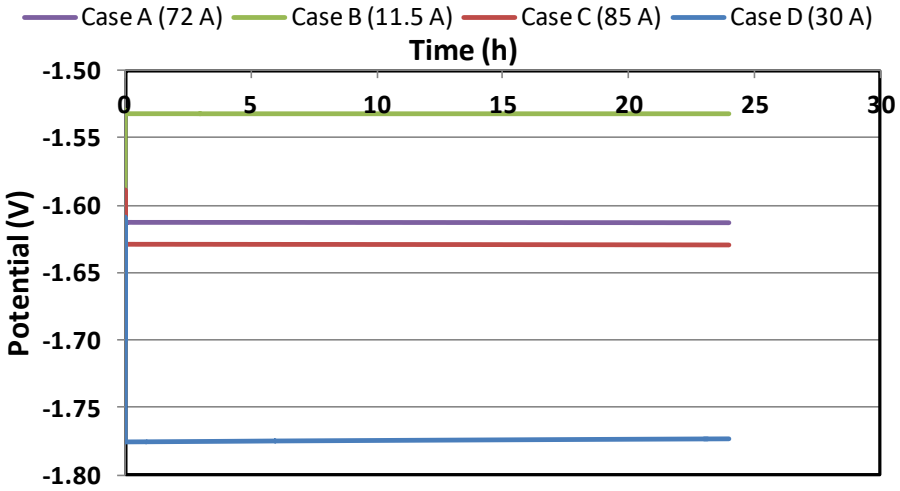

Figure 24- Short Term Cathode Potential Results for Base Cases

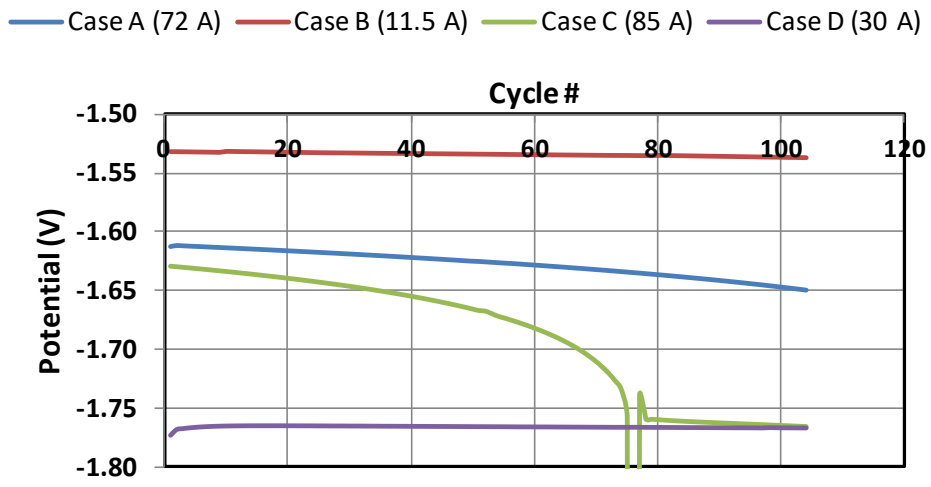

Figure 25- Long Term Cathode Potential Results for Base Cases

The cathode potential results show that for the short-term data that the potential follows a constant value for the majority of the operation. The short-term potentials correspond to the reduction potentials of the species deposited. In the case of the short-term data for the first cycle, only case D has codeposition for the initial cycle and the much more negative potential modeled reflects this. The cases without codeposition during the initial cycle follow a trend where the higher the current, the more negative the potential of operation. The long-term results show that as the U concentration decreases in the salt then the potential decreases along with it. Specifically in case C, the potential decreases until codeposition of Pu and U occurs at which time it levels out at a value around that of the Pu reduction potential. As case D is continuously depositing, it operates for all cycles as a more negative potential below that of the Pu standard reduction potentials. Thus, for long-term cathode potential results piecewise functions are necessary for programming into a systems model, specifically for cases that transition from operating conditions of no codeposition to that of codeposition occurs.

6.2.2 Internal Power Surge

The results of the internal power surge simulations faced complications with respect to ERAD performance. The results derived from base case C could not be adequately simulated due to issues with the ERAD solver failing while finding a solution for the ER mass transport past the twentieth cycle of 104 cycles for the C cases. As it happened in an earlier cycle as well, there are too few data points to make conclusions about later cycles from data present. Thus, the data presented here is for bases cases for A, B, and D.

Figure 26 depicts the long-term cathode deposition results. As seen in the results, for cases derived from A and B (not seen in plot) codeposition does not occur with the application a slightly higher current over the same period of time due to the low Pu/U ratio. This shows that maintaining a low Pu/U ratio in the salt via introduction of salt eutectic would be an effective way to negate off-normal scenarios triggering a safeguard-significant related event. Case D1 and D2, demonstrates similar behavior to base case D where codeposition happens from the start while the amount of Pu codeposited over time decreases. As expected, the total U deposited converges to a maximum value that increases with higher current. In total though, the mass of Pu codeposited increases with higher current. These long-term mass data trends are analyzable as functions of cycle number.

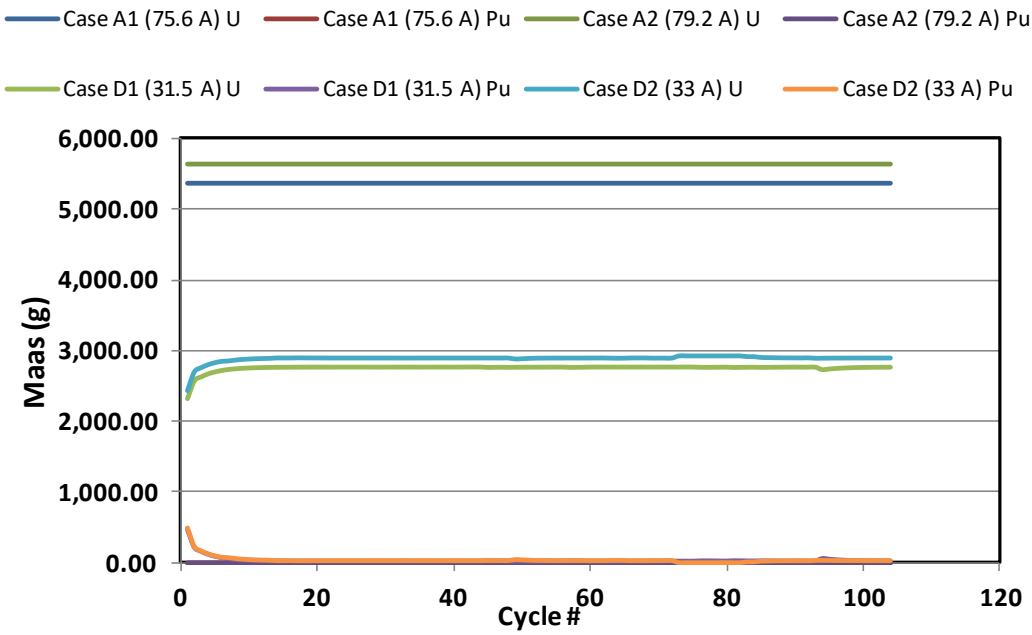

Figure 26- Long Term Cathode Deposition Results for Internal Power Surge Variations

Figure 27 depicts long-term anode results in terms of final masses in the anode per cycle. From the results, the amount transported out of the anode is dependent on current but not based on salt composition over time. Increased current results in more material transported into the salt with the highest current having lowest mass remaining in the anode basket at the end of the run. Thus, the anode function is programmable as a repeated linear function over time based off starting and final masses to determine the slope of the resulting function.

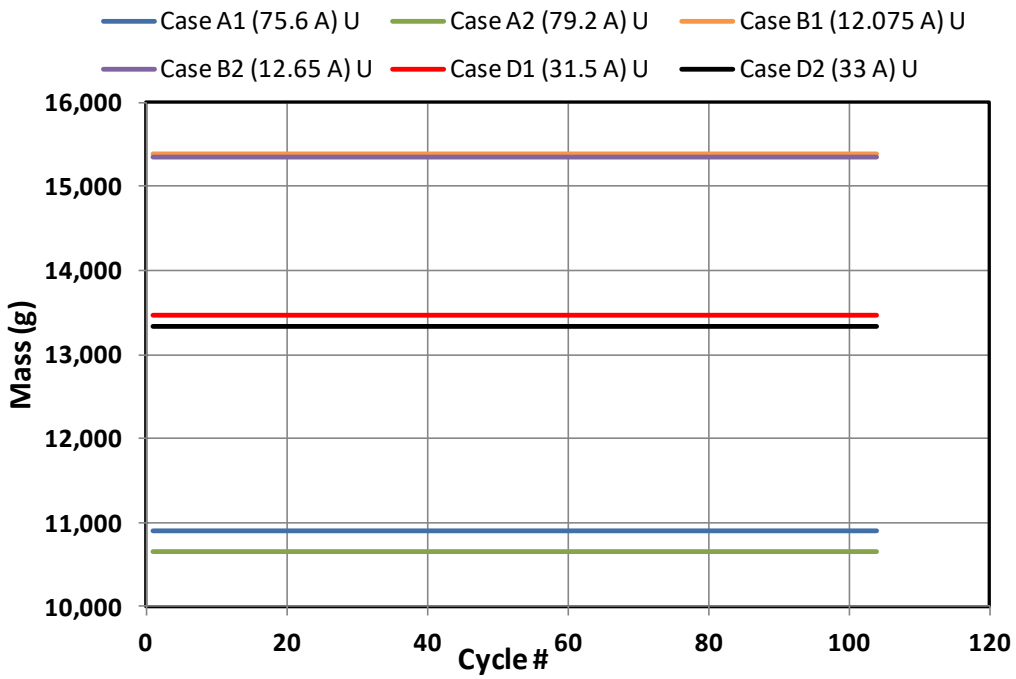

Figure 27- Long term Results for Final Anode Mass for Internal Power Surge Variations

Figure 28 shows long term results for change in salt weight percentage. For cases derived from base case A, the concentration of U decreases substantially and the concentration of Pu increases substantially. Though codeposition did not occur, it could quickly become a possibility thus demonstrating the significance of this kind of failure especially for higher concentrations of Pu starting in the salt combined with a higher current of operation. Runs derived from base case B (not seen in plot) demonstrate that for a low current and low Pu/U ratio, the effect of a higher current is less as the magnitude of the current is not high. This is less likely to lead to a codeposition scenario with an extended number of cycles past the 104 simulated here. Finally, in cases derived from base case D, similar behavior steeper slopes to base case D occurs. Thus from all cases, the rate of change of mass of actinides in the salt is dependent on the operational current.

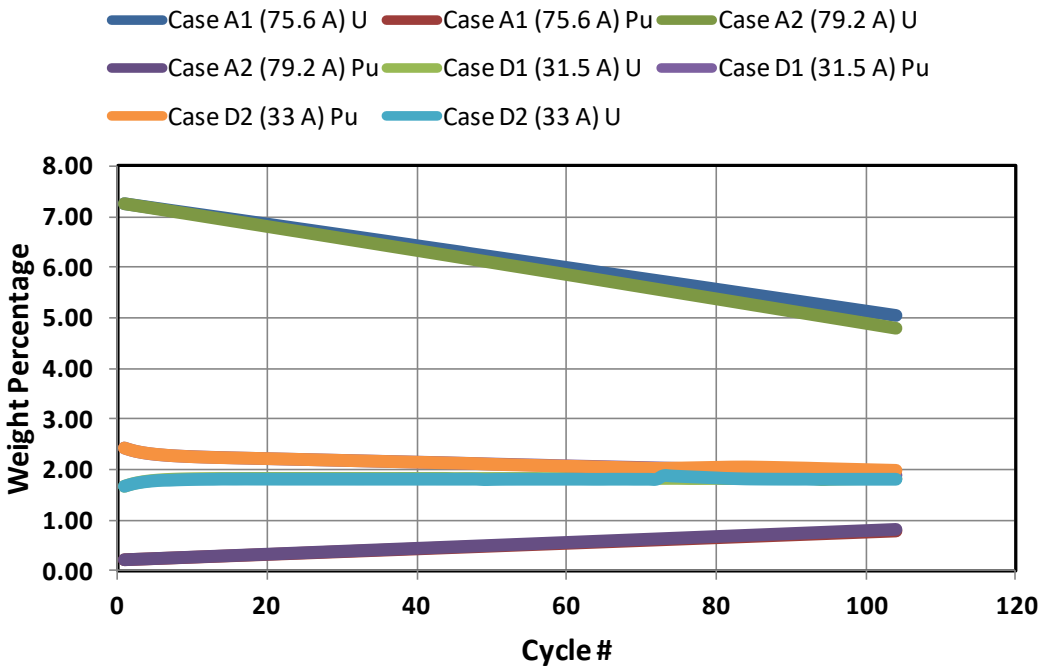

Figure 28- Long Term Salt Concentration Results for Internal Power Surge Variations

Figure 29 and Figure 30 show the long term average electrode potential results for the anode and cathode, respectively. The anode potentials demonstrate that the higher current translates to more positive potential results. Specifically for the low current runs (B & D), the average potential changes very little between cycles throughout the 104 cycle run. The higher current runs derived from base case A runs see an increase in the potential with each respective cycle. This is expected as the A runs are the only ones with significant changes in actinide composition due to significantly increased amount of Pu mass transport into the salt as well as the increased rate of U removal. The potential calculated at the anode by the Nernst equation reflects these changes. However, despite this the potential never comes close to reaching the value required for the oxidation of Zr

or U (IV) into the salt, thus avoiding the negative effects associated with the existence of these materials in the salt.

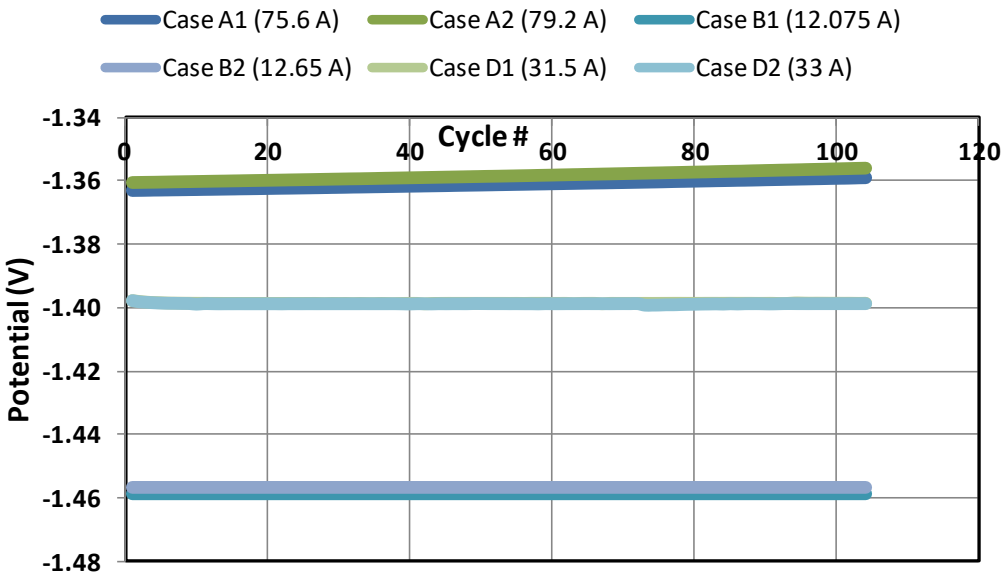

Figure 29- Long-term Average Anode Potential for Internal Power Surge Variations

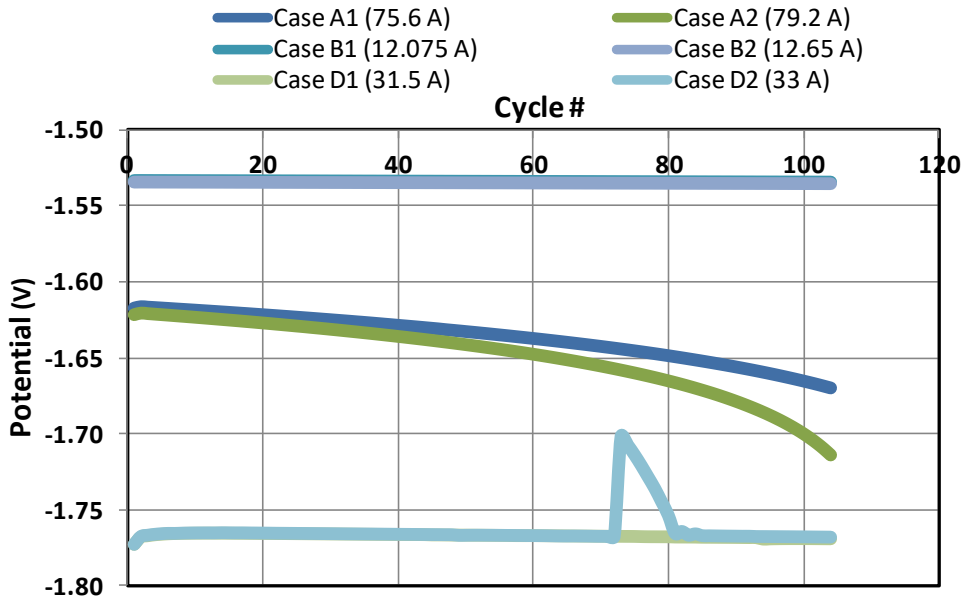

Figure 30- Long-term Average Cathode Potential for Internal Power Surge Variations

The cathode potential results demonstrate that for the A cases that over time, as the U began to reduce significantly at the cathode, the potential continued to become

more negative at a rate directly proportional to current. Thus, with an extended number of cycles past the 104 simulated, high current with low Pu/U ratio will eventually lead to codeposition. This continues to demonstrate the importance of designing a facility to operate where salt cleanup and scheduled addition of chloride salts to the ER bath occurs. For the base case B derived cases, due to low current and low starting Pu/U, the potential changes very little, thus showing that from a safeguards perspective a low current is beneficial as it requires more drastic failures to result in negative safeguards consequences. Low current operation can cause a handicap with regards to total throughput. The base case D derived results operate at their start at a value less than the Pu reduction potential and steadily increase towards the Pu reduction potential as the amount of Pu in the salt bath decreases. In addition, these cases also demonstrate that, with increasing current, the Pu codeposited can exhaust itself. This situation results in operations that do not reach the potential for codeposition as in the case of D2, where a positive jump in potential occurs around cycle 70. However, if this exhaustion does not occur over the length of the operation the potential is a potentially useful signal to determine if codeposition has occurred and can subsequently be correlated with other measurements to develop conclusions as to a failure origin and consequence.

6.2.3 External Power Surge

As the external power surge simulations occur for only the initial operation cycle, the short-term data is the only data collected and presented in this subsection. Figure 31 and Figure 32 depict the short-term results for the base case C and D derived cases, respectively. The base case A and B derived cases are not presented as no codeposition occurs; only an overall increase in the total amount of U mass deposited. The U mass

deposits from the A and B cases will be modeled as a function of current when translated into a systems code.

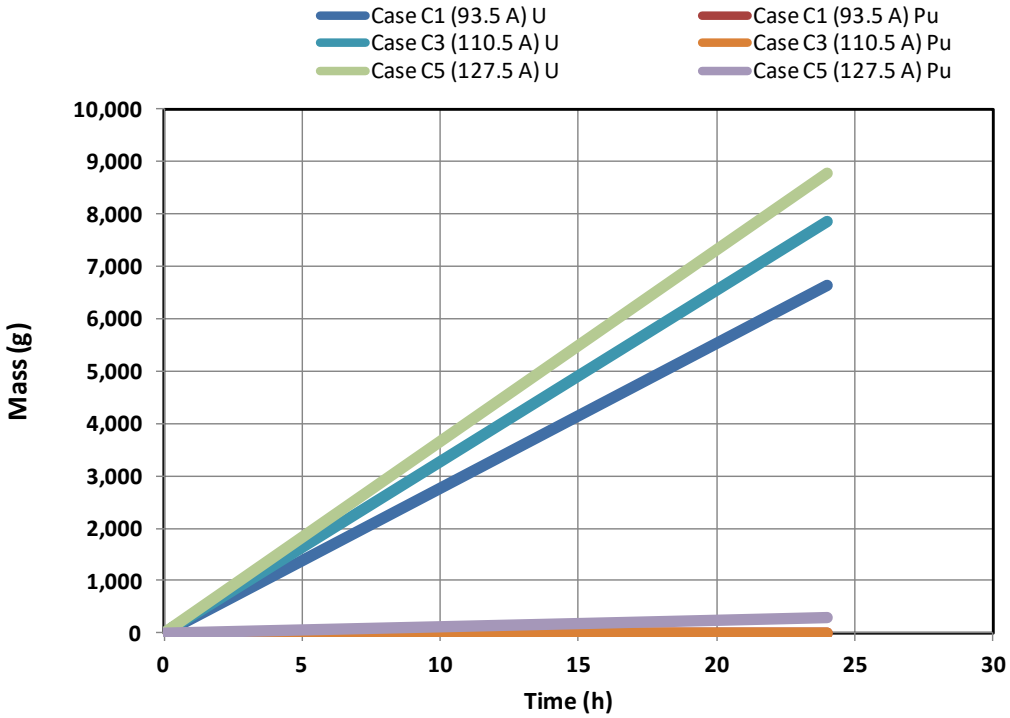

Figure 31- Cathode Deposition Results for C Derived Cases (External Power Surge Variations)

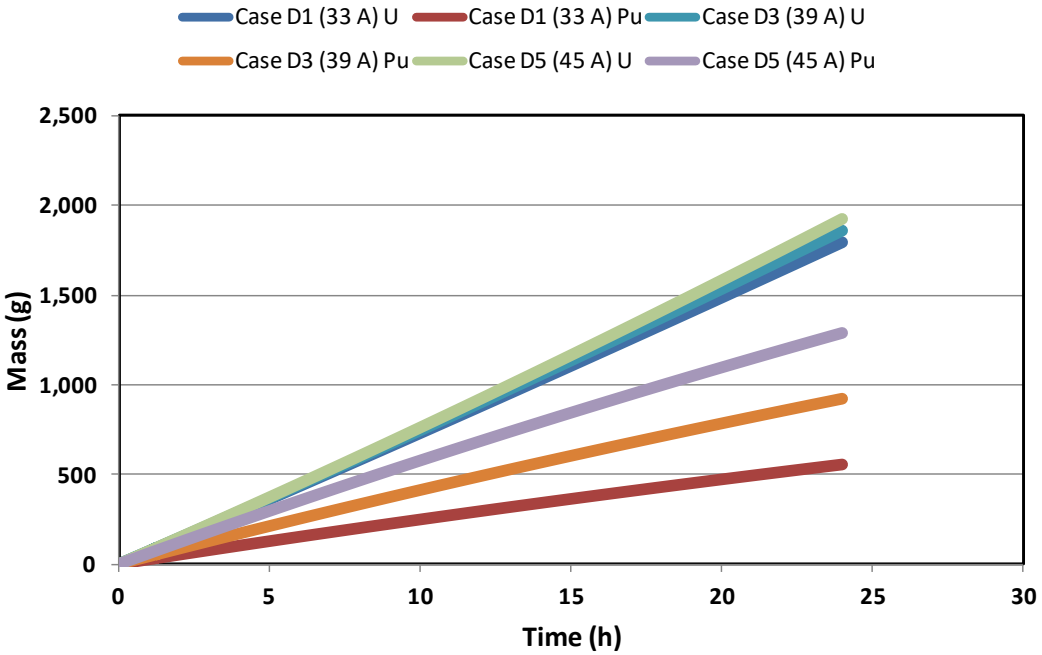

Figure 32- Cathode Deposition Results for D Derived Cases (External Power Surge Variations)

The results for the C derived cases show a steady increase in total U deposited that is proportional to current for cases C1-C4. For Case C5 codeposition does occur thus showing that for high currents and high Pu/U ratio, current should be monitored as codeposition effects will develop. The results for the Case D derived runs also provide other useful observations. In these cases, the amount of U deposited at higher currents is not significantly greater than the previous case, but the Pu codeposited increases with each increasing current. This indicates that the limiting current has been reached and surpassed. Thus, U only deposits at a rate governed by its limiting species current. To reach the total current density of the cell, a greater partial species current of Pu is present thus the increased deposition of Pu.

For the sake of brevity, the anode results displayed here are similar to that of the base cases. The transport of species is linear with a negative slope proportional to the current being supplied with greater current meaning more actinides transport out of the anode into the salt over the period of 24 hours. This shows that regardless of the current, the anode is analyzable as a linear function over time with only alterations made to the slope to reflect the change in current.

Like the anode results, the results for the salt over time have the same conclusions of the bases cases and are not shown here graphically. U concentration decreases, while Pu concentration increases for the A-C derived cases. The D derived cases have an increase in U concentration while Pu decreases. The functions are linear and can have the mass modeled as a linear function over time. The slope of the lines are proportional to the current with a greater value meaning a more rapid decrease in U and increase in Pu for

the A-C derived cases. In the D derived case, an increase in the rate of U growth occurs with a Pu decrease.

The anode potential results follow expected trends and do not reach a potential high enough to oxidize zirconium at the anode. The potentials for all cases are straight, constant values for the entirety of the operation with the constant value becoming more positive with increasing current. There is no need for graphical representation in this section since results already presented relate the same trends and conclusions.

Figure 33 and Figure 34 depict the cathode potentials results for the C and D derived case, respectively. The A and B derived cases follow the same previous conclusions as the changes in current in the internal power surges in that the potential becomes more negative proportionally with increased current and stays at a near constant value for the length of the operation. For the C derived cases, cases C1-C3 all have similar expected trends which involve proportionally more negative potentials that stay constant for the entire operation. However, the C4 case has results with a negative slope indicating, that over the course of the ER operation, the salt has a considerable change in concentration of U to make it approach codeposition. Thus, in the circumstance, assuming return to normal operation after the one cycle, a subsequent codeposition would be seen at an earlier cycle than in the base case due to changes identified with the potential here for the given high current operation. Case C5 operates at a current sufficient for codeposition resulting in there being a constant value at the reduction potential of Pu.

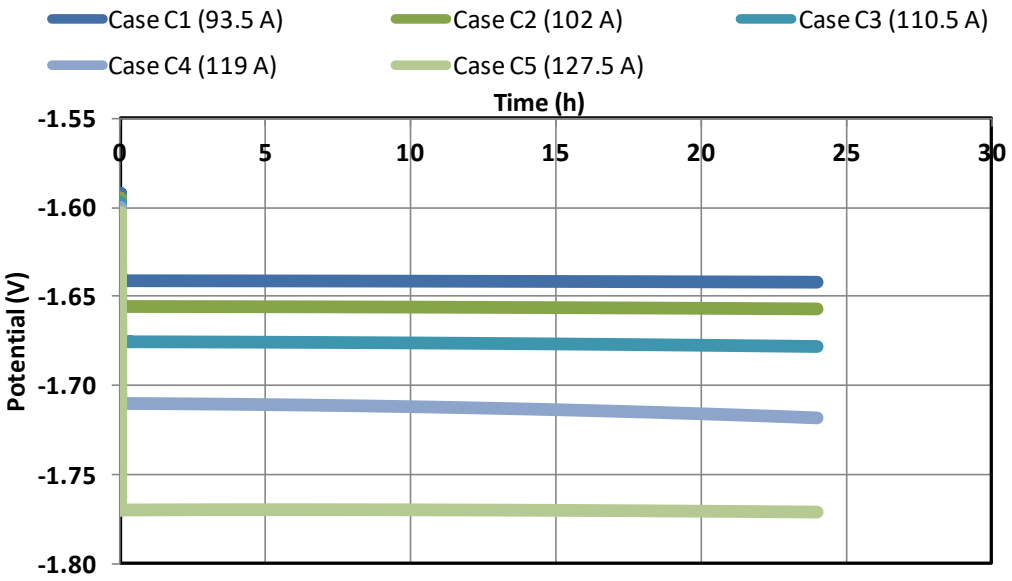

Figure 33- Cathode Potential Results for C Derived Cases (External Power Surge Variations)

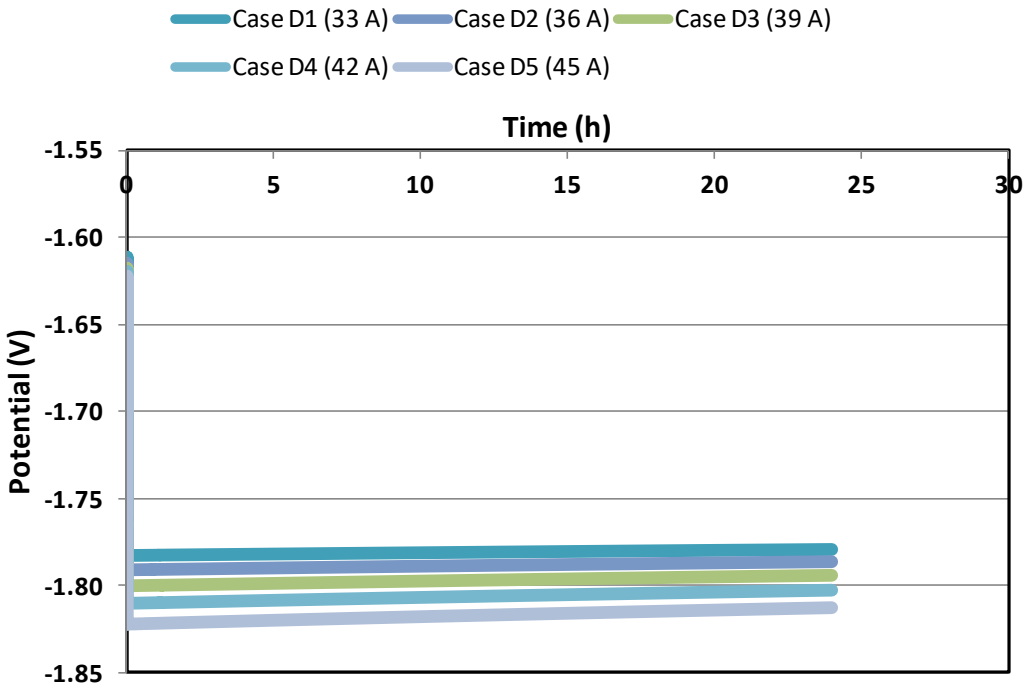

Figure 34- Cathode Potential Results for D Derived Cases (External Power Surge Variations)

The D derived cases demonstrate that the expected higher current translates to more negative potential. However, as the operation continues over the twenty four hours, the

potential slowly becomes more positive. This positive slope increases with increasing current. Thus, as Pu codeposits, the calculated potential reflects changes in salt composition. This demonstrates that codeposition can be detected via setting a threshold level for the measured potential. Translating this into either salt or cathode compositions, however, becomes more difficult as the potential changes over time generate uncertainty in an mass estimation.

6.2.4 Anode Rotation Rate

Over the range of the test matrix, very little changes occur in the results of these tests compared to the base case. No codeposition occurs and there is very little effect on anode transport and potential. A graph of the anode rotation failure cases would look no different from the base cases. These results indicate that the classification of the significance in the FMEA should be changed to Class III and requires less significant future investigations as to effects on the greater system.

6.2.5 Temperature Variation

The results with regards to variations in temperature depict a failure mode of particular significance. Figure 35 and Figure 36 show the results of the temperature variations for the cathode depositions of U and Pu for C derived cases, respectively. Appendix B contains the results for A and D derived cases. The results of base case B derived cases differ slightly than those of the base case B results showing no codeposition occurring.

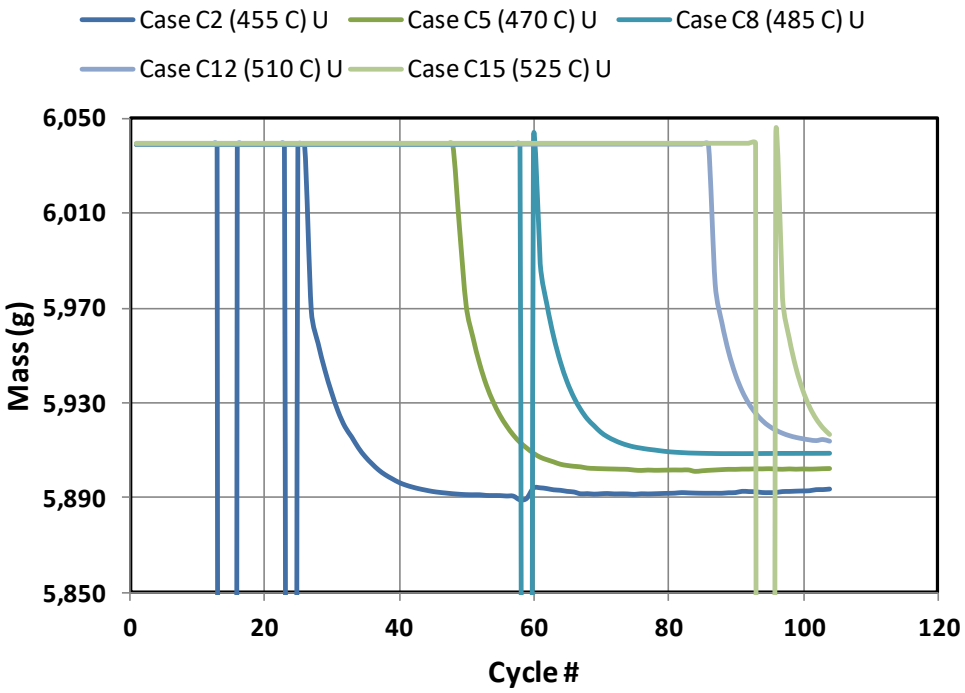

Figure 35- U Cathode Deposition Results for Temperature Variations of C Derived Cases (Temperature Variations)

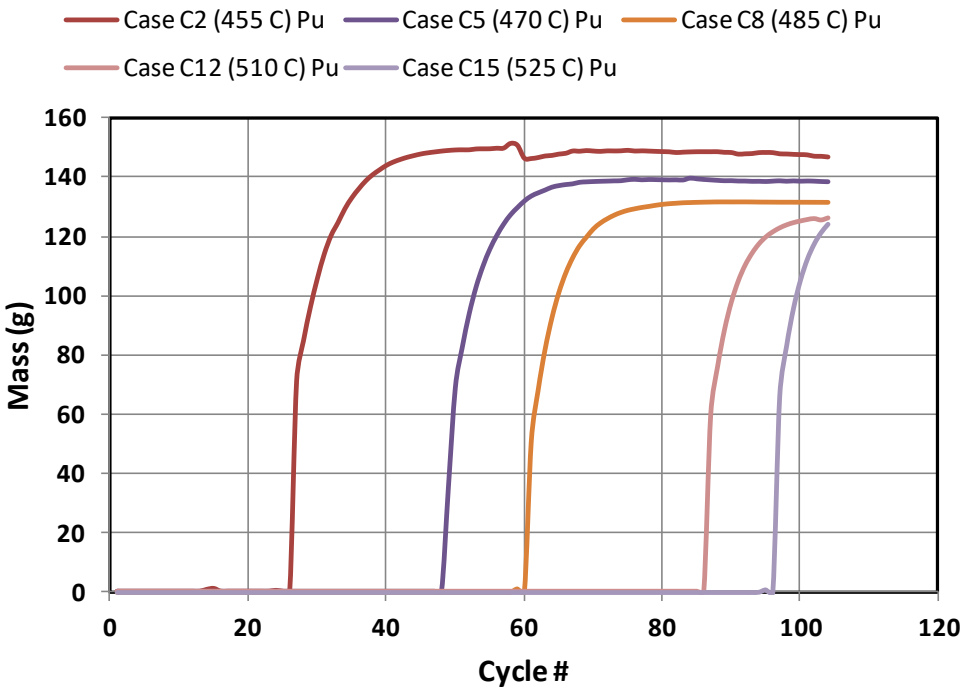

Figure 36- Pu Cathode Deposition Results for Temperature Variations of C Derived Cases (Temperature Variations)

Among A and C cases several noticeable trends arise. With a lower temperature, an increased amount of codeposition occurs. In addition, cases where codeposition does not occur during the base case (Case A), codeposition does occur in the long-term if operation takes place at a lower temperature. Contrarily, as temperature increases the less codeposition occurs. The results also indicate that with lower temperature the transition occurs sooner from no codeposition to codeposition. For this reason, a surge in temperature in the salt will be reclassified in the FMEA as a Class III failure and a partial heater failure will be reclassified as a Class I failure mode especially for higher currents of commercial operation. In addition, for case D derived failure modes, the amount of codeposition is increased and the rate at which the Pu codepositon diminishes as the temperature decreases. Thus, monitoring temperature is of the utmost importance from an operations and safeguards perspective as it can significantly affect throughput after very few cycles without cleanup.

The anode transport for all cases did not depart from that of the base cases. This indicates that the change in salt temperature affects the deposition at the cathode as well as the movement of elements within the salt itself but has little effect on the reactions at the anode.

Figure 37 displays the results for the change in weight percentages in the salt for C derived cases. Appendix B contains the results for A and D derived cases. The results show the same trends as previous operations involving codeposition. The weight percentage of U in the salt for cases A and C decreases at a constant rate until the point at which codeposition occurs at the cathode. This is a trend seen in all codeposition cases. Once codeposition occurs, the weight percentage of U in the salt becomes more or less

constant. The Pu results show that the concentration increases up until the point of codeposition at which it decreases as Pu transports into the salt at a greater rate than it oxidizes at the anode basket. As codeposition occurs at an earlier cycle for the low temperature cases, the effects described reflect these conditions.

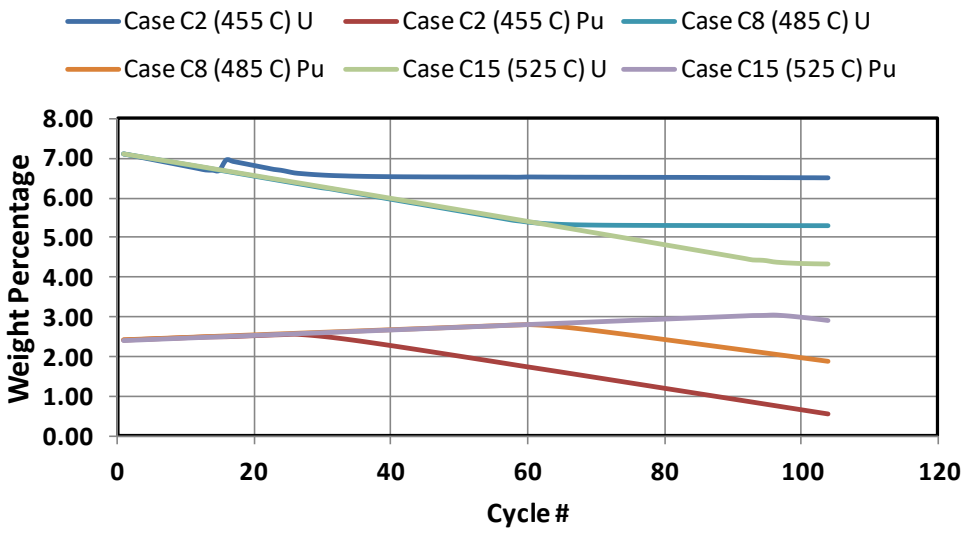

Figure 37-Salt Composition Results for Temperature Variations of C Derived Cases (Temperature Variations)

For the D derived cases, the Pu decreases as the U increases with each increasing cycle number. The rate at which this occurs however is dependent on the temperature, with the decrease being significantly more rapid at the lower temperature. Because of this expediency of removal of Pu from the salt, the difference between sampling on cycle 10 and cycle 20 would be substantially different. This would make it easier to detect the removal of Pu via codeposition, however this will produce challenges with regards to estimating the total that has left the salt due to codeposition. Thus, operators must consult long-term data such as this when determining a sampling schedule for safeguards related purposes to know what potential challenges could arise for a given set of conditions.

Figure 38 shows the results for the cathode potentials for the C derived cases. Appendix B contains the results for A and D derived cases. The cathode potential results for the A derived cases indicate that for each case that potential decreases per cycle. The rate at which the potential becomes more negative increases with decreasing temperature. The decrease in potential continues until it reaches the potential at which codeposition occurs, at which it becomes more negative at a slower rate as codeposition occurs. The large drop seen in the potential interrupts this decreasing trend. This is due to errors in the modeling performed by ERAD and do not reflect expected data points from the scenario simulated. As the temperature rises, the rate of the decrease in potential slows.

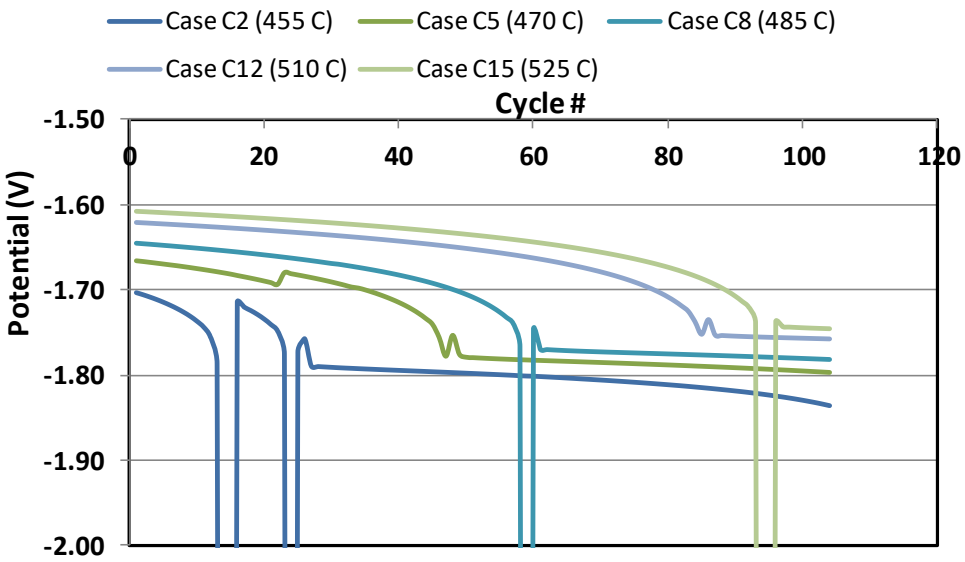

Figure 38- Cathode Potential Results for C Derived Cases (Temperature Variations)

The C derived cases show very similar behavior to the A derived cases, but the C cases all result in codeposition. Each case reaches the codeposition potentials at later and later cycles with increasing temperature. In addition, the results of the C derived cases, like the A derived cases, contain visible failures in the solver. Finally, for D related cases the potential becomes more positive as the amount codeposited decreases for each case. It

then slowly decreases as the operation continues. The potential becomes more negative with decreasing temperature. Thus, it's beneficial to correlate thermocouple and reference electrode measurements for process monitoring.

Figure 39 shows the anode potential results for A derived cases. Only A derived cases are shown as all cases follow the same trends. The higher the temperature, the more positive the anode potential is. The anode potential measurements, though not indicative of much in terms of salt transport behavior, are linkable with potential results from the cathode and the temperature to detect off-normal conditions.

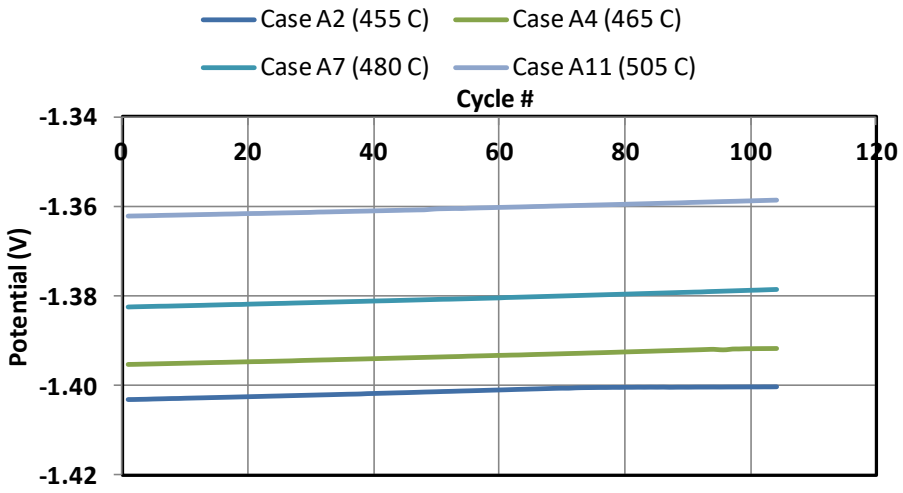

Figure 39- Anode Potential Results for A Derived Cases (Temperature Variations)

6.2.6 Cathode Area Variation

Studies involving cathode area variation simulations to model failure in the retraction linkages of electrodes have been previously performed and this work expands these studies further [12]. Previous work demonstrated that reduction in cathode area can lead to codeposition and the codeposition is proportional to the area reduction. However, long-term studies were not performed previously with regards to cathode area variations

and this work explores these effects in-depth. With regards to these studies, the base case A derived case could not be adequately addressed by the solver in ERAD, and challenges developed with case B. Cathode rotation rate failure modes exhibit this behavior as well. This demonstrates that cathode failure modes do not simulate with high fidelity long term studies cases where the Pu/U ratio is low, but base cases C and D which possess a high Pu/U ratio can be analyzed.

Figure 40 and Figure 41 show the long-term cathode deposition results for U and Pu depositions in the C derived cases. Appendix B contains results for base case D derived cases. It is shown that in the C derived cases that with decreasing surface area, the point at which codeposition occurs is an earlier cycle. Past short-term results indicated this same effect of cathode surface area on transport in the salt. Once the surface area is small enough to where codeposition occurs at the first cycle, there occurs a steady decrease in Pu mass with a steady increase in deposited U mass.

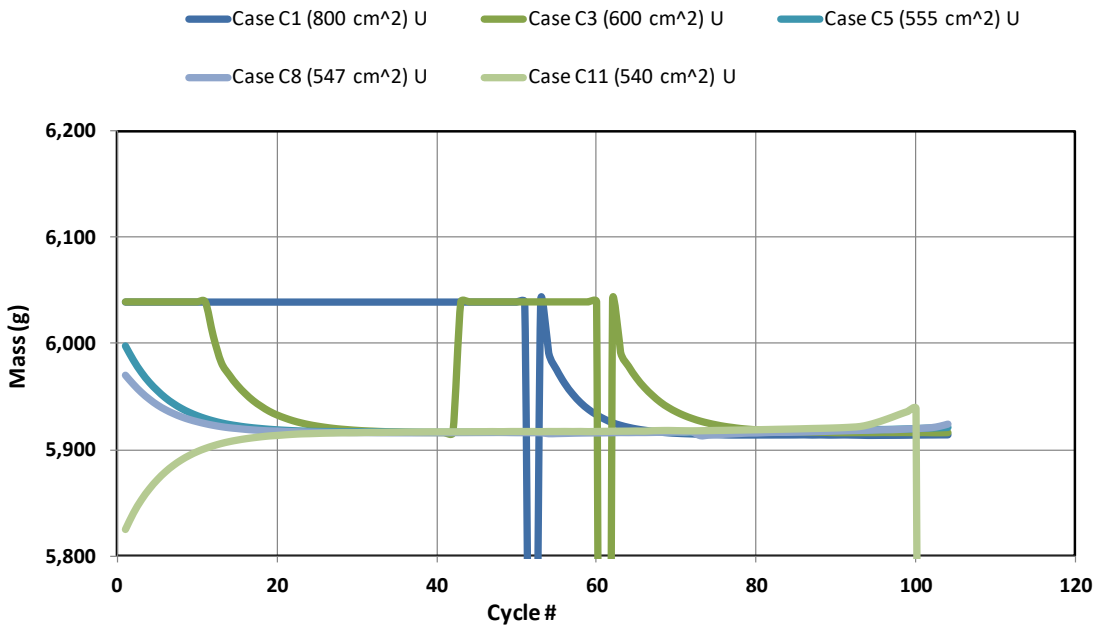

Figure 40- Long Term Cathode U Codeposition Results for C Derived Cases (Cathode Surface Area Variations)

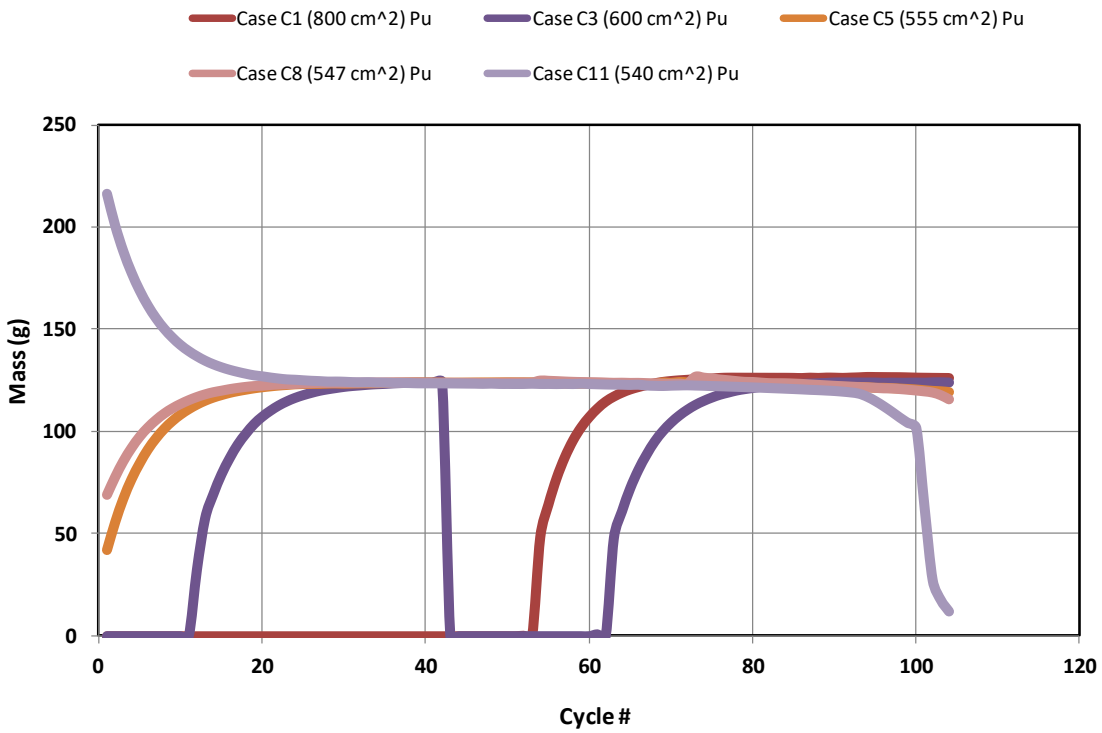

Figure 41- Long Term Cathode Pu Codeposition Results for C Derived Cases (Cathode Surface Area Variations)

With C derived cases, one particular simulation of interest is that of Case C3. In this case, it does not initially have codeposition, but after 10 cycles deposition begins. After a short period of codeposition, it returns to zero and then codepositions at a later cycle again. This is not reflective of a physical mechanism, but due to an error in the model itself and this conclusion is further verified in the salt results presented next. Inspecting the results for this case in particular at the cycle 43 where this discontinuity occurs, the sum of the partial currents equal that of the applied current. In addition, the mass depositions at the cathode seen in Figure 41 and anode transports into the salt which are the same as base case C reflect the calculated partial currents. Thus, given these conditions there should be a decrease in the mass of U in the salt along the lines of 40 grams. Instead, the mass increases over the cycle 43 by an amount greater than 3000

grams. This reflects a failure in the ability of the model to solve for the mass transport in the salt bath. This can be attributed to salt bath being represented as a single bulk homogenous cell significantly geometrically larger than all other cells in the mesh representing the ER. This is to ensure a fast approximate estimation, but the simplification leads to challenges in finding a solution for the concentration of the masses within it over time. The case D derived results demonstrate that with increasing surface area, the longer it takes for the deposition to diminish to a steady value, and the greater the codeposition occurring during earlier cycles. Thus, the more the surface area decreases the greater the observed long term effects.

Figure 42 shows long term salt results for cases derived from bases case C. Appendix B contains the results from D derived cases. The salt composition results match many of the expected results from experience and the cathode data. The C derived cases have U concentration that decreases steadily until codeposition occurs at which point it flattens out. In addition, for the case where codeposition occurs from the start, it remains generally flat while the Pu concentration decreases steadily over the entirety of the period.

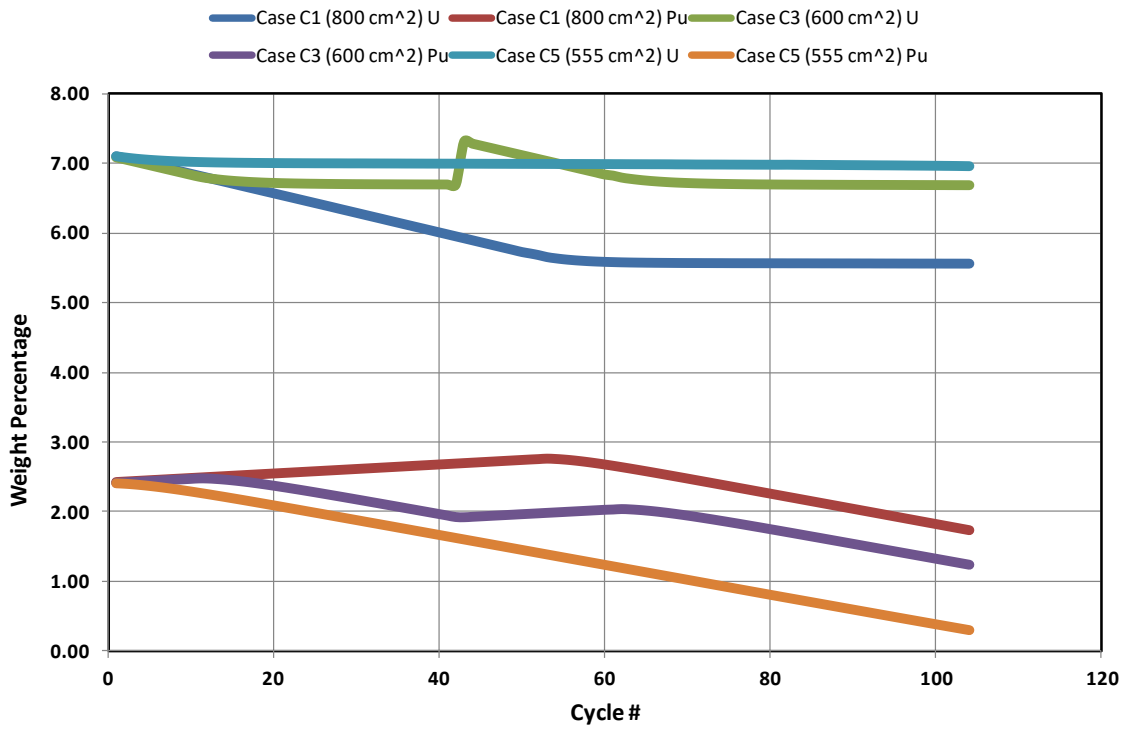

Figure 42- Long Term Salt Composition Results for C Derived Cases (Cathode Surface Area Variations)

Case C3 as noted before is an anomaly, it displays the expected behavior of decrease followed by flattening out, but at one point it has a distinct jump back to near initial concentrations. This indicates that an error occurred within the model itself. Case D results match the expected results where Pu decreases while U increases from the start. The amount of increase/decrease is proportional to the area where the slopes increase with decreasing surface area of the cathode.

As noted in previous work, cathode failure modes do not affect the behavior of the anode and its properties [12]. The anode and anode potential results match those of its associated base cases and thus the anode results are displayed in this section.

Figure 43 displays the cathode potential results for cases derived from base case C. Appendix B contains plots of the results from base case D derived cases. The long-term cathode potential results match results from the previous failure modes involving

codeposition. C derived case involve a decrease in potential until codeposition occurs at which the decrease continues at a more steady rate. Those results already exhibiting codeposition involve a steady decrease in potential as the failure mode progresses with codepositions at each step. In D derived cases, the potential increases slightly followed by a small steady decrease similar to the results of the other failure modes such as temperature variation.

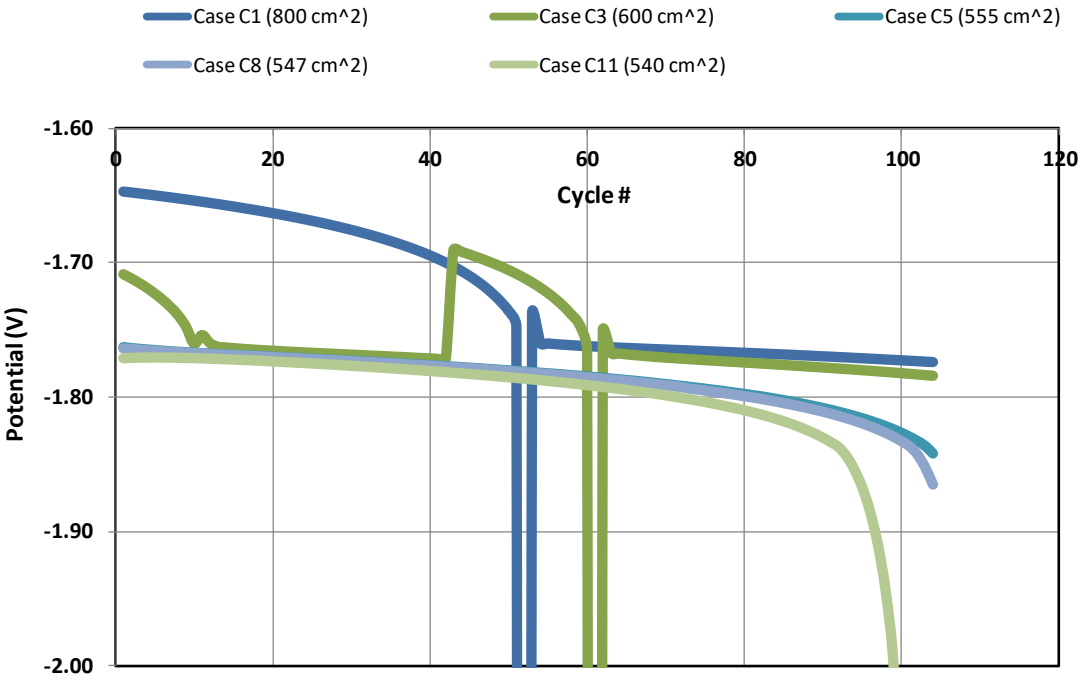

Figure 43- Long Term Cathode Potential Results for C Derived Cases (Cathode Surface Area Variations)

6.2.7 Anode Area Variation

The variations in anode area produced scenarios of great interest from the perspective of mass tracking. To determine its impact, I first present the results of the anode transport effect for the short term of one operational cycle. Figure 44 shows the results of anode transport in the simulations regarding base case A derived failure modes.

All results match this basic pattern. The results show that due to less surface area, less total mass is in contact with the salt and thus the starting mass decreases in the anode with each reduction in surface area. Thus, there is metal in the basket that does not react with the salt. However, as the slope does not change, the amount remaining in the basket does not change. With this, the total amount of actinides transferred into the salt does not change from the base cases.

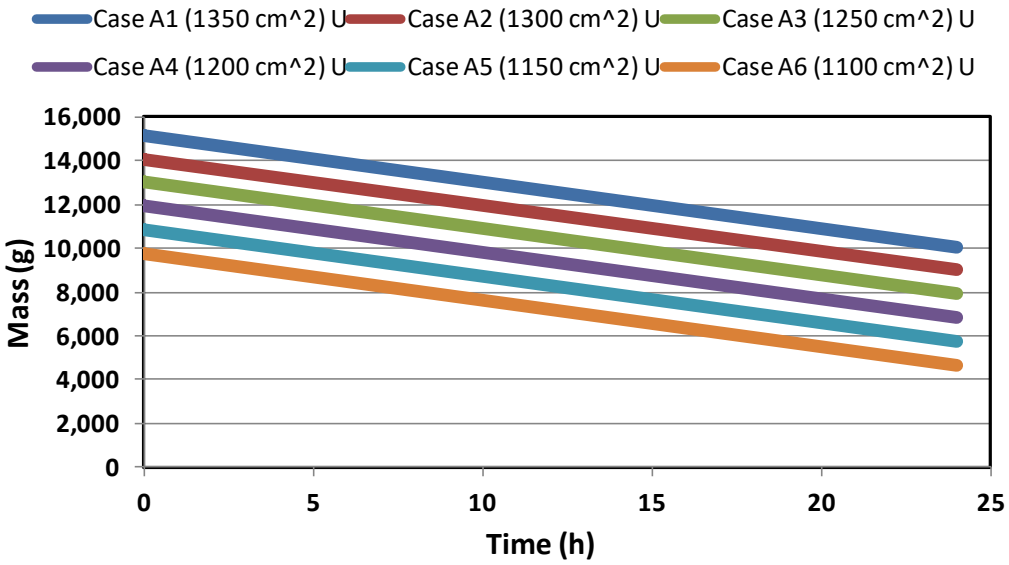

Figure 44- Short Term Anode Data for A Derived Cases (Anode Surface Area Variations)

This change in anode surface area does however have an effect due to reduced mass and area on the total cell potential. There is less mass to limit the reaction at the anode. Thus, the reactions of the total cell specifically at the cathode are affected. Figure 45 and Figure 46 exhibit these effects as seen in the long term cathode results for U and Pu depositions for base case C derived cases. Appendix B contains the results for A and D derived cases. Base case B derived cases results are not included as codeposition does not occur under the circumstances of the low current and low initial Pu/U ratio.

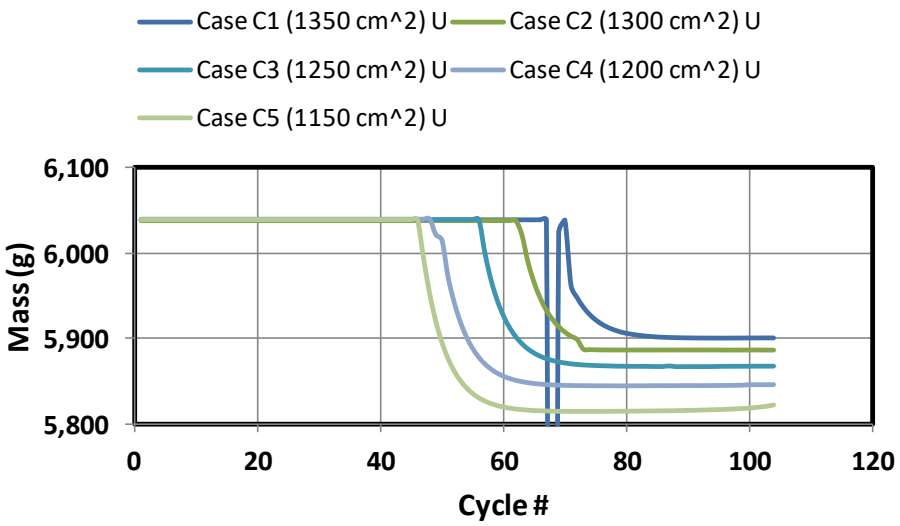

Figure 45- Long Term U Cathode Data for C Derived Cases (Anode Surface Area Variations)

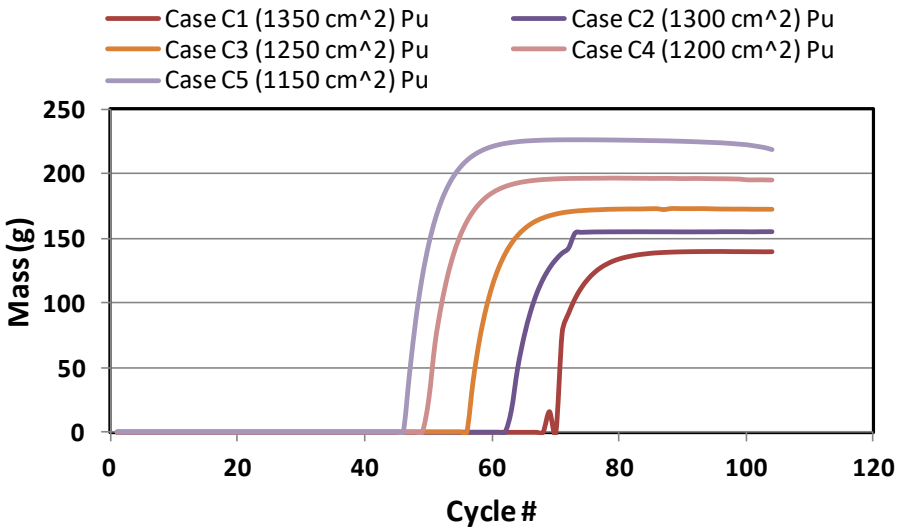

Figure 46- Long Term Pu Cathode Data for C Derived Cases (Anode Surface Area Variations)

Interpreting the data, for the A and C derived cases, codeposition circumstances arise with reduction of surface area. There is an observable trend where the smaller the surface area of the anode, the earlier the cycle at which codeposition occurs. The earlier cycle of codeposition results in a greater total amount of codeposition of Pu during the

four month operating period. Thus, there is a notable significance to the amount of surface area reduction. Case A derived results show that codeposition may not in fact occur if the anode area does not change by a significant enough amount. However, in the A cases similar failures in the code occur as in the cathode surface area reduction, and the necessary simulations cannot be completed. This is the result of the solver stopping the run at around 1 hour as opposed to the full 24 hours. These results cannot be fully imported into a systems model like the results from the base case C derived failure modes. As for the D case derived results, the failure mode has very little total effects on the cathode depositions for D derived cases, and for the case of high starting Pu/U ratio this failure has less severity.

Figure 47 shows the long-term salt results for C derived cases. Appendix B contains the results for A and D derived cases. As observed in previous cases, the results follow the expected trends of previous codeposition cases. Cases derived from A and C involve a steady increase in Pu with a steady decrease in U until codeposition occurs where the U flattens out in concentration with regards to the total mass of the salt while Pu decreases as it transports out at a faster rate than it is transported in. The D derived cases involve the decrease in U coordinated with an increase in Pu as the operations progress, as seen in other failure mode effects on D derived cases.

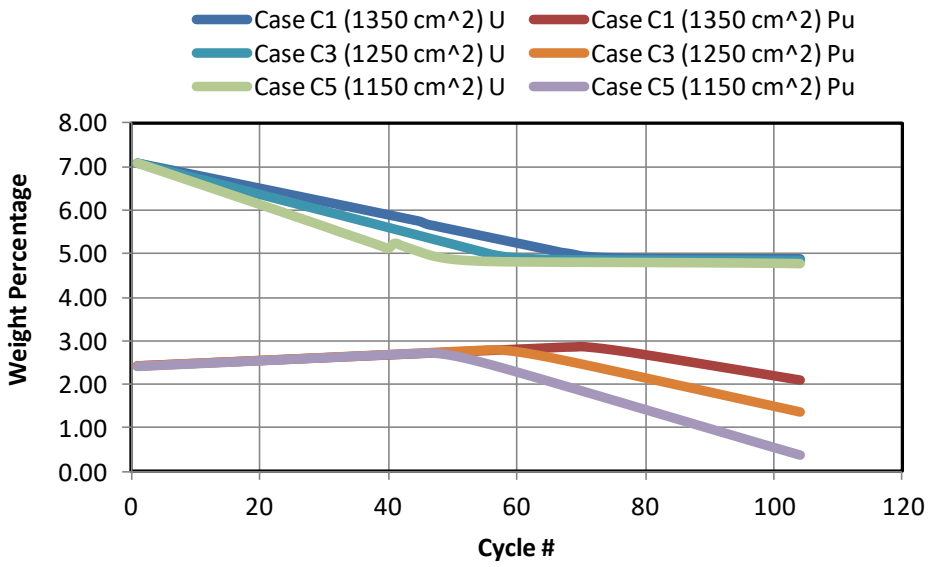

Figure 47- Long Term Salt Data for C Derived Cases (Anode Surface Area Variations)

Figure 48 and Figure 49 show long term cathode potential results for the C and D derived cases, respectively. No significant additional commentary is necessary given that the results follow trends demonstrated by the previous failure modes in this chapter. Case A has the same trends observed for its codeposition cases as the trends for C derived cases in Figure 45. Namely, the decrease in potential at an increasingly negative rate until reaching the codeposition potential at which point it decreases at a reduced rate.

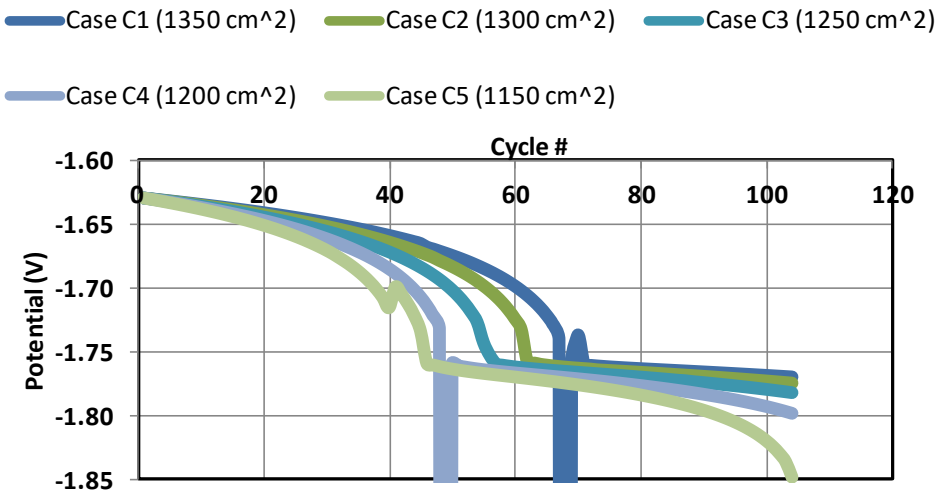

Figure 48- Long Term Cathode Data for C Derived Cases (Anode Surface Area Variations)

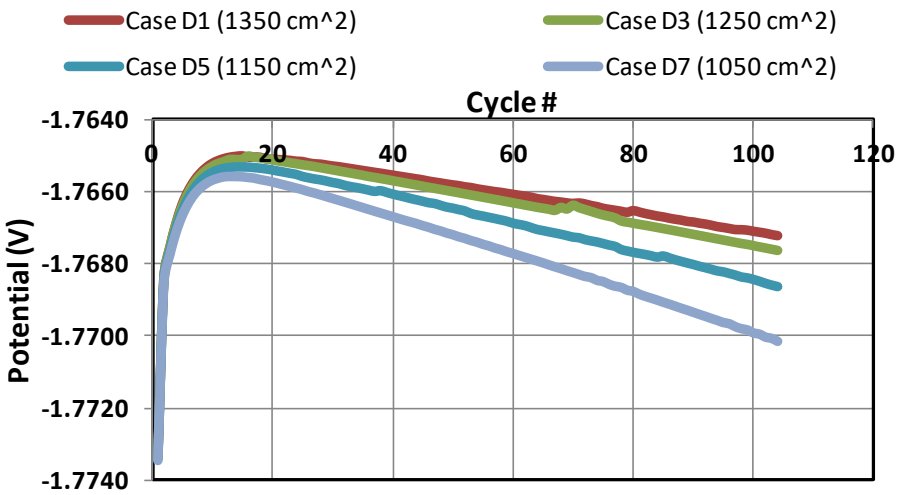

Figure 49- Long Term Cathode Data for D Derived Cases (Anode Surface Area Variations)

Figure 50 and Figure 51 shows long term anode potential results for C and D derived cases respectively. The data calculated here differs from what has generally been observed for the anode potential. For C derived cases, the potential becomes more positive until it reaches the cycle during which codeposition occurs, at which point it

increases and becomes more positive at a slower rate per cycle. The challenge with this is that it would be difficult to detect.

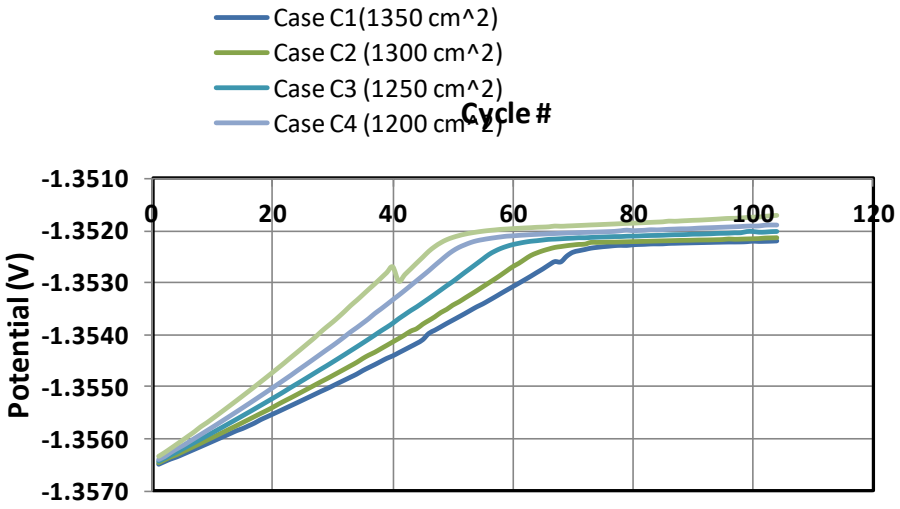

Figure 50- Long Term Anode Data for C Derived Cases (Anode Surface Area Variations)

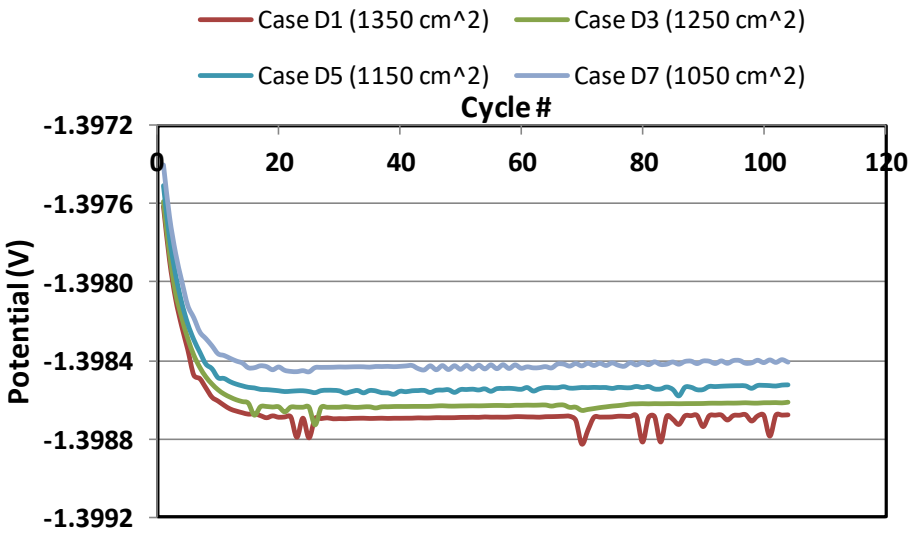

Figure 51- Long Term Anode Data for D Derived Cases (Anode Surface Area Variations)

Observing the scale of the y axis, these results show that these changes are on a very small-scale and unless the reference electrode was incredibly sensitive and accurate. Experience shows they are not to this degree, so that this deviation would not be easily detectable by monitoring the reference electrode outputs. Case D derived anode potentials

show that the smaller the surface area, the more positive the potential. However, like case C the difference is so minute that registering the change with a reference electrode would not be practical in an actual facility application.

6.2.8 Cathode Rotation Rate Variation

Like the cathode area data, I have previously performed [12] cathode rotation rate variation previously for short term data as well as for long term data. It has been significantly expanded in this work. Like the area data as well, challenges arose with the range of low Pu/U ratio runs that could be performed, but unlike those A related data could be obtained and is presented here.

Figure 52 and Figure 53 show the long term cathode deposition results for U and Pu for C derived cases. Appendix B contains results for A and D derived cases. The cathode results illustrate, in the A and C derived cases, that the slower the rotation rate, and thus the greater the size of the diffusion layer thickness, the earlier the cycle at which codeposition occurs during long term runs.

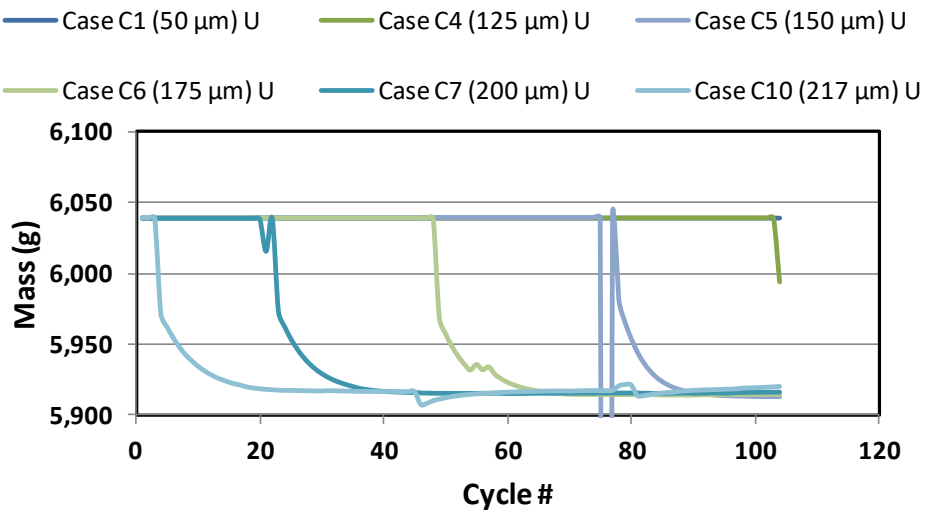

Figure 52- Long Term U Cathode Data for C Derived Cases (Cathode Rotation Rate Variation)

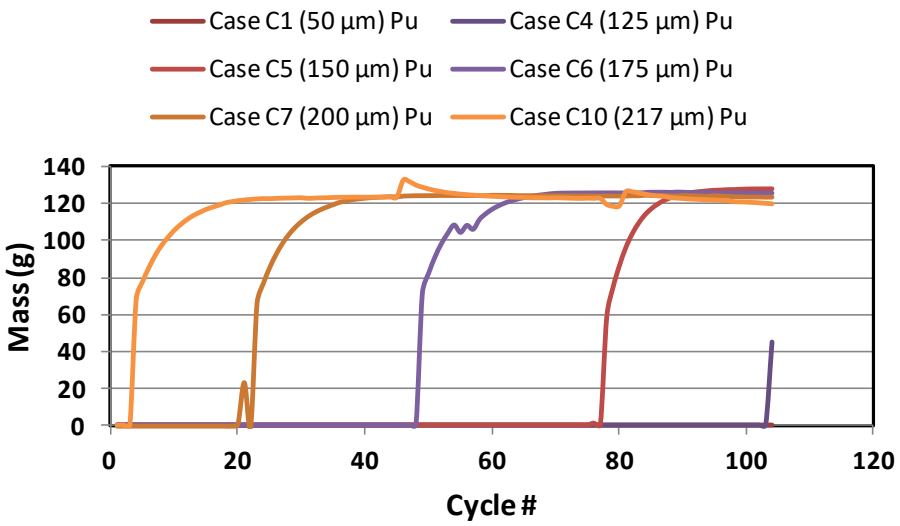

Figure 53- Long Term Pu Cathode Data for C Derived Cases (Cathode Rotation Rate Variation)

For case B derived cases, no codeposition occurred at any point and thus results are not depicted here. This demonstrates that even at high diffusion layer thicknesses and thus slow rotation rates that codeposition did not occur as a result of this failure mode alone. It instead requires internal conditions such as high Pu concentration or current to occur. Case D results illustrate that the slower the rotation rate, the greater the deposition mass of Pu at the initial run and with it the longer it takes before it converges around 20 grams deposited per run seen in the base case. In all cases, a faster rotation rate did not cause codeposition, leading to the classification of a Class III severity failure in the FMEA worksheet.

Figure 54 shows the long-term salt concentration results for C derived cases. Appendix B contains results for A and D derived cases. The changes in salt concentrations reflect the trends already determined for cases in which codeposition occurs as well as those where it does not occur for the results of cases derived from base cases A and C. The diffusion layer thickness has no effect on the rate at which the U

decreases or the Pu increases as the amount being removed is the same and the current is the same. All allow for trends to be developed within systems codes for use in determining safeguards significance.

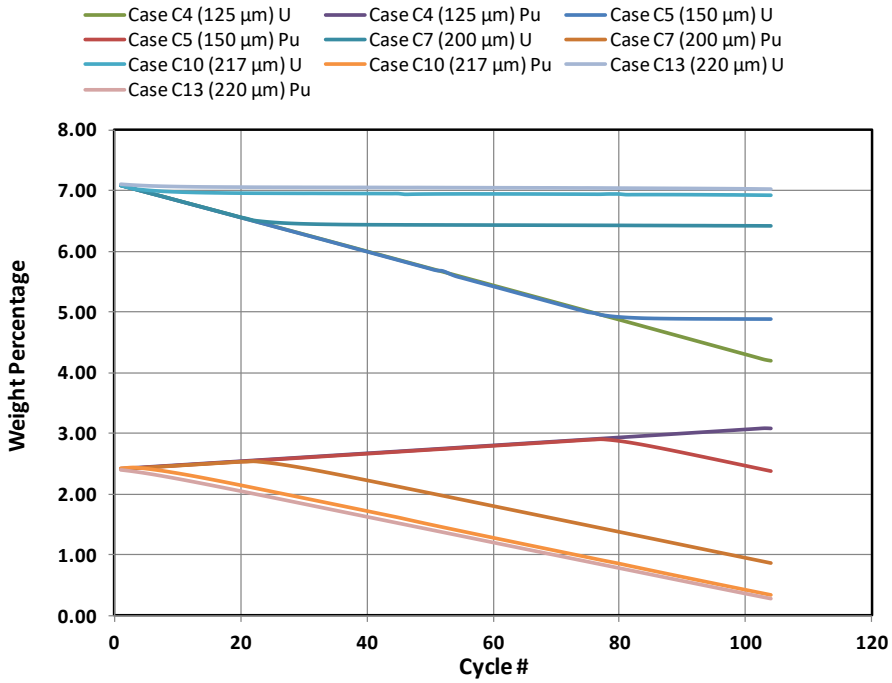

Figure 54- Long Term Salt Data for C Derived Cases (Cathode Rotation Rate Variation)

Figure 55 shows cathode potential results for simulations derived from base case C. Appendix B contains the results for D derived cases. The potential results all demonstrate trends expected from previous simulation as well as theory. Though not shown, the A results show expected trends. Those cases that never have codeposited Pu involve a steady decrease in potential, never reaching that of reduction Pu at the cathode. Those cases that have delayed codeposition have a rapid decrease to the potential at which reduction of Pu will occur, with a slower decrease after codeposition occurs. Finally, the cases that begin with codeposition show a slight increase in potential before the potential decreases continually as operation continues all at or below the Pu reduction potential.

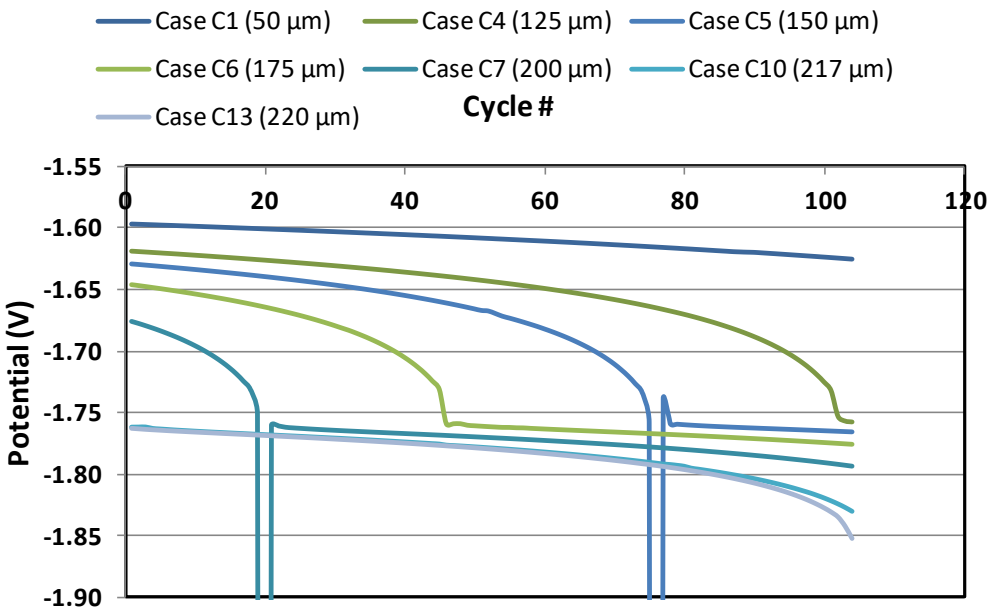

Figure 55- Cathode Potential Results C Derived Cases (Cathode Rotation Rate Variation)

6.3 Conclusions

From the whole of the ERAD results, several overarching themes have been identified. The first is that an FMEA approach is an effective tool to determine what failure modes can occur and can assist in the introductory steps of event identification for SBS. Most of the failure modes postulated within the FMEA pose safeguard significant effects depending on the conditions of the ER operation, especially given that no flush out or clean-up of salt is occurring over a four-month period. The only postulated failure mode that did not possess a significant effect was that of a decrease in anode rotation rate due to failure in the anode motor. The remainder of the simulated failure modes all provided circumstances, that given a facility expected mass flow, could generate a false alarm.

The most notable failure mode cases were from and A and C derived cases where the current was higher and thus more susceptible to impact of slight parameter variations over a long period of time. They are also important to note that high currents would be a feature of any engineering or industrial scale facility. The current imposed here reflects that of engineering scale facility, given the total throughput needs of each cycle in terms of mass of U deposited at the cathode and removed from anode. Case B is a much lower current than what would most likely be expected in an actual facility. This is not as susceptible to many of the failure modes presented, often not resulting in codeposition results as for higher current results. Case D is also not as an expected type condition as the results of Case C demonstrate that reaching the type of Pu/U ratio present is not likely as codeposition in most cases would occur before these types of ratios occur. This probability of occurrence type of scenario is something that is hard to determine as the salt would most likely be tested for constituency before addition and thus would require either a large sampling error or measurement error for it to occur.

Given this, the focus of importation and testing of data from a system's perspective leads to focusing on cases A and C. To do so, several considerations are made in order to import into a model like Echem-SSPM. The first is the manner in which it is imported. From results seen, linear relations are present for each cathode and anode. Thus, short-term data is derivable from the long-term data. Only long-term data is transplanted into the model's ER subsystems, inherent continuous commands in simulink can simulate the short-term linear relationship. Each failure mode or normal operation must be selected from the beginning of model simulation as data is only given a day 0 failure and is too computationally expensive to make the failure dependent by day given

the nature of the ERAD data. A Monte Carlo approach to multiple Echem simulations providing distributions for normal operation and failure mode operation with histogram type distributions is the most easily implementable choice for simulating the failure modes within Echem.

For the implementation, considerations of the assumptions Echem uses in modeling of the entire system, and the ER in particular, and how that compares to the assumptions of ERAD is necessary. Echem assumes a recycling of salt continuously within the operation based off of sampling the mass of the inputs of the ER. In addition, Echem model assumes that the ER posseses both an U and U/TRU cathode. These are two features that are not present within the assumptions of the long-term ERAD model and for importation; Echem must be altered to reflect this. This would involve a simplification where the model of the ER in Echem is a straight through process with just two outputs, U product and metal waste product with no salt removal over time from the ER itself. This assumes the operator replaces distilled salt in the ER and salt concentration does not change as a result within the ER. Making these alterations does not change that the evaluation of the mass balance or the impact of PM, the calculation of the ID within the safeguards subsystems just needs to be changed accordingly. With these alterations made and which will be detailed in the section discussing the systems model ERAD; imported functions can be handled within the Echem-SSPM model to evaluate the impact of failure modes on the system ID and SEID as well as the assistance that SBS provides in reducing these values.

CHAPTER 7: SSPM ECHEM SIMULATIONS FOR DETERMINATION OF EFFECTS OF ER FAILURE MODES

With failure modes simulated at the ER level, I performed additional analysis to determine the effect of the failure modes on the entire system. This additional analysis was to investigate the hypothesis that a disruption due to failure mode can have a negative effect on the overall mass balance of the facility. Thus, I perform SSPM Echem simulations with ERAD ER data to determine if these effects on the mass balance are viable. This chapter details the requirements to import this data as well as simulated results of three different simulation studies involving the modified SSPM Echem model to determine the effects of various failure modes, the mass balance period, and U product measurement uncertainty on the U and Pu SEID of the system.

7.1 ECHEM SIMULATION METHOD

To integrate simulation results from ERAD into SSPM Echem, several modifications needed to be made to the SSPM model to integrate the ERAD results. The next subsections detail the adjustments made to SSPM to use the ERAD results and the testing of the ER subsystem to determine if the data from ERAD had been integrated properly.

7.1.1 MODIFICATIONS OF SSPM

The first major modification to the SSPM was the simplification and scaling down of the model to match that of the assumptions of ERAD. The first step was reducing the total number of unit operations in the SSPM. To do so, the tail end processes for salt treatment and recycling were removed as these stages were not include in the long term ERAD simulations. In addition, the U/TRU output stream, representing the LCC), was

removed as the ERAD simulations assumed that a U cathode was the only location of product removal from the ER. All of the associated mass measurements with these unit operations were removed from the subprograms calculating the NMA and PM mass balances.

In addition to modifications of the flowsheet, changes were made to the streams/signals of mass transport within the model. The first change was the reduction of the number of mass streams. Echem SSPM was developed to track 99 elements plus the mass of the salts. To simplify the model this was reduced to the 10 elements from the ERAD simulations and the bulk salt mass was not treated as an input. The input source was changed from a 1x100 vector to a 1x10 vector and the mass of the source was changed to match the anode basket input from the ERAD simulations. Also, the initial ER salt mass was changed to be the initial salt composition from ERAD for each derived case. The anode basket source terms were pulsed every 28 time units to simulate the long term cycle assumptions of the ERAD model.

The final modification of the SSPM was the reprogramming of the ER subsystem to accommodate the results from the ERAD simulations. Whereas the subsystem originally consisted of the input and salt streams passing through a number of gain blocks to simulate separations within the ER, the subsystem in this case was reduced to a MATLAB subprogram that outputted pulsed masses derived from the ERAD results. These were then subtracted from the total salt mass of the ER and passed to product processing stages for outputs at the end of each simulated ER operation. How I modeled these ERAD results will be expounded upon further in the next section. The differences

between the systems models are seen in Figure 56 and Figure 57 and the differences in the ER subsystem modeling are seen in Figure 58 and Figure 59.

7.1.2 ERAD RESULTS INTEGRATION

The ER model is programmed in MATLAB as a function and integrated into the SSPM Echem model using multiple inputs and producing several key outputs. For inputs, the ER subprogram has three: simulation time, an input mass signal, and what is known as a mode signifier. The simulation time is the overall simulation time of the system and is produced by a simulation time source block from the Simulink library. The mode signifier is a three-digit numeric signifier programmed by the input file into the MATLAB workspace that is called by a constant source term block in the Echem SSPM. The failure mode or mode of normal operation is indicated by this numeric identifier. The input mass signal is more complex than the other two inputs. When the mass from the source term enters the ER subsystem block, the signal splits into two equal signals. One of the signals is integrated and added to the current salt inventory. The other goes through a 24-hour delay followed by a relay block. If the signal of U mass is greater than 0.1 kg, then the relay block outputs a signal of 1, otherwise it is 0. This relay signal is multiplied by the ER inventory and this signal is the input to the ER subprogram.

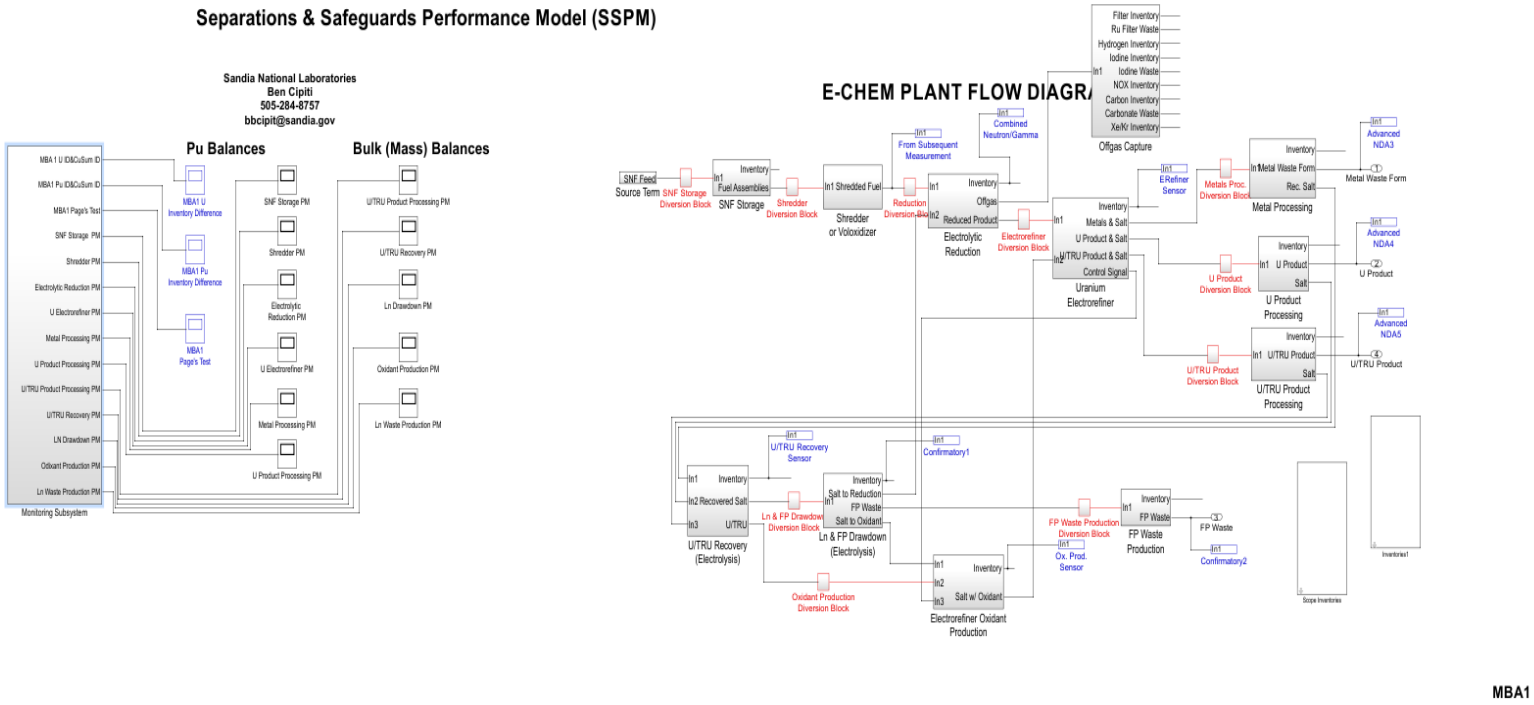

Figure 56-SSPM Flowsheet before simplification

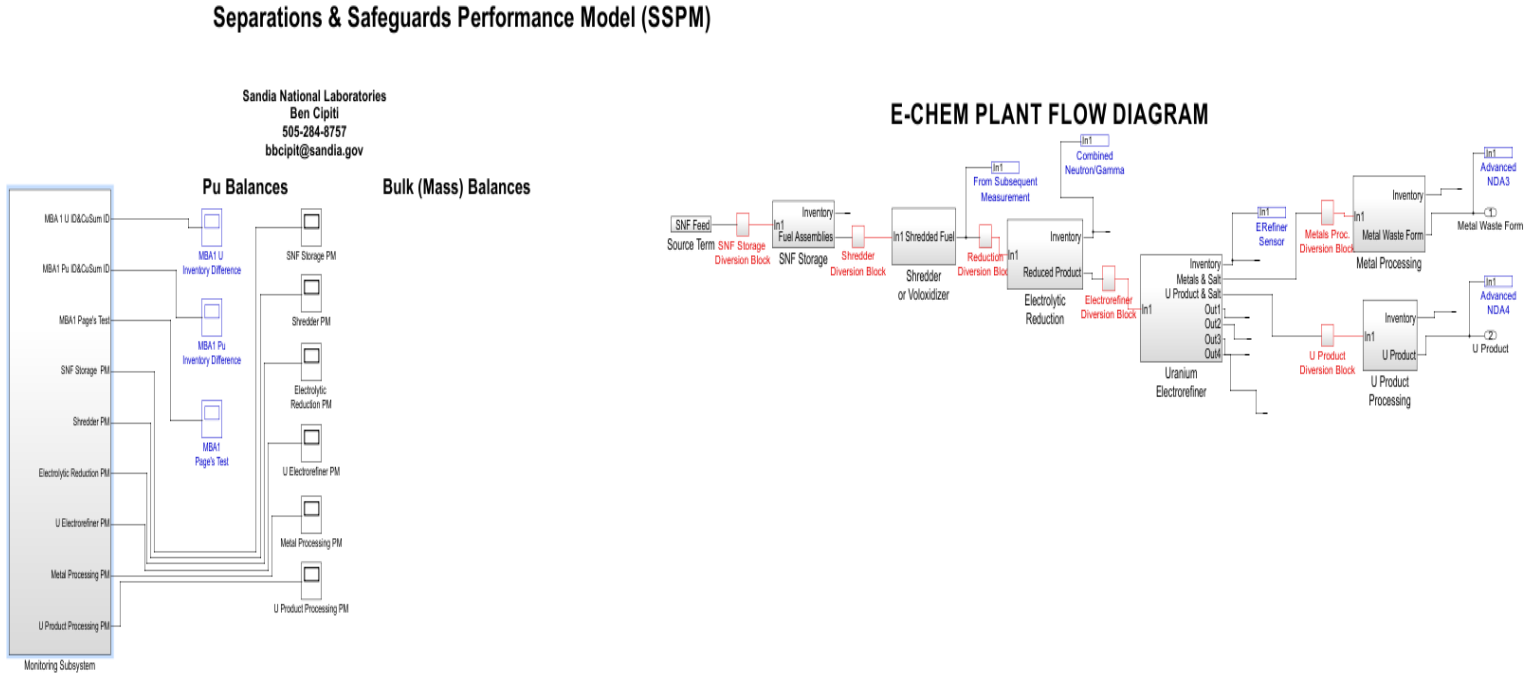

Figure 57-SSPM Flowsheet after simplification

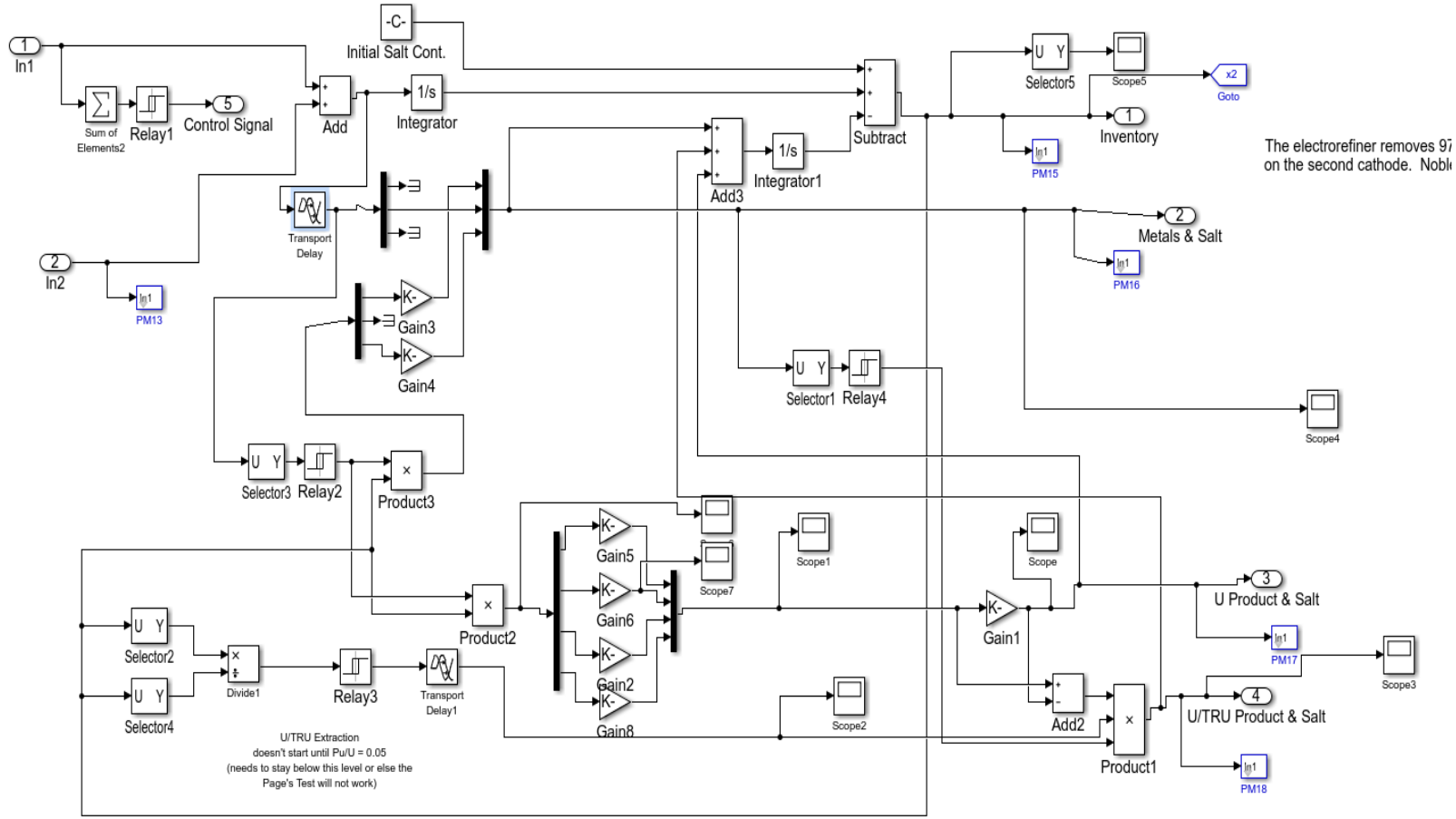

Figure 58-ER Subsystem before simplification

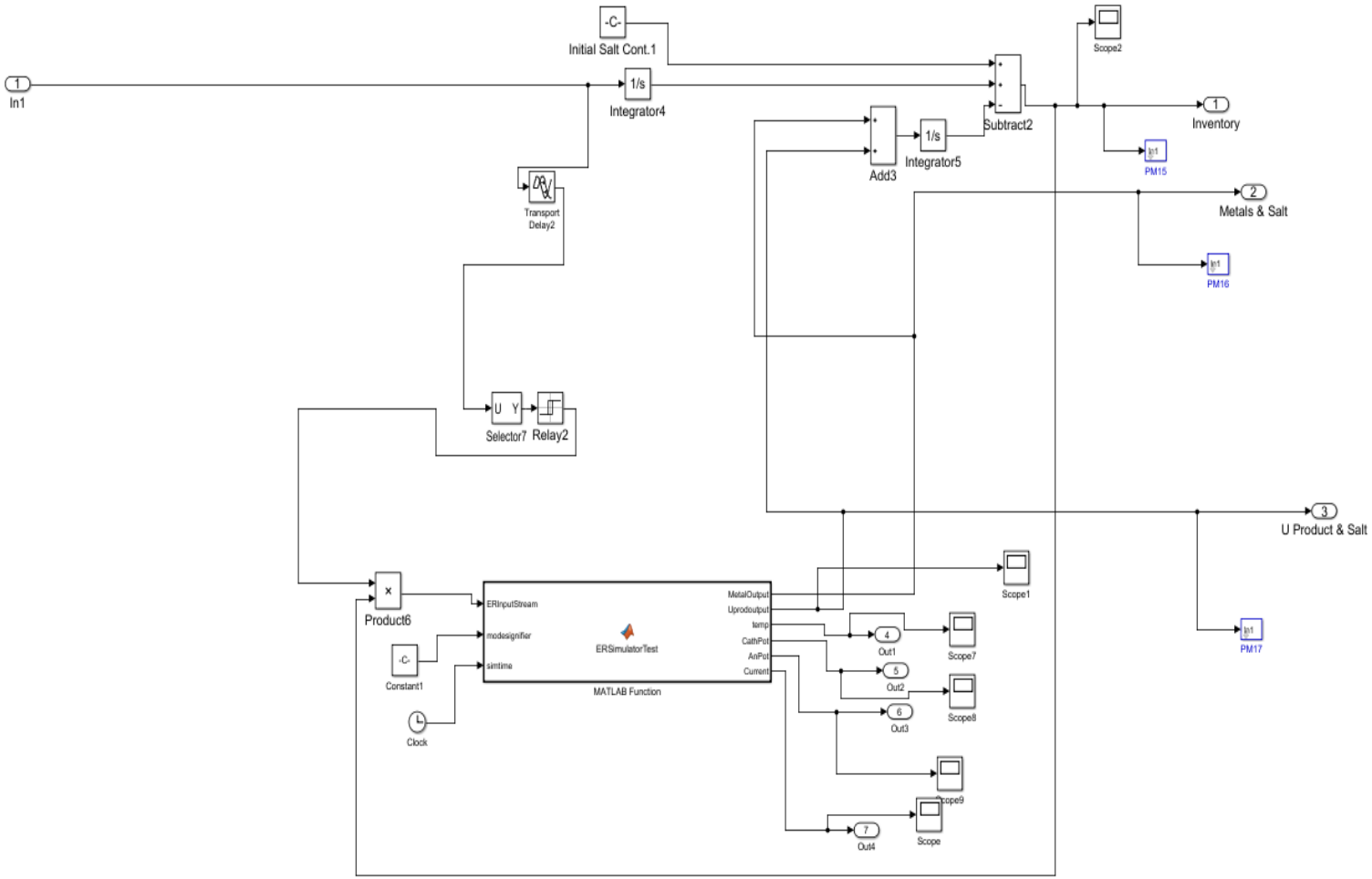

Figure 59-ER Subsystem after Simplification

In processing the three inputs, the subprogram performs several tasks. The first task is determining which operations cycle the system is on. This is performed by summing the delays of the unit operations of the facilities up to the ER and subtracting that number from the simulation time input. If this value is less than 0, then the cycle number is registered as 0. If it is greater than 0, it is divided by 28 and rounded to the next highest integer. This cycle is then used to calculate the outputs of the model as they are a piecewise function of cycle number. The subprogram is programmed with many different piecewise functions with ones used to calculate the outputs determined by the input case signifier. For each cycle calculation, the output calculated from the cycle number is zero if the sum of the input mass signal is zero, and is non-zero otherwise.

The output signals are of two different types, mass signals and measurement signals. The mass signals are the U product output and metal waste output. The metal waste output is the remains of the anode basket after dissolution. The U product is the cathode product. Both have been developed as a function of cycle number in previous ERAD simulations and thus the output is calculated from trends developed there. The outputs are one time unit wide pulses of the output masses from the ERAD simulations that are only outputted when the input mass signal is greater than zero. The reason for this output width is the integral is equal to the calculated cathode and anode masses from the ERAD calculations. These output signals are split into two separate streams, one is subtracted from the ER inventory and the other is sent to its associated processing stage outside the ER subsystem. Measurement data simulated in ERAD, such as current and potential, are also functions of cycle number and are outputted from the ER subprogram as measurement signals.

After each case has been programmed into the subprogram with its own case identifier, each case was run for a time of 3000 time units to determine if the trends developed in ERAD were modeled properly in SSPM. In total 72 cases derived from the A and C cases were programmed into the subprogram and debugged in this fashion. The following plots demonstrating the data that was integrated in particular the salt stream in the ER as well as the cathode output of the ER. Figures 60, 61, and 62 show results representing the base case A with a U/Pu of 0.03 and an operating temperature of 500 C°. During this base case no codeposition of U and Pu occurs and there is a constant deposition of U at the cathode and transported into the salt from the anode.

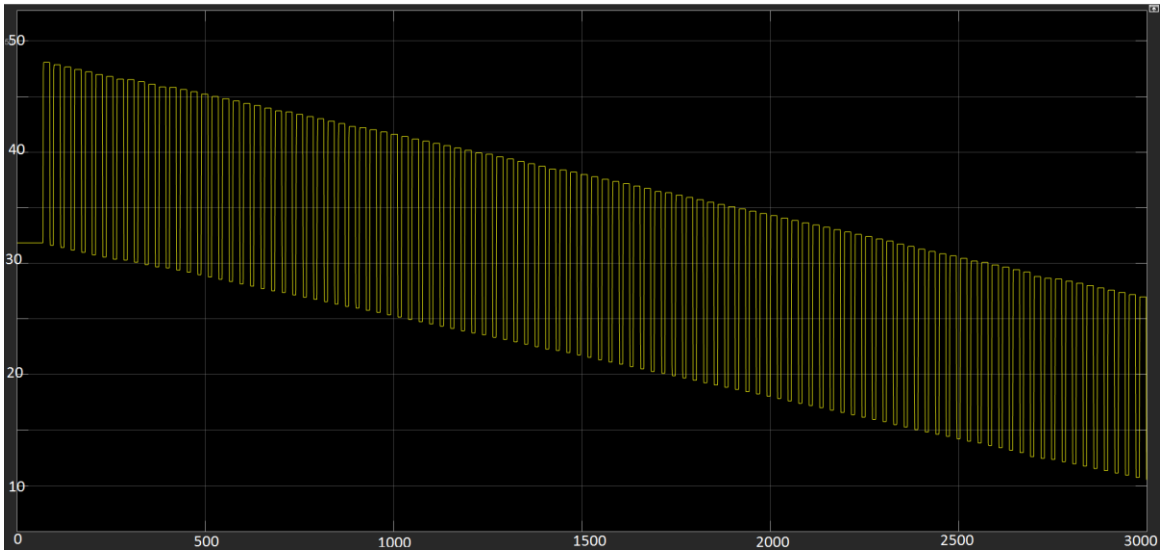

Figure 60- U Mass in Salt (kg) versus time (days) for Case A, 500 C°. (y-axis: Mass U (kg), x-axis: time (hours))

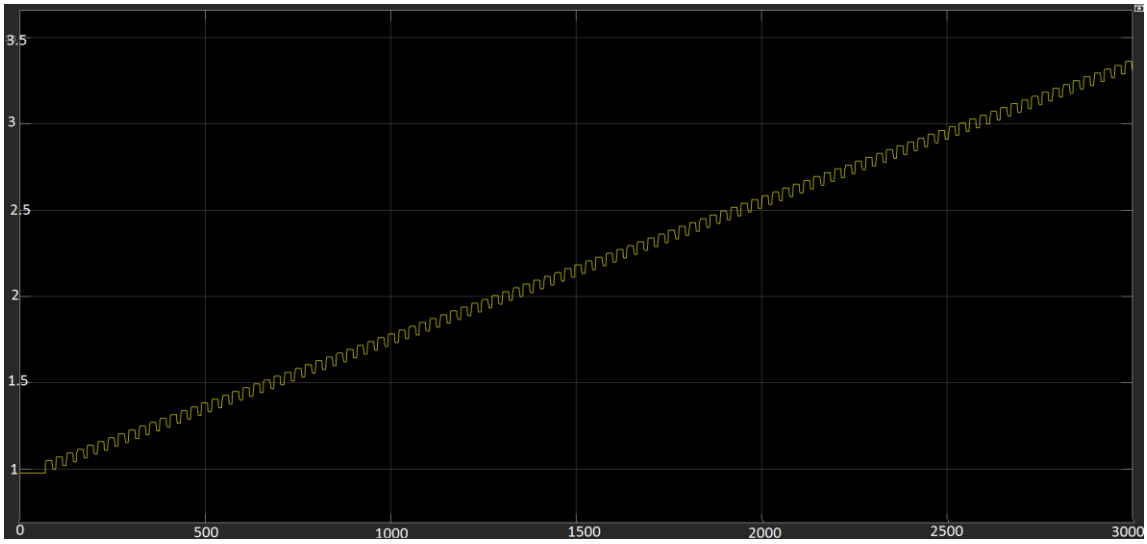

Figure 61- Pu Mass in Salt (kg) versus time (days) for Case A, 500 C°. (y-axis: Mass Pu (kg), x-axis: time (hours))

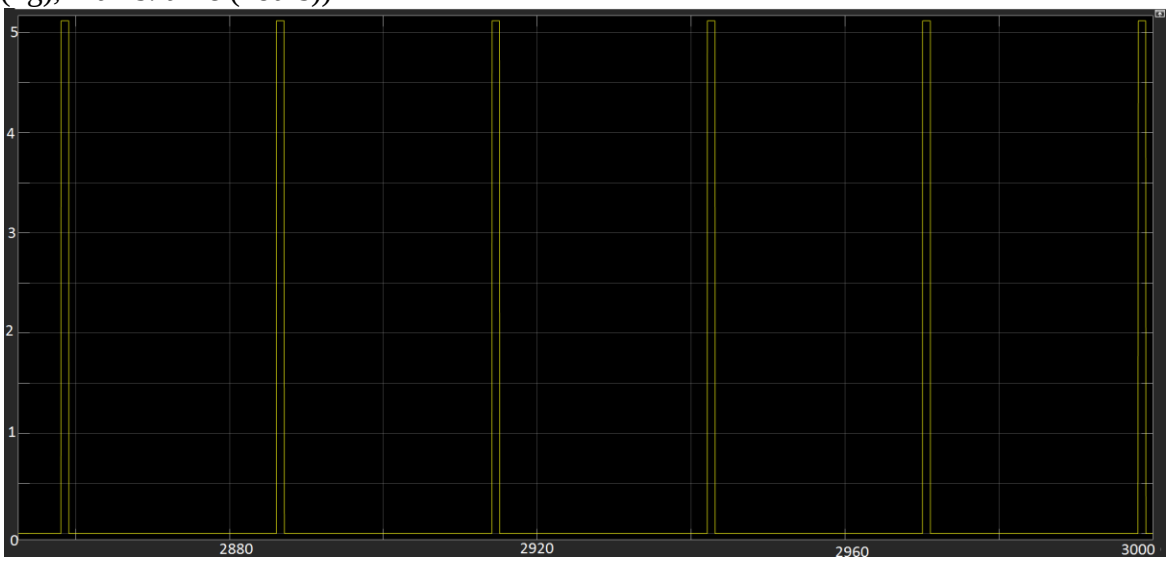

Figure 62-U Mass (kg) at Cathode output between times 2850 hours and 3000 hours (y-axis: Mass U (kg), x-axis: time (hours))

The figures illustrate that the mass in the salt versus time matches what was predicted by the ERAD runs in Chapter 6. U mass decreases at constant rate from the beginning of operation to the end while Pu increases at the same constant slope. The cathode behaves as a single pulse of width of one hour and a height of the mass of deposition from ERAD data which can then be subtracted from the salt mass along with anode mass to generate the results seen in Figures 60 and 61Figure 60.

Figures 63-66 shows results for Case A U/Pu ratio with an operating temperature of 460 C°. In this case, codeposition of U and Pu at the cathode occurs at cycle 85 and continues the remainder of the operation.

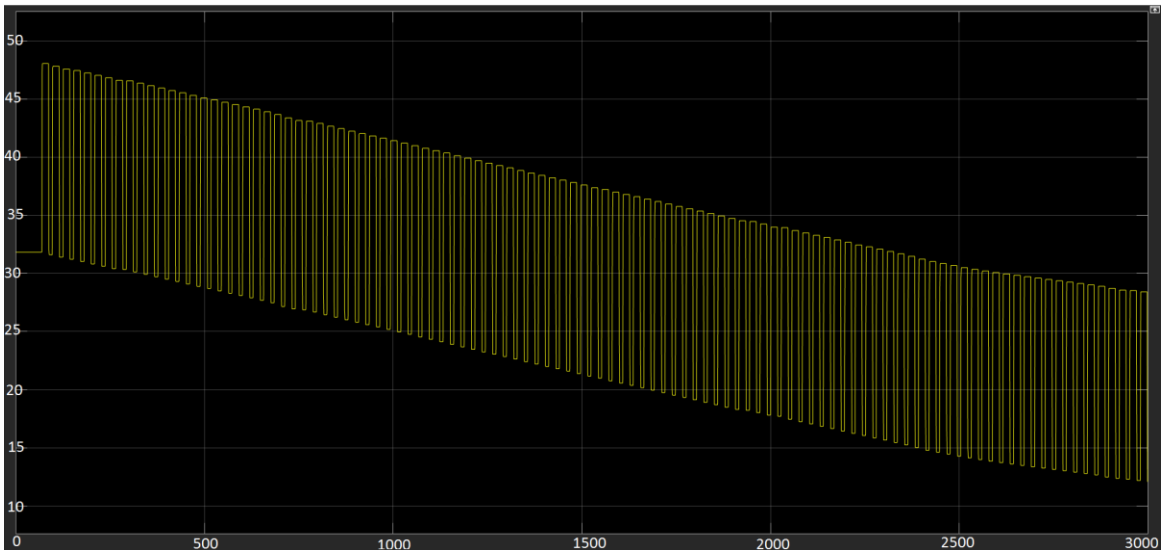

Figure 63- U Mass in Salt (kg) versus time (days) for Case A, 460 C°. (y-axis: Mass U (kg), x-axis: time (hours))

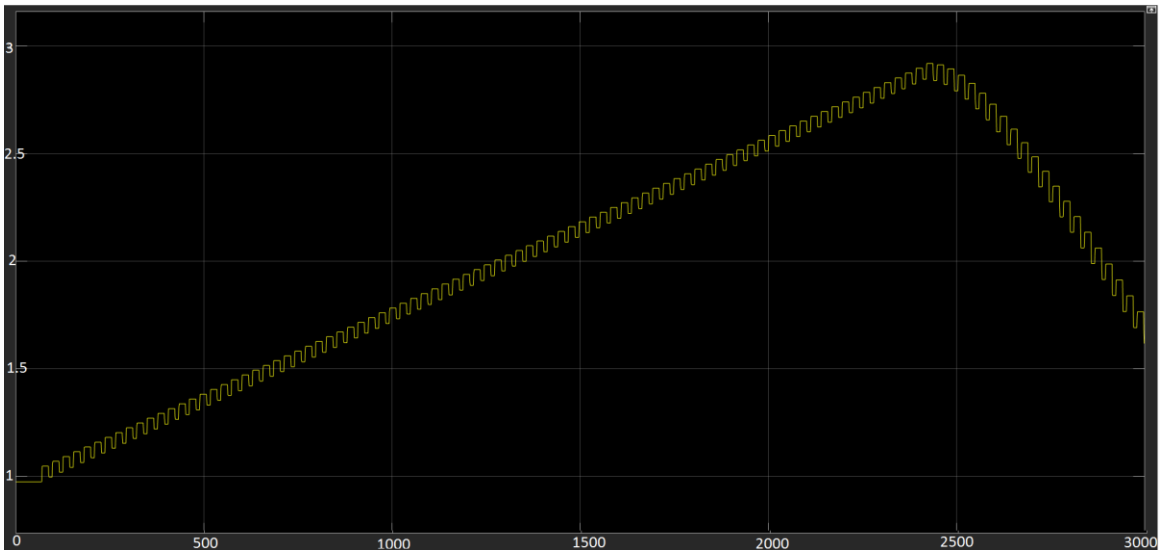

Figure 64- Pu Mass in Salt (kg) versus time (days) for Case A, 460 C°. (y-axis: Mass Pu (kg), x-axis: time (hours))

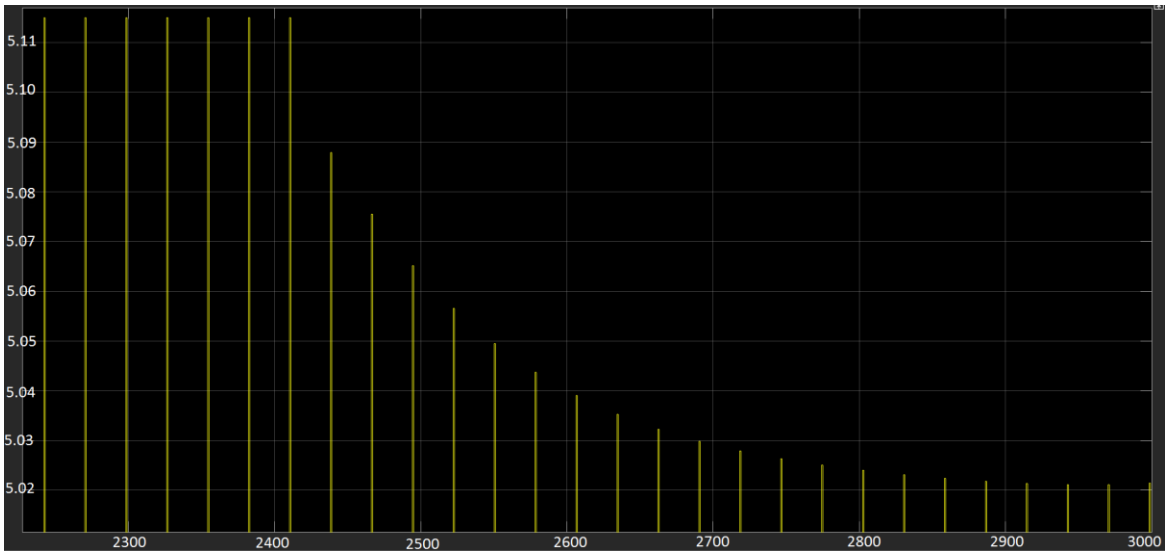

Figure 65- U Mass (kg) at Cathode output between times 2250 hours and 3000 hours for Case A, 460 C°. (y-axis: Mass U (kg), x-axis: time (hours))

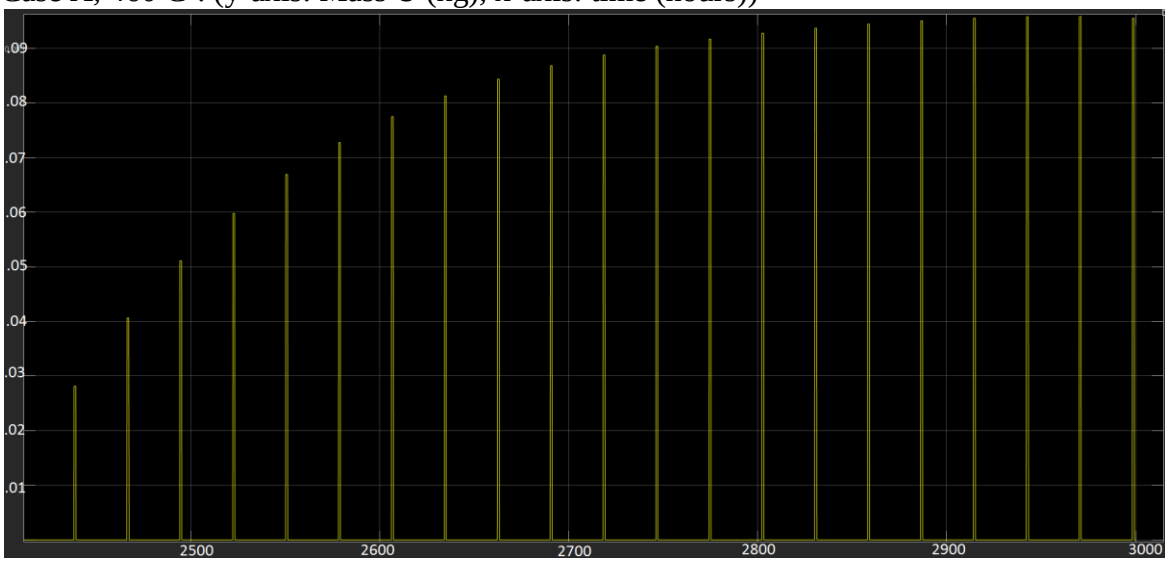

Figure 66- Pu Mass (kg) at Cathode output between times 2400 hours and 3000 hours for Case A, 460 C°. (y-axis: Mass Pu (kg), x-axis: time (hours))

The figures illustrate that ER subsystem models the expected trends from ERAD. The U mass in salt decreases at a constant rate until the codeposition of U and Pu occurs at the cathode resulting in the slope of the U mass in the salt to level out as less is transported out each step. Likewise, the Pu in the salt increases until codeposition occurs, at which point it decreases rapidly as it is removed via deposition at the cathode. In addition, the cathode depositions in the codeposition range, illustrated by Figure 65 and

Figure 66, demonstrate the mirror quality of the data predicted by ERAD showing that the piecewise fits properly model the ERAD data.

Figures 67-70 illustrate plots of the U and Pu in the Salt and deposited at the cathode after the start of codepositions for the base C case where Pu/U is 0.333, the current is 85 A, and the operating temperature is 500 C°. Codeposition of U and Pu begins at the cathode at operating cycle 73.

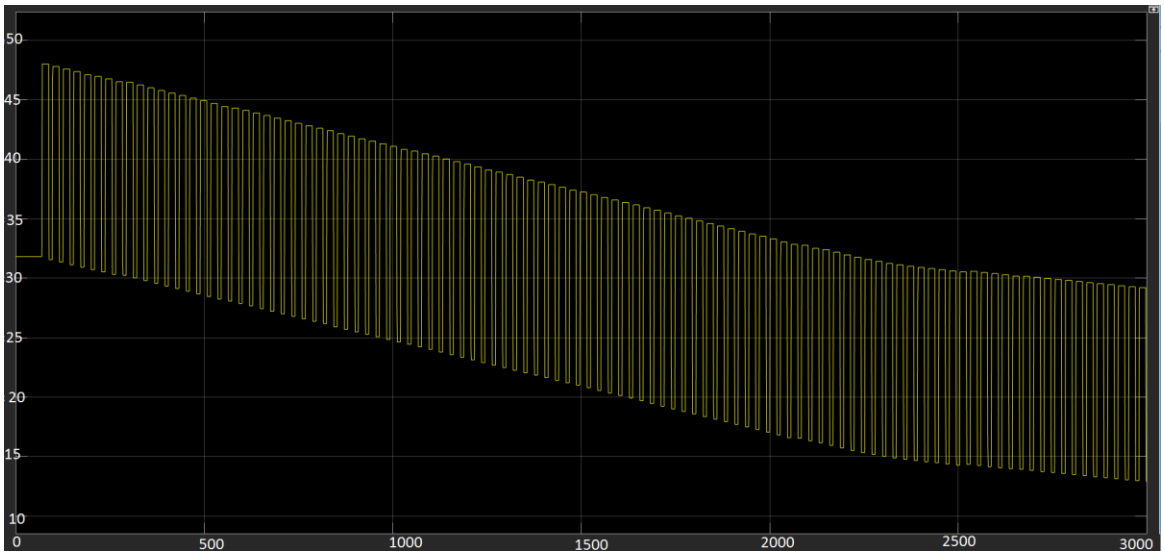

Figure 67- U Mass in Salt (kg) versus time (hours) for Case C, 500 C°. (y-axis: Mass U (kg), x-axis: time (hours))

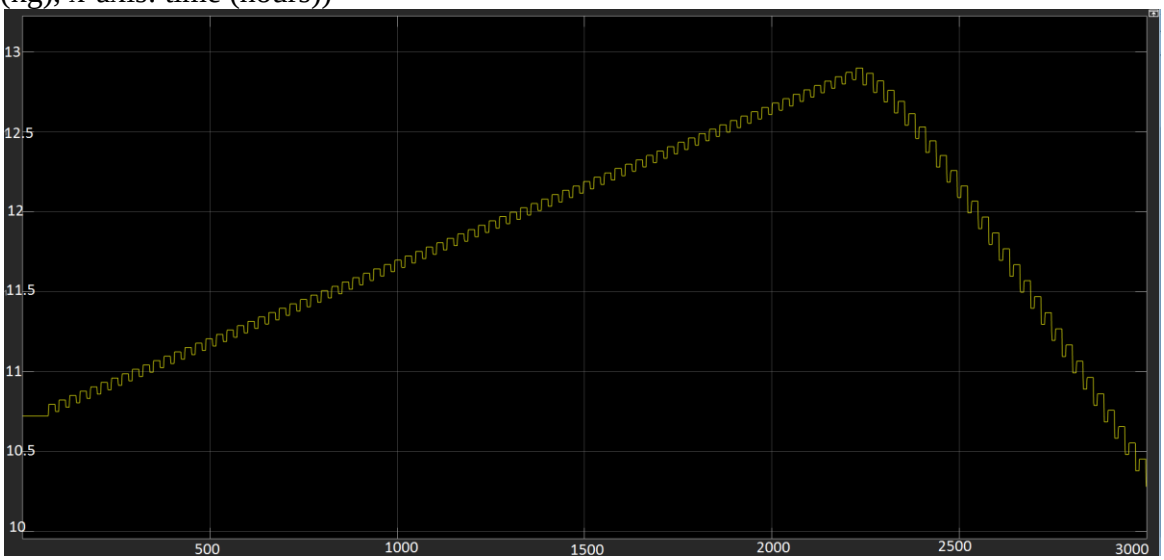

Figure 68- Pu Mass in Salt (kg) versus time (hours) for Case C, 500 C°. (y-axis: Mass Pu (kg), x-axis: time (hours))

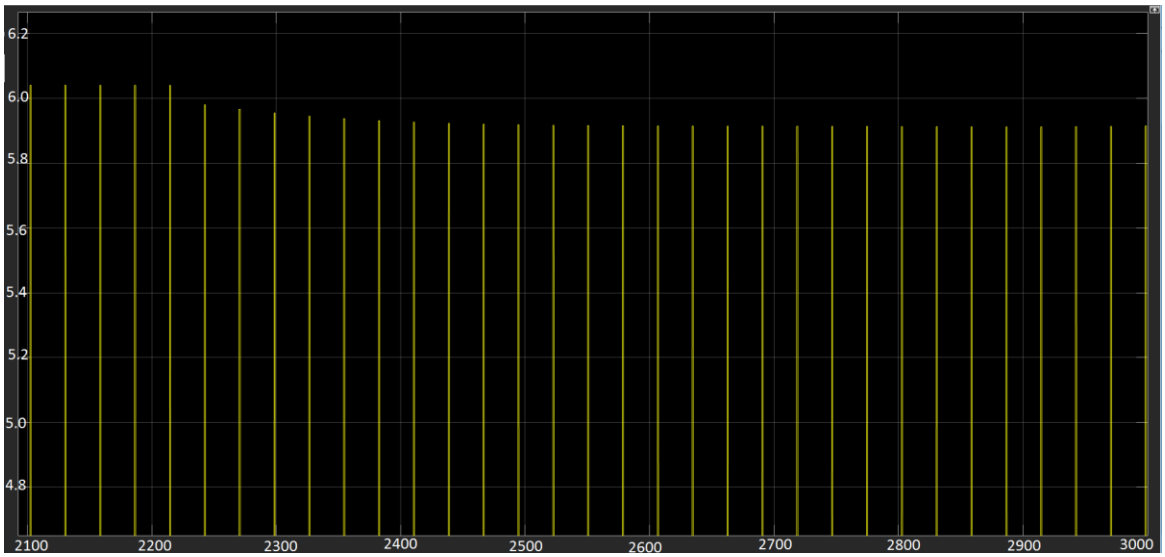

Figure 69- U Mass (kg) at Cathode between time 2100 and 3000 hours, 500 C° (y-axis: Mass U (kg), x-axis: time (hours))

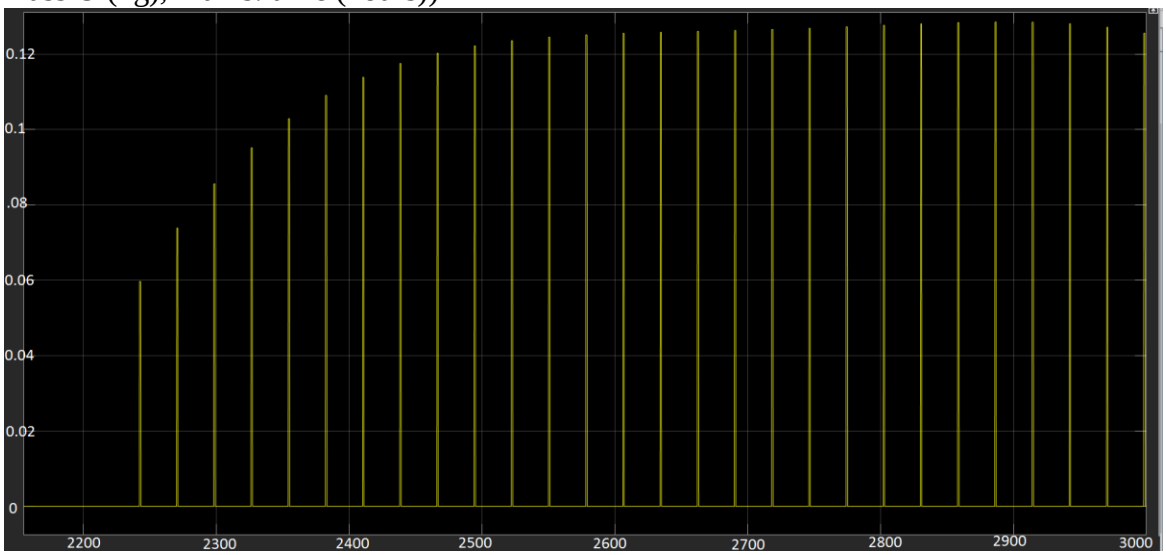

Figure 70- Pu Mass (kg) at Cathode between time 2100 and 3000 hours, 500 C° (y-axis: Mass Pu (kg), x-axis: time (hours))

These results demonstrate the same conclusions as previous results where the trends of salt masses follow what is expected from previous ERAD simulations verifying that the importation of ERAD data into the Echem model has been performed properly. The cathode codepositions mirror each other and add to the same total mass deposition in each case. The codeposition starts at the cycle that it is intended to illustrating that the

mechanism by which the simulation time is used to compute the cycle number for the imported ERAD results is properly programmed.

Figures 71-74 show the U and Pu in the salt as well as during codeposition at the cathode for the Case C operated at 460 C° with Pu/U of 0.333. Codeposition of U and Pu is to begin at operational cycle 24 of 104 and continued throughout as calculated by ERAD.

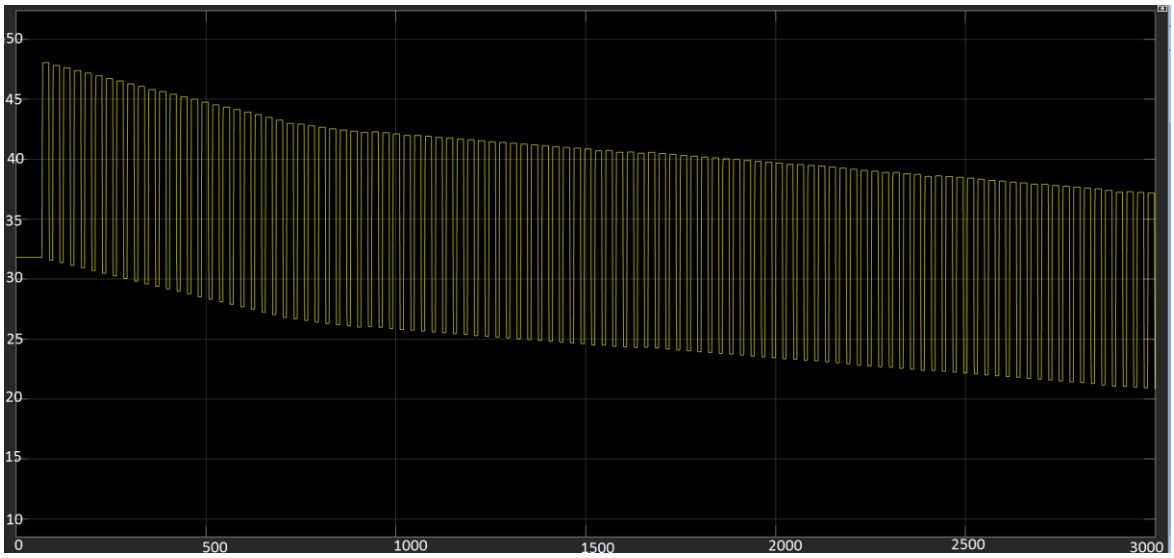

Figure 71- U Mass in Salt (kg) versus time (hours) for Case C, 460 C°. (y-axis: Mass U (kg), x-axis: time (hours))

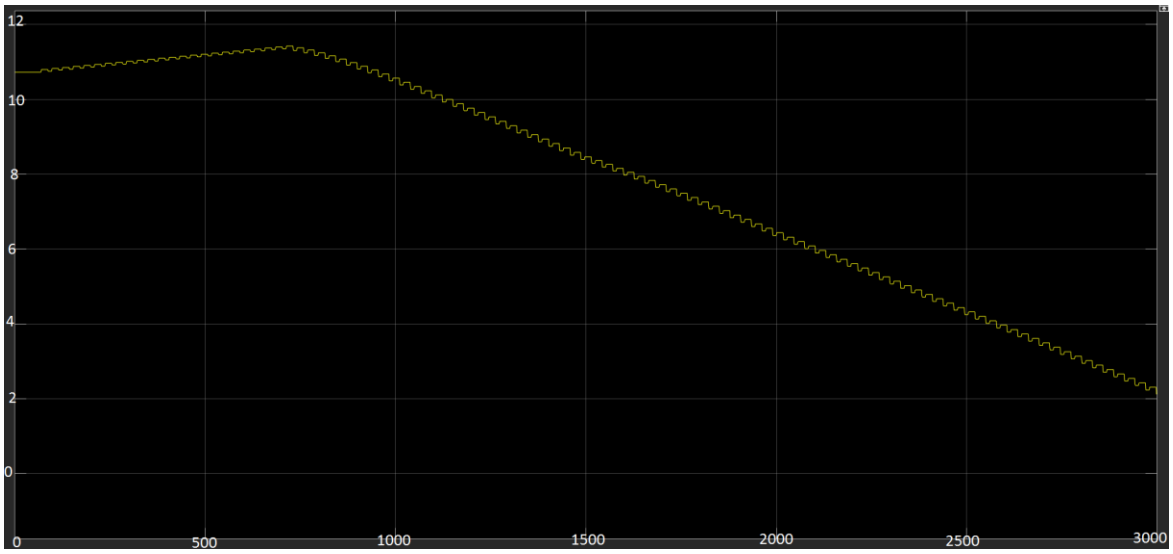

Figure 72- Pu Mass in Salt (kg) versus time (hours) for Case C, 460 C°. (y-axis: Mass Pu (kg), x-axis: time (hours))

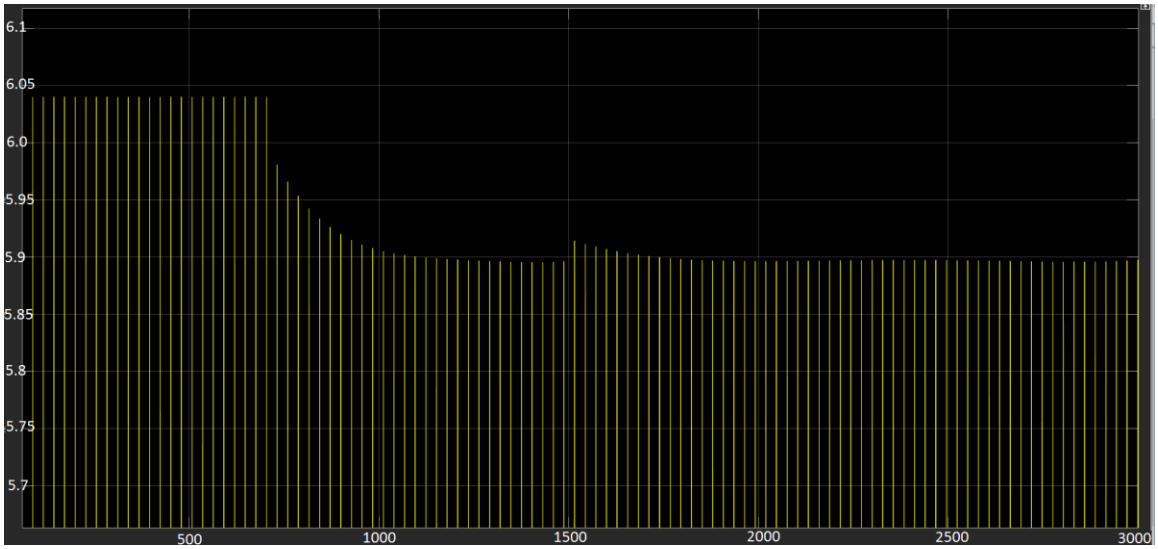

Figure 73- U Mass (kg) at Cathode between time 0 and 3000 hours 460 C° (y-axis: Mass U (kg), x-axis: time (hours))

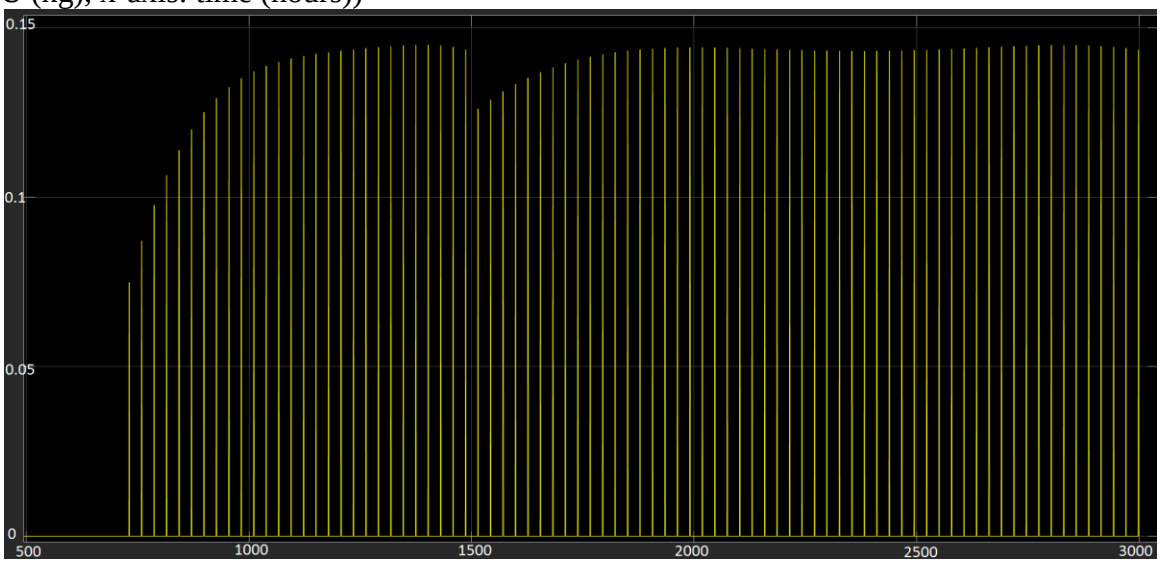

Figure 74-Pu Mass (kg) at Cathode between time 0 and 3000 hours, 460 C° (y-axis: Mass Pu (kg), x-axis: time (hours))

The plots of Figures 71-74 illustrate that failure modes can be called with their identifiers by the ER submodel. This is depicted by the behavior of the model that matches the failure mode in the time at which codeposition behavior occurs. Like the previous sets of data both salt and cathode outputs reflect the expected outputs from previous ERAD simulations.

7.2 Simulation Campaigns Involving Modified Echem SSPM

With the modified Echem and verified ER subsystem, three separate simulation campaigns were undertaken to determine the effects of the programmed failure modes, product measurement uncertainty, and NRTA balance period duration on the total system U SEID and Pu SEID. This was performed by running the model for 3000 time units, one hundred times for all investigations. The time units of these simulink simulations represent hours of operation in an actual facility. The results were collected for the calculated IDs and SEIDs. The mean and standard deviation of mean values for the ID and SEID are calculated over the total set of results for a given condition. The first of the simulation campaigns was a sensitivity analysis determining the effect of changes in the measurement uncertainty of the U product processing stage over a variable set of uncertainties. The second campaign was undertaken to determine the effects of the failure modes on the SEIDs for the system. The third campaign determined the effect of the length of the NRTA period on the effects on the system developed. This section details the results of these simulation campaigns.

7.2.1 U Product Measurement Uncertainty Sensitivity Analysis Results

For the product measurement uncertainty sensitivity analysis, a test matrix was developed and performed on both base cases A and C for each combination of uncertainties. Base case A is the case in which 72 A of current are passed and the Pu/U ratio is 0.03. Only U deposits at the cathode and proceeds to the U product processing stage for all 104 cycles in case A. Base case C is the case where 85 A of current are passed with a 0.333 Pu/U ratio resulting in the long term of codeposition of Pu and U at

the cathode after 73 operational cycles resulting in 31 cycles with greater than 0.1 kg of Pu codepositing at the cathode. This product, containing both U and Pu in later stages, then proceeds to the U product processing stage. The details of the parameters used in the ERAD simulation that were transferred to Echem for cases A and C are shown in Table 24. The Pu/U ratios were altered to demonstrate the different starting salt concentrations that could be present in the ER at the beginning of the operation. A summary of the masses at the different locations within the ER for cases A and C are shown in Table 25 and Table 26, respectively.

Table 24- Details of Cases A and C

Run	A	C
Current (A)	72	85
Time (h)	24	24
Surface Area Cathode (cm^2)	1350	1350
Surface Area Anode (cm^2)	800	800
Anode Diffusion Layer Thickness (µm)	50	50
Cathode Diffusion Layer Thickness (µm)	150	150
Temperature (K)	773	773
Pu/U Ratio in Salt	0.03075	0.3368

Table 25- Summary of Mass Movement in Case A

Value	Mass (kg)	Cycle
U in Salt Start of Operation	32.5	0
U Deposited at Cathode	5.116	1-104
U remaining in Anode Basket	11.163	1-104
U in Salt End of Operation	23.6	End 104
Pu in Salt Start of Operation	1.02	0
Pu Deposited at Cathode	0	1-104
Pu remaining in Anode Basket	0.05	1-104
Pu in Salt End of Operation	3.36	End 104

Table 26- Summary of Mass Movement in Case C

Value	Mass (kg)	Cycle
U in Salt Start of Operation	31.7	1
U Deposited At Cathode	6.039	1-77
U Deposited At Cathode (Max for codeposition)	5.981	78
U Deposited At Cathode (Min for Codeposition)	5.912	104
U Remaining at Anode	10.25	1-104
U in Salt End of Operation	21.9	104
Pu in Salt Start of Operation	1.08	1
Pu Deposited At Cathode	0	1-77
Pu Deposited At Cathode (Min for Codeposition)	0.0582	78
Pu Deposited At Cathode (Max for Codeposition)	0.127	104
Pu Remaining at Anode	0.0459	1-104
Pu in Salt End of Operation	1.07	104

The variations for the analysis involved nine different cases varying both the systematic and random uncertainty of the U and Pu measurements for the U product processing inventory measurement known in Echem as Advanced NDA 4. Table 27 and Table 28 show the test matrices performed.

Table 27- Test Matrix for Uncertainty Sensitivity Analysis for Base Case A (72 A, no Pu codeposition)

Case	U Syst σ	U Rand σ	Total U σ	Pu Syst σ	Pu Rand σ	Total Pu σ
A-1	0.01	0.01	0.02	0.01	0.01	0.02
A-2	0.01	0.03	0.04	0.01	0.03	0.04
A-3	0.03	0.01	0.04	0.03	0.01	0.04
A-4	0.03	0.03	0.06	0.03	0.03	0.06
A-5	0.03	0.05	0.08	0.03	0.05	0.08
A-6	0.05	0.03	0.08	0.05	0.03	0.08
A-7	0.05	0.05	0.1	0.05	0.05	0.1
A-8	0.01	0.05	0.06	0.01	0.05	0.06
A-9	0.05	0.01	0.06	0.05	0.01	0.06

Table 28- Test Matrix for Uncertainty Sensitivity Analysis for Base Case C (85 A, Pu codeposition after cycle 73)

Case	U Syst σ	U Rand σ	Total U σ	Pu Syst σ	Pu Rand σ	Total Pu σ
C-1	0.01	0.01	0.02	0.01	0.01	0.02
C-2	0.01	0.03	0.04	0.01	0.03	0.04
C-3	0.03	0.01	0.04	0.03	0.01	0.04
C-4	0.03	0.03	0.06	0.03	0.03	0.06
C-5	0.03	0.05	0.08	0.03	0.05	0.08
C-6	0.05	0.03	0.08	0.05	0.03	0.08
C-7	0.05	0.05	0.1	0.05	0.05	0.1
C-8	0.01	0.05	0.06	0.01	0.05	0.06
C-9	0.05	0.01	0.06	0.05	0.01	0.06

Figures 75-78 show the results of these analyses to determine the effect of changes in the SEIDs versus total uncertainties. The results presented for U and Pu SEID are the SEIDs for the last 28 hour NRTA balance period of their respective A and C operations. Inspecting the results of the study, it can be determined that at least for the engineering-scale facility simulations being performed, only U SEID has sensitivity to the uncertainty of the U product measurement while the Pu value is not affected significantly by the change in uncertainty. The U SEID increases with increasing total uncertainty as would be expected due to increased uncertainty in one measurement within the sum of measurements that comprises the SEID of both U and Pu.

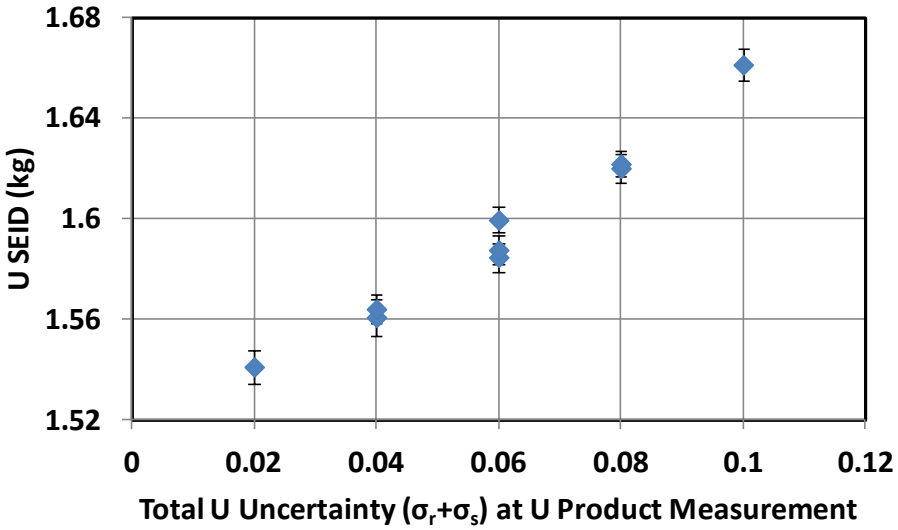

Figure 75- Sensitivity Study Results for U SEID in Base Case A

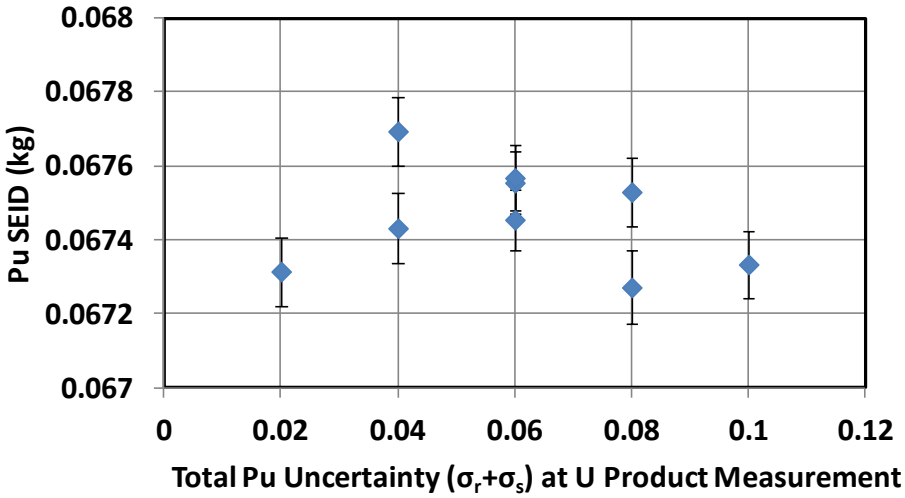

Figure 76- Sensitivity Study Results for Pu SEID in Base Case A

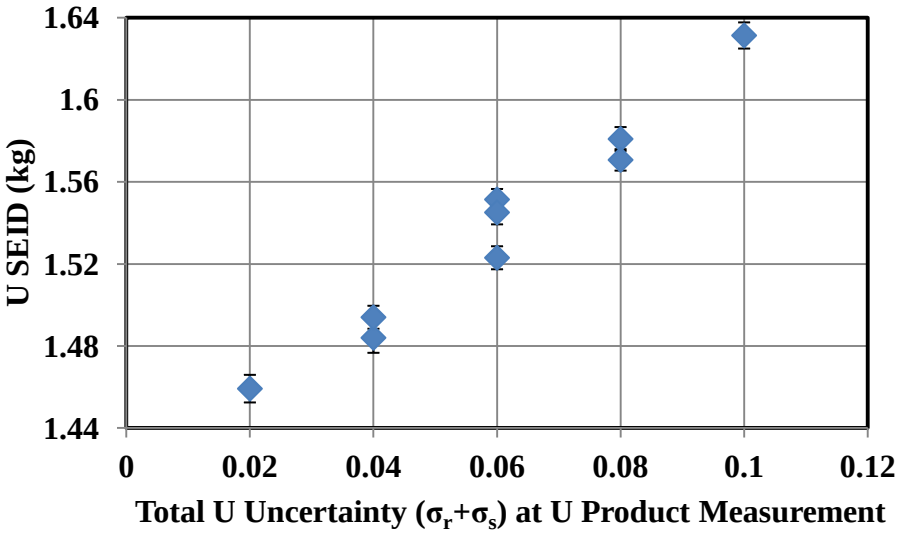

Figure 77- Sensitivity Study Results for U SEID in Base Case C

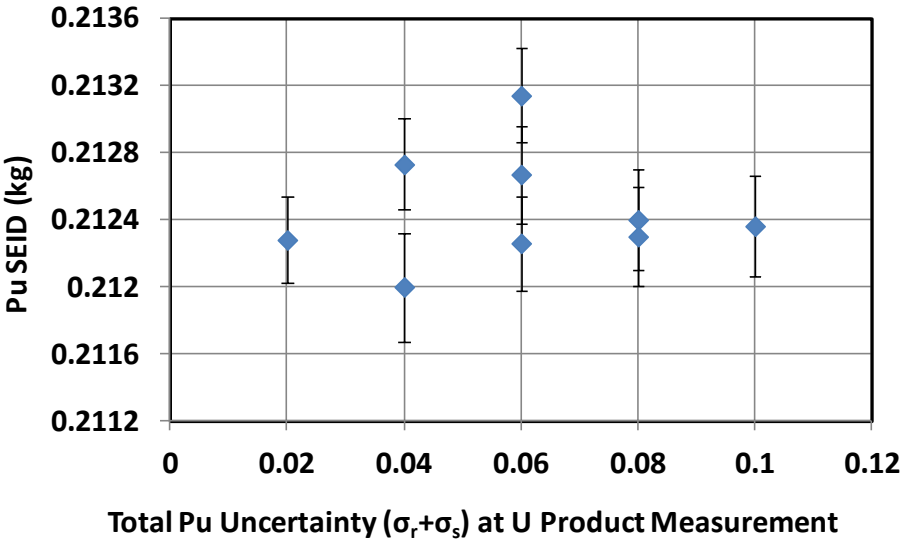

Figure 78- Sensitivity Study Results for Pu SEID in Base Case C

The effect on U SEID can be attributed to the difference in masses present and being transported through the system as well as the fact that majority of the mass measured resides in the ER. In addition, the ER contains the bulk of both U and Pu mass and thus dominates the calculation. Only U has enough mass to be transported out of the salt to make a difference when calculating the SEID. The amount of Pu product transported out versus the amount in the salt for when it codeposits is insignificant. Thus,

the change of measurements uncertainty has a significant effect on U SEID calculation, but not Pu SEID.

7.2.2 Failure Mode Effects Studies Results

The simulation campaign undertaken with regards to failure modes focused on multiple different cases derived from both the A and C bases cases. Table 29 and Table 30 show a summary of the parameters varied for A and C cases, respectively. These varied parameters were chosen to simulate a postulated failure mode that had been simulated in ERAD for the given parameter and imported into the modified Echem Model. The simulations in ERAD varied these parameters in the input deck while holding all others from the base case parameters constant. The values selected for Echem runs are the base case followed by those conditions that in ERAD led to codeposition or increased deposition of U. Each Echem run was run with cathode measurement uncertainties for Pu and U of 0.05 as well as random and systemic uncertainty in the U processing measurement also set at 0.05. The ER measurement uncertainty was 0.01 for both the random and systemic uncertainty of both Pu and U. This ER measurement uncertainty comes from past research in Echem SSPM. The past research dealt with the determination of safeguards measurement goals to ensure that detection needs are met. The report recommended that uncertainties be reduced to 1% or 0.01 for the ER [1]. The uncertainties for the cathode processor are set based off the study in the previous section. Echem SSPM studies indicated a need for at least 1% uncertainty for the U product measurement [1]. However, as my results from the previous section indicate that the uncertainties of 0.05 have no effect on Pu SEID and only a small effect on U SEID on this scale, the higher uncertainty is chosen as it would be an easier to attain this

uncertainty in an actual facility. The set uncertainties are summarized in Table 31. The end result was to determine the effect of the failure modes and their changed parameters that lead to codeposition on the SEID of the system.

Table 29- Base Case A Derived Failure Mode Test Matrix

Failure Mode	Parameter Varied	Value
Surge in ER Power Supply	Current	72, 75.6, 79.2 A
Partial ER heater failure	Temperature	500,465,460,45,,450 C°

Table 30- Base Case C Derived Failure Mode Test Matrix

Failure Mode	Parameter Varied	Value
Failure of Anode Retraction Linkage	Anode Surface Area	1350, 1300, 1200, 1100 cm^2
Partial ER heater Failure	Temperature	500, 490, 480, 470, 460, 450 C°
Failure of Cathode Retraction Linkage	Cathode Surface Area	800, 700, 575, 549, 547, 545 cm^2
Failure of Cathode Rotation Motor	Cathode Diffusion Layer Thickness	150, 175, 210, 217, 219 µm

Table 31- Uncertainties of Measurement Points

Measurement Point	U Random	U Stochastic	Pu Random	Pu Stochastic
Input	0.01	0.01	0.01	0.01
Electrorefiner	0.01	0.01	0.01	0.01
Cathode Product	0.05	0.05	0.05	0.05

The results for the A base case derived failure modes for both U and Pu SEID are seen in Figures 79-82. Results for base case C derived failure modes are seen in Figures 83-90. Like with the previously presented results, the SEID's presented are those of the last 28 hour NRTA balance period of operation.

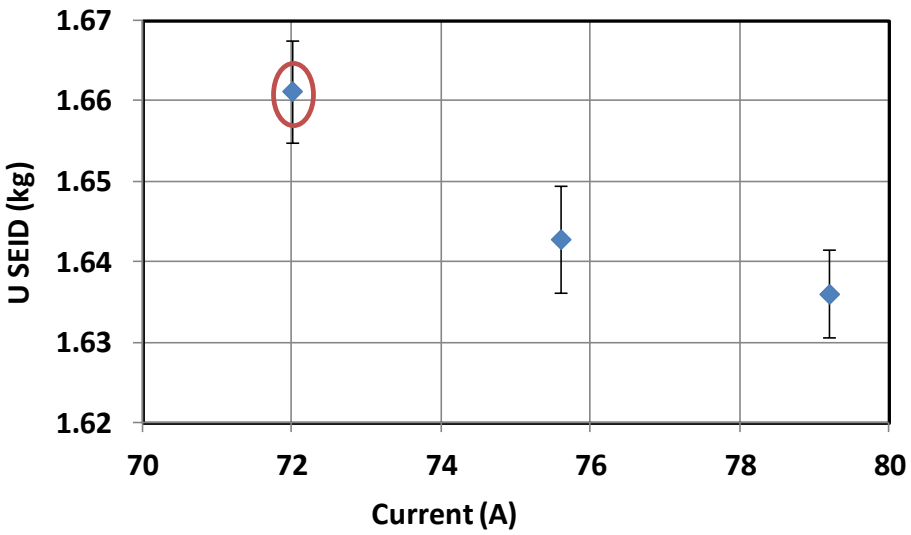

Figure 79- U SEID Surge in Power supply, A Derived Cases (Normal Operation Circled)

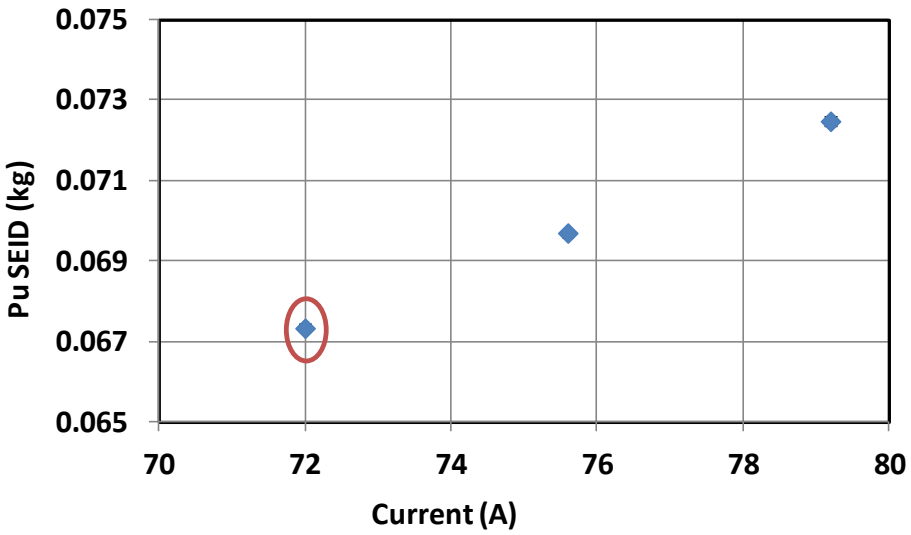

Figure 80- Pu SEID Surge in Power Supply, A Derived Cases (Normal Operation Circled)

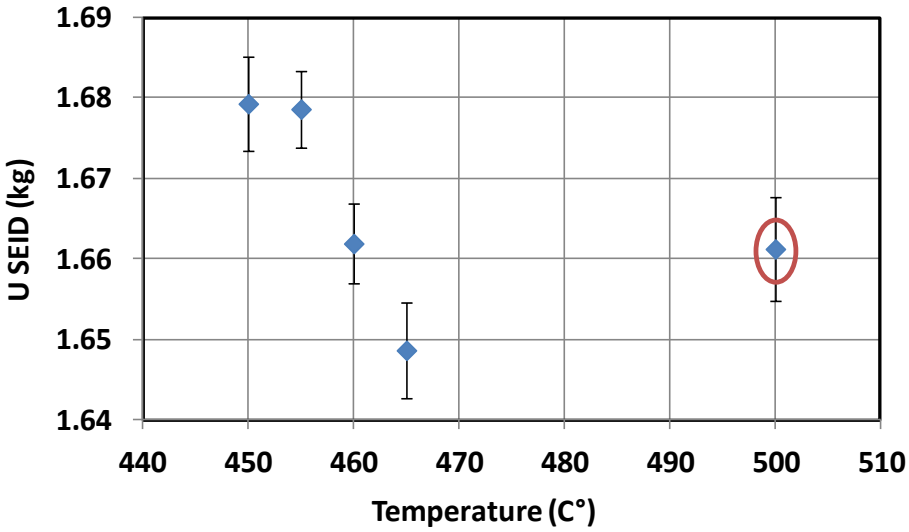

Figure 81- U SEID Partial Heater Failure, A Derived Cases (Normal Operation Circled)

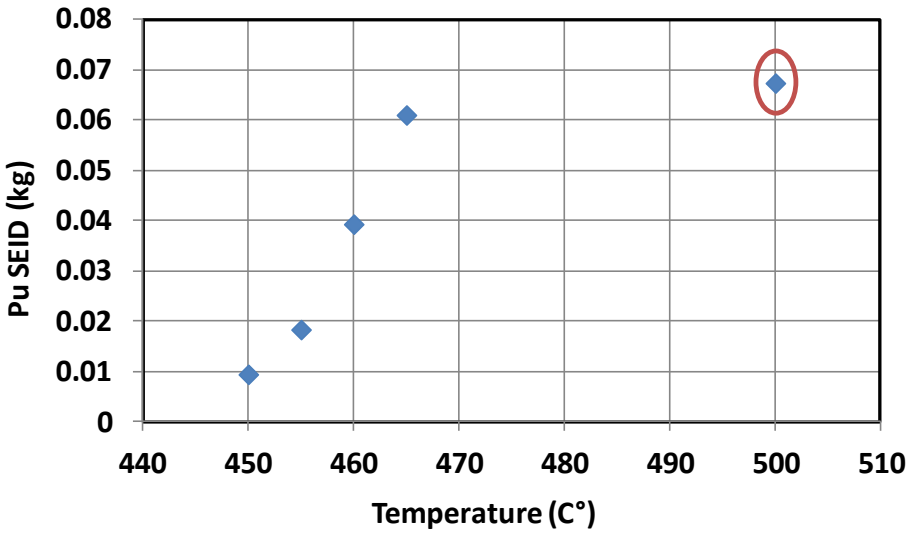

Figure 82- Pu SEID Partial Heater Failure, A Derived Cases (Normal Operation Circled)

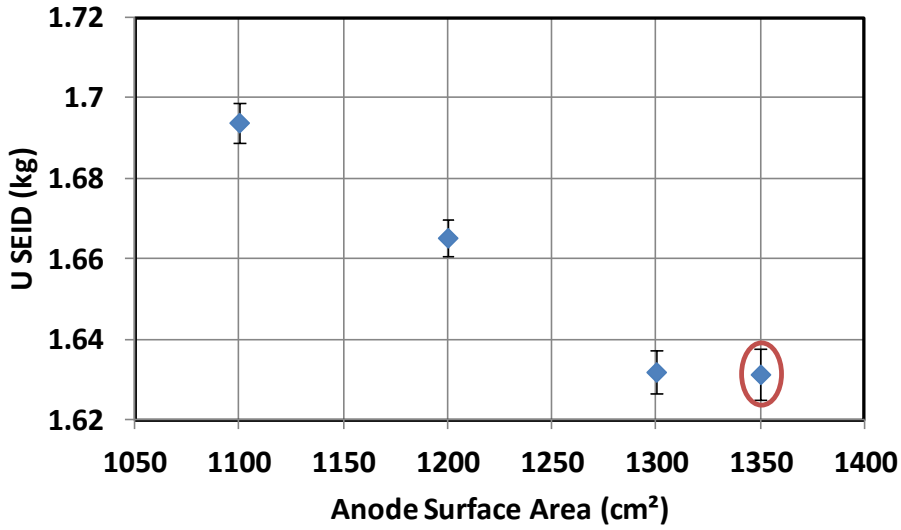

Figure 83- U SEID Anode Retraction Linkage failure, C Derived Cases (Normal Operation Circled)

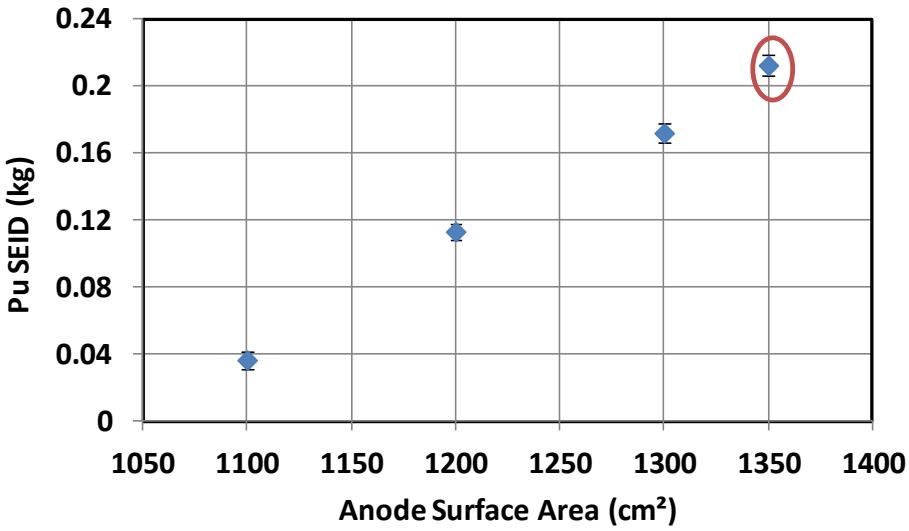

Figure 84- Pu SEID Anode Retraction Linkage Failure, C Derived Cases (Normal Operation Circled)

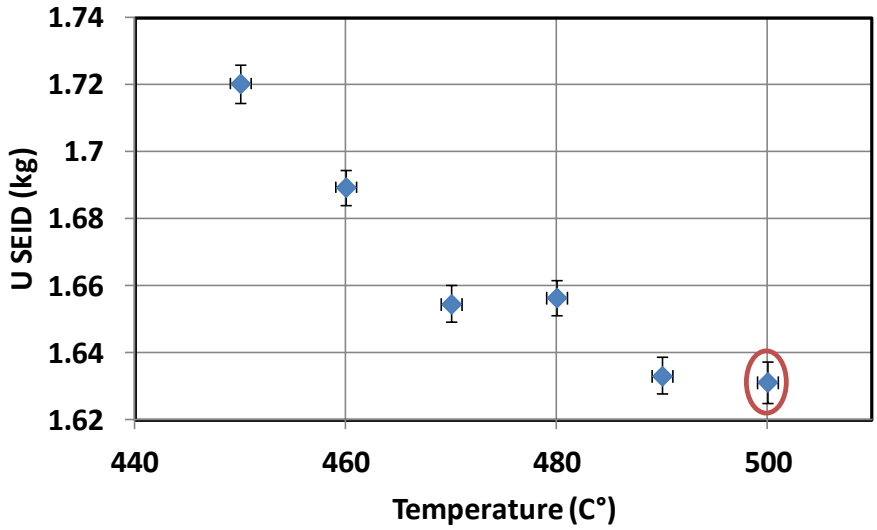

Figure 85- U SEID Partial Heater Failure, C Derived Cases (Normal Operation Circled)

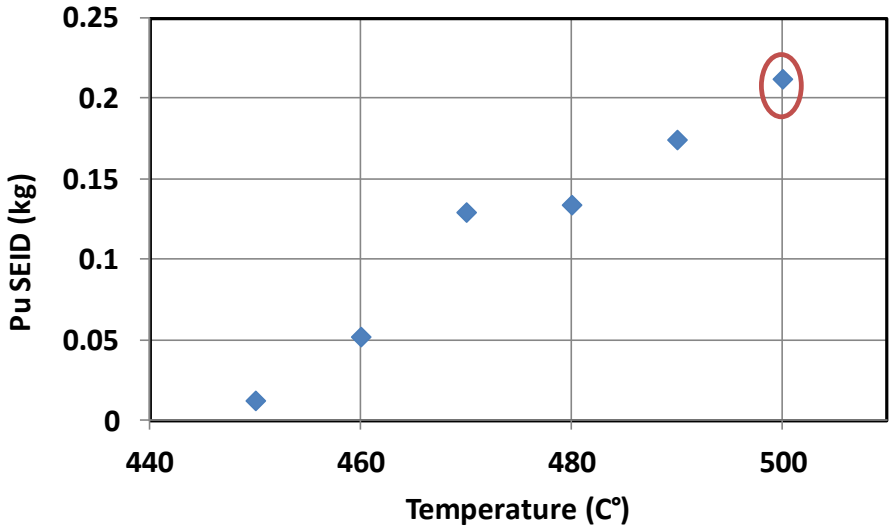

Figure 86- Pu SEID Partial Heater Failure, C Derived Cases (Normal Operation Circled)

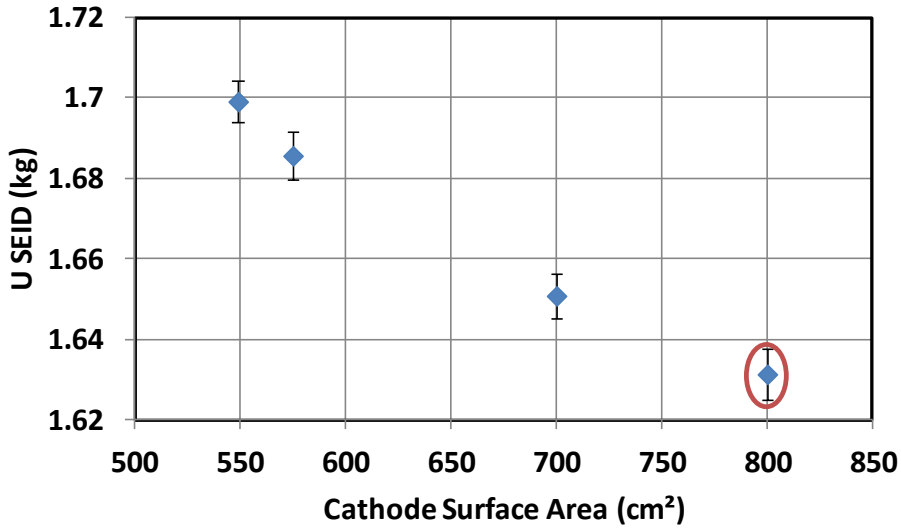

Figure 87- U SEID Cathode Retraction Linkage Failure, C Derived Cases (Normal Operation Circled)

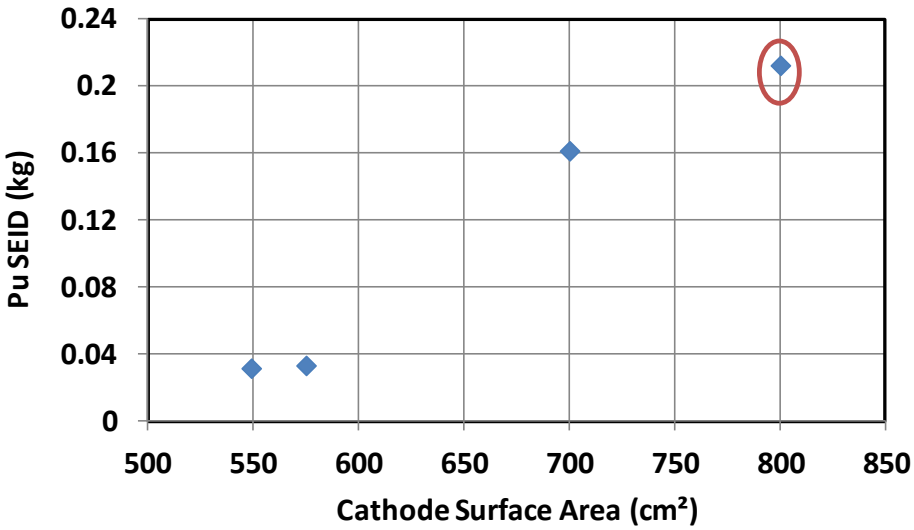

Figure 88- Pu SEID Cathode Retraction Linkage Failure, C Derived Cases (Normal Operation Circled)

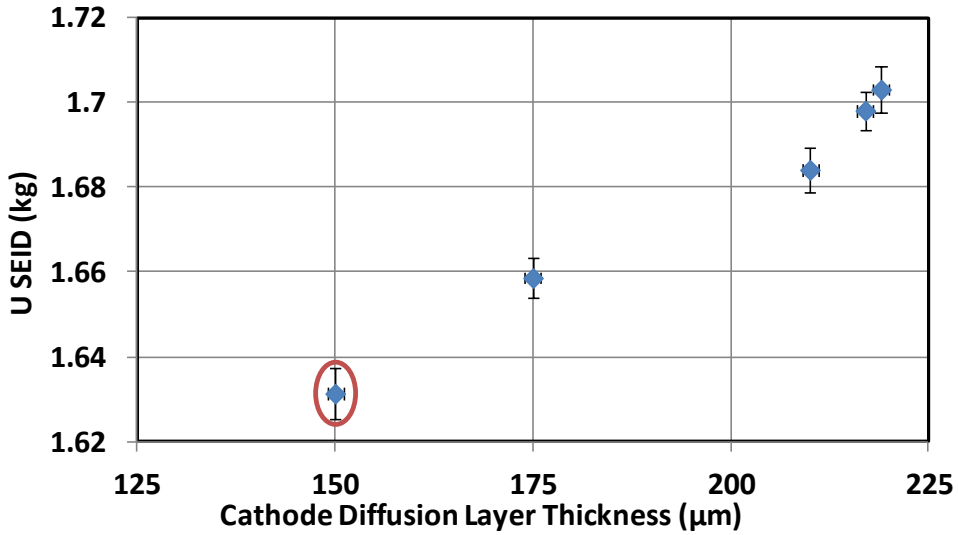

Figure 89- U SEID Cathode Motor Failure, C Derived Cases (Normal Operation Circled)

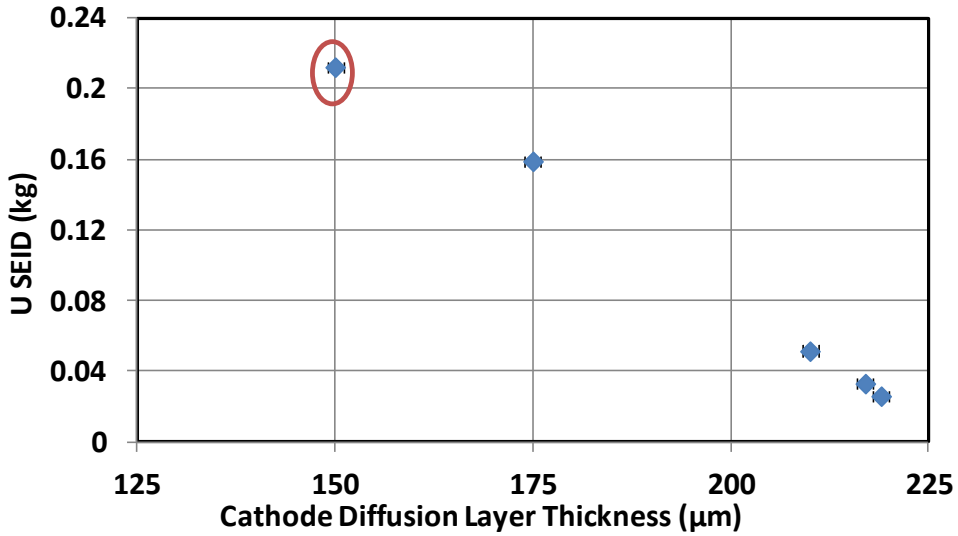

Figure 90- Pu SEID Cathode Motor Failure, C Derived Cases (Normal Operation Circled)

A couple major trends are seen in the change in the value of the SEID as a result of failure modes. For the trends that result in increased codeposition over the 104 cycles of operation, e.g. decrease in temperature or electrode surface area, there is a reduction in the Pu SEID and increase in U SEID calculated as a result. For the case of no

codeposition as in the increased currents seen in Figure 79 and Figure 80, we see a decrease in U SEID and increase in Pu SEID. These two sets of trends point to the idea that at least in the case of the system simulated upon here, the majority of measurement error in the calculation of SEID is the assaying of the inventory of U and Pu in the eutectic salt and thus increased or decreased removal of material from the salt results in an inverse effect on their respective SEIDs. Further, an increase in the amount of material remaining in the salt or dissolving into the salt results in a response involving an increase in SEID while an increased removal of material from the salt results in a decreased SEID.

As a result of these trends, the simulated ER failure modes from a safeguards perspective may not have a significant effect since the change in SEID is small between the failure and normal cases (at least for this analysis). As no material is actually removed from the system and just moves to the wrong location, changes in ID and SEID are expected, but the simulations show that the change in SEID is not drastic. Though not displayed here there is also no significant effect on ID. Thus, failure mode analysis is beneficial, but the results depicted here indicate that they are more beneficial from an operation design perspective rather than safeguards system design purposes.

7.2.3 NRTA Balance Period Variation Study Results

The final simulation campaign in SSPM dealt varying the balance period of the NRTA. The simulations were performed on the 500 °C of base case C and varying the balance period in the NRTA subsystem. An increase in the balance period effectively increases the total mass measured during the period of time selected for the NRTA. Of interest was the impact this had on SEID and the possible balance periods that NRTA

could be set for in an actual facility. Table 32 details the different balance periods analyzed for this case. The uncertainties of the measurement points were the same as those seen in Table 31.

Table 32- Balance Periods for NRTA Study

Value	Time (h)
NRTA Balance Period	28,56, 112, 196, 392, 784

The results of the SSPM study into the variation of the NRTA timing is seen in Figures 91-94 for U Cumulative ID and SEID and Figures for Pu Cumulative ID and the SEID for the last NRTA balance period. This last balance period differs based on the duration. For example, the last NRTA balance period for a 28 hour balance period is hour 2968 to hour 2996 in the contest of the simulation, while the last NRTA balance period for a 784 hour balance period is hour 2184 to hour 2912 in the context of the simulation. These results are displayed for the base case C at a temperature of 500 C°.

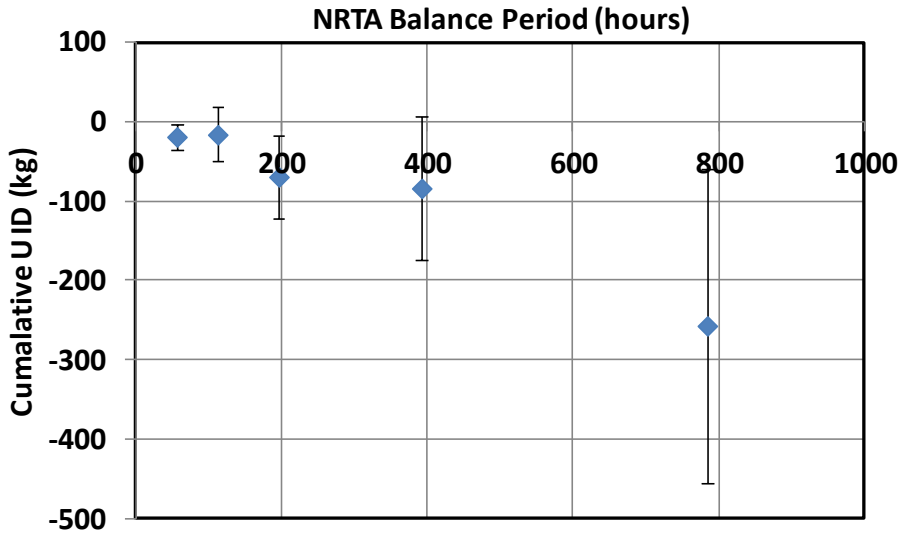

Figure 91- Cumulative U ID vs NRTA Balance Period

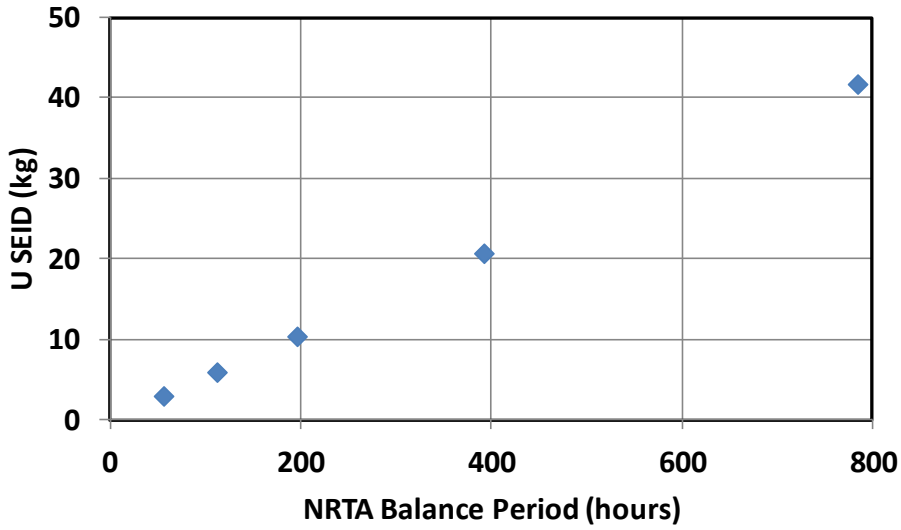

Figure 92- U SEID vs NRTA Balance Period

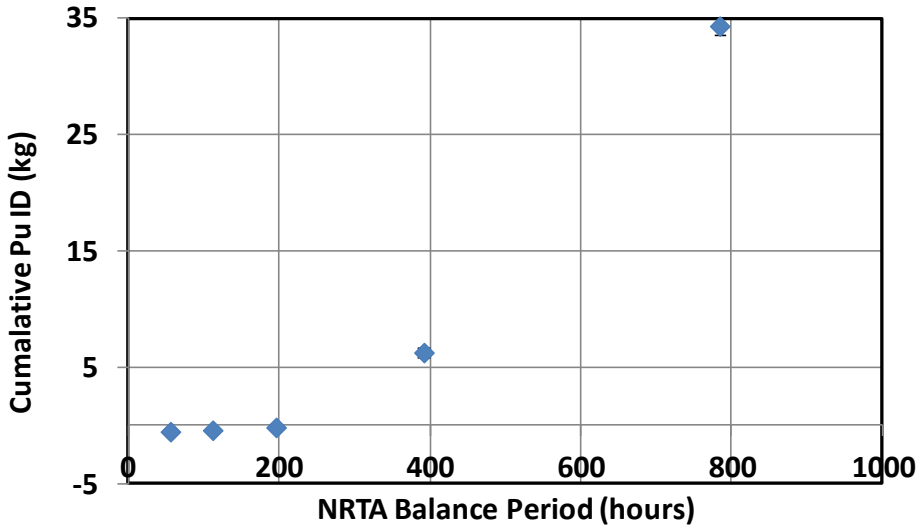

Figure 93- Cumulative Pu ID vs NRTA Balance Period

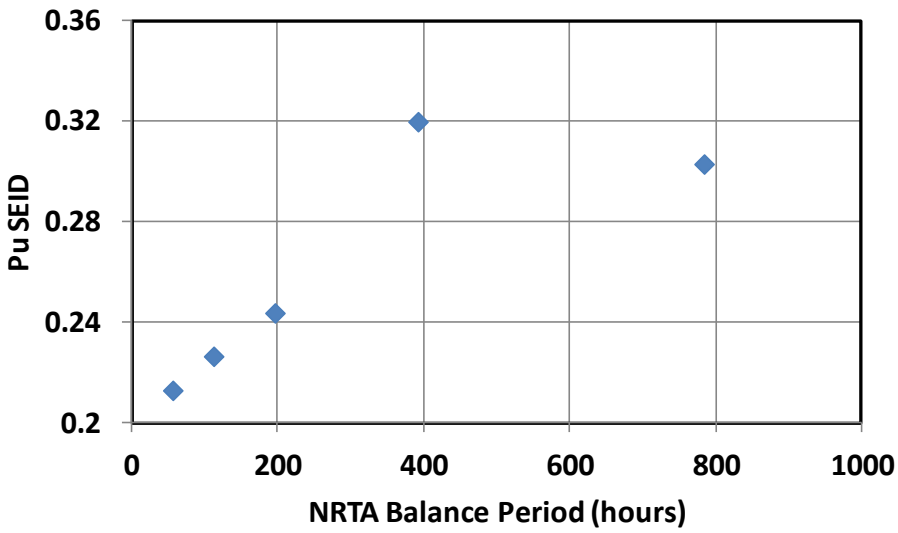

Figure 94- Pu SEID versus NRTA Balance Period

As indicated by these results, the cumulative ID and SEID for both Pu and U increase with increasing duration of the NRTA balance period. This is expected as there is greater mass being surveyed per period, thus resulting in greater error in measurement, which in turn contributes to an increased ID averaged over the simulations. In the case of the U balance, the SEID only exceeds the limits for low enriched U of the IAEA requirements at 792 hours, equivalent to one month. The remainder for this scale of simulation does not exceed the requirements of the IAEA. For Pu, the SEID does not exceed the uncertainty requirements of the IAEA regardless of balance period length. This can be attributed to the fact that the total mass of Pu transferred through multiple measurement points (i.e. codeposited Pu at the cathode processing stage) is not large and as a result the standard error reflects this. A larger throughput of Pu as would be seen in higher currents representative of commercial facilities, e.g. 300 A, would see an increase in SEID to levels most likely above IAEA limits. More investigation is required though the results indicate that weekly balances, as opposed to after a single operational cycle,

periods would provide adequate results while reducing the costs of safeguards efforts and subsequent holdup.

An interesting result is that of the Pu SEID. The 392 hour balance period has a higher Pu SEID than the 784 hour balance period which contradicts the expectations of longer period means high SEID. This can be resolved by inspecting the Pu deposition at the cathode in Figure 70. The last 784 hour balance period covers the period of hour 2184 to hour 2912 while the last 392 hour balance period covers hour 2352 to hour 2744. By looking at the mass depositions in the plot, the 784 hour balance period covers cycles with no deposition of Pu or less than the full deposition seen from hour 2500 to 3000. The last 392 hour balance period covers depositions of over 100 grams per cycle for the entirety of the period. Thus comparing between these balance periods, the SEID is greater for the 392 hour balance period as the total amount of mass that is measured is greater.

7.3 Conclusions

Several conclusions and inferences can be drawn from the simplified Echem model coupled with the programmed ERAD results for ER simulation. The U SEID is sensitive to the U measurement uncertainties in the U product stage while the Pu SEID does not display a relationship to the uncertainty of the Pu measurement in the U product stage. This is due to the majority of mass of both U and Pu being in the ER thus the SEID is dominated by the ER measurement. As there are over 5 kg in both ER operational cases of total U product deposited at the cathode, there is enough mass being measured at the product to have an effect on the U SEID. The amount of mass removed in terms of Pu from the salt compared to that which is present is not large enough to make a significant

difference on Pu SEID. Thus, improvements of current NMA technologies for the backend product measurements may not significantly reduce the SEID. The focus of mass quantification R&D by these results should be focused on more sophisticated techniques such as microfluidic sampling or laser induced breakdown spectroscopy (LIBS).

From the Echem runs using the ER data from ERAD for the reduction in temperature failure mode, it is observed that when failure modes do occur, the SEID of the U will increase while SEID for Pu will decrease. This is explained by what was seen in the uncertainty studies that the ER measurement dominates the SEID calculation. In the case of failure modes, more U remains in the ER while less Pu remains in the ER, thus contributing to a reduced Pu SEID and increased U SEID. As the severity of the failure mode increases, more Pu is codeposited reducing the Pu SEID and increasing the U SEID further. These results assume that the measurement uncertainty of the U and Pu measurement in the product is held constant regardless of how much Pu is codeposited. This may not be a realistic assumption as it is more challenging to quantify mass in mixed metal products as opposed to pure U products. However, other technologies such as melt sampling may be able to address this problem. For a given NRTA scheme, the overall effect on SEID of a given period balance due to failure modes effects is either positive or not significant enough to raise a false alarm. Finally, the duration of these NRTA balances have a mild effect on the ID and SEID; however, results on the scale of these simulations demonstrate that the balance for NRTA need not be every ER operational cycle of 28 hours. Instead, it can be occurring on a weekly basis. However, as throughput increases the NRTA balance period duration will have to be adjusted.

As for the role of PM in identifying when failure modes are occurring, the results indicate that focus of future research should be on improving NRTA measurement techniques for the mass balance. PM techniques should be used in a more operational and quality control type role with additional safeguards support. PM tuned to detect off-normal occurrences can assist operators in identifying conditions that need proper corrective action so as to ensure proper throughput. The methods used in identifying failure modes and simulating can also assist in providing an operator a sense of the needs to address the problems that occur within the facility and what amount of downtime, and thus reduction in throughput may be required to address it. From a quality control perspective, PM data can identify when failure modes are occurring and notify the operator that codeposition may be occurring. The PM information can be used to track what batches need future processing or attention and connect that with tags or stamps of the consolidated output products. This also plays a role in safeguards in that it identifies batches for more advanced measurements by both operators and inspectors assuming that the off-normal batches are properly kept on the log books of the facility.

CHAPTER 8: CONCLUSIONS AND FUTURE WORK

8.1 CONCLUSIONS

I performed significant research effort to develop systematic method of evaluating pyroprocessing failure modes and assessing their impact on the mass balance of the pyroprocessing facility. In validating the assumptions of the unit operations models, expanding the methodology to determine and simulate off-normal scenarios, and developing a methodology by which system models can better represent these failure modes, the understanding of SBS's usefulness for assessing failure modes impacts is expanded.

The work to evaluate the assumptions of ERAD involved lab-scale experiments to compare experimental results to the analytical results in ERAD. The results of both mass depositions at the cathode and electrode potentials were compared between the analytical and experimental results to determine the efficacy in applying ERAD to SBS analyses. The results determined that ERAD is able to predict trends from postulated failure modes such as change in cathode surface area as the same trends are seen in both the experimental and analytical results. In addition, its predictions should be treated as more qualitative than quantitative as the results from ERAD represent the theoretical scenario where all charge transferred adheres to the cathode while experimental results show that some will either be scraped off upon removal of cathode or dissolved back into the salt. ERAD results can provide an understanding of the effects of postulated failure modes and used to yield ER results for integration into systems simulations but should not be applied to an actual operational design of an ER.

The manner by which SBS determines off-normal scenarios was refined substantially and now encompasses a more effective systematic approach for off-normal scenario identification. This was achieved by performing an FMEA adapting the traditional Department of Defense Standard while changing definitions of terms such as severity to reflect the potential safeguards impact of the failure. This systematic method allowed for a significant increase in the scope of failure modes considered compared to past studies as well as more robust predictions of the effects of the failures on multiple levels from the unit operation to the entire facility. This approach should be considered in future efforts between designers, operators, and safeguards authorities in developing facility layout. In addition, I recommend that this be performed as a step within safeguards by design efforts to best design the facility's safeguards system by linking the safeguards review and design with the safety FMEA that will most likely be developed by the operations and safety factions of the design team.

The ability of FMEA to identify potential failure modes of significance was confirmed by ERAD simulations of the postulated failure modes. In addition to playing a role in confirming the failure modes postulated, ERAD simulations of the failure modes generated adjustments to the initial FMEA in terms of postulated failure modes severity designation as well as the effects. A summary of these adjustments to previous postulated severities is seen in Table 33. This ability to reevaluate the FMEA through simulation demonstrates the iterative method by which FMEA engineers and design engineers can iteratively assist each other in making key design decisions for a proposed facility. If certain failure modes have less severe effects when simulated than postulated then adjustments can be made to design as well as operations to put less attention to the failure

if it occurs, thus resulting in a reduction in down time of the facility. If the severity is actually found to be greater than assumed, then designers should add redundancy and maintenance to that specific operation or component in the final design of the unit operation.

Table 33- Summary of Severity Adjustments after ERAD Simulations

Failure Mode	Previous Severity	New Severity
Cracking of Anode Retraction Linkage	II	I
Decrease in anode rotation speed due to failure in windings in electric motor	II	III
Partial heater failure	II	I

This also indicates a value of applying SBS within the design space. In particular, SBS as demonstrated here can be applied in conjunction with other advanced design methods such as safeguards by design (SBD) which integrates safeguards within the design process itself and with 3S (Safety, Security and Safeguards) design approaches [63, 64]. SBS provides a manner with which to identify key off normal scenarios that could have impact from the perspective of safeguards and thus be designed around with proper redundancy, mitigation, and maintenance in place. These specific failure modes have implications beyond safeguards as they affect safety and operations. To integrate this FMEA type approach within the design would address potential issues with the facility more efficiently and better streamline the design process by not having to rectify the safety and safeguards impacts of given events in final design composition.

Another application within the design space in which the methodology of SBS can be of value is with the maximization of the faradaic efficiency of the ER and with this how to best design a facility provided this information. My experimental work determined that faradaic losses within an ER cell do occur as metal at the cathode reacts

back into the salt. This is especially important to note as this would reduce the throughput of a facility and make it more challenging to track the mass transport as less metal would be present than expected by simulations of the facility during the design process. Thus, the FMEA portion of SBS can focus not only on safeguards effects from codeposition, but effects on throughput and mass movement of the facility due to conditions that reduce the faradaic efficiency. This assessment can also assist in the design of the unit operations themselves. Parameters such as number of cathodes within the ER, operating temperature and current, number of ERs within the hot cell, and duration of operation can be selected by a collective effort among the designers, operators, and safeguards authorities. This was the not the focus of this dissertation, but should be taken into account with future research into pyroprocessing in particular at the demonstration facility PRIDE.

ERAD simulations provide a wealth of data that can be translated effectively via regression into system models such as SSPM Echem. This allows determination of the impact of the failure modes on the system and thus their impacts. The systems model simulations of failure modes do not indicate that there are significant safeguards related effects as long as the measurement systems are tuned and failure modes can be detected by the operator in an efficient manner. In fact, due to the nature of the mass flow in the system, failure modes with properly tuned measurements systems may have a reduced uncertainty given a failure mode occurring. Thus, the use of failure mode analysis as well as system simulation involving them provide a greater benefit from an operations planning and design perspective than impact on safeguards. This is because the simulated data can help operators to adjust the schedule of repair and maintenance of the facility depending on the effects specifically at the level of the ER unit-operation. Finally, these

models can be used to verify other system models involving simulated ER systems, in particular the impact of models that also possess a more physics-based approach to ER modeling.

Beyond model development, this knowledge of total system impact provides input as to how an SBS methodology could be effectively implemented in an actual facility. The greatest information this analysis provides is the placement of measurement technologies and development of thresholds of detection for these measurements to inform the operators that anomalous scenarios such as failure modes are occurring. Algorithms that can provide insight to operators as to what the potential problems are within the facility will need to be developed. These algorithms are analogous to those that identify errors within automobiles and provide data in the form of error codes connected to the check engine light. When errors arise, an operator can deem investigation and maintenance necessary based on the known severity of the failure mode detected. Certain failure modes as indicated by this research will have little to no impact on the mass flow and thus neither on operations and safeguards. They instead can be addressed as is timely during the maintenance schedule. More severe scenarios such as temperature fluctuations can be addressed in a much more immediate manner. These failure modes can be logged within the operator's books to help in resolving errors in the mass balance as well as identifying which potential batches of product need attention to resolve issues with the mass balance of the facility. SBS in this work appears not to be a panacea to the challenges presented by safeguarding with traditional NMA. On the contrary, even with SBS added to the process, additional methods such as extended containment and surveillance will need to be applied harmoniously with NMA and SBS to create the most

robust safeguards regiment possible for the facility [65]. SBS can help in resolving this method by integrating all three within its analytical models to design an effective safeguards triad that will minimize negative effects that it may have on the throughput and operation of the facility.

8.2 Future Work

Additional work can be done in the future to build on SBS given the results of this dissertation. One area of research in particular is expanding experimentation to evaluate the ERAD computer codes assumptions and applicability as a viable ER model for facility modeling. This would best be approached by increasing the scale of the experimental ER cell to determine the affect of which scaling up the equipment has compared to the predictions made by ERAD. With this, conditions where ERAD starts to be less reliable for simulation can be determined. In addition, other forms of off-normal behavior can be subject to experimental verification such as the change in temperature due to the failure in the heater failure mode. In addition to experimental work, the FMEA approach developed here can be further applied to all major critical unit operations such as electroreduction, electrowinning, and fuel product processing. Of the most pertinent interest would be the electrowinning stage as failures in the separation and treatment of SNM in the salt could have even more significant safeguard and operations effects. To best model these unit operations from the perspective of SBS, advanced simulation packages must be developed to simulate these unit operations effectively. In addition, further simulations among these developed simulations can be integrated into a total virtual pyroprocessing facility simulation. This virtual facility should be a primary end goal of computational research in pyroprocessing and pyroprocessing safeguards

development. This would be in parallel with the end goals of the simulation component of the DOE MPACT campaign.

Beyond pyroprocessing, SBS can be applied to different proposed designs within nuclear engineering. In particular, Gen-IV reactor designs involving a fluid fuel design or a pebble bed reactor. For example, a fluid fuel design would have similar challenges to pyroprocessing as the SNM within the process exists since countable bulk material is not available as in a traditional light water reactor. Applying SBS can indicate possible locations where material could be misappropriated or boost knowledge of the location of material at a given time. As such, SBS could add both safeguards and operational benefits as has been demonstrated in pyroprocessing to all advanced nuclear facilities.

LIST OF APPENDICES

APPENDIX A- COMPLETED FMEA WORKSHEETS

System: Commercial Pyroprocessing Facility ER
Indenture Level: ER Component Level/Lowest Level
Reference Drawing
Mission: Separation and refining of U from UNF

Date 11/18/2016
Sheet 1 of 14
Compiled by: Philip Lafreniere
Approved by:

					Failure Effects				
Identification Number	Item/Functional Idenfitication	Function	Failure Modes and Causes	Operational Mode	Local Effects	Next Higher Level	End Effects	Failure Detection Methods	Severity Class
A-01	Facility Power Source	Provides power to all unit operations and power sources in facility	Loss of Off-Site Power due to Blackout or Act of God	Normal Commercial Operation of ER	Cease of operations of ER	Loss of all throughput until return of power	Total Facility throughput for entire cycle reduced	Human Observation/ Loss of Signals from on yard transformers	Class III
			Unexpected Large Surge in Power	Normal Commercial Operation of ER	Sudden Increase in ER current density at both electrodes	Codeposition of actinides, the amount of determined by duration and frequency of surges	Slight change in total mass balance due to Pu may be in the output in some amount	Refernce electrode	Class II
A-02	Computer Control System	utilzing sensor information and sending signals to the facility to ensure operations continue as normal	Crashing of computer system due to programming error and/or cyberattack	Normal Commercial Operation of ER	Cease of operations of ER	No ouput until computer are up and functional	Total throughput for cycle reduced but no change in balance	Human Observation	Class III
			Readout and manipulation of computer control system does not match actual conditions due to virus/cyberattack.	Normal Commercial Operation of ER	Codeposition at Cathode consistently with no recgonizable response by operator	Large output of U/TRU to U fuel fabrication	Potential for large amounts of MUF depending on nature of the virus used	Analog Sensor Reading from Sensor Ouputs by Operator	Class I

System: Commercial Pyroprocessing Facility ER
Indenture Level: ER Component Level/Lowest Level
Reference Drawing
Mission: Separation and refining of U from UNF

Date 11/18/2016
Sheet 2 of 14
Compiled by: Philip Lafreniere
Approved by:

					Failure Effects				
Identification Number	Item/Functional Idenfitication	Function	Failure Modes and Causes	Operational Mode	Local Effects	Next Higher Level	End Effects	Failure Detection Methods	Severity Class
A-03	Manual Manipulator System	Manipulators for Removal of Anode and Cathode manually operated by faciility operators outside hot cell	Manipulator drops cathode or other materials while moving them within hot cell	Removal of Electrode from ER	No effect on operation of ER just a delay in operations during cleanup	No change in ouput	Reduction in overall throughput	Human Observation	Class III
			Insertion of electrode causes metal parts (e.g. Bolts, screws) , fuel, or unscraped dendrites to accidentally fall into salt	Inerstion of electrodes into salt	Shorting of ER anode-cathode circuit	Reduction in total throughput. Oxidation reaction dominates leading to unaccounted material not separated from salt	MB potentially disrupted as a signifcant material can be held up in ER salt defying book expected values	Reference Electrode	Class II
B-01	Inductive heater	Heater comprising of series of Wires that has currents passed to heat wires	Total failure of heater due to failure in governing circuitry	Continouos operation of Pyro Facility	Freezing of salt	Now throughput until heater restored	Reduction in overall throughput	Thermocouple, Reference Electrode	Class III
			Partial heater failure in specific inductive coil sets	Continouos operation of Pyro Facility	Reduction in total salt temperature, potential for partial freezing	Potential for codepositon as reduction potential is reduced as well as partial currents. Total throughput reduces due to change in kinetics	Mass balance upset by lower output and potential codeposition	Thermocouple, Reference Electrode	Class II

System: Commercial Pyroprocessing Facility ER
Indenture Level: ER Component Level/Lowest Level
Reference Drawing
Mission: Separation and refining of U from UNF

Date 11/18/2016
Sheet 3 of 14
Compiled by: Philip Lafreniere
Approved by:

					Failure Effects				
Identification Number	Item/Functional Idenfitication	Function	Failure Modes and Causes	Operational Mode	Local Effects	Next Higher Level	End Effects	Failure Detection Methods	Severity Class
B-02	Insulation Layer	Insulates Heat from Inductive Heater being Delivered to the ER Salt Bath and Container	Failure of thermal insulation due to fracturing from radiation/aging	Continouos operation of Pyro Facility	Increase in total temperature of salt with hot spots with regards to location of insulator damage	Change in kinetics, faster reaction rate. Higher potential and species partial currents. Potential of codeposition if U removal rate is too high.	Mass balance may have slight change if operations is over prolonged period of time due to increased output per ER operation	Thermocouple, Reference Electrode	Class II

System: Commercial Pyroprocessing Facility ER
Indenture Level: ER Component Level /Lowest Level
Reference Drawing
Mission: Separation and refining of U from UNF

Date 11/18/2016
Sheet 4 of 14
Compiled by: Philip Lafreniere
Approved by:

					Failure Effects				
Identification Number	Item/Functional Idenfitication	Function	Failure Modes and Causes	Operational Mode	Local Effects	Next Higher Level	End Effects	Failure Detection Methods	Severity Class
B-03	Anode Power Source	Acts as power source for motor and facilitates passing of current for oxidation reaction at anode	Loss of power supplied due to issues with circuitry resulting from radiation damage	Normal Commercial Operation of ER	Open circuit for operation of ER. No Current Passed	Reduction in throughput of ER	Reduction in overall throughput	Reference Electrode	Class III
			Surge in power passed through circuit due to failure	Normal Commercial Operation of ER	Greater dissolution of Rare Earths and zirconium into salt due to increased current density. Potential for oxidation of U(IV)		Potential reduced U	Reference Electrode	Class II
B-04	Cathode Power Source	Acts as power source for motor and facilitates passing of current for reduction reaction at cathode	Loss of power supplied due to issues with circuitry resulting from radiation damage	Normal Commercial Operation of ER	Open circuit for operation of ER. No Current Passed	Reduction in throughput of ER	Reduction in overall throughput	Reference Electrode	Class III
			Surge in power passed through circuit due to failure control mechanisms	Normal Commercial Operation of ER	Increase passage of current resulting in drop in potential	Powerful enough surge for long term can lead to long term codeposition	Facility MUF due to sucessive ER codeposition operations	Reference Electrode	Class I

System: Commercial Pyroprocessing Facility ER
Indenture Level: ER Component Level/Lowest Level
Reference Drawing
Mission: Separation and refining of U from UNF

Date 11/18/2016
Sheet 5 of 14
Compiled by: Philip Lafreniere
Approved by:

					Failure Effects				
Identification Number	Item/Functional Idenfitication	Function	Failure Modes and Causes	Operational Mode	Local Effects	Next Higher Level	End Effects	Failure Detection Methods	Severity Class
B-05	Stirrer Motor	Motor Driving the Rotation of the ER Stirrer	Complete failure of rotation motor due to radiation damage	Normal Commercial Operation of ER	Reduction of homogeneity of constituents of the salt	Issues in Concentration Gradient may lead to high concentration regions of TRU that may lead to codeposition	Potential for MUF if salt remain heterogeneuous	Tachometer	Class II
			Increased rotational speed from motor due to failure in commutator	Normal Commercial Operation of ER	Greater salt mixing, possible increase in diffusion layer thickness of both electrodes	The rotation could potentially push the heavier elements to outside of salt bath which will disrupt transport to cathode	Signficant disruption in concentration gradient could lead to reduced overall throughput and more U in salt waste treatment than expected thus potentially leading to a MUF issue	Tachometer	Class II
			Decrease rotational speed due to failure of windings in electric motor	Normal Commercial Operation of ER	Reduction of homogeneity of constituents of the salt	Issues in Concentration Gradient may lead to high concentration regions of TRU that may lead to codeposition	Potential for MUF if salt remain heterogeneuous	Tachometer	Class II

System: Commercial Pyroprocessing Facility ER
Indenture Leve ER Component Level/Lowest Level
Reference Dra
Mission: Separation and refining of U from UNF

Date 11/18/2016
Sheet 6 of 14
Compiled by: Philip Lafreniere
Approved by:

					Failure Effects				
Identification	Item/Functional Idenfiticatio	Function	Failure Modes and Causes	Operational Mode	Local Effects	Next Higher Level	End Effects	Failure Detection Methods	Severity Class
B-06	Anode Motor	Motor Driving the Rotation of the Anode Basket	Complete failure of rotation motor due to radiation damage	Normal Commercial Operation of ER	Loss of rotation, diffusion layer reverts to steady state diffusion layer	Reduction of limiting current densities. Potential for oxidation U(IV)	Potential movement of increased U movement to salt waste. Reduction in overall throughput	Tachometer, Reference Electrode	Class II
			Increased rotational speed from motor due to failure in commutator	Normal Commercial Operation of ER	Diffusion layer thickness decreases, increased limiting currents	Little effects on overall transport	Little effect on overall throughput	Tachometer	Class III
			Decrease rotational speed due to failure of windings in electric motor	Normal Commercial Operation of ER	Increase in diffusion layer thickness	Reduction of limiting current densities. Potential for oxidation U(IV)	Potential movement of increased U movement to salt waste. Reduction in overall throughput	Tachometer, Reference Electrode	Class II

System: Commercial Pyroprocessing Facility ER
Indenture Level: ER Component Level/Lowest Level
Reference Drawing
Mission: Separation and refining of U from UNF

Date 11/18/2016
Sheet 7 of 14
Compiled by: Philip Lafreniere
Approved by:

					Failure Effects				
Identification Number	Item/Functional Idenfitication	Function	Failure Modes and Causes	Operational Mode	Local Effects	Next Higher Level	End Effects	Failure Detection Methods	Severity Class
B-07	Cathode Motor	Motor Driving the Rotation of the Cathode Basket	Complete failure of rotation motor due to radiation damage	Normal Commercial Operation of ER	Loss of rotation, diffusion layer reverts to steady state diffusion layer	Potential TRU codeposition due to increase in diffusion layer thickness	Potential for Signficant MUF if motor not fixed	Tachometer, Reference Electrode	Class I
			Increased rotational speed from motor due to failure in commutator	Normal Commercial Operation of ER	Increase in rotation, reduction in diffusion layer thickness, and an increase in limiting current	No codeposition	No change in overall throughput	Tachometer	Class III
			Decrease rotational speed due to failure of windings in electric motor	Normal Commercial Operation of ER	Increase in diffusion layer thickness, reduced limiting current	Codeposition occurs if drop large enough, may only be slight	Potential for Signficant MUF if motor not fixed	Tachometer, Reference Electrode	Class I
C-01	Salt Stirrer	Screw type agitator for mixing salt in ER bath to ensure homogeneity	Surface damage to stirrer due to environmental effects such as radiation and corrosion	Continouos operation of Pyro Facility	Reduction of homogeneity of constituents of the salt	Issues in Concentration Gradient may lead to high concentration regions of TRU that may lead to codeposition	Potential for MUF if salt remain heterogeneuous	Visible inspection, salt sampling (delayed detection	Class II

System: Commercial Pyroprocessing Facility ER
Indenture Level: ER Component Level/Lowest Level
Reference Drawing
Mission: Separation and refining of U from UNF

Date 11/18/2016
Sheet 8 of 14
Compiled by: Philip Lafreniere
Approved by:

					Failure Effects				
Identification Number	Item/Functional Idenfitication	Function	Failure Modes and Causes	Operational Mode	Local Effects	Next Higher Level	End Effects	Failure Detection Methods	Severity Class
C-02	Anode Retraction Linkages	Ascends and descends anode into Salt bath and rotates the electrode through connection to motor	Partial fracture linkage due to thermal and physical stresses on linkage	Normal Commercial Operation of ER	Anode partially submerged in salt instead of fully, current density increases	More positive potential at anode, potential for oxidation of U(IV) that cannot be reduced at cathode	More U will remain in salt and has potential to disrupt mass balance over a long period of time.	Reference electrode, Double Bubbler	Class II
			Total fissioning of linkage due to thermal and physical streses	Normal Commercial Operation of ER	Electrode falls into salt bath	Operation ceases, no throughput	Reduced total throughput of facility little effect on actual mass balance	Reference electrode, Double Bubbler	Class III
C-03	Cathode Retraction Linkages	Ascends and descends cathode into Salt bath and rotates the electrode through connection to motor	Partial fracture linkage due to thermal and physical stresses on linkage	Normal Commercial Operation of ER	Cathode partially submerged in salt instead of fully, current density increases	More negative potential at cathode, potential for codeposition of TRU at cathode.	Codeposition leads to disruption of mass balance	Reference electrode, Double Bubbler	Class II
			Total fissioning of linkage due to thermal and physical streses	Normal Commercial Operation of ER	Electrode falls into salt bath	Operation ceases, no throughput	Reduced total throughput of facility little effect on actual mass balance	Reference electrode, Double Bubbler	Class III

System: Commercial Pyroprocessing Facility ER
Indenture Level: ER Component Level/Lowest Level
Reference Drawing
Mission: Separation and refining of U from UNF

Date 11/18/2016
Sheet 9 of 14
Compiled by: Philip Lafreniere
Approved by:

					Failure Effects				
Identification Number	Item/Functional Idenfiticat	Function	Failure Modes and Causes	Operational Mode	Local Effects	Next Higher Level	End Effects	Failure Detection Methods	Severity Class
C-04	Anode Basket	Holds chopped fuel and acts as location of oxidation reaction in ER	Development and expansion of holes in wire mesh	Normal Commercial Operation of ER	Unreacted metal falls into salt bath separate from anode basket	Loss of difficult to recover material, potentially U/TRU, potential shorting of circuit due to reaction with free floating material	Shorting reduces overall throughput, solid material falling out difficult to recover and can be lost forever within the mass balance thus potentially leading to false alarm if enough scenarios occurs over time.	Visual inspection, reference electrode	Class II

System: Commercial Pyroprocessing Facility ER
Indenture Level: ER Component Level/Lowest Level
Reference Drawing
Mission: Separation and refining of U from UNF

Date 11/18/2016
Sheet 10 of 14
Compiled by: Philip Lafreniere
Approved by:

					Failure Effects				
Identification Number	Item/Functional Idenfitication	Function	Failure Modes and Causes	Operational Mode	Local Effects	Next Higher Level	End Effects	Failure Detection Methods	Severity Class
C-05	Cathode Rod	Metal rod where reduction reaction occurs	Cracks in surface of solid cathode due to improper scraping	Normal Commercial Operation of ER	Loss of surface for electroplating, change in surface area and thus current density though slight	Rough metal challenging to electroplate, some deposits may not adhere in dendritic form and thus fall off the reducing throughput per operation slightly, but signficant crack required for large amount of metal to not adhere due to plating site disrupted	If enough material cannot plate, concentration of salt will increase with a reduced throughput that over a long period of time could be signifcant though the amount lost per cycle will most like be less than 1 SQ	Visual inspection, reference electrode, electronic balance	Class III
C-06	Cathode Perforated Surface	Provides contact surface for ions to migrate through to catalyze reaction of U ions at cathode.	Development and expansion of holes in surface	Normal Commercial Operation of ER	Greater bulk salt contact with cathode, reaction dynamics altered	Disruption in electroplating mechanism causes difficulties in maintaing throughput of ER	Loss of material most likely minimal and still will be reacted over time and being samplable through salt	Visual Inspection	Class III
C-07	Salt Bath Container	Liner and Crucible of ER Salt Bath	Large cracks in container due to thermal stresses and radiation damage	Continouos operation of Pyro Facility	Salt leaks through cracks into insulator layer	Decrease in overall salt level, damage to insulator leading to potential temperature excursions, loss of material through the container that reduces concentration of U/TRU	Increase of MUF due to loss of unattainable salt containing U/TRU can be signficant if allowed to continue	Double Bubbler, Thermocouple	Class I
C-08	LiCl-KCl Salt Bath	Electrolyte Bath Where Separations Reactions Occur	N/A						

System: Commercial Pyroprocessing Facility ER
Indenture Level: ER Component Level/Lowest Level
Reference Drawing
Mission: Separation and refining of U from UNF

Date 11/18/2016
Sheet 11 of 14
Compiled by: Philip Lafreniere
Approved by:

					Failure Effects				
Identification Number	Item/Functional Idenfitication	Function	Failure Modes and Causes	Operational Mode	Local Effects	Next Higher Level	End Effects	Failure Detection Methods	Severity Class
D-01	Reference Electrode	Measures Current and Potential of Electrodes in ER	Crack in housing of reference electrode due to thermal stresses	Continouos operation of Pyro Facility	Potential reading shifted in either a more negative or positive direction. Disrupting process monitoring	Due to migration of potential, codepoistion operation could be normal operation while being masked by failure of reference electrod	Large throughput of codeposited material if drift is in more positive direction	Visual inspection, operator intuition, sampling of cathode melt	Class I
			Severing of electrode wire due to human error in moving and manipulation of it	Continouos operation of Pyro Facility	Loss of all ref. electrode signal to computer control system	Shutdown of ER operation til reference electrode replaced	Reduction in overall throughput	Computer control system	Class III
D-02	Thermocouple	Measures Temperature	Failure of resistance circuit for temperature measurement due to radiation damage	Continouos operation of Pyro Facility	Temperature read out contains large systematic error due to being less than the actual	Temperature of ER salt bath increases due to response from computer control system, same ER effects as failure of insulation layer	Mass balance may have slight change if operations is over prolonged period of time due to increased output per ER operation	Computer control system	Class II
			Fraying of thermocouple wiring due to repetitive operator interactions	Continouos operation of Pyro Facility	Loss of all thermocouple signal to computer control system	Shutdown of ER operation til thermocouple replaced	Reduction in overall throughput	Computer control system	Class III

System: Commercial Pyroprocessing Facility ER
Indenture Level: ER Component Level/Lowest Level
Reference Drawing
Mission: Separation and refining of U from UNF

Date 11/18/2016
Sheet 12 of 14
Compiled by: Philip Lafreniere
Approved by:

					Failure Effects				
Identification Number	Item/Functional Idenfitication	Function	Failure Modes and Causes	Operational Mode	Local Effects	Next Higher Level	End Effects	Failure Detection Methods	Severity Class
D-03	Anode Tachometer	Measures Rotational Speed of Anode	Calibration of Tachometer out of Sync	Commercial Operation of ER	Anode RPM Reading has increased systematic error	Change in rotation rate to address error that cause it to depart from intended speed. Refernce failure modes for anode motor to see potential effects depending on increase or decrease of speed	Refer to Anode motor failure modes for anode motor for effect depending on increase or decrease of speed	Reference Electrode, Computer Control system	Class II
			Radiation Damage to tachometer wiring and electronics	Commercial Operation of ER	Loss of all tachometer signal to computer control system	Shutdown of ER operation til tachometer replaced	Reduction in overall throughput	Computer control system	Class III
D-04	Cathode Tachometer	Measures Rotational Speed of Cathode	Calibration of Tachometer out of Sync	Commercial Operation of ER	Cathode RPM Reading has increased systematic error	Change in rotation rate to address error that cause it to depart from intended speed. Refernce failure modes for cathode motor to see potential effects depending on increase or decrease of speed	Refer to cathode motor failure modes for anode motor for effect depending on increase or decrease of speed	Reference Electrode, Computer Control system	Class II
			Radiation Damage to tachometer wiring and electronics	Commercial Operation of ER	Loss of all tachometer signal to computer control system	Shutdown of ER operation til tachometer replaced	Reduction in overall throughput	Computer control system	Class III

System: Commercial Pyroprocessing Facility ER
Indenture Level: ER Component Level/Lowest Level
Reference Drawing
Mission: Separation and refining of U from UNF

Date 11/18/2016
Sheet 13 of 14
Compiled by: Philip Lafreniere
Approved by:

					Failure Effects				
Identification Number	Item/Functional Idenfitication	Function	Failure Modes and Causes	Operational Mode	Local Effects	Next Higher Level	End Effects	Failure Detection Methods	Severity Class
D-05	Stirrer Tachometer	Measures Rotational Speed of Stirrer	Calibration of Tachometer out of Sync	Continouos operation of Pyro Facility	Cathode RPM Reading has increased systematic error	Change in rotation rate to address error that cause it to depart from intended speed. Refernce failure modes for strirrer motor to see potential effects depending on increase or decrease of speed	Refer to stirrer motor failure modes for anode motor for effect depending on increase or decrease of speed	Computer control system	Class II
			Radiation Damage to tachometer wiring and electronics	Continouos operation of Pyro Facility	Loss of all tachometer signal to computer control system	Shutdown of ER operation til tachometer replaced	Reduction in overall throughput	Computer control system	Class III

System: Commercial Pyroprocessing Facility ER
Indenture Level: ER Component Level/Lowest Level
Reference Drawing
Mission: Separation and refining of U from UNF

Date 11/18/2016
Sheet 14 of 14
Compiled by: Philip Lafreniere
Approved by:

					Failure Effects				
Identification Number	Item/Functional Idenfitication	Function	Failure Modes and Causes	Operational Mode	Local Effects	Next Higher Level	End Effects	Failure Detection Methods	Severity Class
D-06	Double Bubbler	Measures Density and Salt Level in ER	Calibration of Pressure Transducer Falls out of Sync	Preparation period before ER operation	Induced systematic error in the salt level and density reading.	May lead to slight adjustment of height of electrodes to adjust surface error. If significant enough could cause codeposition	Increased in error of mass balance due to codeposition as well as higher error in density measurement	Computer control system	Class II
			Leak in double bubbler tubes	Preparation period before ER operation	Large stochastic errors develop for both density and surface area	Adjustments in electrode level to compensate for misreading. Could be large if leak is high up in bubbler tube leading to large pressure differential reading	Propagated errors in mass balacne as well as potential throughput disruption due to codeposition	Computer control system	Class I
			Calibration of gas flow rate meter falls out of sync	Preparation period before ER operation	Induced systematic error in the salt level and density reading.	May lead to slight adjustment of height of electrodes to adjust surface error. If significant enough could cause codeposition	Increased in error of mass balance due to codeposition as well as higher error in density measurement	Computer control system	Class II

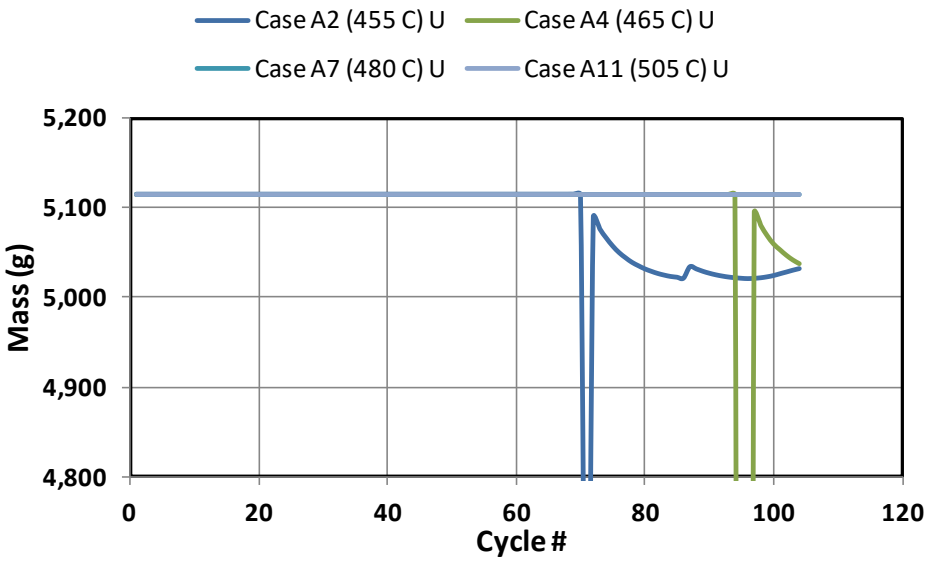

Figure 95- U Cathode Deposition Results for Temperature Variations of A Derived Cases (Temperature Variations)

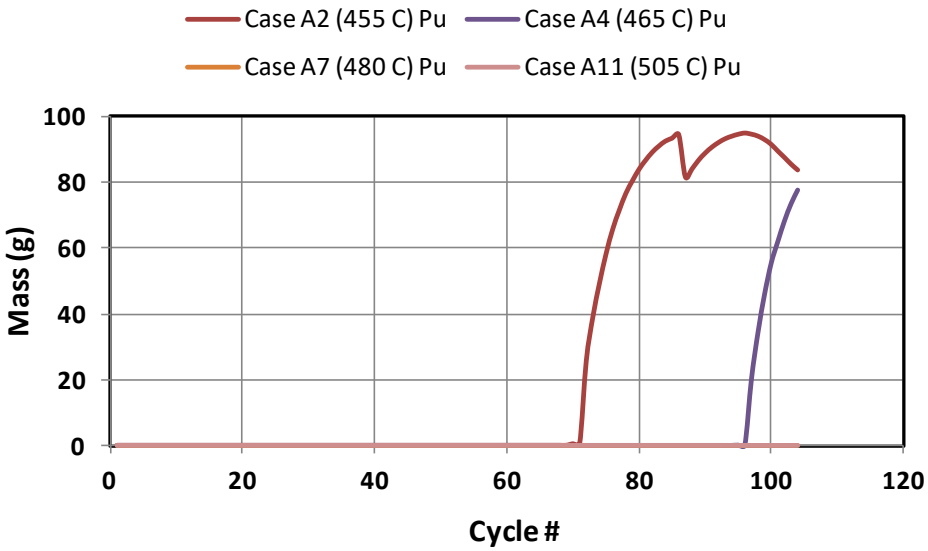

Figure 96- Pu Cathode Deposition Results for Temperature Variations of A Derived Cases (Temperature Variations)

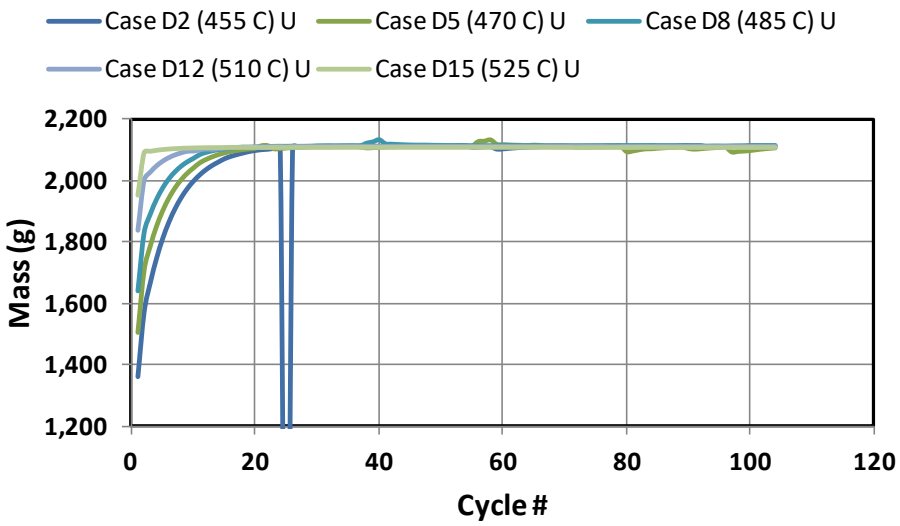

Figure 97- U Cathode Deposition Results for Temperature Variations of D Derived Cases (Temperature Variations)

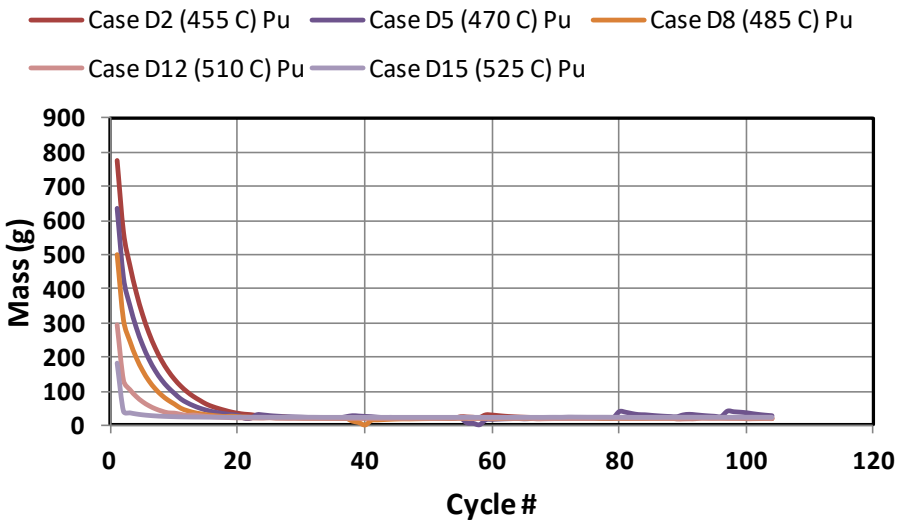

Figure 98- Pu Cathode Deposition Results for Temperature Variations of D Derived Cases (Temperature Variations)

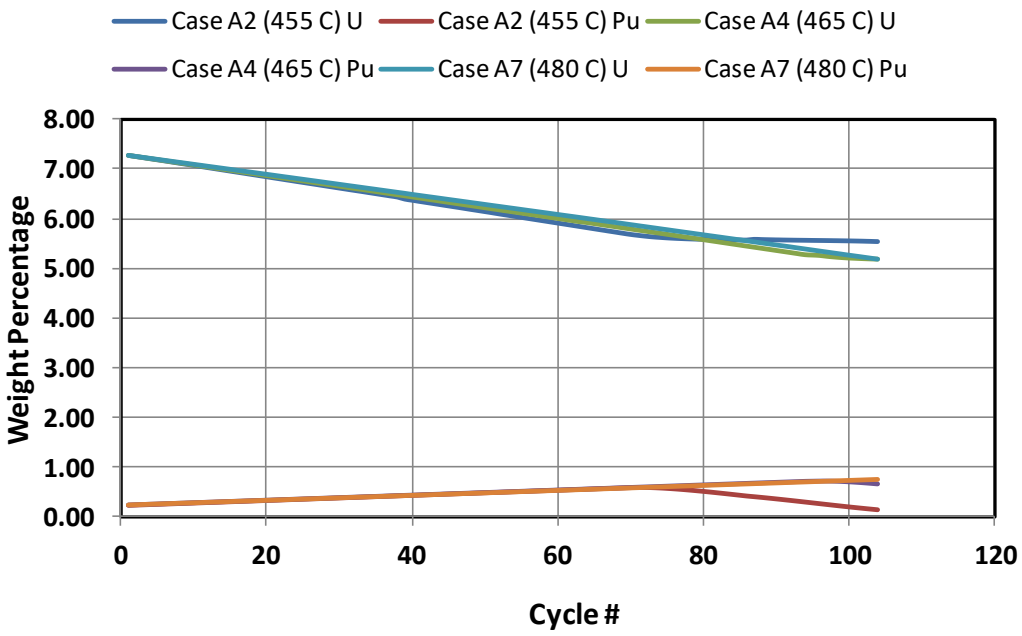

Figure 99- Salt Composition Results for Temperature Variations of A Derived Cases (Temperature Variations)

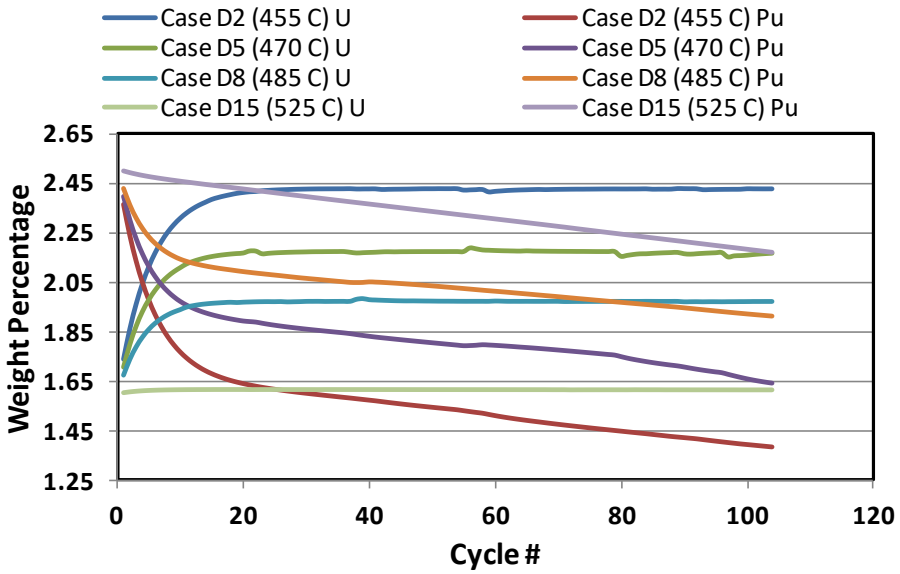

Figure 100-Salt Composition Results for Temperature Variations of D Derived Cases (Temperature Variations)

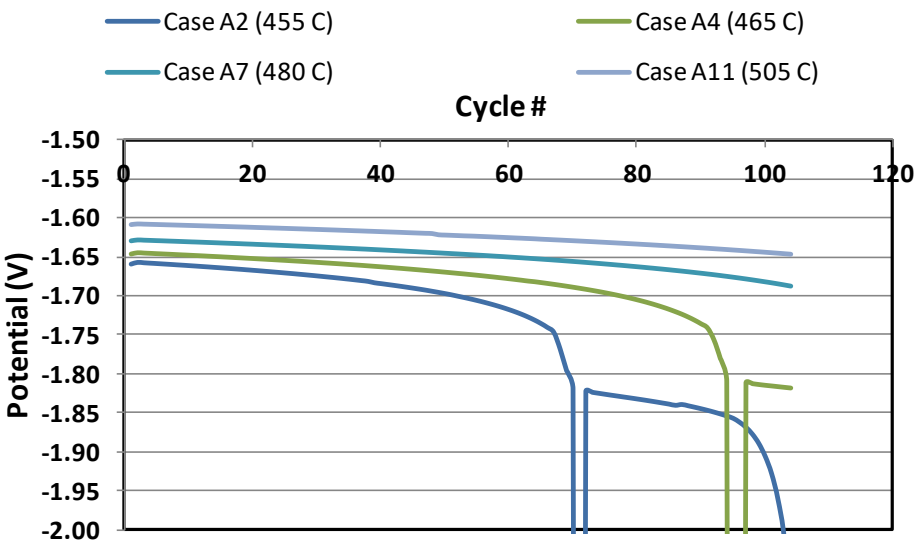

Figure 101- Cathode Potential Results for A Derived Cases (Temperature Variations)

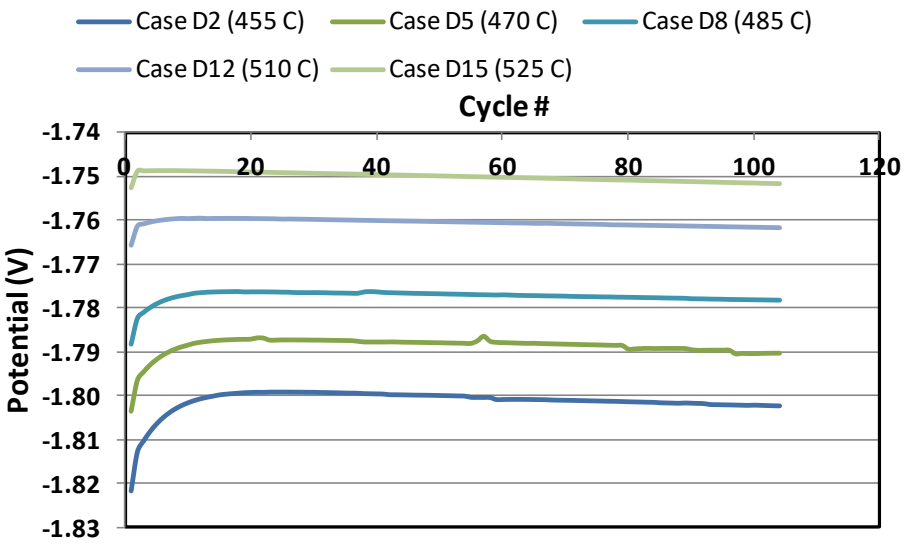

Figure 102-Cathode Potential Results for D Derived Cases (Temperature Variations)

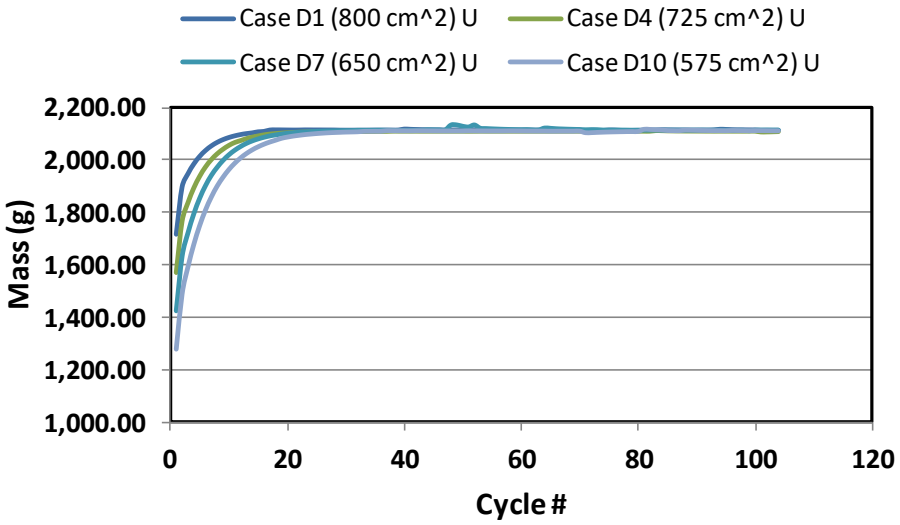

Figure 103- Long Term U Cathode Codeposition Results for D Derived Cases (Cathode Surface Area Variations)

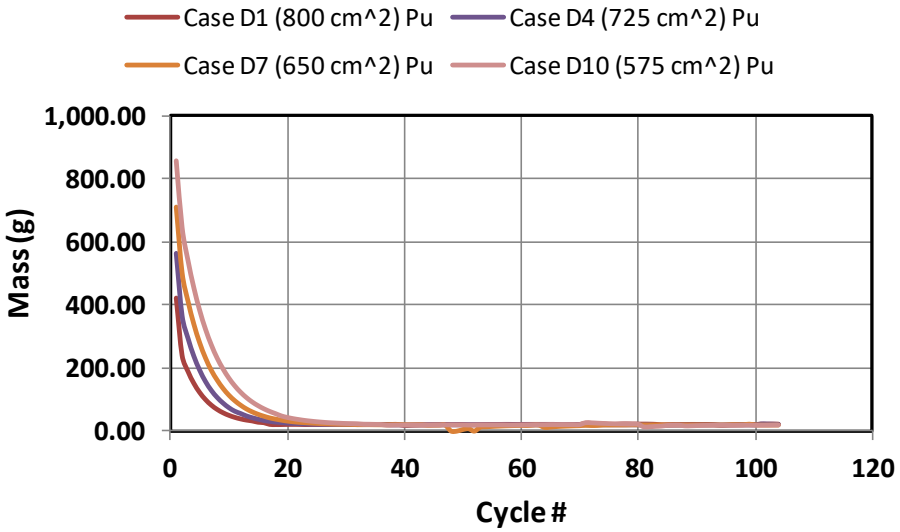

Figure 104- Long Term Cathode Pu Codeposition Results for D Derived Cases (Cathode Surface Area Variations)

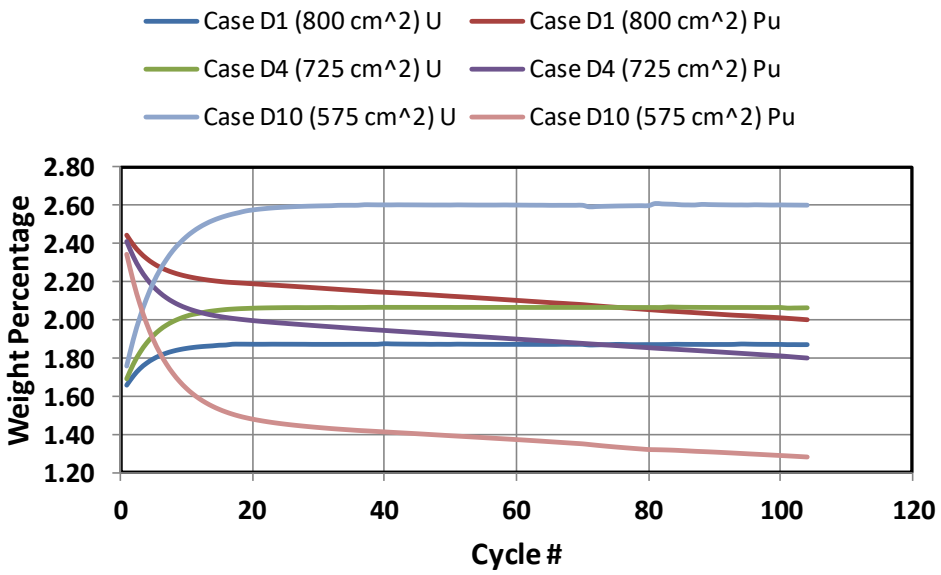

Figure 105-Long Term Salt Composition Results for D Derived Cases (Cathode Surface Area Variations)

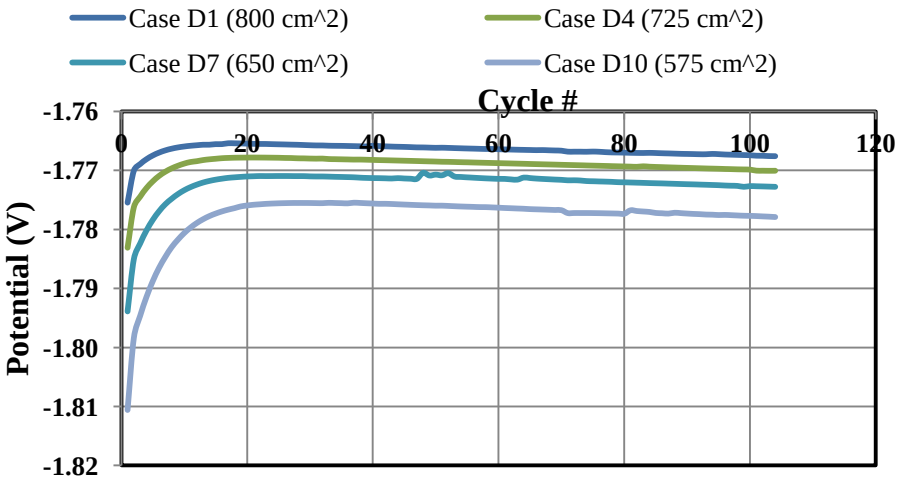

Figure 106- Long Term Cathode Potential Results for D Derived Cases (Cathode Surface Area Variations)

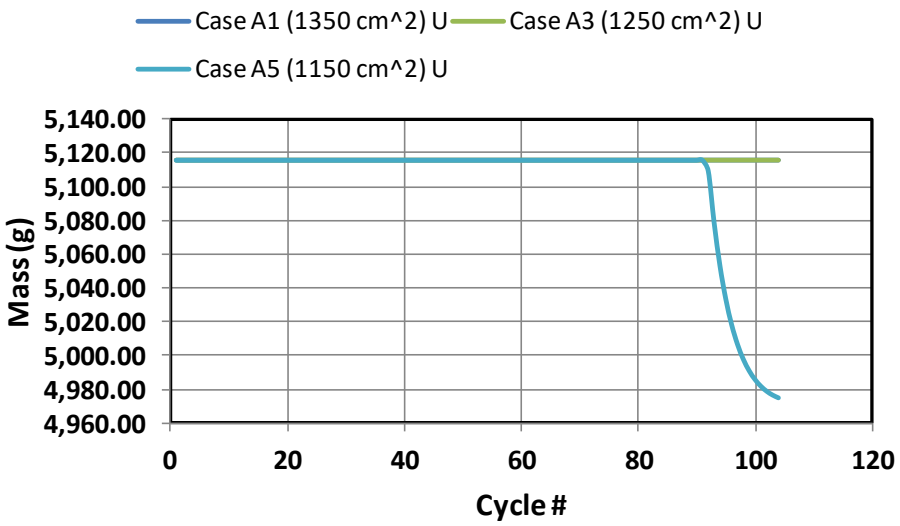

Figure 107- Long Term U Cathode Data for A Derived Cases (Anode Surface Area Variations)

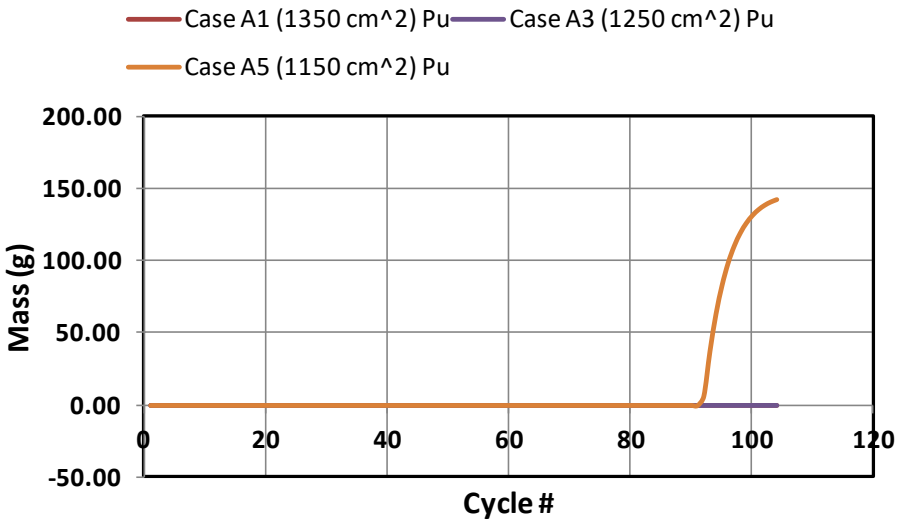

Figure 108- Long Term Pu Cathode Data for A Derived Cases (Anode Surface Area Variations)

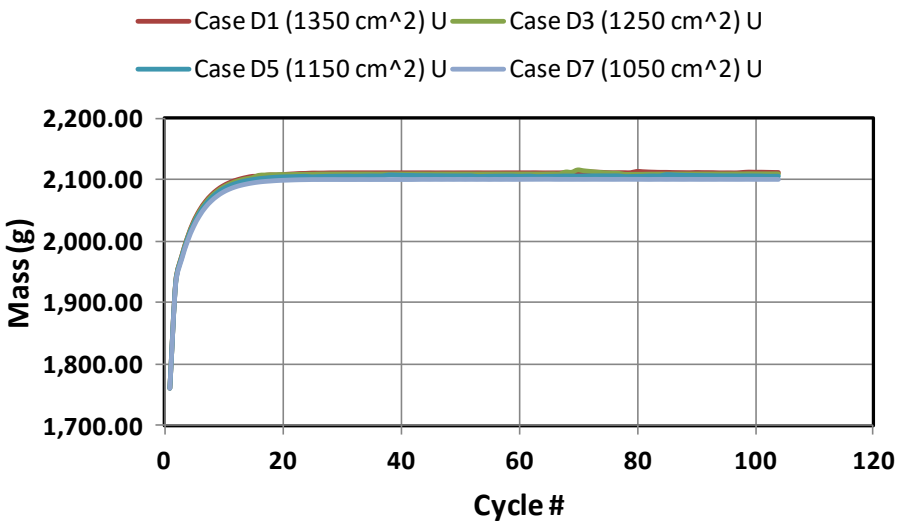

Figure 109- Long Term U Cathode Data for D Derived Cases (Anode Surface Area Variations)

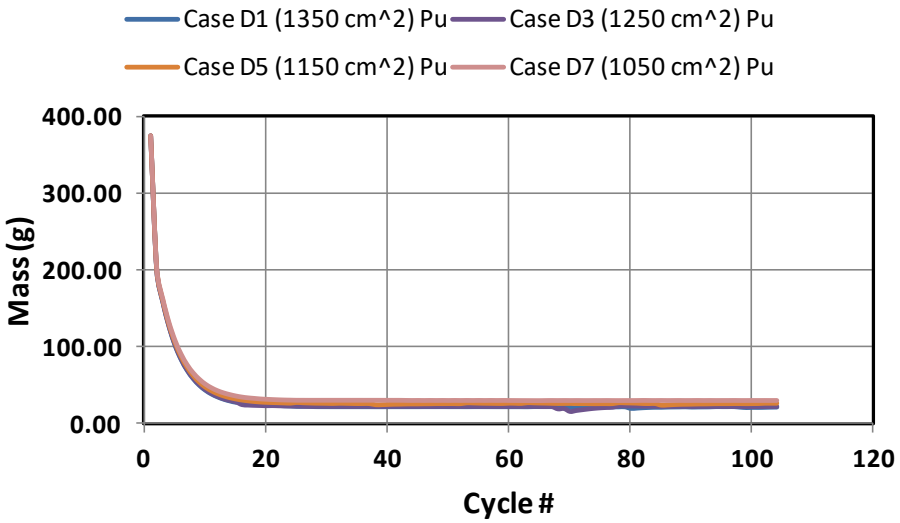

Figure 110- Long Term Pu Cathode Data for D Derived Cases (Anode Surface Area Variations)

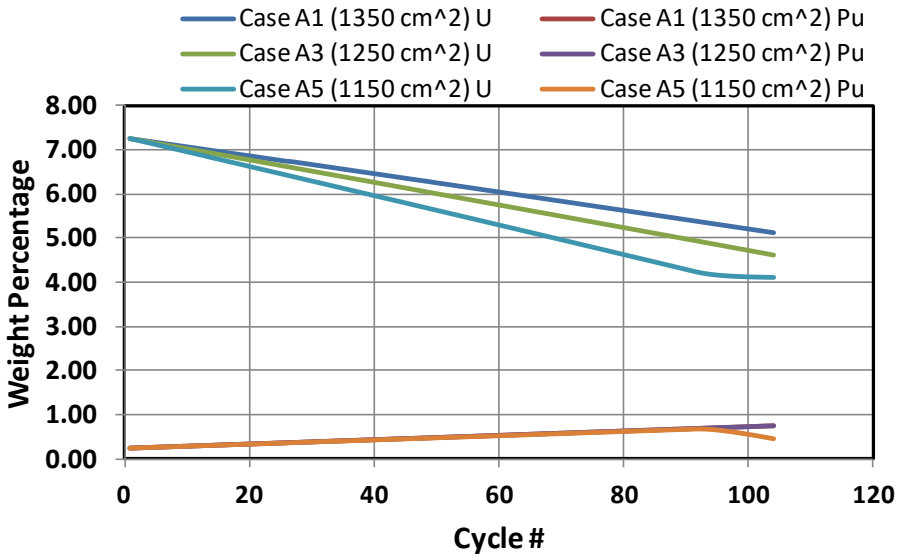

Figure 111- Long Term Salt Data for A Derived Cases (Anode Surface Area Variations)

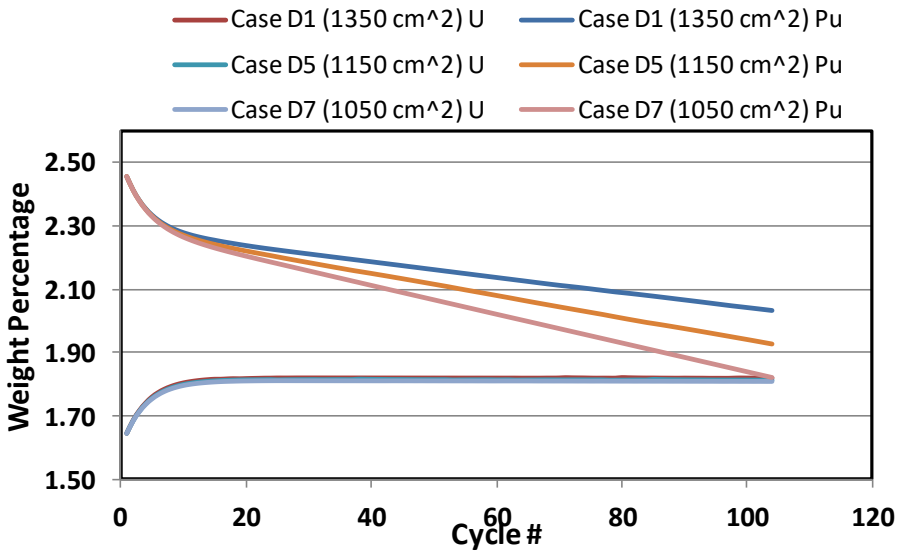

Figure 112-Long Term Salt Data for D Derived Cases (Anode Surface Area Variations)

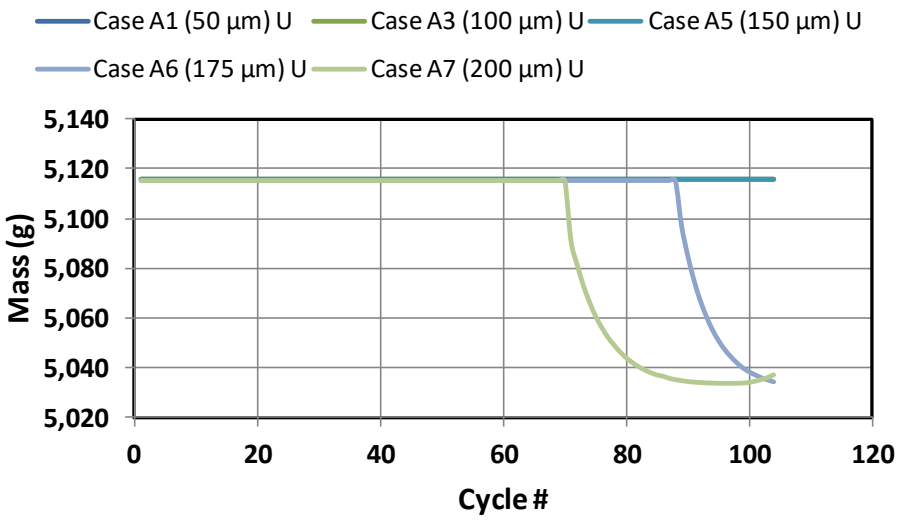

Figure 113- Long Term U Cathode Data for A Derived Cases (Cathode Rotation Rate Variation)

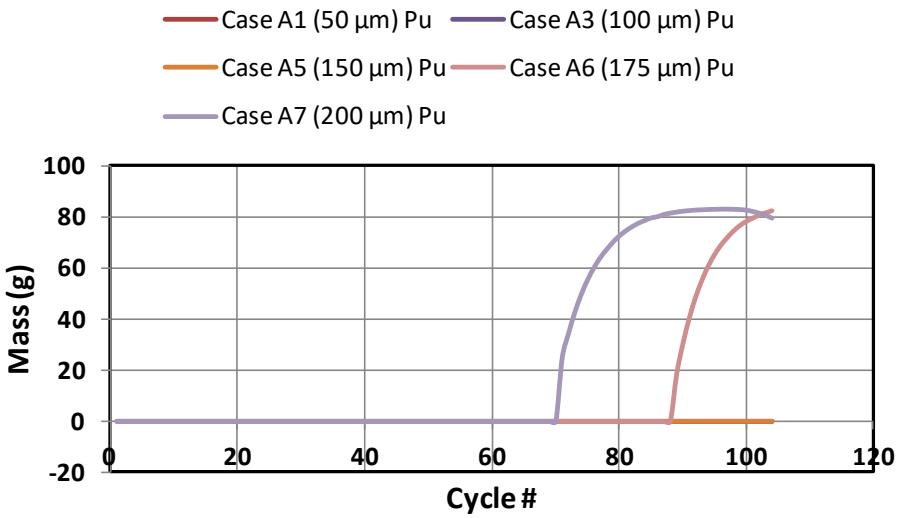

Figure 114- Long Term Pu Cathode Data for A Derived Cases (Cathode Rotation Rate Variation)

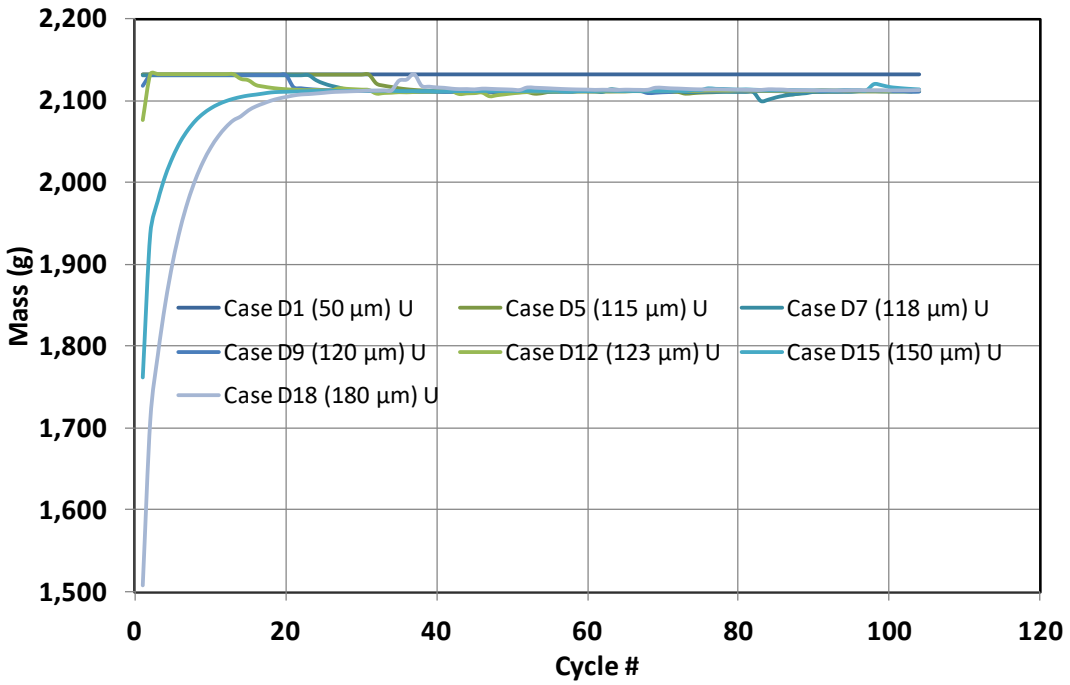

Figure 115- Long Term Cathode Data for D Derived Cases (Cathode Rotation Rate Variation)

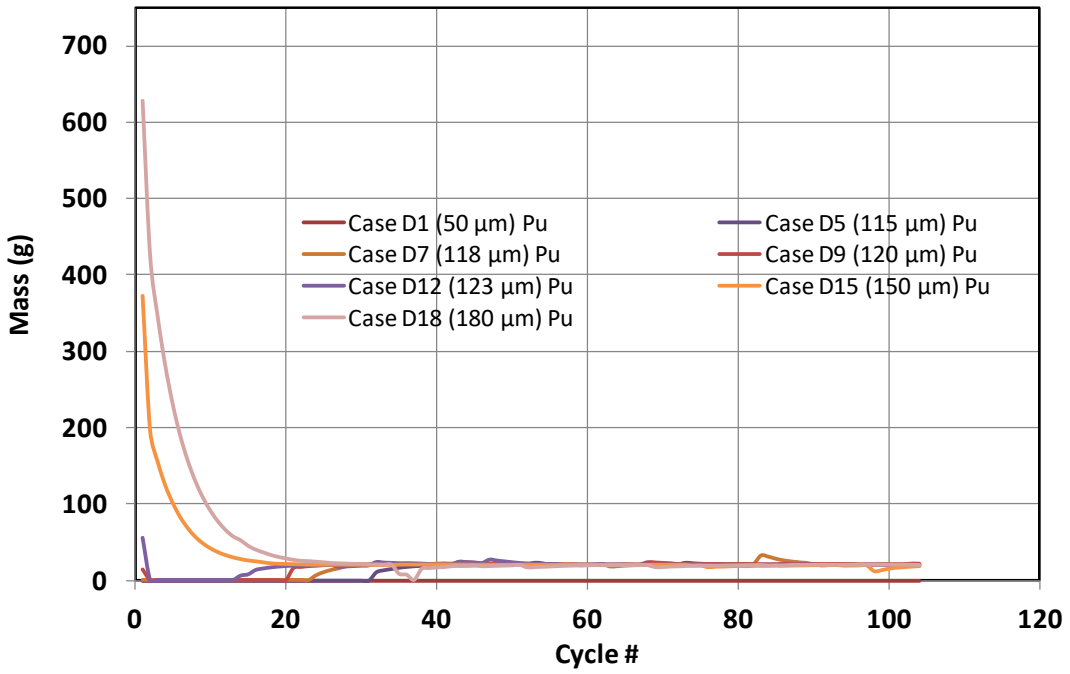

Figure 116- Long Term Pu Cathode Data for D Derived Cases (Cathode Rotation Rate Variation)

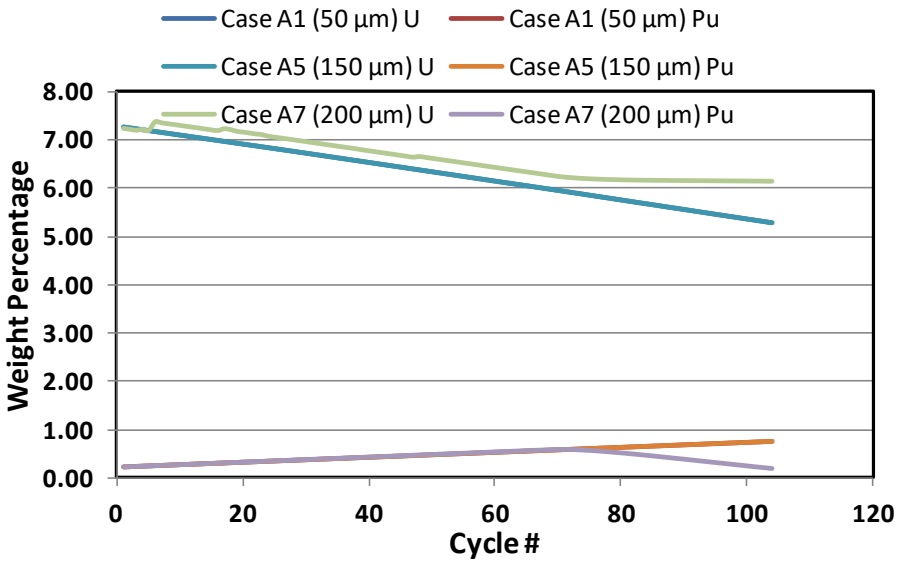

Figure 117- Long Term Salt Data for A Derived Cases (Cathode Rotation Rate Variation)

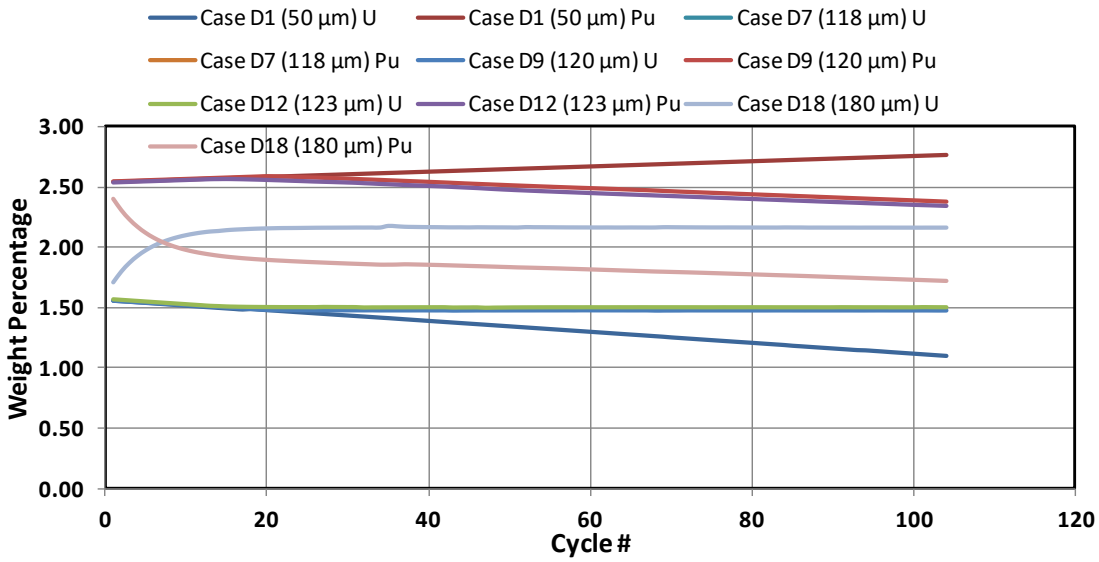

Figure 118- Long Term Salt Data for D Derived Cases (Cathode Rotation Rate Variation)

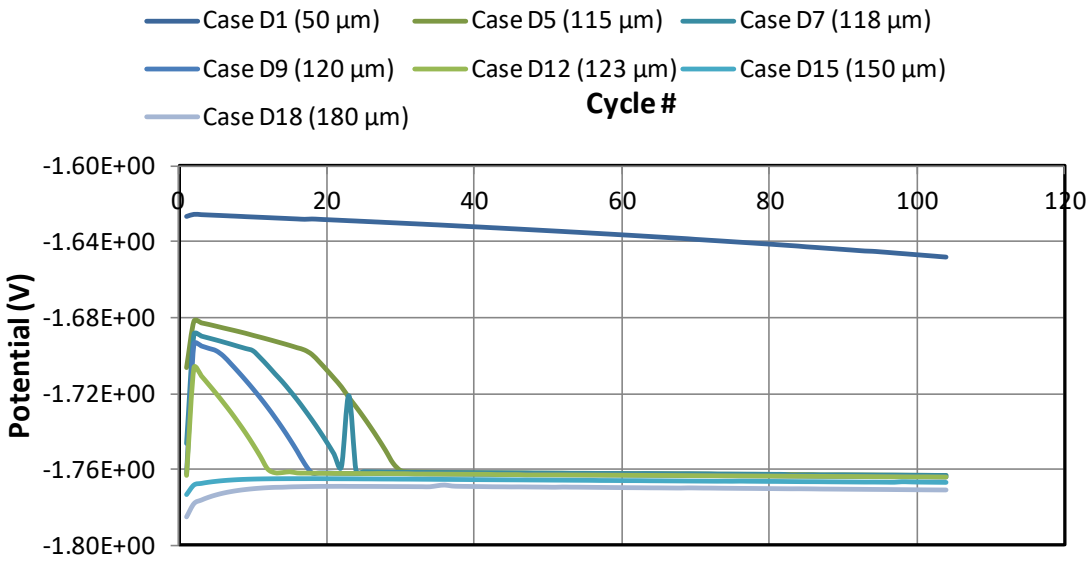

Figure 119- Cathode Potential Results D Derived Cases (Cathode Rotation Rate Variation)

APPENDIX C- LIST OF INITIALISMS

ANL- Argonne National Labs
AP-Additional Protocol
BNL- Brookhaven National Labs
CA-Chronoamperometry
CP-Chronopotentiometry
CSA- Comprehensive Safeguards Agreement
CV- Cyclic Voltammetry
DP- Detection Probability
ER- Electrorefiner
ERAD- Enhanced REFIN with Anodic Dissolution
FCF- Fuel Conditioning Facility
FMEA- Failure Mode and Effects Analysis
IAEA- International Atomic Energy Agency
IAT- Input Accountability Tank
ICPMS- Inertial Confined Plasma Mass Spectrometry
ID- Inventory Difference
INL- Idaho National Lab
KAERI- Korea Atomic Energy Research Institute
KMP- Key Measurement Point
LANL- Los Alamos National Labs
LCC- Liquid Cadmium Cathode
LIBS- Laser Induced Breakdown Spectrometry
LSODE- Livermore Solver Ordinary Differential Equations
MUF- Material Unaccounted For
NMA- Nuclear Material Accountancy
NNWS- Non-nuclear Weapon State
NPT- Non-proliferation Treaty
NPV- Normal Pulse Voltammetry
NRTA- Near Real Time Accountancy
ORNL- Oak Ridge National Labs
PM-Process Monitoring
POD- Probability of Detection
PRIDE- PyRoprocess Inactive integrated Demonstration
PV- Pulse Voltammetry
REPF- Reference Engineering Scale Pyroprocessing Facility
ROK- Republic of Korea
RPM- Rotations per Minute
SBD- Safeguards by Design
SBS-Signature Based Safeguards
SEID- Standard Error of Inventory Difference
SNM-Special Nuclear Material
SQ- Significant Quantity
SSPM- Safeguards and Security Performance Model
SWV- Square Wave Voltammetry

UNF- Used Nuclear Fuel

LIST OF REFERENCES

[1] B. Cipiti, F. Duran, B. Key, Y. Liu, I. Lozano and R. Ward, "Modeling and Design of Integrated Safeguards and Security for an Electrochemical Reprocessing Facility," Sandia National Laboratories, Albuquerque, 2012.

[2] R. Benedict, C. Solbrig, B. Westphal, T. Johnson, S. Li, K. Marsden and K. Goff, "Pyroprocessing Progress at Idaho National Laboratory," Idaho National Laboratory, Idaho Falls, 2007.

[3] IAEA, "Spent Fuel Reprocessing Options," IAEA, Vienna, 2008.

[4] H. Lee, G. Park, J.-W. Lee, K.-H. Kang, J.-M. Hur, J.-G. Kim, S. K.-T. Paek and I.-J. Cho, "Current Status of Pyroprocessing Development at KAERI," *Science and Technology of Nuclear Installations,* vol. 43, no. 4, pp. 317-328, 2011.

[5] T. Burr and etal., "Roles for Process Monitoring in Nuclear Safeguards at Aqueous Reprocessing Plants," *Journal of Nuclear Materials Management*, pp. 42-52, 2012.

[6] S. Johnson and M. Ehinger, "Designing and Operating for Safeguards: Lessons Learned from the Rokkasho Reprocessing Plant (RPP)," Pacific Northwest National Labs, Richland, 2010.

[7] T. Burr, C. Boyle, M. Baker, P. Felsher, M. Frank, G. Hemphill, B. Martinez and L. Ticknor, "Tool for Inventory Difference Evaluation with Flexible Material Balance Areas," Los Alamos National Laboratories, Los Alamos, 2012 .

[8] H. Garcia, M. Simpson, W. Lin, T. Yoo and R. Carlson, "Detecting Proliferation Activities via System-Centric Integration and Interpretation of Multi-Modal Data Collected from a System of Sensors," in *Proceedings of the 54th Annual INMM Meeting*, Palm Desert, 2013.

[9] M. F. Simpson, D. Rappleye, E. D. Blandford and H. Garcia, "Signature Based Safeguards Alternative to Nuclear Material Accountancy," in *Annual Institute for Nuclear Materials Management Meeting,* Atlanta, 2014.

[10] H. Garcia, W.-C. Lin and T.-S. Yoo, "Process Monitoring for Safeguards Via Even Generation, Integration, and Interpretation," in *Proceeds of the 51st Annual Institute for Nuclear Materials Management Meeting*, Baltimore, 2010.

[11] H. E. Garcia, W.-C. Lin and T.-S. Yoo, "Process Monitoring for Safeguards Via Event Generation, Integration, and Interpretation," Idaho National Labs, Idaho Falls, 2010.

[12] P. Lafreniere, D. Rappleye, R. Hoover, M. Simpson and E. Blandford, "Application of Signature- Based Safeguards to Electrorefining and the Ingot Casting Process," *Nuclear Technology,* vol. 189, no. 2, pp. 173-185, 2015.

[13] R. Hoover, P. Lafreniere and E. Blandford, "Commercial-Scale Electrorefiner Failure Modes and Implications for Operations and Safeguards," in *American Nuclear Society Transactions*, Reno, 2014.

[14] K. Kim, S. Choi, D. Ahn, S. Paek, B. Park, H. Lee, K. Yi and L. Hwang, "Computational Analysis of a molten-salt electrochemical system for nuclear waste treament," *Journal of Radioanalytical Nuclear Chemistry,* vol. 282, no. 1, pp. 449-453, 2009.

[15] P. Lafreniere, D. Rappleye, R. Hoover, M. Simpson and E. Blandford, "Modeling Non-Destructive Assay Based Signatures for Application to Safeguarding Pyroprocessing," in *Proceedings of ICAPP*, Charlotte, 2014.

[16] M. Williamson and J. Willit, "Pyroprocessing Flowsheets for Recycling Used Nuclear Fuel," *Nuclear Engineering and Technology,* vol. 43, no. 4, pp. 329-333, 2011.

[17] C. M. Hall, "Process of Reducing Aluminum from it Fluoride Salts by Electrolysis". US Patent 400664, 2 April 1889.

[18] Nuclear Energy Agency, "Pyrochemical Separations in Nuclear Applications," Organization for Economic Cooperation and Development, Paris, 2004.

[19] J. K. Jeon, "Safeguards Inspection Regime for Reference Pyroprocessing Facility in the ROK," in *Transactions of the Korean Nuclear Society Autumn Meeting*, Gyeongju, 2011.

[20] C. Baker, T. M. Pfeiffer, S. D. Hermann, S. B. Park and S.-H. Kim, "Development of a kg-Scale Oxide Reduction Module for Spent Light Water Reactor Fuel," in *2012 International Pyrorpocessing Research Conference*, Fontana, 2012.

[21] B. Westphal, K. Mardsen, J. Price and L. D.V., "On the Development of a Distillation Process for the Electrometallurgical Treatment of Irradiated Spent Nuclear Fuel," *Nuclear Engineering and Technology,* vol. 40, no. 3, pp. 163-174, 2008.

[22] G.-Y. Kim, T.-j. Kim, D. Yoon, D.-H. Ahn and S. Paek, "Development of Anode Structure for Electrowinning Process," in *Pyroprocessing Research Conference*, Fontana, 2012.

[23] Y.-Z. Cho, G.-H. Park, H.-C. Yang, D.-S. Han, H.-S. Lee and I.-T. Kim, "Minimization of Eutectic Salt Waste from Pyroprocessing by Oxidative Precipitation of Lanthanides," *Journal of Nuclear Science and Technology,* vol. 46, no. 10, pp. 1004-1011, 2009.

[24] A. N. Williams, S. Phongikaroon and M. F. Simpson, "Separation of CsCL from a ternary CsCl-LiCl-KCl Salt via a Melt Crystallization Technique for Pyroprocessing Waste Mimization," *Chemical Engineering Science,* vol. 89, no. 1, pp. 258-263, 2013.

[25] M. F. Simpson, T.-S. Yoo, R. W. Benedict, S. Phongikaroon, S. Frank, P. Sachdev and K. Hartman, "Strategic Minimization of High Level Waste From Pyroprocessing of Spent Nuclear Fuel," Idaho National Lab, Idaho Falls, 2007.

[26] J.-G. Kim, S.-J. Lee, S.-B. Park, S.-C. Hwang and H. Lee, "High-throughput Electrorefing System with Graphite Cathodes and Bucket-type Deposit Receiver," *Procedia Chemistry,* vol. 7, no. 1, pp. 754-757, 2012.

[27] K. Davies and S. X. Li, "Simplified Reference Electrode for Electrorefining of Spent Nuclear Fuel in High Temperature Molten Salt," in *Global*, Boise, 2007.

[28] A. Bard and L. Faulkner, Electrochemical Methods, New York: 1980, Wiley.

[29] International Atomic Energy Agency, "IAEA Safeguards Glossary," IAEA, Vienna, 2001.

[30] T. B. Cochran, "Adequacy of IAEA's Safeguards for Achieving Timely Detection,"

in *Nonproliferation Policy Education Center Conference*, London, 2005.

[31] United Nations, *Treaty on the Non-Proliferation of Nuclear Weapons*, Washington DC: United Nations, 1968.

[32] T. Burr, M. Hamada and C. Orton, "Data-Driven Versus Period-Driven Change Detection for Process Monitoring," in *Proceeding of the 53rd Annual Institute for Nuclear Materials Management Meeting*, Orlando, 2012.

[33] Nuclear Threat Initiative, "Additional Protocol," Nuclear Threat Initiative, Washington DC, 2012.

[34] IAEA, "IAEA Safeguards Technical Manual: Part F Statistical Concepts and Techniques Vol. 1," IAEA , Vienna, 1980.

[35] J. T. Nakos, "Uncertainty Analysis of Thermocouple Measurements Used in Normal and Abnormal Thermal Environment Experiments at Sandia's Radiant Heat Facility and Lurance Canyon Burn Site," Sandia National Labs, Albuquerque, 2004.

[36] B. F. G. Serrano, "Double bubbler precision differential pressure measurement system," in *Proceeding of 2012 ICAPP Working Group Meeting*, Chicago, 2012.

[37] H. Labert, "Study of a Dobule Bubbler for Material Balance in Liquids: Training Report 2013," Idaho National Laboratory , Idaho Falls, 2013.

[38] P. J. Brewer, D. Stoica and R. J. C. Brown, "Sensitivities of Key Parameters in the Preparation of Silver/Silver Chloride Electrodes Used in Harned Cell Measurements of pH," *Sensors*, vol. 11, no. 8, pp. 8072-8084, 2011.

[39] B. Rossiter and J. F. Hamilton, Physical Methods of Chemistry, New York: John Wiley and Sons Inc., 1986.

[40] M. Iizuka, T. Inoue, O. Shirai and Y. Arai, "Application of normal pulse voltammetry to on-line monitoring of actinide concentrations in molten salt electrolyte," *Journal of Nucelar Materials*, vol. 297, no. 1, pp. 43-51, 2001.

[41] Teratec, "LT880: Laser Tachometer Spec Sheet," Teratec, Oriskany, 2017.

[42] D. Henry and L. Palma, "Calibration of optical tachometers using a generator system of light pulses," in *Conference on Precision Electromagnetic Measurements*, Rio De Janeiro, 2014.

[43] A&D Company, Limited, "Estimates of the Uncertainty of the Calibration of Balances," A&D Company, Limited, Tokyo, 2016 .

[44] S. Metzger, H. Henschel and O. L. W. Kohn, "Silicon Carbide Radiation Detector for Harsh Environments," *IEEE Transactions on Nuclear Science*, vol. 49, no. 3, pp. 1351-1355, 2002.

[45] G. F. Knoll, Radiation Detection and Measurement, Hoboken: John Wiley and Sons, 2010.

[46] D. Reolly, N. Enselin, H. Smith Jr and S. Kretner, Passive Nondestructive Assay of Nuclear Materials, Los Alamos: Nuclear Regulatory Commission, 1991.

[47] IAEA, "Consultancy Meeting on Proliferation Resistance Aspects of Process Management and Process Monitoring/Operating Data," IAEA, Vienna, 2011.

[48] J. W. J. Durkee, "Characterization of Delayed-Neutron and Delayed-Gamma Pyroprocessing Emission Signatures Using MCNP6," Los Alamos National Labs,

Los Alamos, 2012.

[49] C. Hanson, S. Phongikaroon and J. R. Scott, "Temperature effect on Laser-induced breakdown spectroscopy spectra of molten and solid salts," *Spectrochimica Acta Part B:Atomic Spectroscopy,* vol. 97, no. 1, pp. 79-85, 2014.

[50] P. Lafreniere, R. Hoover and E. Blandford, "Determination of Pyroprocessing Cathode Processor Failure Modes and Intregation into a Signature-Based Safeguards (SBS) Framework," in *Proceeding of INMM Meeting*, Atlanta, 2014.

[51] US Department of Defense, *Military Standard: Procedures for Perofrming a Failure Mode, Effects and Criticality Analysis*, Washington DC: US Department of Defense, 1980.

[52] U.S. Army, "Failure Modes, Effects and Criticality Analysis (FMECA) for Command, Control, Communications, Computer, Intelligence, Surveillance, and Reconnaisance (C4ISR) Facilities," US Army, Washington D.C., 2006.

[53] D. Stamatis, Failure Mode and Effect Analysis: FMEA from Theoy to Execution, Milwaukee: ASQ Quality Press, 2003.

[54] R. Cumberland and M.-S. Yim, "Development of a 1D Transient Electrorefiner Model for Pyrprocess Simulations," in *Transactions of the American Nuclear Society*, Washington D.C., 2011.

[55] R. Cumberland, R. Hoover, S. Phongikaroon and M.-S. Y, "Analysis of Equilibirium Methods for the Computation Model of the Mark-IV Electrorefiner," *Nuclear Engineering and Technology,* vol. 43, no. 6, pp. 547-556, 2011.

[56] R. Cumberland, "1D and 3D Simulation of Electrochemical Behavior of U/UCl3 and Pu/PuCl3 in Molten Salt Systems (Thesis)," Korean Advanced Institute of Science and Technology, Daejon, 2013.

[57] P. Masset, R. Konings, R. Malmbeck, J. Serp and J. Glatz, "Thermochemical Propoerties of Lanthanides (Ln= La, Nd) and Actinides (An= U,Np,Pu,Am) in Molten LiCl-KCl Eutectic," *Journal of Nuclear Materials*, vol. 344, no. 1, pp. 173-179, 2005.

[58] T. Bechtel and T. Storvick, "Activity Coefficients of Actinide and Rare Earth Chlorides in Molten LiCl/KCl Eutectic Salt," *Industrial & Engineering Chemistry Research,* vol. 38, no. 1, pp. 1723-1728, 1999.

[59] P. Lafreniere, C. Zhang, M. Simpson and E. Blandford, "Lab Scale Electrochemical Codeposition Experiments for Comparison to Computational Predictions," *Submitted to Nuclear Engineering and Technology*, 2017.

[60] S. Li, "Experimental Observations on the Roles of the Cadmium Pool in the Mark-IV Electrorefiner," *Nuclear Technology,* vol. 162, no. 1, p. 144, 2008.

[61] J. P. Ackerman and W. E. Miller, "Electrorefining process and apparatus for recovery of uranium and a mixture of uranium and plutonium from spent fuels". US Patent US4880506A, 5 November 1987.

[62] Health and Safety Executive, "Report of the investigation into the leak of the dissolver product liquor at the Thermal Oxide Reprocessing Plant (THORP), Sellafield, notified to HSE on 20 April 2005," Health and Safety Executive , Sudbury, 2007.

[63] T. Lee, H. Kim, K. Jung and S. Park, "Status and Prospect of Safeguards by Design for the Pyroprocessing Facility," International Atomic Energy Agency, Vienna, 2010.

[64] T. Bjornard, R. Bean, P. C. Durst, J. Hockert and J. Morgan, "Implementing Safeguards-by-Design," Idaho National Laboratory, Idaho Falls, 2010.

[65] R. Wigeland, T. Bjornard and B. Castle, "The Concept of Goals-Driven Safeguards," Idaho National Labs, Idaho Falls, 2009.

[66] S. Phongikaroon, "Pyrochemical Research Group," University of Idaho, January 2014. [Online]. Available: https://sphongikaroon.files.wordpress.com/2014/01/pyro11.jpg. [Accessed 15 October 2014].

[67] S. M. Frank, "I-NERI Annual Technical Progress Report 2007-004-K Development and Characterization of New High-Level Waste Forms for Achieving Waste Minimization from Pyroprocessing," Idaho National Laboratory, Idaho Falls, 2010.